


École Doctorale Galileè
Laboratoire LSPM - Université Paris 13 **Laboratoire PMMH - ESPCI**

Crystal Plasticity Theory Accounting for GL(2,$\mathbb{Z}$) Symmetry

THÈSE

en vue de l'obtention du grade de

Docteur de Université Sorbonne Paris Cité

(spécialité Science des Matériaux)

par

Roberta BAGGIO

Composition du jury

Président :	Ioan Ionescu, Professeur Université Paris 13
Rapporteurs :	Marc Fivel, DR CNRS Université Grenoble Alpes Stefano Zapperi, Professeur Università degli Studi di Milano
Examinateurs :	Stéphanie Deschanel, MCF INSA Lyon Aurélien Vattré, Chercheur CEA
Directeurs de thèse :	Brigitte Bacroix, DR CNRS Université Paris 13 Lev Truskinovsky, DR CNRS ESPCI
Co-encadrant de thèse :	Oguz Umut Salman, CR CNRS Université Paris 13
Invité :	Jérôme Weiss, DR CNRS ISTerre

Acknowledgments

This work would not have been possible without the constant help and the advice of my thesis directors Lev Truskinovsky and Brigitte Bacroix. I am really grateful to them for their theoretical and human support during these three years of PhD. In particular, Lev Truskinovsky's theoretical advice is what gave the main structure to this Thesis work, and he was always available to help me in following my physical intuitions. I am equivalently grateful to my co-director Oguz Umut Salman for his help and advice. He was very generous in helping me with the numerical code, with the theory and the bibliography every time was needed.
I am extremely grateful to Sylvain Patinet of the PMMH laboratory, he offered himself to help me, by performing very interesting atomistic simulations. The fifth Chapter of this Thesis will not exist without his collaboration. I hope there will be the opportunity to develop further this work, which is still at an early stage.
I also thank all the members of the jury for agreeing to participate to my Thesis defense, they all gave very useful comments for improving this work. I am particularly grateful to professors Marc Fivel and Stefano Zapperi, who accepted the role of reviewers, providing very accurate reports.
My sincere thanks also to Sylvain Queyreau of LSPM, who helped me during my first year at Paris 13. I would therefore like to express my gratitude to Damien Vandembroucq, who was always available to help me and gave me very useful suggestions in preparing my thesis speech.
I then wish to acknowledge professor Giovanni Zanzotto, who first introduced me to $GL(2,\mathbb{Z})$ invariant energies.
I thank all the people that help me during this very first time in France. In particular, I am very grateful to my companion Benedettu, who has always supported and encouraged me, even in the most difficult times. Lastly, I thank my parents Paolo and Cristiana, to whom I owe who I am today.

Résume en Français

Cette thèse de doctorat porte sur le développement et l'étude d'une fonction de densité d'énergie pour les réseaux cristallins 2D dans le contexte de l'élasticité en déplacements finis. Ceci est réalisé par la mise en œuvre d'une nouvelle manière de prendre en compte la symétrie des matériaux. La méthodologie développée n'est plus limitée aux opérations orthogonales telles que l'invariance du réseau par rotation et réflexion, mais inclut également d'autres transformations non orthogonales, comme les cisaillements invariants. Ce type d'invariance est dicté par le groupe de symétrie globale qui, pour les réseaux de Bravais, coïncide avec le groupe de matrices entières et inversibles $GL(n, \mathbb{Z})$. La mise en œuvre de ce potentiel a pour effet d'obtenir un paysage énergétique contenant un nombre infini de puits de potentiel et caractérisé par un comportement périodique le long des directions de déformations en cisaillement. Ce comportement périodique est défini de manière tensorielle pour les déformations finies génériques. C'est donc un paysage beaucoup plus riche que celui utilisé par d'autres modèles dans lesquels une énergie périodique n'est associée que dans des directions prédéterminées, en termes de cinématique et formulée en termes de petites déformations. La thèse est structurée en six chapitres.

Dans le premier chapitre, qui a pour rôle d'introduction, le contexte général et l'état de l'art sont traités de manière synthétique. Les raisons pour lesquelles une meilleure compréhension de la plasticité cristalline est très importante sont brièvement rappelées. C'est un phénomène très complexe dans lequel le rôle déterminant est assumé par les dislocations, défauts du réseau cristallin qui facilitent le glissement relatif entre les plans du réseau et permettent ainsi la propagation de déformations permanentes. Le phénomène est rendu extrêmement compliqué par le fait que les dislocations peuvent interagir entre elles de plusieurs manières mais également avec d'autres défauts qui caractérisent le réseau cristallin, ce qui rend difficile la formulation de modèles capables de décrire le phénomène de manière précise et exhaustive. D'autre part, même avec les puissances de calcul actuelles, la description de ce phénomène en termes d'interactions entre atomes individuels est souvent prohibitive. Le chapitre décrit brièvement le concept de dislocation et son interprétation dans le contexte du solide continu, élastique et linéaire. Ensuite, les différentes méthodes utilisées pour modéliser les écoulements plastiques à l'échelle micro et nano sont rappelées, des modèles atomistiques aux approches dans lesquelles une

cinématique prenant en compte la présence de plans glissants est intégrée dans une formulation continue. Parmi les nombreux modèles proposés par la communauté scientifique, nous nous limitons à une exposition synthétique de certains des plus connus, en soulignant, pour chaque méthode, les principaux aspects, avantages et inconvénients, et la longueur d'échelle typique des simulations.

Dans le deuxième chapitre, on introduit l'énergie de déformation utilisée, pour le moment formulée sous forme d'énergie de réseau. Le chapitre commence par la discussion de quelques concepts de base de la cristallographie, dont la compréhension est nécessaire à la formulation de la densité d'énergie introduite. En particulier, nous décrivons les réseaux cristallins simples, appelés réseaux de Bravais, et définis comme des structures périodiques de points dans l'espace qui peuvent être décrites en termes de répétitions entières de deux vecteurs linéairement indépendants, les vecteurs de base $\mathbf{e}_I$ du réseau cristallin:

$$\mathcal{L}(\mathbf{e}_I) = \left\{ \mathbf{x} \in \mathbb{R}^2,\, \mathbf{x} = v_I \mathbf{e}_I,\, v_I \in \mathbb{Z} \right\} , \tag{1}$$

A partir d'un réseau, on associe une matrice de la métrique $C_{IJ} = \mathbf{e}_I \mathbf{e}_J$, par définition symétrique et définie positive. L'espace de configuration des métriques est donc le sous-espace Q_2^+ de matrices définies symétriques et positives. C'est l'espace 3D délimité par l'hyperboloïde $\det \mathbf{C} = C_{11}C_{22} - C12^2 > 0$. Contrairement aux vecteurs de base, la métrique $\mathbf{C}$ est invariante dans des rotations rigides et nous allons donc définir directement l'énergie en fonction de $\mathbf{C}$ plutôt que en fonction des vecteurs de base $\mathbf{e}_I$, l'énergie élastique devant satisfaire au principe d'invariance par rotation. L'invariance sous $GL(2,\mathbb{Z})$ prend en compte le fait que le même réseau peut être décrit avec des bases distinctes infinies, toutes reliées les unes aux autres au moyen d'opérations non orthogonales. Lorsque deux bases $\mathbf{e}_I$ et $\bar{\mathbf{e}}_I$ (et donc les métriques respectives) décrivent le même réseau, elles sont liées par l'action du groupe $GL(2,\mathbb{Z})$. Cela signifie que les deux métriques sont liées à travers l'opération:

$$\bar{\mathbf{C}} = \mathbf{m}^T \mathbf{C} \mathbf{m} \quad \bar{C}_{IJ} = m_{KI} C_{KL} m_{LJ} \, . \tag{2}$$

Puisque l'action du groupe $GL(2,\mathbb{Z})$ ne modifie pas le volume du réseau, les réseaux avec surface unitaire, situés sur l'hyperboloïde $\det \mathbf{C} = 1$, sont choisis comme référence. Cet hyperboloïde sera visualisé sur le disque de Poincaré. L'action de $GL(2,\mathbb{Z})$ sur l'espace des métriques divise cet espace en cinq orbites, chacune correspondant à l'un des 5 types possibles de réseau de Bravais en 2D (monoclinique primitif, orthorhombique primitif, orthorhombique centré, tétragonal primitif et hexagonal primitif). Pour nos besoins, il est utile de définir un domaine fondamental pour l'action de $GL(2,\mathbb{Z})$, afin que chaque type de réseau de Bravais ait un et un seul représentant. En fait, une fois qu'un domaine fondamental D a été identifié, il sera possible de définir une énergie de référence φ_0 uniquement sur celui-ci, puis d'étendre sa validité à l'ensemble de l'espace métrique en utilisant:

$$\varphi(\mathbf{C}) = \varphi(\mathbf{m}^t \mathbf{C} \mathbf{m}) = \varphi_0(\tilde{\mathbf{C}}) \, . \tag{3}$$

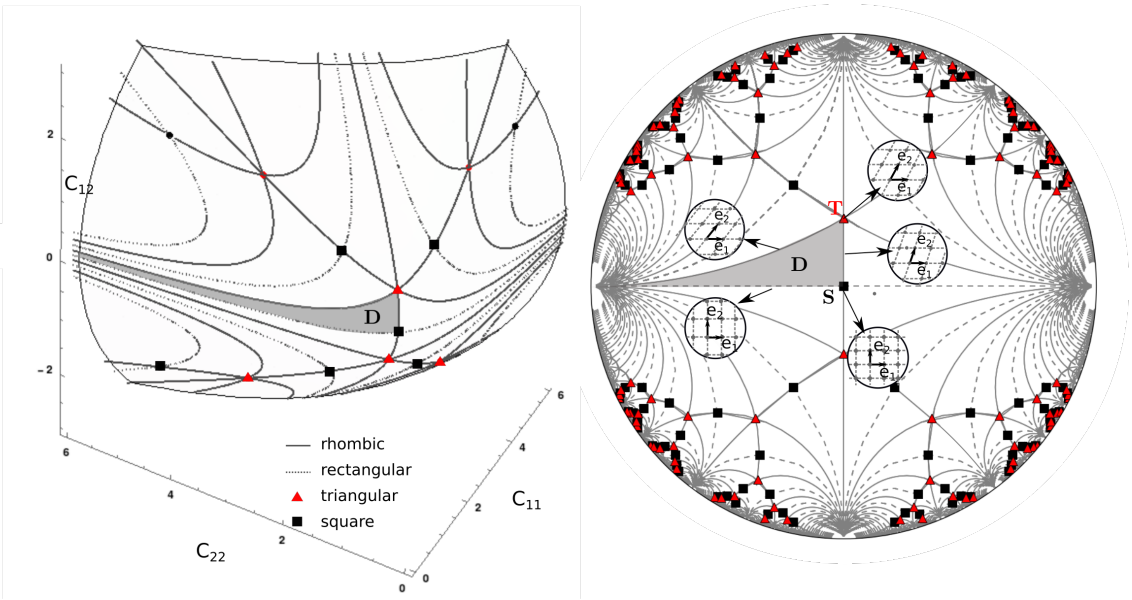

Pour que cela soit réellement possible, il est nécessaire de disposer d'un mapping qui, à partir du $\mathbf{C}$ générique, renvoie le $\tilde{\mathbf{C}}$ correspondant sur le domaine fondamental. Ceci peut être facilement réalisé si D est choisi comme:

$$D = \left\{ C \in \mathcal{Q}_2^+, \quad 0 < C_{11} \leq C_{22}, \quad 0 \leq C_{12} \leq \frac{C_{11}}{2} \right\}. \tag{4}$$

En fait, pour ce choix de D, la matrice $\mathbf{m}$ qui relie une base générique à la base de référence correspondante est une procédure itérative appelée réduction de Lagrange. Elle consiste à choisir parmi toutes les métriques équivalentes possibles celle à laquelle correspond la base réduite, qui est donnée par:

- $\tilde{\mathbf{e}}_1$ est le vecteur du réseau le plus court.
- $\tilde{\mathbf{e}}_2$ est le vecteur du réseau le plus court non colinéaire avec $\tilde{\mathbf{e}}_1$ et pour lequel le signe est choisi de sorte que l'angle entre les deux soit aigu.

Une fois que D a été choisi de cette manière, il est nécessaire de définir l'énergie de référence sur celle-ci. Elle doit satisfaire au moins une continuité $\mathcal{C}^2$ sur les contours de D, de manière à assurer la continuité du module d'élasticité. On utilise la procédure développée par Conti et Zanzotto [CZ04], où l'énergie de référence est définie par l'assemblage de polynômes appropriés satisfaisant la continuité requise. Ce φ permet de modéliser, pour un choix de coefficients appropriés, un réseau carré à symétrie carrée ou un réseau triangulaire à symétrie hexagonale. Après la construction de l'énergie, le paysage énergétique périodique ainsi obtenu est décrit en détail, pour les symétries carrée et hexagonale. L'énergie prend

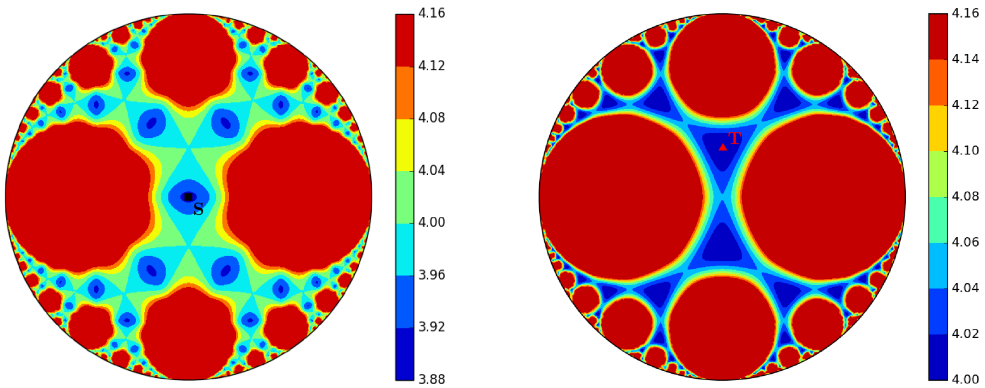

automatiquement en compte la présence de directions à faible coût énergétique le long des plans cristallographiques. De plus, elle représente pleinement l'asymétrie d'énergie qui caractérise les directions génériques du cisaillement. Les trajets de chargement qui coïncident avec les bords de D sont particulièrement intéressants. Ce sont des cisaillements purs qui, dans une formulation non linéaire, diffèrent des cisaillements simples en termes de déformation réelle et pas seulement en termes de rotation rigide. Ce sont des trajets de chargement qui déforment le réseau dans des configurations rectangulaires et rhombiques respectivement. Le trajet qui relie le point de symétrie carré S au point de réseau triangulaire T est, pour les deux énergies considérées, le trajet caractérisé par la barrière d'énergie la plus basse de tous les trajets de chargement apparaissant à partir de la configuration de référence non déformée. L'autre frontière de D convergeant dans la symétrie considérée (il s'agit d'une transformation rectangulaire dans le cas de S et d'un autre type de déformation rhombique dans le cas de T) est le trajet qui évolue vers l'infini vers une barrière énergétique de plus en plus haute, sans rencontrer aucun autre puits de potentiel.

L'importance de la définition du modèle en termes de déformations non linéaires est également abordée dans le chapitre 2. En fait, les configurations qui, en termes de $\mathbf{C}$, sont distinctes et identifiées par différents points de l'hyperboloïde se superposent en termes de déformation linéaire. Un exemple concret de ceci est donné.

Au chapitre 3, la densité d'énergie introduite jusqu'à présent en termes d'énergie de réseau est introduite dans une formulation continue et hyperélastique. Pour que cela soit possible, il est nécessaire de supposer que l'hypothèse de Cauchy Born est valide. Cette hypothèse affirme que le réseau cristallin associé à un point générique de l'objet $\mathbf{X}$ est

déformé selon le gradient de déformation en ce point $F = \frac{\partial \mathbf{x}}{\partial \mathbf{x}}$:

$$\mathbf{e}_i = F_{iJ}\mathbf{e}_J. \tag{5}$$

Par conséquent, dans cette hypothèse, il est possible de faire coïncider la densité d'énergie ϕ du corps continu avec la densité d'énergie φ introduite pour le réseau cristallin:

$$\phi(\mathbf{F}) := \varphi(\mathbf{F}\mathbf{e}_I) = \varphi(\mathbf{e}_i), \tag{6}$$

En particulier, le tenseur métrique coïncide avec le tenseur de déformation non linéaire de Cauchy-Green droit, exprimé dans la base de référence.

Le problème élastique est introduit dans sa forme forte et une fonction introduisant l'énergie potentielle associée au corps est introduite. La méthode utilisée pour la solution, appelée méthode des éléments finis, est ensuite brièvement décrite. Elle consiste à trouver une solution approchée du problème exprimé sous une forme faible, c'est-à-dire rechercher un minimum pour l'énergie potentielle. Dans notre cas, la discrétisation rendue nécessaire pour résoudre le problème prend également un sens physique, l'énergie invariante $GL(2,\mathbb{Z})$ nécessitant une régularisation. Le domaine est divisé en une série d'éléments réguliers. Chacun de ces éléments représente un ensemble d'atomes tel que le paysage énergétique qui leur est associé est périodique. Avec un exemple simple, il est montré que le nombre d'atomes associé à cette hypothèse est en réalité réduit. Le chapitre se termine par une illustration d'une dislocation isolée telle qu'elle apparaît dans le modèle. Deux exemples simples d'interaction entre deux dislocations distinctes sont également discutés.

Au chapitre 4, le modèle introduit est utilisé pour étudier la nucléation homogène de dislocations dans un cristal parfait. Deux symétries différentes sont montrées (cristal carré et triangulaire) et différents trajets de chargement sont étudiés. En particulier, différents cisaillements simples sont considérées en plus des cisaillements purs mentionnés ci-dessus. Cette étude est accompagnée d'un critère de stabilité analytique, basé sur la positivité définie du tenseur acoustique q_{ik}:

$$q_{ik} = n_j n_k \mathsf{a}_{ijkl}\,, \tag{7}$$

avec:

$$\mathsf{a}_{ijkl} = F_{jR}F_{lS}\mathcal{A}_{iRkS} \quad \mathcal{A}_{iRkS} = \frac{\partial^2 \phi}{\partial F_{iR}\partial F_{kS}}\,, \tag{8}$$

Ce tenseur est lié aux conditions de propagation des ondes d'accélération dans le matériau, dont le lien avec la stabilité et l'unicité de la solution homogène est connu. En particulier, lorsque la positivité définie est perdue pour une certaine direction $\mathbf{n}$, une onde stationnaire est admise dans cette direction de propagation. Donc l'unicité de la solution homogène fait défaut et de nouvelles augmentations de charge entraînent une instabilité de cette

solution. Le cristal se réorganise en un équilibre différent dans lequel différents puits de potentiel sont occupés simultanément, donnant lieu à une microstructure caractérisée par la présence de défauts de réseau. Les résultats numériques sont en accord avec cette analyse. Pour les deux symétries, il existe un bon accord avec la charge critique fournie par l'analyse basée sur le tenseur acoustique. Les deux symétries montrent la formation de microstructures diverses et complexes dès la première perte d'instabilité. Les situations les plus intéressantes se produisent aux transformations rhombiques et rectangulaires correspondant aux limites du domaine fondamental, tandis que les simples déformations de cisaillement réparties de manière variable dans le paysage énergétique donnent lieu à des situations intermédiaires. En particulier, le long de la transformation rhombique entre les points T et S, les deux symétries montrent la présence d'une nucléation simultanée de deux types de dislocations différents, en accord avec l'analyse du tenseur acoustique qui prévoit la présence simultanée de deux modes d'instabilité. Dans les deux cas, le point selle associé à l'autre symétrie (c'est-à-dire T pour le réseau S et S pour le réseau T) est un point de selle connecté à un couplage non trivial entre différents systèmes de glissement. L'autre cisaillement pur donne également lieu à des phénomènes intéressants. Dans le cas de la symétrie carrée, il y a une réorganisation globale du cristal, qui semble être en rotation. En analysant la microstructure, nous constatons que cette rotation est obtenue par une combinaison fine des cisaillements invariants. Dans le réseau triangulaire, on peut encore voir une double activation du système de glissement, du fait que la direction du mode d'instabilité est orientée exactement à mi-chemin entre ces deux systèmes de glissement. On déduit de ces résultats que le paysage périodique identifié par $GL(2,\mathbb{Z})$ permet de décrire le phénomène de nucléation de manière beaucoup plus riche et variée que ne le permettent d'autres modèles périodiques formulés en termes de déformations linéaires.

Dans le chapitre 5, une autre densité d'énergie $GL(2,\mathbb{Z})$ invariante est développée directement à partir d'un potentiel interatomique de type Lennard-Jones. Nous montrons que nombre des effets décrits plus haut par l'énergie polynomiale se retrouvent également dans ce cas, et sont donc associés à la forme périodique imposée par la symétrie globale et non à l'effet de la construction particulière de l'énergie de référence dans le domaine fondamental D. Certaines différences apparaissent à la suite de la modélisation différente utilisée pour la partie volumique de l'énergie. Cela avait été modélisé empiriquement dans le cas de l'énergie polynomiale alors que dans ce cas, il est directement imposé par la forme du potentiel interatomique utilisé. En conséquence de la modélisation différente du volume, certains types de défauts apparaissent, tels que les vides et les microfractures, qui n'avaient pas été mis en évidence auparavant. Nous avons nommé l'énergie ainsi construite "Lennard-Jones homogène". En fait, il ne s'agit pas d'une approche purement atomistique, puisque l'invariance de $GL(2,\mathbb{Z})$ suppose qu'un certain nombre d'atomes se déforment de manière homogène autour du point considéré. Pour mieux quantifier les effets de cette approximation, une comparaison directe est faite ensuite entre cette méthode et certaines simulations atomistiques utilisant le même potentiel. Bien que la structure du cœur de la dislocation

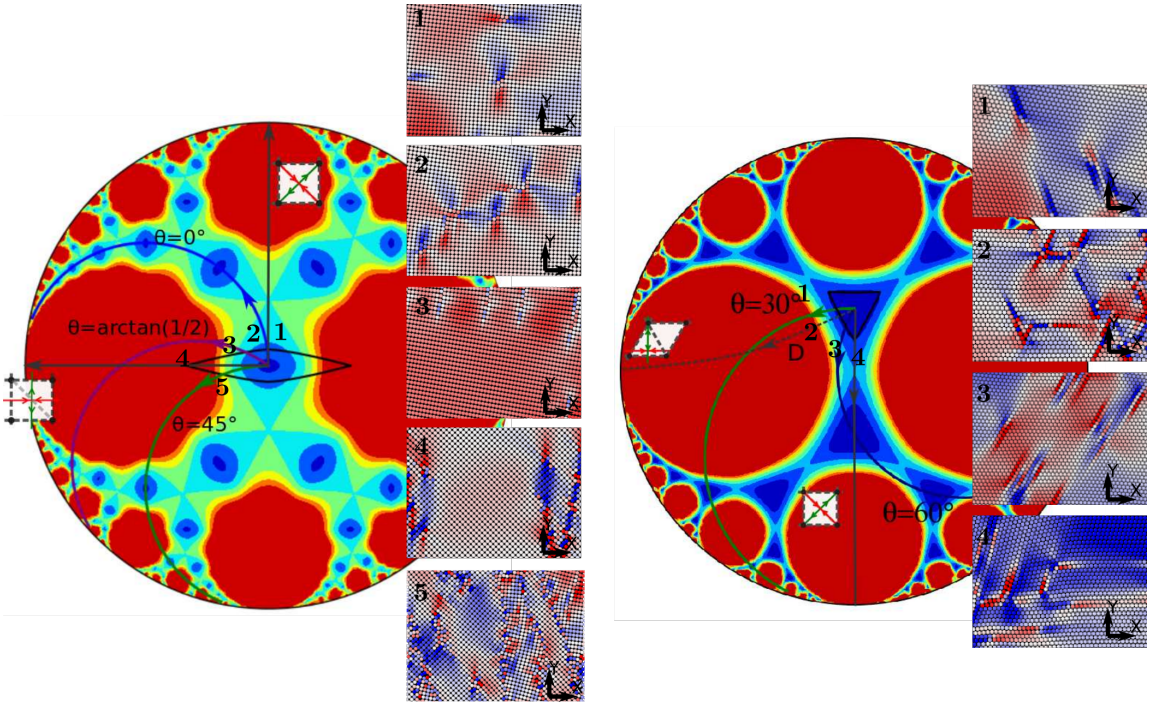

soit représentée de manière approximative, d'importantes analogies sont observées concernant les types de microstructure observées à la suite d'une nucléation homogène. Des résultats des simulations de nanoindentation sont ensuite présentés. Ici aussi, il existe une certaine analogie en termes de charge critique et de type de nucléation. Cependant, le modèle $GL(2,\mathbb{Z})$ présente certaines limites dans la représentation de l'évolution des microstructures qui, soumises à la contrainte de compatibilité, (implicite dans la formulation continue), s'avèrent parfois trop rigides.

Le chapitre 6 est réservé aux conclusions et développements futurs. La méthode proposée est comparée aux autres approches présentées au chapitre 1 pour mettre en évidence ses caractéristiques innovantes. Nous discutons ensuite des développements possibles, dont le plus important est certainement l'extension du modèle aux trois dimensions.

Contents

1 Introduction **1**
- 1.1 The Idea of Dislocations . . . 3
- 1.2 Atomistic Modelling . . . 5
- 1.3 Multiscale Models . . . 8
  - 1.3.1 The Quasi-Continuum Method . . . 9
  - 1.3.2 Discrete Dislocations Dynamics . . . 12
  - 1.3.3 Phase Field Method . . . 14
  - 1.3.4 Crystal Plasticity Theory . . . 16
  - 1.3.5 Conclusions . . . 18

2 The Model **21**
- 2.1 Notions of Crystallography . . . 25
  - 2.1.1 Bravais Lattices in **C** Space . . . 28
- 2.2 Energy Construction . . . 32
  - 2.2.1 Polynomial Energy . . . 34
  - 2.2.2 Energy Landscape . . . 38
  - 2.2.3 Additional Remarks . . . 46

3 Continuum Formulation and Numerical Implementation **51**
- 3.1 The Hyperelastic Boundary Value Problem . . . 52
- 3.2 The Energy φ in the Continuum Formulation . . . 56
- 3.3 Regularization . . . 58
- 3.4 Numerical Implementation . . . 59
- 3.5 Model Validation . . . 62
  - 3.5.1 Dislocation Core Sructure . . . 62
  - 3.5.2 Dislocation Interactions . . . 66

4 Homogeneous Nucleation **71**
- 4.1 Stability Criterion . . . 72
- 4.2 Square Lattice . . . 74
  - 4.2.1 Stability analysis . . . 74

4.2.2 Simulations Results 80
4.3 Triangular Lattice 92
4.3.1 Stability analysis 92
4.3.2 Simulations Results 97
4.3.3 Beyond the First Instability: Some Perspectives 106
4.4 Conclusive Remarks 109

5 GL(2,$\mathbb{Z}$) Invariant Energy based on Interatomic Potentials 113
5.1 Energy Construction 114
5.1.1 Energy Landscape 117
5.1.2 Homogeneous Nucleation 123
5.2 Comparison with Molecular Statics 133
5.2.1 Dislocation Core 134
5.2.2 Homogeneous Nucleation 135
5.2.3 Nanoindentation 146
5.2.4 Concluding Remarks 151

6 Conclusions and Perspectives 155

List of Figures

1.1 Left: **Schematic Representation of a Dislocation:** it can be considered as the lattice distortion associated to the presence of an extra crystallographic plane that is inserted in the upper half of the crystal (a) or as the distortion separating the slipped from the unslipped part of the crystal (b). Image taken from [ST12]. Right: **The Burgers Circuit:** defining the Burgers vector associated to the enclosed dislocation(s) (from [HB01]) . . . 4

1.2 **Cauchy Stress Contours** about a positive edge dislocation. 5

1.3 **Lennard-Jones Pair Interaction:** Both long range attraction and short range repulsion are represented. It is possible to notice that upon a certain distance r interaction becomes zero. 7

1.4 **Modelling Techniques and Spanned Lenght Scales:** Schematic illustration of the tipical lenght scales spanned by simulations with the four illustrated models for small-scale plasticity. 10

2.1 **Lattice Invariant Shears:** Schematic representation of shear invariance for a square lattice subjected to simple shear $\mathbb{S} = \mathbf{I} + \alpha \mathbf{e}_1 \otimes \mathbf{e}_2$. Energy density φ has to be minimum in correspondence of equivalent lattice configurations, i.e. for every integer α. 22

2.2 **Energetic Profile of a Dislocation:** Schematic representation of a dislocation as the boundary between sheared and unsheared crystal regions. Two energetically equivalent square crystal configurations are made compatible thanks to the presence of an edge dislocation. Lattice elements belonging to the core are higher in energy and their energetic state is located up the energy barriers. 22

2.3 **Bravais Lattice:** Schematic representation of a simple, Bravais, lattice. It is fully described by an integer basis $\{\mathbf{e}_I\}$ which, periodically translated in space, defines the lattice. Choices for the integer basis $\{\mathbf{e}_I\}$ are infinite, but all these basis are in relation by the action of the global symmetry group $GL(2, \mathbb{Z})$. 26

2.4 **Configurational Space:** a) Illustration of strain space C_{11},C_{12},C_{22}. Admissible metric tensors should satisfy condition $\det \mathbf{C} > 0$, which corresponds to a hyperboloid in the C_{11},C_{12},C_{22} space. A portion of the infinite hyperbolic surface $\det \mathbf{C} = 1$, containing all simple lattices of unit volume, is shown as reference. b) Relation between different square symmetry metric points is illustrated schematically. These lattices are equivalent but characterized by a different choice of the lattice basis vectors $\{\mathbf{e}_I\}$. 31

2.5 **Poincaré Representation of the Configurational Space:** space $\det \mathbf{C} = 1$ in the Poincaré disk representation. For the sake of clarity, only some of the infinite square and triangular lattices are illustrated explicitly. Full and dashed lines, corresponding to rhombic and rectangular lattices, respectively, are geodesics in the hyperbolic space. . . 32

2.6 **Maximal EPNs:** Examples of maximal EPNs in $\mathcal{Q}_2^+$, indicated as dashed areas (fundamental domain D is also shown). Maximal EPN for a square lattice metric (on top), and for a triangular lattice metric (on bottom). In both cases, the boundary does not belong to the (open) maximal EPN. 36

2.7 **Energy Landscape:** Energy landscape corresponding to energy density (2.27) for square symmetry $\beta = -\frac{1}{4}$ (on top) and hexagonal symmetry $\beta = 4$ (on bottom) is illustrated on the Poincaré disk. Color indicates the energy level, blue-low, red-high. An upper cut-off of 4.15 has been used for the highest-energy values for an improved visualization of low-energy barriers and wells. 39

2.8 **Shear Loading Paths:** Energy landscape for different shearing paths $\theta = 0°$, $\theta = \arctan(1/2)$ and $\theta = 45°$ is shown. Shear asymmetry and different periodic behavior along general shearing directions are fully described. 41

2.9 **Square Symmetry Reference Well:** Configuration of square wells near reference well $\mathbf{S}$, the simple shears $\theta = 0°$ and $\theta = 90°$ are showed with continue blue lines while pure shear paths are showed with differently dashed blue lines (b). Energy landscape along these low energy barriers is illustrated with evidence of triangular lattice point $\mathbf{T}$, located in the upper vertex of the fundamental domain. In (c) the graphs of energy profiles corresponding to skinny and fat rhombic paths are shown, together with the $\theta = 0°$ shear path. 43

2.10 **Linear and Nonlinear Configurational Spaces:** Representation of nonlinear and linear $\theta = 0°$, $\theta = 90°$ shearing paths. Linearized strain components are situated on plane $tr(\mathbf{C}) = 2$, tangent to the initial undeformed configuration $\mathbf{S}$. As the square configurations $\mathbf{S}_0^{+1}$ and $\mathbf{S}_{90}^{-1}$ differ for a nonlinear component, they result merged in one point the linearized strain space. 44

2.11 **Shear Loading Paths in the Triangular Lattice:** Energy landscape for shearing paths $\theta = 30°$ and $\theta = 60°$ is shown. The different periodic behaviors along general shearing directions are fully described. 45

2.12 **Hexagonal Symmetry Reference Well:** Configuration of triangular wells near the reference well **T**. Simple shears $\theta = 0°$, $60°$ and $120°$ are showed with continue blue lines while pure shear paths are showed with differently dashed lines (a). Energy landscape near the reference well, with evidence on the fact that energy is significantly lower along the fat rhombic path (b). 47

3.1 **Finite Deformation:** Schematic representation of the Lagrangian undeformed configuration and of the Eulerian deformed configuration in a finite deformation problem. . . . 53

3.2 **Cauchy-Born Rule:** Representation of the Cauchy-Born assumption. The continuum formulation is linked to the lattice based one by assuming the lattice vectors $\{\mathbf{e}_I\}$ to behave like the element of infinitesimal lenght $d\mathbf{X}$ in the continuum formulation. 56

3.3 **Periodic Behavior and Length Scale:** Construction of a periodic energy density function $\phi(\mathbf{C})$ implies that the fundamental element of the model is given by a certain number of atoms deforming homogeneously. Here, MS energy profile corresponding to a domain of $N \times N$ atoms interacting with a Lennard-Jones potential is shown in correspondence of a simple shear deformation. Note that periodicity manifests already in correspondence of small sizes N. 60

3.4 **Dislocation Stress Field in the Square Lattice:** On the left: Cauchy stresses along an horizontal middle section of the analyzed domain. On the right: stress fields corresponding to the three stress components σ_{xx}, σ_{xy} and σ_{yy} (values showed are in between -0.1 and 0.1.) 63

3.5 **Dislocation Structure in the Square Lattice:** On the left: distribution of metrics associated with discrete elements on configurational space C_{11}, C_{22}, C_{12}, with evidence on engaged wells S and S_0^{+1}. On the right: A picture of the full domain is showed along with a detail of the triangulation in correspondence of the dislocation core, showing the presence of sheared element configurations. 64

3.6 **Dislocation Stress Field in the Triangular Lattice:** On the left: Cauchy stresses along an horizontal middle section of the analyzed domain. On the right: stress fields corresponding to the three stress components σ_{xx}, σ_{xy} and σ_{yy} (values showed are in between -0.03 and 0.03). 65

3.7 **Dislocation Structure in the Triangular Lattice:** On the left: finite element distribution on configurational space C_{11}, C_{22}, C_{12} with evidence on engaged wells T and T_0^{+1}. On the right: A picture of the full domain is showed along with a detail of the triangulation in correspondence of the dislocation core, showing the presence of sheared element configurations. 65

3.8 **Dislocation Annihilation:** Initial configuration imposed to the system which ends with annihilation of the two dislocations of opposite sign. On the left, we show the analyzed domain with colors corresponding to the Cauchy stress σ_{xy} field. On the right, the elements distribution in the configurational space is shown. 66

3.9 **Dislocation Annihilation Process:** Some steps of the minimization procedure are shown, in correspondence of which the gradual approaching of dislocations is observed, up to the point in which the two dislocations annihilate originating a perfect crystal. On the top, Cauchy stress σ_{xy} field is shown, along with the corresponding elements distribution in the configurational space (on bottom). 67

3.10 **Initial (top) Configuration and Final Equilibrium State (bottom) for the Case of the Two Dislocations of the Same Sign.** The two dislocation repel each other up to an equilibrium distance in which attractive and repulsive forces are balanced. In this case the engaged wells are $\mathbf{S}$, $\mathbf{S}_0^{+1}$ and $\mathbf{S}_0^{+2}$. Some readjustments of the elements occupying the low-energy valleys between the wells is observed between initial and final configuration. 68

4.1 **Yield Surface for the Square Lattice:** a) Simple shear trajectory $\theta = 0°$ is shown, with evidence on the point in which the bifurcation appears. b) Bifurcation points, drawing the yield surface, are showed for different simple shears in which the angle θ is progressively increased of $5°$. We show also the bifurcation points corresponding to the fat rhombic and rectangular pure shears (grey stars). c) The yield surface, obtained by interpolation of bifurcation point, is shown. 76

4.2 **Analyzed Shear Paths on the Configurational Space:** Two pure shears, the rectangular and the rhombic paths coinciding with boundaries of D, and the three simple shears $\theta = 0°$, $\arctan(\frac{1}{2})$, and $45°$ are analyzed. 76

4.3 $\det q_{ik}$ **Profiles along the Fat Rhombic and the Rectangular Paths**: Evidence on load α_c for which equality in (4.10) is satisfied. The fat rhombic pure shear (on top) shows the simultaneous appearence of two instability directions while just one appears in case of the rhombic path (on bottom). On the side of each graph we show the orientation of wave direction $\mathbf{n}^\perp$ with respect of the deformed lattice cell at $\alpha = \alpha_c$. 77

4.4 $\det q_{ik}$ **Profiles for the Simple Shears** $\theta = 0°$, $\arctan(\frac{1}{2})$, $45°$**:** Evidence on critical load $\alpha = \alpha_c$. Lattice configurations corresponding to $\alpha = \alpha_c$ and associated unstable modes $\mathbf{n}^\perp$ are also shown. 79

4.5 **Homogeneous Nucleation:** In this picture, a perfect crystal with fixed boundary conditions is loaded quasistatically up to load value α at which stability of the homogeneous configurations is lost. System deforms homogeneously up to point a), and all the elements are mapped on a single point on configurational space. In the post instability equilibrium, point b), the system show patterning and more than one wells are occupied on configurational space. 81

4.6 **Energy Density up to Nucleation:** Evolution of energy density ϕ along the four considered paths. On the left: the fat rhombic and the rectangular pure shears. On the right: The three simple shears $\theta = 0°, \arctan(\frac{1}{2})$, and $45°$. A good agreement between the analytic value α_c and the numerical α_c^* is observed in all these loading directions. The showed data were obtained from a $N = 10^4$ simulation. 82

4.7 **Homogeneous Nucleation along the two Pure Shears:** These loading paths respectively the paths for which instability happens at lowest and higher value of loading parameter α. These two "extremal" paths are representative of two different mechanisms of nucleation. 83

4.8 **Post-Instability Pattern for the Rhombic Pure Shear:** Results are shown for a $N = 10^4$ domain with both periodic (left) and fixed (right) boundaries. On top: the Cauchy stress σ_{xy} is shown in the full domain with evidence on two edge dislocations. On bottom: The element points in the configurational space. Wells $\mathbf{S}$, $\mathbf{S}_1^{0^\circ}$, and $\mathbf{S}_{-1}^{90^\circ}$ are simultaneously activated. The points on the valleys connecting these wells correspond to the elements in the dislocation core. 84

4.9 **Post-Instability Pattern for the Rectangular Pure Shear:** A $N = 10^4$ domain is considered. Results for a simulation with periodic boundaries (left) and fixed (right). On top: the Cauchy stress σ_{xy} in the full domain with evidence on a region, to better illustrate the final, 45°-rotated cristal lattice structure. On bottom: the elements points in the configurational space show the engagement of the two wells $\mathbf{S}_1^{0^\circ}$, and $\mathbf{S}_{-1}^{0^\circ}$ (or more precisely a 45°-rotated equivalent of these two), with some residual defects variously placed. 86

4.10 **Crystal Rearrangement along the Rectangular Path** On top: details of the crystal structure along the rectangular path before (a), and after (b), nucleation. On the bottom, a detail of the post-instability pattern, where elements of the triangulation are shown. The crystal structure experiences a global rearrangement where the 45° rotated version of wells $\mathbf{S}_1^{0^\circ}$ and $\mathbf{S}_{-1}^{0^\circ}$ are finely mixed. This rearrangement gives again a square lattice, but rotated by 45°. 87

4.11 **Cauchy Stress σ_{xy} and Lattice Structure for the Rhombic and the Rectangular Paths:**. (a) rhombic, (b) rectangular. In yellow we highlight the dislocation cores and the other observed topological defects. While in (a) the shear is limited to specific lattice planes, in (b) the rearrangement is global. 88

4.12 **Post-Instability Patterns for the Considered Simple Shears:** A $N = 10^4$ domain is considered. Cauchy stress σ_{xy} is showed on the entire domain and on a blown-up detail, to better appreciate the difference of the obtained patterns. Distribution of the elements points in the configurational space it is also shown. 90

4.13 **A detail of the Simple Shear $\theta = 45^\circ$ Post-Instability Pattern:** colors indicate the values of σ_{xy} component of Cauchy stress. Regions with different orientations are accorded with various topological defects. As in the rectangular path, the lattice rotation is actually a mixture of compatible sheared phases. Dislocations are also observed. . . . 91

4.14 **Post-Instability Pattern for a $N = 10^6$ Simulation with Periodic Boundary Conditions for $\theta = 0^\circ$ Simple Shear:** Colors indicate the σ_{xy} stress field. 92

4.15 **Post-Instability Pattern for a $N = 10^6$ Simulation with Periodic Boundary Conditions for $\theta = 45^\circ$ Simple Shear:** Colors indicate the σ_{xy} stress field. 93

4.16 **Yield Surface for the Triangular Lattice:** a) The *yield surface* enclosing the region surrounding the reference triangular well $\mathbf{T}$ is illustrated with a thick black line. b) The analyzed shear paths and their relation with the yield surface are shown. 94

4.17 $\det q_{ik}$ **Profiles along the Fat Rhombic and the Skinny Rhombic Paths:** Evidence on the load α_c for which equality in (4.10) is satisfied. the fat rhombic pure shear (a) shows the simultaneous appearence of two instability directions, while just one appears in case of fat rhombic path (b). On the side of each graph, we show the orientation of wave direction $\mathbf{n}^\perp$ with respect of the deformed lattice cell at $\alpha = \alpha_c$. 95

4.18 $\det q_{ik}$ **Profiles along The Considered Simple Shears:** Profiles for $\theta = 60°$ and $\theta = 30°$ loading paths are shown, with evidence on load α_c for which equality in (4.10) is satisfied. Both these simple shears are characterized by the presence of one unstable mode only, not aligned with crystallographic directions. 96

4.19 **Precursors of the Incipient Instability:** Inhomogeneous states, precursors of the incipient dislocation nucleation, for the considered loading paths. These precursors are characterized by the appearence of higher energy bands, periodically spaced, and whose orientation match the direction of the unstable mode $\mathbf{n}^\perp$ predicted analytically. 98

4.20 **Energy Density up to Nucleation for the Triangular Lattice:** Evolution of the energy density ϕ along the four considered trajectories. On the left: the fat rhombic and the skinny rhombic pure shears. On the right: the two simple shears $\theta = 60°$, and $30°$. Instability happens systematically later than what predicted analytically, and we observe $\alpha*_c \approx 1.1\alpha_c$ 99

4.21 **Dislocation Nucleation in the Triangular Lattice along $\theta = 60°$ Simple Shear:** Evolution of the energy density and the Cauchy stress σ_{xy} field representing three different phases of the instability which leads, from the first appearence of inhomogeneous bands, to the formation of dislocations. These are not equilibrium states, but are part of the overdamped dynamics implicit in the minimization procedure. The sequence shows nucleation in the $\theta = 60°$ simple shear. On bottom we show the corresponding distribution of the elements in the configurational space, which highlights the importance of the square point in driving the development of the banded precursors. 100

4.22 **Dislocation Nucleation in the Triangular Lattice along $\theta = 30°$ Simple Shear:** Evolution of the energy density and the Cauchy stress σ_{xy} field representing three different phases of the instability which leads, from the first appearence of inhomogeneous bands, to the formation of dislocations. These are not equilibrium states, but are part of the overdamped dynamics implicit in the minimization procedure. The sequence shows nucleation in the $\theta = 30°$ simple shear. On bottom we show the corresponding distribution of the elements in the configurational space, which highlights the importance of the square point in driving the development of the banded precursors. 101

4.23 **Rotation Distribution in the Band Patterning:** $\theta = 30°$ (left) and $\theta = 60°$ (right) simple shears. This inhomogeneous equilibrium configuration immediately preceeds the instability process described in Figure 4.21, where the interval of observed rotations furter increases, up to the formation of dislocation dipoles. 102

4.24 **Bands Patterning in configurational space:** Dispersion of elements in configurational space corresponding to the first instants of instability, when bands spread originating a new inhomogeneous pattern. The two case of the skinny and the fat rhombic paths are shown. Here the Dispersion is originated by the bands which are respectively tangential and perpendicular to the yield surface. 102

4.25 **Post-Instability Pattern along the Fat Rhombic Pure Shear:** A $N = 10^4$ domain is considered. On top and bottom, results from simulations with fixed and periodic boundary conditions are shown, respectively.(b) Cauchy stress σ_{xy} field is shown in the full domain. (c) The distribution of elements points in configurational space. The simultaneous presence of the three wells $\mathbf{T}$, $\mathbf{T}_1^{60^\circ}$, and $\mathbf{T}_{-1}^{0^\circ}$ is evident when one considers the corresponding triangulation in which we show a detail in (a). 104

4.26 **Post-Instability Pattern along the Skinny Rhombic Pure Shear:** A $N = 10^4$ domain is considered. On top, the intermediate stable twin obtained with periodic boundary conditions is shown, followed by the dislocation pattern obtained under further loading. On bottom, results of a simulation with fixed boundary conditions are showed. In this case, the twin cannot form and dislocations nucleate without an intermediate equilibrium phase. On the left (a), a detail of the triangulation is showed to highlight the simultaneous presence of the three wells $\mathbf{T}$, $\mathbf{T}_{-1}^{120^\circ}$ and $\mathbf{T}_1^{60^\circ}$. (b) Cauchy stress σ_{xy} field is shown in the full domain. (c) Elements points in the configurational space. 105

4.27 **Post-Instability Pattern for Simple Shear $\theta = 60^\circ$:** A $N = 10^4$ domain is considered. On top, the configuration obtained for fixed boundary conditions is shown, while on bottom, results for an analogous simulation with periodic boundaries are illustrated. (a) a detail of the domain triangulation, (b) Cauchy stress σ_{xy} field on the full domain, (c) corresponding elements distribution in the configurational space. 107

4.28 **Post-Instability Pattern for Simple Shear $\theta = 30^\circ$:** A $N = 10^4$ domain is considerd. On top, the configuration obtained for fixed boundary conditions is shown, while on bottom results for an analogous simulation with periodic boundaries are illustrated. (a) a detail of the domain triangulation, (b) Cauchy stress σ_{xy} field on the full domain, (c) corresponding elements distribution in the configurational space. 108

4.29 **Pattern Evolution in the Square Lattice:** A $N = 4 \cdot 10^4$ square lattice domain with periodic boundaries is loaded along the simple shear path $\theta = 0^\circ$. The system present hardening up to a second stress drop where some grains, initially small, appears. These grains gradually increase allowing the system to deform almost without additional hardening. Notice how the configurational space show the development of increasing complexity. 110

4.30 **Pattern Evolution in the Triangular Lattice:** A $N = 4 \cdot 10^4$ triangular lattice domain with periodic boundaries is loaded along the simple shear path $\theta = 0^\circ$. The system present hardening up to a second stress drop where additional dislocations are activated. Then, deformation localize along a shear band in the upper region of the periodic domain. . . . 111

5.1 **Energy Construction based on Cauchy-Born Rule:** If the atomic lattice is assumed to follow the macroscopic deformation $\mathbf{F}$, the position of all atoms can be determined starting from the deformation of an atomic cell only, described by vectors $\mathbf{e}_1$ and $\mathbf{e}_2$. All the needed distances entering the computation of ϕ can then be evaluated as linear combinations of these vectors. The advantage of using the reduced vectors consist in the fact that one may consider the same atomic cell during the entire deformation, without changing the cut-off radius. If reduction is not used, distances of the sampled atoms starts to exceed the cut-off and the periodic behavior is gradually lost. 116

5.2 **Energy landscape for the HLJ energy:** (isochoric part) obtained from the considered Lennard-Jones potential is shown on the Poincaré disk with evidence on the shearing paths $\theta = 30°$ and $\theta = 60°$. Cut-off = 0 has been used for an improved visualization of low-energy barriers and wells. Notice how, qualitatively, the landscape resembles the one obtained for the polynomial energy. 118

5.3 **Comparison of Post-Instability Patterns in Polynomial and HLJ:** Post-instability patterns (on a $N = 10^4$ domain) for the $\theta = 60°$ simple shear are shown in terms of Cauchy stress component σ_{xy}. Polynomial energy on top and HLJ on bottom. While the overall behaviour of the crystal is the same, the case of HLJ is richer, more wells are engaged and different types of defects appear. 119

5.4 **Histograms of Metric Component C_{12} and of Elements Volume:** (a) Distribution of metric component C_{12} show that $\mathbf{T}_1^{60°}$, of metric $C_{12} = -0.5774$, is the most active well (other than reference well $\mathbf{T}$, with metric component $C_{12} = 0.5774$) for both polynomial and HLJ energies. (b) Distribution of elements volume, the great majority of elements preserve their volume (unitary), but HLJ shows the presence of few elements whose volume is very high. Histogram y-axis has been cut to better visualize the distribution. 120

5.5 **Volumetric Defects:** (a) HLJ energy is characterized by the appearence of defects such as voids and nano-cracks, associated, in our modeling framework, with element dilatation. (b) The instability of a sample, to which dilatation is imposed, manifests itself with the formation of more pronounced nano-cracks. 120

5.6 **Volumetric Response** On top: response to uniaxial tension and compression of the Polynomial and HLJ energies is compared. The pair-potential based strain energy density is characterized by a flattening in correspondence of tension. On bottom, we show the evolution of the HLJ energy landscape in correspondence of different values of $\det \mathbf{C}$. While in compression one observes an overall increase of the energy density which causes steepening of the barriers, the tension response is characterized by a progressive flattening of the overall landscape. 121

5.7 **Dependence on $\det \mathbf{C}$ of the Yield Surface:** Evolution of the stability region, that we called *yield-surface*, is shown for the Polynomial and the HLJ energy. The peculiar response to tension in the HLJ energy causes the progressive shrinking of its stability region, up to a complete disappearance. 122

5.8 **HLJ Yield Surface:** By using criterion (4.10), the yield surface is constructed. As in the Polynomial energy, maximum and minimum values of α_c are found along the fat rhombic and the skinny rhombic shear paths, respectively. 124

5.9 **HLJ** $\det q_{ik}$ **Profiles along the Fat Rhombic and the Skinny Rhombic Paths:** Evidence on load α_c for which equality in (4.10) is satisfied. the fat rhombic pure shear (on top) shows the simultaneous appearance of two instability directions, while just one appears in case of skinny rhombic path (on bottom). On the side of each graph we illustrate the orientation of the wave directions $\mathbf{n}$ and the polarization vectors $\mathbf{m}$, with respect of the deformed lattice cell at $\alpha = \alpha_c$. In the fat rhombic path, differently from the polynomial energy, wave polarization $\mathbf{m}$ is not aligned with $\mathbf{n}^{\perp}$, (while it is still the case in the skinny rhombic path). 126

5.10 **HLJ** $\det q_{ik}$ **Profiles along** $\theta = 60^{\circ}$ **and** $\theta = 30^{\circ}$ **Simple Shear Paths:** Profiles for $\theta = 60^{\circ}$ and $\theta = 30^{\circ}$ loading paths are shown with evidence on load α_c for which equality in (4.10) is satisfied. Both these simple shears are characterized by the presence of one unstable mode only, not aligned with the crystallographic directions. Differently from the polynomial energy, the wave polarization $\mathbf{m}$ is not aligned with $\mathbf{n}^{\perp}$. 127

5.11 **First Instability in HLJ:** On top, profiles of the energy density from $\alpha = 0$ up to first instability α_c^*, together the considered path, are shown for simulations of $N = 10^4$ nodes and fixed boundary conditions. In all cases, there is a good agreement with the analytical prediction α_c (highlighted with a red star symbol). On bottom, the equilibrium configuration just preceding instability is shown. Even in this case, it is possible to observe the appearance of a modulation oriented along $\mathbf{n}^{\perp}$. 129

5.12 **Post-Instability Pattern along the Fat Rhombic Pure Shear:** A $N = 10^4$ domain is considered. on the top and bottom, results from simulations with fixed and periodic boundary conditions are shown respectively. (a)Cauchy stress σ_{xy} field is showed in the full domain. (b) Elements distribution in the configuration space. The simultaneous presence of the three wells $\mathbf{T}$, $\mathbf{T}_1^{60^{\circ}}$, and $\mathbf{T}_{-1}^{0^{\circ}}$ is evident when one considers the corresponding triangulation, of which we show a detail in Figure 5.14. 130

5.13 **Post-Instability Pattern along the Skinny Rhombic Pure Shear:** A $N = 10^4$ domain is considered. on the top and bottom, results from simulations performed with fixed and periodic boundary conditions are shown, respectively. (a) Cauchy stress σ_{xy} field is shown in the full domain. (b) Elements distribution in the configurational space. The simultaneous presence of the three wells $\mathbf{T}$, $\mathbf{T}_1^{60^{\circ}}$, and $\mathbf{T}_{-1}^{120^{\circ}}$ is evident when one considers the corresponding triangulation (Figure 5.14). When periodic boundaries are used, dislocation nucleation is preceded by a stable modulation, illustrated on the top of the figure. 131

5.14 **Details of the Post-Instability Patterns along the two Rhombic Pure Shears:** Details of the triangulation corresponding to post instability patterns along the fat rhombic (a), and the skinny rhombic (b) pure shears show clearly the activation of two different wells simulaneously. These are $\mathbf{T}_1^{60^{\circ}}$, and $\mathbf{T}_{-1}^{0^{\circ}}$ in the case of the fat rhombic path, and $\mathbf{T}_1^{60^{\circ}}$ and $\mathbf{T}_{-1}^{120^{\circ}}$ in the case of the skinny rhombic path. 132

5.15 **Dislocation Energy Density:** Comparison between the energy density associated to an edge dislocation core in HLJ and MS. 134
5.16 **Dislocation Stress Field:** Comparison between dislocation stress fields for a single dislocation in HLJ and MS. 135
5.17 **Energy Landscape for Different Values of** $\det \mathbf{C}$ From top to bottom, we show the HLJ energy landscape in corresponedence of different values of $\det \mathbf{C}$, respectively, we use $\det \mathbf{C} = 0.7$, 1.0 and 1.3. 137
5.18 **Analytic Yield Surface and MS Calculations:** The black line show the yield surface evaluated analytically, based on acoustic tensor criterion (4.10). Grey stars show (C_{11}, C_{12}, C_{22}) points at which first instability was observed in MS simulations, along different shearing deformations. The showed results are obtained from simulations performed on a domain containing $\approx 10^4$ atoms deformed with fixed boundaries. 138
5.19 $\theta = 60^\circ$ **Post-Instability Patterns at Different Values of** $\det \mathbf{C}$**:** From top to bottom, post instability patterns corresponding to $\det \mathbf{C} = 0.7$, $\det \mathbf{C} = 1.0$ and $\det \mathbf{C} = 1.3$ shearing deformations are shown for HLJ and MS, respectively. Edge dislocations are observed in the first two cases, together with voids and other volumetric defects. The patterns obtained for $\det \mathbf{C} = 1.3$ show the localization of the deformation along cracks. 139
5.20 $\theta = 30^\circ$ **Post-Instability Patterns at Different Values of** $\det \mathbf{C}$**:** From top to bottom, post instability patterns corresponding to $\det \mathbf{C} = 0.7$, $\det \mathbf{C} = 1.0$ and $\det \mathbf{C} = 1.3$ shearing deformations are shown for HLJ and MS, respectively. Edge dislocations are observed in the first two cases, together with voids and other volumetric defects. The patterns obtained for $\det \mathbf{C} = 1.3$ show the localization of the deformation along cracks. . 140
5.21 **Detail of the** $\det \mathbf{C} = 1.3$ **Post-Instability Patterns:** Fractures appear in the HLJ model in the form of highly extended elements. The same interpretation can be used in MS simulations plotting atoms and their links with the initial neighbours. 141
5.22 **Detail of the** $\det \mathbf{C} = 1.0$ **Post-Instability Patterns:** Activation of the same slip system is observed in HLJ and MS simulations. 141
5.23 $\theta = 60^\circ$ **Element Distribution in the Configuration Space and Histograms of Metric Components:** Distribution of elements in the configuration space is similar in HLJ and MS simulations, and shows the clustering of a large number of elements along the low-energy valley connecting wells $\mathbf{T}$ and $\mathbf{T}_1^{60^\circ}$. Analogies in the distributions can be deduced also looking at the histograms of metric components. 143
5.24 $\theta = 30^\circ$ **Element Distribution in the Configuration Space and Histograms of Metric Components:** Distribution of elements in the configuration space is similar in HLJ and MS simulations. Elements are sparser with respect of the shearing path $\theta = 60^\circ$, but a large number of elements along the low-energy valley connecting wells $\mathbf{T}$ and $\mathbf{T}_{-1}^{120^\circ}$ is observable, together with a minor engagement of several other wells. Analogies in the distributions can be deduced also looking at the histograms of metric components. . . . 144
5.25 $\det \mathbf{C} = 7$ **Element Distribution in the Configuration Space :** elements arrange similarly in HLJ and MS simulations, showing the major activation of the same energy valley. 145

5.26 $GL(2,\mathbb{Z})$ **and Atomistic simulations for two different values of indenter radius** R. Crystal orientation is $0°$. 148
5.27 $GL(2,\mathbb{Z})$ **and Atomistic simulations for two different values of indenter radius** R. Crystal orientation is $90°$. 149
5.28 **Critical indenter depht** d_c**:** on top, orientation O_1, on bottom orientation O_2. Critical indenter depht d_c in MS simulations and in the mesoscopic model for different system sizes and values of the indenter radius R. 150
5.29 **A detail of the Post-Nucleation Pattern:** In the right we show a detail of the HLJ post-instability pattern from a O_1 nanoindentation test, while on the left we illustrate a detail from an analogous MS simulation. Clearly, the compatibility requirement implicit in the $GL(2,\mathbb{Z})$-invariant model results in an excessive constraintment. 151

Chapter 1

Introduction

Crystalline solids flow plastically when macroscopic stresses reach certain given thresholds. It is well known that the plastic deformation of crystals is originated from the generation and motion of interacting lattice defects, called dislocations. Dislocations of a material evolve collectively in a complex energy landscape, driven by the applied loading and long range mutual interactions [Wil54]. Controlling crystal plasticity is needed in a variety of applications, among which, metal hardening [Cot02], fatigue failure [ILVSVP$^+$16], nano-scale forming and micro-pillar optimization [CCPS10, ZSZ$^+$17, PWW$^+$19]. Plastic deformation of crystalline materials is a very complex phenomenon as it involves many length scales. Indeed, the typical spatial heterogeneities involved in crystal plasticity extend from the atomistic length scale (dislocation cores and grain boundary structures), to mesoscale dislocations patterns and grain microstructures, up to the macroscopic scale of the specimen. At the macroscale, plasticity appears as a smooth flow described by a continuous stress-strain response, however, this is not the case when one considers micro and nano-samples. In order to describe and understand plastic deformation, several theories have been developed. The classical continuum theory of plasticity is based on the assumption that crystalline materials flow irreversibly when maintaining yield thresholds. Stress-strain response is modelled with continuous curves, an approach implying that the aforementioned heterogeneities are homogenized out. This approach has been very successful in reproducing some of the most important plasticity phenomena such as yield, hardening and shakedown. In some cases (bulk bcc metals, tetrahedral covalent crystals, etc.) the obstacles are strong, the dislocation interaction is weak and the plastic flow can be seen as a sum of uncorellated events. However, in other cases (such as fcc metals, hcp crystals with basal glide etc.) dislocation mobility is high and the elastic interaction among distant dislocations is important [ST12]: then, the collective behavior at the macroscale emerges as a correlated outcome of many events at the microscale. In particular, such plastic flows exhibit in the steady state irregular isolated bursts and reveal apparently randomly localized active slip volumes, with both spatial and temporal fluctuations spanning many

scales. Moreover, temporal intermittency manifests itself through acoustic emissions with power law statistics of avalanches. The associated spatial heterogeneities take the form of coherent dislocation structures characterized by the alternation of low and high dislocation density regions. The emergence of power laws suggests that the relation between microscopic and macroscopic pictures of plastic flow is rather complex and in some extent, more akin to turbulence than to elasticity. The critical nature of plastic flow has direct consequences for industrial applications beyond its obvious fundamental interest. A better understanding of finite-size effects in plasticity is relevant for miniaturization of devices such as the micro- and nano-electromechanical systems (MEMS and NEMS) [LCL$^+$10, HJY$^+$15, FLH12, NN09], and in general for the integration of micro and nano-components, whose importance is increasing in many fields of engineering.

While the continuum phenomenological laws describe well the effects of macro-scale plasticity, a more detailed description of defect interactions is necessary to capture essential features of plasticity at small scales, including the formation of complex microstructures. The most accurate modelling of material behavior should involve quantum mechanics and incorporate every atom to atom interaction. However, atomistic modelling techniques are prohibitively expensive in terms of computational time in the majority of applications, even at the small scales of interest. Much effort has been devoted by the scientific community in order to develop strategies suitable to the task of modelling small-scale plasticity at a reasonable computational cost. Most of the proposed models of this type attempt to include in a continuum framework the discrete features necessary to model small-scale plasticity while maintaining a reasonable level of approximation. Indeed, continuum description is advantageous as it reduces drastically computations and allows for more straightforward analytical and numerical treatments. However, capturing discrete effects within a continuous description is not straightforward. The formulation of this type of models is complicated even further by the fact that the evolution of dislocations and the resulting plastic flow are extremely complex. Dislocations move collectively and can interact in many different ways (including annihilation, multiplication, formation of locks, etc.). Moreover, both long range interactions due to the elastic far-fields, and short range reactions involving deformations of the defect cores, are fundamental features in the evolution of the plastically deformed solid. It is then not straightforward to find a compromise between accounting properly for all these phenomena and keeping the computational cost at a reasonable level.

In this context, this PhD Thesis focuses on the development of an innovative mesoscopic model of crystal plasticity. The main idea is to construct an energy functional that depends on such mechanical macroscopic quantities as tensorial strain with lattice discreteness inherently accounted for. The proposed approach is advantageous due to the fact that, while keeping many features of the continuum formulation, it accounts for long and short-range interactions, allowing dislocations to nucleate and interact without the need for ad-hoc relations.

We are entering a very active field of research, as existing strategies for the modelling of small scale plasticity are numerous and new ones are continuously proposed. These methods spans the different scales involved in the phenomenon of plasticity, varying from about 10^{-1} nm, the atomic dimensions, up to the 100 of μm typical of lattice microstructures.

In the following, we will present a background on the most successful modelling strategies already developed in the literature. This background is crucial to better contextualize the subject of this Thesis and to highlight the innovative features of the proposed approach. Therefore, we start with a general overview and discuss briefly the existing approaches that attracted most of the attention of the scientific community. We keep the of the previous work at the minimal level and focus on athermal dynamics only, omitting approaches which incorporate finite time scales. More comprehensive expositions can be found in [McD19, TM11].

Before introducing the models we provide the necessary background on dislocations, which is essential for the understanding of our notations (for a more detailed discussion of dislocation, see the books of Hirth and Lothe [HL06] and of Hull and Bacon[HB01]). We begin our review from microscale starting from the lowest level possible, where interatomic forces are resolved in full detail. Then we cover progressively larger scales while illustrating methods allowing one to reduce the number of degrees of freedom at the expense of adopting phenomenological rules governing dislocations kinematics and interaction.

1.1 The Idea of Dislocations

Dislocations are common defects in crystalline materials and can be viewed as distortions of the perfect lattice structure. Dislocations appeared first as mathematical objects in the work of Vito Volterra [Vol07]. However it was only much later that their connection to plastic flow was understood, mostly due to the work of Orowan [Oro34], Taylor [Tay34] and Polanyi [Pol34]. These scientists independently understood how the presence of dislocations explains the experimental fact that resistance of a crystal to an imposed shear is much lower than the theoretical strength needed to slide two perfect lattice planes relatively to each other. They realized that it is the massive dislocation flow along crystal slip systems that causes macroscopic plastic deformation, and therefore, these microscopic defects are called the "carriers of plasticity". In a general 3D framework dislocations may be of three different types: edge, screw and mixed. To illustrate the main ideas in a 2D setting, we show the edge dislocations, schematically represented in Figure 1.1. In this figure we put in evidence two different ways of interpreting dislocations: one presents the edge dislocations as the distortion resulting from the insertion of an extra atomic plane, the other considers it as the boundary between slipped and unslipped regions of the lattice. The latter interpretation

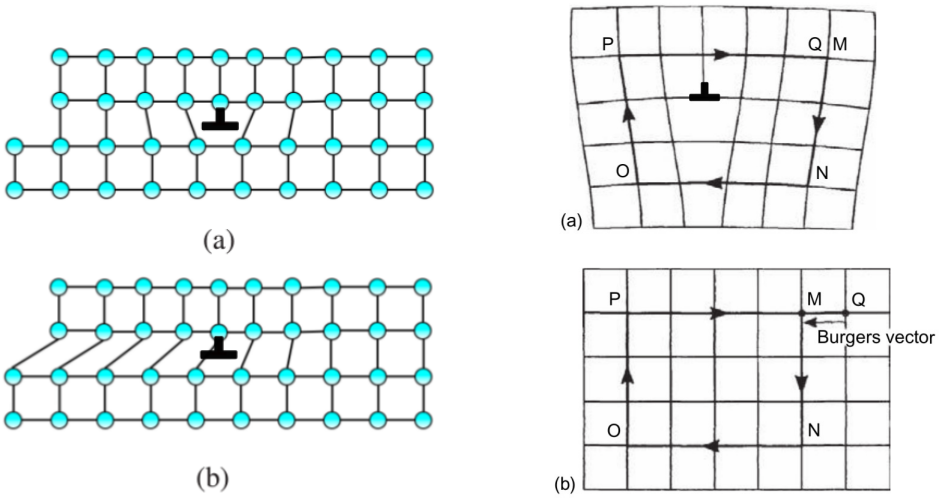

Figure 1.1: Left: **Schematic Representation of a Dislocation:** it can be considered as the lattice distortion associated to the presence of an extra crystallographic plane that is inserted in the upper half of the crystal (a) or as the distortion separating the slipped from the unslipped part of the crystal (b). Image taken from [ST12]. Right: **The Burgers Circuit:** defining the Burgers vector associated to the enclosed dislocation(s) (from [HB01])

implies finite deformations of the original lattice and it is very important for the subject of this PhD Thesis. We will often refer to it in the discussions to follow.

A dislocation is characterized by its Burgers vector **b**, that can be defined as its "topological charge". Imagine a closed circuit connecting atom to atom in a deformed crystal (a Burgers circuit) containing one or more dislocations. The same circuit will be open if encloses a region of perfect crystal. The vector connecting the two open ends of the circuit is called the Burgers vector. The Burgers vector obtained for circuits containing more than one dislocation will be equal to the sum of the Burgers vector of the single dislocations enclosed in the circuits. Dislocations create lattice distortions, then causing an internal stress in the lattice.

In the case of isotropic linear elasticity, expressions for Cauchy stress generated by a straight edge dislocation in an infinite media can be obtained analytically [HB01, HL06].

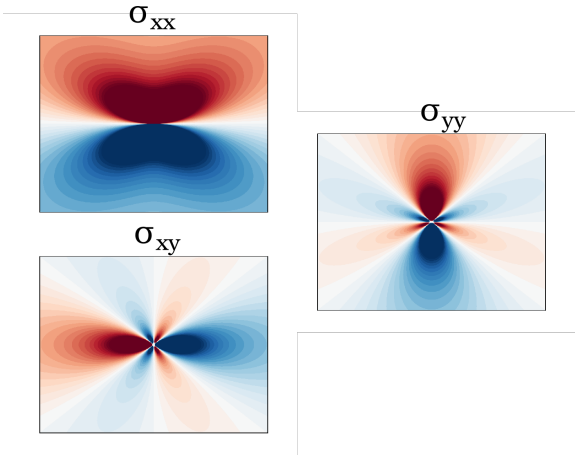

Figure 1.2: **Cauchy Stress Contours** about a positive edge dislocation.

At distance **r** from the dislocation core we obtain:

$$\sigma_{xx} = -\frac{Gb}{2\pi(1-\nu)}\frac{y(3x^2+y^2)}{(x^2+y^2)^2} \tag{1.1}$$

$$\sigma_{xy} = \frac{Gb}{2\pi(1-\nu)}\frac{x(x^2-y^2)}{(x^2+y^2)^2} \tag{1.2}$$

$$\sigma_{yy} = \frac{Gb}{2\pi(1-\nu)}\frac{y(x^2-y^2)}{(x^2+y^2)^2}\,, \tag{1.3}$$

with

$$G = \frac{E}{2(1+\nu)}\,, \tag{1.4}$$

the shear modulus, written in term of the Young Modulus E and the Poisson ratio ν. As already mentioned, these solutions are reliable at some distance from the dislocation core. However they break down in the vicinity of the core where they show instead a singularity ($\sigma_{ij} \to \infty$ for $\mathbf{r} \to 0$). In view of this failure of linear elasticity, lattice discreteness and non-linearities play an important role in determining the characteristics of the core region. On the other hand, far from the dislocation core, the linear elasticity theory remains adequate. This observation constitutes the basis of many mesoscale models, as we will illustrate in what follows.

1.2 Atomistic Modelling

Most accurate approaches existing for the description of crystals are based on the direct modelling of atomistic interactions. A common approach in this category is known as

Molecular Dynamics MD. It is usually based on regularizing atomistic interactions by an *interatomic potential* [Pau93, Bar18]. This is already an approximation: a rigorous, *ab initio*, treatment of atomic behavior would imply the solution of the Schrödinger's equation. For solids, approximate solutions of this equation can be obtained by means of the Density Functional Theory (DFT) [Par80], developed by Hohenberg and Kohn [HK64] and Kohn and Sham [KS65]. In DFT, electronic wave functions are not considered explicitly and energy of the ground state is assumed to depend only on the electron density. However this method is still very expensive computationally, and even the biggest simulations reach a maximum of 10^3 atoms. A way to reduce this computational cost is to discard electronic degrees of freedom. This is the main assumption of the Born-Oppenheimer theory, which states that electrons arrange instantaneously with respect to the slowly evolving nuclei. Then, nuclei are assumed to behave as rigid particles that move in response to nonlocal forces. This hypothesis does not hold in all situations, however it is reasonable when the Broglie wavelenght is much smaller than an interatomic spacing, which is the case, for instance, at near zero temperatures $\approx 0\,K$. In this case waves are spatially localized and atoms can be modelled as rigid particles. Atomic interactions may then be simplified using suitable phenomenological functions which are used to represent potential energy Π of a certain set of atoms.

Let's consider a system of N atoms and let's $\mathbf{r}_i$ be the position of atom i. The total potential energy Π of the system can be written as a function of all atomic positions:

$$\Pi = \Pi(\mathbf{r}_1, \mathbf{r}_2, \ldots, \mathbf{r}_N)\,. \tag{1.5}$$

Once Π is known, the force on each atom i can be evaluated as the derivative of Π with respect to atom position $\mathbf{r}_i$. Then, for a given assembly of N particles, evolution of the system can be obtained by solving Newton equations:

$$\mathbf{f}_i = -\frac{\partial \Pi}{\partial \mathbf{r}_i}\,. \tag{1.6}$$

Interatomic potentials are needed for the construction of Π and should be calibrated to reproduce the thermodinamical properties of the specific material. The simplest way to obtain Π is to use a pair-potential. Then the total energy can be written as the sum of pair interactions between atoms:

$$\Pi = \sum_{i=1}^{N-1} \sum_{j=i+1}^{N} \varphi_p(r_{ij})\,, \tag{1.7}$$

where $r_{ij} = \|\mathbf{r}_i - \mathbf{r}_j\|$ is the distance between atoms i and atom j. Here φ_p is a suitable pair potential dependent only on interatomic distance r_{ij}. An usual choice, accounting for both long-range attraction and short range repulsion, is the Lennard-Jones potential:

$$\varphi(r_{ij}) = 4\varepsilon \left[\left(\frac{\sigma}{r_{ij}} \right)^{12} - \left(\frac{\sigma}{r_{ij}} \right)^{6} \right], \tag{1.8}$$

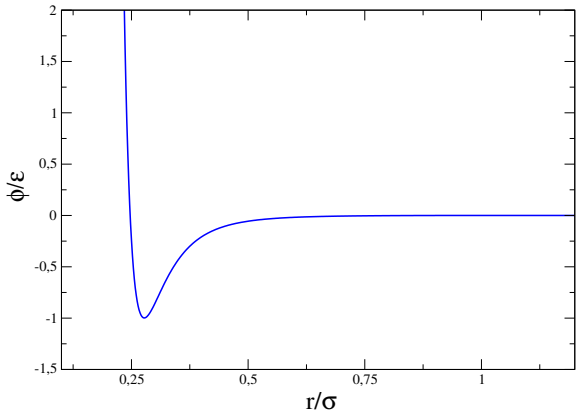

Figure 1.3: **Lennard-Jones Pair Interaction:** Both long range attraction and short range repulsion are represented. It is possible to notice that upon a certain distance r interaction becomes zero.

where ε is the depth of the energy minimum and $r = 2^{1/6}\sigma$ is the correspondent atomic scale. An example of Lennard Jones potential is shown in Figure.1.3.

Noticing that the value of $\varphi_p(r_{ij})$ tends to zero when atom j moves far from atom i, a cut-off radius r_c can be often introduced to simplify calculations. Then we can write:

$$\varphi(r_{ij}) = \begin{cases} \varphi_p(r_{ij}) & \text{if } r_{ij} \leq r_c \\ 0 & \text{if } r_{ij} > r_c \end{cases} .$$

Pair potentials are often used because of their simplicity and numerical efficiency, however they give poor description of the mechanical response for most crystals as they do not account properly for the change in the bonding angle. Moreover, they do not distinguish between surface and bulk atoms. One way to overcome these limitations is to construct multi-body potentials of the form:

$$\Pi = \sum_{i<j} \varphi_p(r_{ij}) + \sum_{i<j<k} \varphi_{three}(\mathbf{r}_i, \mathbf{r}_j, \mathbf{r}_k) + \sum_{i<j<k<l} \varphi_{four}(\mathbf{r}_i, \mathbf{r}_j, \mathbf{r}_k, \mathbf{r}_l) + \dots \tag{1.9}$$

assuming a fast convergence towards real atomistic potential. Use of the three-body term φ_{three} already allows to account for the angles between atomics bonds, as for instance in the Stillinger-Weber potential [SW85]. Angle dependence is important when atoms form well localized coovalent bonds, as in dielectric solids and semi-conductors. Metals are characterized by more diffuse electronic configurations and suitable interatomic potentials can be obtained in the framework of the Embedded Atom Method (EAM) introduced by Daw and Baskes [DB83, DB84]. This method also makes use of a pair potential, which is often the above mentioned Lennard-Jones (1.8). It also incorporates a nonlocal energy

potential accounting for the atomic density of the local environment. The potential energy of the system is defined as:

$$\Pi = \sum_{i<j} \varphi_p(r_{ij}) + \sum_i F(\rho_i)\,, \tag{1.10}$$

where

$$\rho_i = \sum_{i \neq j} f(r_{ij})\,. \tag{1.11}$$

Here F is the embedding function which represents the energy needed to incorporate atom i in an environment characterized by electron density ρ_i and $f(r_i)$ is the contribution of atom i to electron density. Given that the embedding function F is nonlinear, this formulation successfully accounts for many-body effects that cannot be reproduced by a simple superimposition of pair interactions. Differently from simple pair-potentials, the EAM approach has been successfully fitted to reproduce the value of elastic constants of metals. Numerous examples of material-specific EAM realizations are found in the literature (see for instance [CY96]). In particular we mention the Ercolessi-Adams potential for aluminium [EA94, LEA04] and the Mishin potential for copper [MMP$^+$01].

An important feature of interatomic potential models is that they allow one to obtain the *atomic site energy* E_i in a straightforward manner. While the total potential energy Π has a clear physical meaning, the energy E_i, corresponding to a single atom, is a somewhat artificial construction. However, it will be very useful when bridging discrete atomistic description with continuum stress-strain relationships. In the case of a many-body potential, E_i is obtained by considering, in the relative sums, half of every pair-term contribution, a third of every three-body term and so on. In the case of the EAM potential one has:

$$E_i = \frac{1}{2} \sum_j \varphi_p(r_{ij}) + F(\rho_i)\,, \tag{1.12}$$

and it can be easily checked that $\Pi = \sum_i E_i$. Note that site energy E_i is associated with atom i, however it depends on positions of all other atoms within the cut-off trough pair interactions of the type $\varphi_p(r_{ij})$.

1.3 Multiscale Models

The MD techniques rely minimally on phenomenology and do not need any phenomenological assumption concerning the formation of dislocations and their motion. Dislocations emerge automatically as a result of atomistic interactions which also determine their kinetics. MD simulations were successfully used in plasticity, for instance, they were instrumental in the studying of dislocation nucleation in perfect and defected crystals [ZRSOB17],

intermittent plasticity in metals [NS15], and the irreversible behavior of colloidal polycrystals [MCM11].

However, the major drawback of MD method is the limitation on the accessible length scales. Typical MD simulations typically spans length scales varying from tens to hundreds of nanometers. Moreover, a fully atomistic resolution is not necessary far from dislocation cores, where long-range stresses characterizing far-field interaction between dislocations are well described by Volterra linear elastic solution (1.3). An ideal strategy would be to discard unnecessary degrees of freedom while keeping the essential features of dislocations cores. In view of this, the majority of small-scale plasticity models attempt to exploit the advantages of a continuum formulation while simultaneously keeping track of the discreteness characterizing small scale interaction. This type of modelling is called multi-scale, as it attempts to span different length scales simultaneously [McD19, TM11], a fine scale, the dislocation core, and different coarse ones, where a progressively less description is sufficient. Some of these methods introduce dislocations explicitly as specific objects moving in a linear-elastic medium. These dislocation-like objects obey specific rules which account for the short range interactions, for instance, ad-hoc criteria are added to implement nucleation and annihilation.

To this category belong *Discrete Dislocation Dynamics* (DDD) and the *Phase Field Method (PFM)*, discussed below. Other strategies instead, literally split the analyzed system in an atomistic, MD-based, subdomain and a continuum one, characterized by a coarser type modelling. These are known in literature as *coupled methods*, of which the Quasi-Continuum method (QC) is probably the most typical example. In this case the accessible system sizes are somewhat constrained by the fact that resolution is fully atomistic in some regions, while their advantage is that only minimal phenomenology is needed. Among all the discussed strategies, *Crystal Plasticity* (CP) is the most coarse. In this case, dislocations are not included explicitly but are present implicitly in the form of a constrained kinematics which mimics slip-plane localized deformation. We illustrate schematically the length scales spanned by the models mentioned above in Figure 1.4, (based on analogous schemes in [Caz13, PKM13, McD19]). Smaller length scales imply less phenomenology and higher resolution.

1.3.1 The Quasi-Continuum Method

The *Quasi-Continuum method* (QC) was originally proposed by Ortiz and co-authors in [TPO96] and was then significantly developed in the following years [SMT$^+$99, MT02, DELT07, SET14]. It is based on the observation that a fully atomistic resolution is actually needed only in limited regions of the modeled problem, where deformation gradients are high. The majority of the modeled domain is instead characterized by slowly varying deformation fields and can be modeled by means of the classical continuum theory.

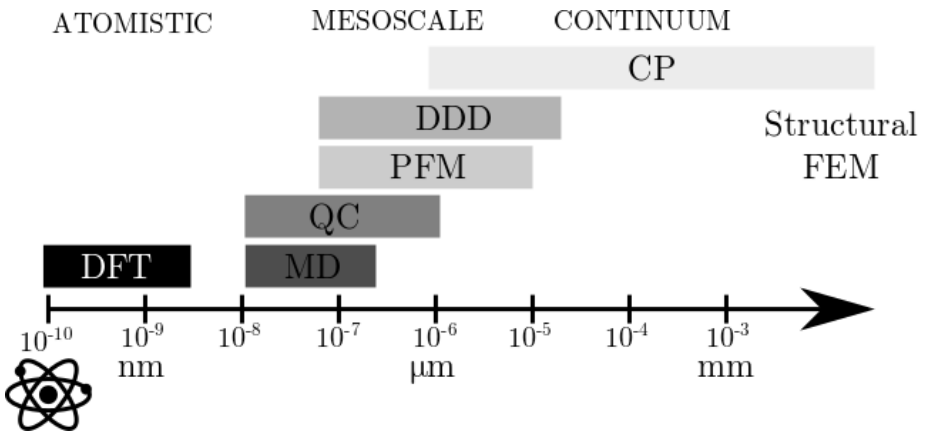

Figure 1.4: **Modelling Techniques and Spanned Lenght Scales:** Schematic illustration of the tipical lenght scales spanned by simulations with the four illustrated models for small-scale plasticity.

Considering this, authors subdivide the domain in a subdomain Ω^{cont}, where the formulation is continuum, and a subdomain Ω^{atom}, where the formulation is atomistic. In a quasistatic setting, equilibrium is found by parametric minimization of the total potential energy Π of the system. The latter is taken as a sum of potential energies on these two subdomains:

$$\Pi = \Pi^{cont} + \Pi^{atom} \,. \tag{1.13}$$

Potential energy Π^{atom} is evaluated as the sum of the site energies E_i of all atoms in Ω^{atom}:

$$\Pi^{atom} = \sum_{\Omega^{atom}} E_i \,, \tag{1.14}$$

In the continuum subdomain Ω^{cont} site energies E_i are replaced with a continuum energy density ϕ. Differently from the site energy E_i (1.12), which depends on the displacement $\mathbf{u}$ of all other atoms within its cut-off radius, the continuum energy density $\phi(\mathbf{X})$ at a generic point $\mathbf{X}$ depends only on the displacement gradient at that point. An important feature of QC is that the continuum energy density ϕ is evaluated directly on the basis of interatomic potentials. This can be done assuming that deformation gradient $\mathbf{F} = \nabla(\mathbf{X} + \mathbf{u})$[1] is homogeneous in the neighborhood of point $\mathbf{X}$ and that the atomic lattice is deforming accordingly. Consequently, all site energies E_i of atoms in the lattice underlying continuum point $\mathbf{X}$ are equivalent and depend only on the homogeneous deformation gradient $\mathbf{F}(\mathbf{X})$. This means that the corresponding continuum energy density ϕ is given simply by:

$$\phi(\mathbf{X}) = \frac{1}{\Omega_0} E_i(\mathbf{F}(\mathbf{X})) \,, \tag{1.15}$$

[1] We will discuss in full detail this deformation tensor in Chapter 3.

where Ω_0 is the volume of the undeformed lattice cell.

Practically, in order to minimize (1.13) numerically, the continuum subdomain Ω^{cont} has to be subdivided in a number n_e of discrete elements with volume Ω^e such that $\Omega^{cont} = \sum_e^{n_e} \Omega^e$. The potential energy Π^{cont} is then approximated by:

$$\Pi^{cont} \approx \tilde{\Pi}^{cont} = \sum_e^{n_e} \Omega^e \phi(\mathbf{F}_e)\,, \tag{1.16}$$

where $\mathbf{F}^e$ is the homogeneous deformation gradient within element e. It is important to notice that computation of a continuum energy density by means of (1.15) implies the important physical assumption that the continuum deformation gradient $\mathbf{F}$ actually describes the deformation of the underlying atomic lattice. This hypothesis is known as Cauchy-Born rule and has important consequences. We will explain these concepts in more detail in Chapter 3.

An advantage of the QC method is that it is easily integrated in a Finite Element Method (FEM), a well developed technique for the numerical solution of continuum problems[2]. Moreover, QC allows one to coordinate the evolution of Ω^{cont} and Ω^{atom} with the deformation process, in a way that the atomistic description can be limited only where it is truly needed. This can be done with automatic adaption schemes, which can expand the atomic region to the detriment of the continuum one and vice-versa [SMT$^+$99].

A inherent weakness of the QC is given by the necessity of patching the continuum and discrete subdomains Ω^{cont} and Ω^{atom} through a sharp interface. Naturally, the differences between the two formulations generate spurious forces, known as *ghost forces*. Their control is not straightforward, but the spurious effects may be reduced, given that some precautions have been taken [MT02, TM11]. The QC method has been used in many applications, including the study of nano-indentation, deformation of grain-boundaries and crack tip evolution [MT02].

The somewhat contradictory nature of the interface connecting subdomains Ω^{cont} and Ω^{atom} led the authors to use, in some applications, a completely continuum formulation, known as the *local QC* [TOP96]. In this case, the potential energy is evaluated on the entire domain Ω by means of the Cauchy-Born based energy density (1.15) and we have $\Pi \approx \tilde{\Pi}^{cont}$, however, this energy can be attributed either to a continuum or to a lattice. This local QC is by itself a meso-scale method mixing continuum and atomistic features. More specifically, it is a mixed discrete-continuum formulation where the constitutive law

[2]We will discuss the FEM method in more detail when discussing the numerical implementation of the proposed model. Important references for this method, now widely used in all branches of continuum mechanichs, are [ZT00a, ZT00a] and [Hug12].

relating stresses and strains is evaluated directly from interatomic potentials and not defined phenomenologically.

Some authors refer to the local QC model as *Cauchy-Born Theory of Crystal Elasticity* [OP98]. This approach was shown to be capable of representing dislocations, even if in an approximated, coarsened, way. The success of this method is due to the fact that the use of the Cauchy-Born assumption imbues the continuum energy density with elastic non-linearity, and most importantly, with the correct crystal invariance[3]. However, at the same time, it underrepresent some truly atomistic features, for instance, deformation gradients varying rapidly within the cut-off distance cannot be adequately represented. Among other approaches using the Cauchy-Born based continuum energies, we mention the *Interatomic Potential FEM* method (IPFEM) by Van Vliet and co-workers [VVLZ$^+$03, ZLVV$^+$04]. This is an independently formulated local QC used for the study of homogeneous nucleation during nanoindentation.

As we have already mentioned, coupled atomistic methods different from QC were also proposed in literature, even if they did not reach the same attention. They also confront the issue of the continuum-atomistic interface. We refer the reader to the dedicated review of Miller and Curtin [CM03], to the more general review of McDowell [McD19] and also to the corresponding chapter in the book of Tadmor [TM11], which contains an exhaustive discussion of these techniques.

1.3.2 Discrete Dislocations Dynamics

Differently from the approaches based on the QC method and its local versions, where dislocations emerge as a result of atomistic interactions or lattice-informed properties of the constitutive functions, in the *Discrete Dislocation Dynamics* (DDD) method dislocations are inserted explicitly, and modeled as line segments which evolve in an elastic medium and interact with each other through linear-elasticity. To account for the core non-linearity, specific rules controlling close-range interactions between dislocations are then added to the formulation. This method was developed to describe the collective motion of a large number of dislocations and it allows one to simulate length scales up to about tens of μm in a 3D setting [Caz13]. The DDD method was first proposed at the beginning of 1990 by Kubin and co-authors [KC92, DPB$^+$92]. Since then, it has been significantly developed and has been widely used to study microscale plasticity, with the main focus on dislocation patterning [DMM$^+$11, ACT$^+$07]. Different DDD codes were developed by different teams of researchers. In particular we mention the French codes microMegas (mM) [DPB$^+$92, DMM$^+$11, DG15], TRIDIS[FGC96] and NUMODIS[DDO$^+$14], and the US code ParaDIS [BCF$^+$04].

[3]This is the reason why the local QC is similar, to some extent, to the model presented in this thesis

The DDD method reduces to the solution of the equations of motion of the dislocation segments, and generally inertial terms are neglected (over-damped dynamics). This leads to a system of differential equations in which the segment instantaneous velocity $\mathbf{v}_i$ is linked directly to the applied force $\mathbf{f}_i$, through some phenomenological mobility law. Despite the simplicity of this main underlying idea, solution of these equations is complicated by the fact that topology of the dislocation network is not fixed: dislocation segments vary in their number and in their connectivity during the simulation.

The method starts with a given network of dislocations, discretized in different ways depending on the particular DDD implementation. Thus, the discrete representation of dislocations can be nodal, when forces and displacements are evaluated at the network nodes [BC06], or based on the subdivision of the dislocation network in rigidly moving, elementary, segments [DPB$^+$92, DMM$^+$11, DG15].

Forces $\mathbf{f}_i$ are then evaluated for every segment (or node, depending on the particular DDD formulation) of the net. In a linear elastic setting, the force per unit length acting on a dislocation line is given by the Peach-Koehler formula:

$$\mathbf{f}^{PK} = (\boldsymbol{\sigma} + \boldsymbol{\sigma}^{ext}) \cdot \mathbf{b} \times \mathbf{a}\,, \tag{1.17}$$

where $\boldsymbol{\sigma}$ is the internal stress resulting from the elastic interaction of a given dislocation with the other dislocation segments, $\boldsymbol{\sigma}^{ext}$ the stress related to the external applied forces, $\mathbf{b}$ is the Burgers vector and $\mathbf{a}$ is an unit vector tangent to the dislocation segment. The analytical expressions for $\boldsymbol{\sigma}$ available in literature for infinite dislocation loops can be corrected to account for finite dimensions [FC99]. The corresponding representations in the case of anisotropic elasticity are also available [RSB$^+$01].

Once forces $\mathbf{f}_i$ are evaluated along every segment i, dislocation motion is given on the basis of mobility functions of the type:

$$\mathbf{v}_i = M(\mathbf{f}_i)\,. \tag{1.18}$$

Mobility of a dislocation line depends on many factors, among which the orientation of the force with respect of the gliding plane, the orientation of the dislocation line and the lattice structure of the considered material. In view of this, many mobility functions were proposed in the literature, depending on the specific problem at hand (see for instance the discussion in the dedicated section of [BC06]). A very simple approach consists in neglecting the component of $\mathbf{f}_i$ orthogonal to the gliding plane and assuming that velocity depends linearly on in plane component τ_i (the resolved shear stress):

$$\mathbf{v}_i \begin{cases} = 0 & \textit{if} \quad \tau_i^* = |\tau_i| - \tau^f \\ = sign(\tau_i)\frac{\tau_i^* \mathbf{b}_i}{B} & \textit{otherwise} \end{cases}. \tag{1.19}$$

where τ^f is a friction parameter and B a viscous drag coefficient.

As already remarked, phenomena intrinsically related to core effects, such as annihilation, nucleation, formation of junctions, climb and cross-slip, need to be accounted through specifically added phenomenology. These corresponding relations can be fitted using data obtained from MD simulations [BAK+98]. However, the necessity of building ad-hoc rules for accounting essential dislocation mechanisms is still a major limitation of this approach. Another problem is how to control the topology of the evolving net. Dislocation lines change their curvatures and their configuration during the simulation and their discretization in linear segments has to be updated accordingly. Changes in the topology due to segments interlocking is notoviously difficult to account.

To summarize, the DDD method is advantageous when one needs to model micrometric samples with a large number of dislocation lines whose long-range interactions are crucial. In the last decades DDD has been used to model many small-scale plasticity phenomena, among which the study of dislocation mechanisms beyond strain hardening [DK97, ZRHdlR00], dislocation patterning in monotonic and cycling loading [WG05, KMG+10] and the intermittency of plastic flow [ILZ+14].

Finally we mention that the effort to couple DDD with MD, developed by Shilkrot et al. [SMC02, SMC04], referred to as the *Coupled Atomistic Discrete Dislocation* (CADD) method, is worth of notice. However examples of applications of such coupled strategy are still very limited.

1.3.3 Phase Field Method

An alternative approach to treat dislocations in a continuum framework is the *Phase Field Method* (PFM), based on the Ginzburg-Landau theory [LL13, Gin04]. This is a general method that can be applied to a wide range of physical problems and it is called so since it was originally applied to study the evolution of different phases in metals and alloys [Che02, SFDS12]. In the application of the phase field model for dislocations, the order parameter (phase-field) ψ assumes integer values reflecting the amount of an elementary shear on a given slip plane. Dislocations can then appear as elements of domain boundaries in finite regions that underwent different amount of shears. The number of order parameters ψ_a can be chosen to represent the number of slip planes and will then characterize the crystal symmetry.

The system is assumed to evolve quasi-statically minimizing at each moment of time its total free energy E, which is given as a functional of the fields $\psi_\alpha(\mathbf{x})$. The spatial-temporal evolution of the phase-fields can be obtained by linking the variational derivatives of the functional $E(\psi_\alpha(\mathbf{x}))$ with the rates of change of the fields $\psi_a(\mathbf{x})$, which leads to a system

of Partial Differential Equations (PDEs). Given that the fields $\psi_a(\mathbf{x})$ are not conserved, the simplest evolution equations of this type take the form:

$$\frac{\partial \psi_a(\mathbf{x})}{\partial t} = -\kappa \frac{\delta E}{\delta \psi_\alpha(\mathbf{x})}\,, \tag{1.20}$$

where κ is a mobility coefficient and $\frac{\delta E}{\delta \psi_a}$ is the variational derivative of functional E with respect of field ψ_α.

The first applications of PFM to dislocation modelling were proposed in [WJCK01, RLBF03] and are based on the elastic equivalence between a localized slip region associated with a dislocation loop and a platelet inclusion, already pointed out by Nabarro [Nab51]. It can be described by a (stress-free) eigenstrain[4] :

$$\epsilon^*_{ij} = \frac{b_i n_j - b_j n_i}{2d}\,, \tag{1.21}$$

where $\mathbf{b}$ and $\mathbf{n}$ are the Burgers vector and the normal to the slip plane. In this way, dislocations can be coherently described in a PFM setting if we associate with every slip system α a phase field $\psi_\alpha(\mathbf{x})$ and the eigenstrain $\varepsilon^{*\alpha}_{ij}$ determined by the corresponding Burgers vector $\mathbf{b}_a$. Since densities $\psi_\alpha(\mathbf{x})$ characterize the slip produced by dislocations passed at point $\mathbf{x}$ along slip system α they must assume integer values (positive or negative). When more than one slip system are present, the total eigenstrain is given by the sum of eigenstrains $\varepsilon^{*\alpha}_{ij}$ associated to the various slip systems:

$$\epsilon^*_{ij} = \sum_\alpha \varepsilon^{*\alpha}_{ij} \psi_\alpha(\mathbf{x})\,. \tag{1.22}$$

Construction of the free energy functional $E(\psi_\alpha(\mathbf{x}))$ reduces to the addition of three terms, an elastic term E^{el}, a lattice term E^{latt} and a gradient term E^{grad}:

$$E^{tot} = E^{el} + E^{latt} + E^{grad}\,. \tag{1.23}$$

In the context of linear elasticity, the elastic energy E^{el} is given by:

$$E^{el} = \frac{1}{2}\int_\omega c_{ijkl}(\varepsilon_{ij} - \epsilon^*_{ij})(\varepsilon_{kl} - \epsilon^*_{kl}) d\omega - \int_\omega \sigma^{ext}_{ij}\varepsilon_{ij} d\omega\,, \tag{1.24}$$

where σ^{ext}_{ij} is an external uniform stress, ε_{ij} is the tensor of small deformations and c_{ijkl} is the tensor of the linear-elastic moduli. The equilibrium state associated with (1.24) can be determined analytically (see [Kha13] and[RLBF03] for more details).

[4]By eigenstrain we mean a stress-free deformation as in the case of thermal expansion or twinning. Being obstructed by the surrounding body, the eigenstrain cannot take place freely and causes an internal stress. The problem of finding the stress associated with an arbitrary inclusion is known in literature as *Eshelby problem* [Esh57]. Its solution requires the knowledge of a Green function, which can be conveniently expressed in Fourier space, as illustrated by Khachaturyan [Kha13].

The lattice term E^{latt} is added to stabilize the phase fields $\psi_\alpha(\mathbf{x})$ to integer values. It takes the form of a sum of periodic potentials (one for each slip system) with infinite number of wells. A simple possible form is:

$$E^{latt} = \int_\omega \sum_\alpha \frac{A_\alpha}{2\pi^2}(1 - \cos(2\pi\psi_\alpha(\mathbf{x})))d\omega\,, \tag{1.25}$$

where A_α are adjustable coefficients (see also [RLBF17] and [ZZNH18] where different forms of E^{latt} have been proposed).

Finally, the gradient term E^{grad} is added in order to penalize inhomogeneous configurations where phase fields ψ_α vary rapidly in space. The presence of this term results in a diffuse structure of the dislocation core. The term E^{grad} it has to be nonzero only along the dislocation line and one suitable form is:

$$E^{grad} = B \int_\omega \sum_\alpha ||\mathbf{n}_\alpha \times \nabla\psi_\alpha(\mathbf{x})||^2 d\omega\,, \tag{1.26}$$

with B adjustable coefficient and $\mathbf{n}_\alpha$ normals to slip systems.

The PFM method has been largely used to study individual dislocations and their interaction with other phases [HC01, Che02]. New versions and applications are continuously proposed and some recent developments were reviewed in [HSLK11]. Extensions of PFM to finite strains have been developed as well [JL16]. One of the inherent challenges for this method is the fact that choosing the appropriate length scale describing the dislocation cores is not straightforward and has to be done phenomenologically. Moreover, the true periodic lattice structure is resolved only very approximately by the use of scalar parameters controlled by scalar periodic functions and by the use of a linear elasticity framework. Considering this, the rigorous account for the lattice-induced coupling between different plastic mechanisms remains a challenge.

1.3.4 Crystal Plasticity Theory

Continuum crystal Plasticity theory (CP) is the most broadly used approach to the modelling of crystal plasticity. It is based on introducing lattice-based kinematics in the classical continuum setting. Its original mathematical formulation was given by Hill [Hil66] and Hill and Rice [HR72], and its first applications were considered in the works of Asaro and Rice [AR77, Asa83] and Pierce, Asaro and Needleman [PAN83]. Since then, it has been developed further by many other authors (see [REH$^+$10] for a complete review). With respect of the previously discussed methods, CP spans larger length scales, varying between μm and mm, due to the coarser representation of plastic deformation. In the recent CP formulations, deformations are assumed to be finite and the adopted continuum description

clearly distinguish between reference and deformed configurations. The incorporation of lattice features in the continuum formulation is done by a multiplicative decomposition of the total deformation gradient $\mathbf{F}$ in an elastic and a plastic component:

$$\mathbf{F} = \mathbf{F}^e \mathbf{F}^p \,. \tag{1.27}$$

Decomposition (1.27) implies that that deformation takes place in two stages. First, $\mathbf{F}^p$ brings the initial reference state Ω to an intermediate state Ω^* characterized by plastic deformation only, and then $\mathbf{F}^e$ brings the body to the final configuration ω through elastic deformation and rigid lattice rotation. Following [Man72, AR77], we assume that $\mathbf{F}^p$ leaves the underlying lattice structure undeformed and unrotated. The absence of rotation of the lattice vectors in the intermediate configuration ensures the uniqueness of the decomposition (1.27). The peculiarity of the CP approach is in the construction used for the plastic component $\mathbf{F}^p$, which is done by constraining dislocation kinematics. Plastic flow is assumed to evolve along pre-selected slip directions by means of volume preserving shears, which leaves the crystal lattice undistorted and stress-free [McH04]. Every slip system α is characterized by two unit vectors $\mathbf{n}_\alpha$ and $\mathbf{a}_\alpha$, indicating respectively the normal to the slip plane and the direction of the slip. Plastic deformation is then modeled as a friction-controlled shear deformation γ_α along these slip planes. When multiple slip planes are active simultaneously, the total plastic strain at the generic point is assumed to be given by the superimposition of shear strains γ_α at that point. In order to coherently include this shear-constraining kinematics in the continuum formulation, it is necessary to link the shear strains γ_α to the tensorial measure of strain $\mathbf{F}^p$. This is done using the spatial velocity gradient $\mathbf{L} = \dot{\mathbf{F}}^p \mathbf{F}^{p-1}$, which is related to the shear strain rates $\dot{\gamma}_\alpha$ through the expression [Ric71]:

$$\mathbf{L} = \sum_\alpha \dot{\gamma}_\alpha \mathbf{a}_\alpha \otimes \mathbf{n}_\alpha \,. \tag{1.28}$$

To relate the shear strain rates $\dot{\gamma}_\alpha$ to the local stress a constitutive law needs to be introduced. Different proposals are found in the literature, some of them phenomenological, others more physically based. One of the simplest phenomenological approaches is to assume that the shear strain rates $\dot{\gamma}_\alpha$ depends on the stress only through resolved shear stress τ_α. Assuming also the dependence on other material parameters g_α, we obtain relations of the type:

$$\dot{\gamma}_\alpha = \dot{\gamma}_\alpha(\tau_\alpha, g_\alpha) \,, \tag{1.29}$$

where parameters g_α allow one to characterize the hardening along different slip systems α. Most importantly, constitutive relations (1.29) allow one to distinguish between inactive ($|\tau_\alpha| < g_\alpha$) and active ($|\tau_\alpha| > g_\alpha$) slip planes. One of the most broadly used expressions is [PAN83]:

$$\dot{\gamma}_\alpha = \dot{\gamma}_\alpha^0 sign(\tau_\alpha) \left(\frac{|\tau_\alpha|}{g_\alpha} \right)^m \,. \tag{1.30}$$

Similar formulations can be found already in [Ric71, Hut76]. Parameters g_α are assumed to be coupled with plastic mechanisms:

$$\dot{g}_\alpha = \sum_\beta h_{\alpha\beta} |\dot{\gamma}_\beta| \tag{1.31}$$

where $\mathbf{h}$ is the hardening matrix, rate independence is ensured by condition $|\dot{\tau}_\alpha| = \dot{g}_\alpha$. The relations (1.31) account for the hardening caused by $\dot{\gamma}_\alpha$ on the slip system (diagonal terms $h_{\alpha\alpha}$, expressing self-hardening) and on the other slip systems $\beta \neq \alpha$ (off-diagonal terms $h_{\alpha\beta}$, expressing latent hardening). Construction of this hardening matrix is generally based on phenomenological observations [McH04].

The incremental equations are completed with the introduction of a constitutive law for the elastic part of the deformation (see for instance [McH04]). The simplest formulations assume linear dependence between the second Piola-Kirchhoff strain tensor $\mathbf{S}^*$ and the Right Cauchy-Green strain tensor $\mathbf{C}^*$[5] in the intermediate configuration Ω^*, however the possibility of using higher order elastic moduli have been considered as well [Teo13]. The obtained incremental equations, relating total (plastic and elastic) stress to the total deformation can be equivalently mapped to the deformed configuration, as it is done in [AN85, Asa83]. The original formulation in the undeformed configuration is summarized in [HDA88, MAS93, CO93].

As we have already mentioned, the continuum CP approach is way more coarser than the previously discussed strategies, in particular, in this approach plastic defects are not resolved individually. Dislocations are effectively replaced by continuously evolving incremental shear strains γ_α. Both short range and long range dislocation interactions are then hidden in this coarse representation. On the other hand, the simplified kinematics allows one to access larger time and length scales and to model complex 3D systems with complex geometries. The method can be easily implemented in a FEM setting, which allows one to model a variety of physical phenomena, ranging from grain boundary evolution to pattern formation in cycling loading [REH$^+$10, AFA$^+$18]. Some other dislocation-related effects, such as kink and shear-band formation, can be also included in the continuum CP model [For98], however, at the expense of introducing a much richer set of kinematic variables.

1.3.5 Conclusions

In this concise review of crystal plasticity models we illustrated different techniques which were proposed to enrich continuum formulations by adding various discrete features. The common objective of such hybrid methods is to achieve an acceptable description of dislocations and, at the same time, reaching length scales that would be inaccessible to purely

[5] In the following chapters we will define these stress and strain measures in more detail.

atomistic models. None of the proposed methods can be thought as uniquely superior in an absolute sense, as they are all designed for different applications and each carries its own advantages and disadvantages. Methods in which dislocations are added "by hand" can handle larger modelling scales, but are characterized by uncertainty implied by the use of the phenomenological rules. On the other hand, methods like QC, which resolve dislocations in full detail, present other types of uncertainties due to the presence of the atomistic-to-continuum interface regions and to the necessity to follow their evolution. In the last decade, the major efforts were directed to the integration of different strategies with each other, in a way that lower-scale models are used to calibrate the phenomenological rules needed at larger scales. In this context, each of the discussed strategies has its own domain of application and often the advancement of one ends up benefiting the other. The local QC is what mostly resembles the mesoscopic model proposed in this PhD thesis in terms of the general setting and the range of spanned length scales. Its formulation is particularly advantageous: it has a purely continuum, non-linear, finite displacement formulation, but at the same time it integrates atomistic features without any phenomenological assumptions other than the ones adopted in lattice models. However, there is an inherent contradiction in assuming that the energy (1.15) remains adequate for every size, no matters how indefinitely small, as implicitly postulated in the continuum setting. We will discuss this point extensively in the rest of this PhD Thesis.

The Thesis is structured as follows. In Chapter 2 we show how to construct the energy density functional on which the proposed mesoscopic model is based. Some basic concepts of crystallography, essential for understanding the theory, are also recalled. A suitable energy for the purpose of modelling plasticity is the polynomial form proposed in [CZ04], that is discussed in detail. After, the obtained energy landscape is shown. In Chapter 3, the energy density functional, introduced before for a crystalline lattice, is extended to a continuum hyperelastic formulation. Some details concerning the numerical implementation are also discussed. The chapter ends with some simple validation tests, where the dislocation core and some basic dislocations interactions are illustrated. Chapter 4 is dedicated to the study of the homogeneous nucleation of dislocations in the framework given by the introduced mesoscopic model. Numerical simulations are accompanied by an analitical stability criterion which allows one to better interpret the obtained results. These show the formation of very complex defect patterns already in correspondence of this early stage of plasticity. In Chapter 5, we introduce a different form for the energy density function, which respects the same symmetry properties as before, but that is based directly on interatomic potentials. We show that the mechanisms of pattern formation previously observed with the polynomial form are robust and manifest also with the use of this energy functional. Then, the obtained results are compared directly with atomistic simulations using the same pair potential. In Chapter 6, we provide concluding remarks and perspectives.

Chapter 2

The Model

In this Chapter, we present the model that will be used throughout this Thesis for the description of crystal plasticity. Generally speaking, when modeling non-isotropic materials characterized by the presence of a lattice structure, the symmetry properties associated with the lattice itself need to be accounted for. This means, for instance, that the energy must have the same value every time the deformation produces a symmetry-related configuration. Such symmetry-based invariance differs from the *material frame indifference*, the invariance related to rigid body motions, and the symmetry associated with the changes of reference coordinate system, and it is known as *material symmetry*. In the classical notion of material symmetry, developed most extensively by Coleman and Noll [CN64] and widely used in elasticity theories [TN04], this invariance is expressed only in terms of rotations applied to the reference lattice. In crystallography, this type of transformations is expressed by the *crystallographic point group* $P(\mathbf{e}_I)$. Later, we will define this object in more detail; for now, we just mention that the invariance of a lattice by means of rotations does not recover fully the material symmetry.

To explain this, we provide a simple example. Consider a regular square lattice deformed by a homogeneous simple shear. When increasing the shear deformation, the associated energy will grow up to a maximum value and then decrease again down to a new minimum where an equivalent lattice configuration is recovered, as illustrated schematically in Figure 2.1. Although this periodicity is not described by the crystallographic point group $P(\mathbf{e}_I)$, it is fundamental for plasticity-related phenomena. For instance, an edge dislocation can be represented as a lattice configuration intermediate between two subsequent wells of the type illustrated in Figure 2.1 (see also Figure 1.1 in the previous chapter). More precisely, a dislocation can be interpreted as the boundary between sheared and unsheared crystal regions, and is then represented by a sequence of distorted lattice elements whose energy is somewhere around the energy barrier separating the two equivalent wells. We schematize this concept in Figure 2.2.

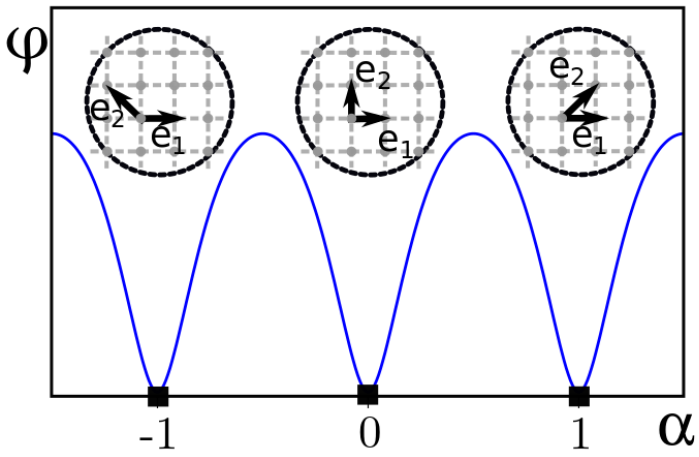

Figure 2.1: **Lattice Invariant Shears:** Schematic representation of shear invariance for a square lattice subjected to simple shear $\mathbb{S} = \mathbf{I} + \alpha \mathbf{e}_1 \otimes \mathbf{e}_2$. Energy density φ has to be minimum in correspondence of equivalent lattice configurations, i.e. for every integer α.

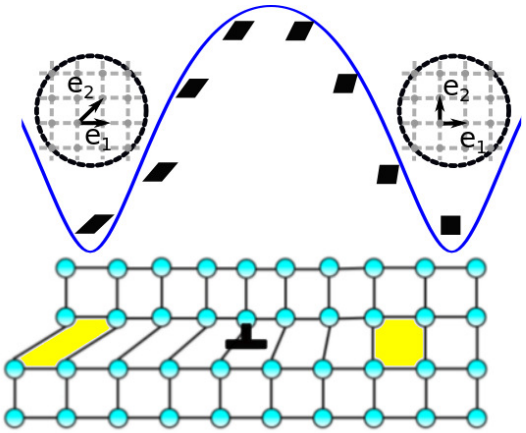

Figure 2.2: **Energetic Profile of a Dislocation:** Schematic representation of a dislocation as the boundary between sheared and unsheared crystal regions. Two energetically equivalent square crystal configurations are made compatible thanks to the presence of an edge dislocation. Lattice elements belonging to the core are higher in energy and their energetic state is located up the energy barriers.

Description of lattice invariant deformations by using periodic energy functionals is not new in literature, and dates back to the one-dimensional model of Frenkel Kontorova [FK39]. Several other 1D models with periodic elastic energies were proposed for the description of dislocation cores [Nab47, KKKL93, CB03], the analysis of dislocation nucleation [LS86, PCB07] and the study of the intermittency characterizing the plastic flow [ST11, ST12]. Extension of these models to a tensorial, multi-dimensional, formulation with linearized kinematics was also considered in [MO07, Onu03, CB05]. However, in all these works, the periodic landscape was defined only along highly symmetric shear directions, and did not reflect adequately the symmetry properties of the crystal. The fact that they all make use of linearized kinematics and define strain as $\epsilon = \frac{1}{2}(\nabla \mathbf{u}^T + \nabla \mathbf{u})$, where $\mathbf{u}$ is the displacement from initial configuration, makes the exact representation of crystal symmetry impossible.

In this Chapter, we introduce a model where a periodic landscape is completely defined in the full tensorial space of finite strains $\mathbf{E} = \frac{1}{2}(\nabla \mathbf{u}^T + \nabla \mathbf{u} + \nabla \mathbf{u}^T \nabla \mathbf{u})$ and which is fully coherent with the symmetry of the lattice for general shear directions. In its innovative work [Eri77, Eri80, Eri05, Eri87, Eri91], Ericksen realized that the required lattice invariance property is not the one associated with the finite group $P(\mathbf{e}_I)$, but rather the one described by the infinite *global symmetry group* $G(\mathbf{e}_I)$. The latter turns out to be coincident with the set of unimodular matrices $GL(2, \mathbb{Z})$. While $P(\mathbf{e}_I)$ expresses the invariance only with respect of orthogonal transformations (i.e. rotation and reflections), $G(\mathbf{e}_I) := GL(3, \mathbb{Z})$ accounts also for non-orthogonal transformations describing lattice invariant shears. These are needed for the description of the slip associated with plastic deformation (as the one illustrated in Figure 2.1).

It has been shown that the invariances described by $P(\mathbf{e}_I)$ and $G(\mathbf{e}_I)$ symmetries are compatible, as the first can be obtained from the second, provided that $G(\mathbf{e}_I)$ is restricted to a suitable neighborhood, known as the *Ericksen-Pitteri neighborhood* (EPN) [Pit84]. Intuitively, the analog of an EPN in the simple scalar example, showed in Figure 2.1, would be the region between -0.5 and 0.5, associated with single well and thus representing the domain where the system deforms "elastically". Point group $P(\mathbf{e}_I)$ invariance can be seen as a "small strain" restriction of $G(\mathbf{e}_I)$ and the two theories are coherent.

In view of the above, only by implementing the crystal invariance dictated by $G(\mathbf{e}_I)$ it is possible to include irreversible crystal deformations in the model [Eri77, Eri80, PZ02]. We remark that, to account for lattice-invariant shears, geometrically non-linear strains are absolutely necessary to distinguish different symmetry-related lattices. Energies accounting for such invariance have been developed for the description of martensitic phase transitions [DRGT88, HGK89, SSL01, CZ04, PRTZ09, DV16], and have been studied in [Fon87, Kin87b, Kin87a, CK88], however a systematic investigation of their capability to

describe plasticity is still missing.

We consider our approach as a combination of two different perspectives. From one point of view, it has been shown that plasticity is suitably described by periodic elastic energies. Indeed, plastic deformation can be interpreted as a change of phase where the lattice goes from a reference state, to a symmetry-related sheared configuration. Dislocations will appear in view of incompatibility between these two phases, represented by two minima of the potential. This understanding led to the development of several scalar models in which periodic energy was assigned along slip directions [FK39, Nab47, Onu03, CB05, ST12]. On the other hand, there were several efforts to include microstructural lattice features directly into the continuum thermoelastic problem [Eri05, Eri87, Eri91, TPO96, CZ04]. Mostly due to Ericksen's efforts, the inadequacy of $P(\mathbf{e}_I)$ for the task of modeling symmetry breaking reconstructive crystal transformations, and therefore plasticity, was finally realized.

An energy landscape with material symmetry based on the $GL(3,\mathbb{Z})$ invariance, must be periodic in shear and is therefore characterized by infinite number of wells. Moreover, in contrast to the previously mentioned scalar models, this landscape must be defined for general finite strains. Considering this, a $GL(3,\mathbb{Z})$ invariant model must be a geometrically nonlinear tensorial extension of the scalar theories. In such model the nucleation of dislocations will result from elastic instability of the system and the interactions of dislocations will be fully described by the periodic energy landscape, without the need of any additional phenomenology.

The ensuing model takes the form of Landau theory, in which the geometrically nonlinear metric tensor, measuring the local deformation, becomes the order parameter [BAB$^+$19]. Different phases are the shear-invariant configurations described by an infinite number of equivalent energy wells, whose position is governed by the global symmetry group $GL(3,\mathbb{Z})$.

We begin this Chapter by discussing some fundamental notions of crystallography (we refer to [Eng12] for deeper insights). Discussion will be limited, for simplicity, to two dimensional systems. We will therefore illustrate invariance under the $GL(2,\mathbb{Z})$ group rather than $GL(3,\mathbb{Z})$, which also allows for a more transparent representation of the associated configurational space. We continue by showing how an energy possessing the desired symmetry can be actually constructed. In particular, we discuss the polynomial energy function developed in [CZ04] for the description of martensitic phase transitions. In particular, we show that this energy is also suitable for description of crystal plasticity. We then describe in detail the properties of the obtained energy landscape for two different type of lattices: square and triangular.

Implementation of this energy in a general continuum mechanics framework will be illustrated in the following Chapter.

2.1 Notions of Crystallography

A Bravais lattice is a structure that can be constructed by infinite integer translations of two linearly independent vectors $\{\mathbf{e}_I\}$, the *lattice basis*, in every space direction, i.e. more formally:

$$\mathcal{L}(\mathbf{e}_I) = \left\{\mathbf{x} \in \mathbb{R}^2,\, \mathbf{x} = v_I \mathbf{e}_I,\, v_I \in \mathbb{Z}\right\}\,, \tag{2.1}$$

where Einstein summation convention is implied. Bravais lattices are also referred to as simple lattices [1]. We can associate with a basis $\{\mathbf{e}_I\}$ a *metric tensor* $\mathbf{C}$:

$$C_{IJ} = C_{JI} = \mathbf{e}_I \cdot \mathbf{e}_J \quad (1 \leq I, J \leq 2) \quad . \tag{2.2}$$

The tensor $\mathbf{C}$ is always symmetric and positive definite. For a given Bravais lattice, there are infinite choices for the basis $\{\mathbf{e}_I\}$, i.e. infinite ways to describe the same lattice. The group of all the transformations leaving a lattice $\mathcal{L}(\mathbf{e}_I)$ invariant is known as the *global symmetry group* $G(\mathbf{e}_I)$ of lattice $\mathcal{L}(\mathbf{e}_I)$. It is the maximal subgroup of group *Aut* of invertible tensors[2] leaving a lattice invariant:

$$\begin{aligned} G(\mathbf{e}_I) &:= \{\mathbf{H} \in Aut: \quad \mathcal{L}(\mathbf{H}\mathbf{e}_I) = \mathcal{L}(\mathbf{e}_I)\} \\ &= \{\mathbf{H} \in Aut: \quad \mathbf{H}\mathbf{e}_I = m_{JI}\mathbf{e}_J, \quad \mathbf{m} \in GL(2,\mathbb{Z})\}\,. \end{aligned} \tag{2.3}$$

All 2D lattices are characterized by the same global invariance, as their symmetry is expressed by groups, that, in suitable bases, do all coincide with $GL(2,\mathbb{Z})$, the set of reversible 2D integer matrices:

$$G(\mathbf{e}_I) := GL(2,\mathbb{Z}) = \{\mathbf{m},\, m_{IJ} \in \mathbb{Z},\, \det(\mathbf{m}) = \pm\mathbf{1}\} \quad . \tag{2.4}$$

In other words, invariance within this group means that we may choose infinite number of different bases for the same lattice. However they must be all in relation through the action of $GL(2,\mathbb{Z})$:

$$\bar{\mathbf{e}}_J = m_{IJ}\mathbf{e}_I \;\text{ with }\; \mathbf{m} \in GL(2,\mathbb{Z}) \quad . \tag{2.5}$$

The corresponding symmetry for metric tensors $\mathbf{C}$ is given by

$$\bar{\mathbf{C}} = \mathbf{m}^T\mathbf{C}\mathbf{m} \quad \bar{C}_{IJ} = m_{KI}C_{KL}m_{LJ}\,. \tag{2.6}$$

[1] Crystals which are characterized by a more complex structure are called *multilattices*. In this case additional parameters $\mathbf{p}_i$, the *lattice shifts*, are needed in addition to the lattice basis $\{\mathbf{e}_I\}$ to describe the crystal structure.

[2] When linear maps are represented in matrix form, we are assuming a reference basis for the description of space $\mathbb{R}^2$. Here, we will always assume as reference basis the Cartesian orthonormal basis $\{\mathbf{I}_I\}$ of $\mathbb{R}^2$, coincident with the square symmetry lattice. The fact that we are implying a reference basis for the description of space $\mathbb{R}^2$ should not be confused with the fact that the same lattice in $\mathbb{Z}^2$ can be represented by several equivalent bases. Indeed, all these different equivalent bases are implicitly expressed in terms of $\{\mathbf{I}_I\}$, chosen for the representation of the space.

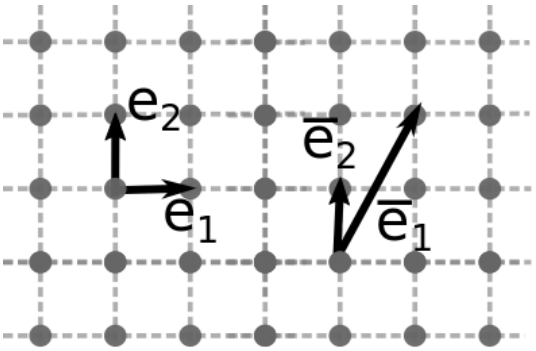

Figure 2.3: **Bravais Lattice:** Schematic representation of a simple, Bravais, lattice. It is fully described by an integer basis $\{\mathbf{e}_I\}$ which, periodically translated in space, defines the lattice. Choices for the integer basis $\{\mathbf{e}_I\}$ are infinite, but all these basis are in relation by the action of the global symmetry group $GL(2,\mathbb{Z})$.

To summarize, every time that we perform a change of basis we are operating within the group $GL(2,\mathbb{Z})$. Similarly, every time that the lattice is deformed into a symmetrically equivalent structure, such deformation can be also described as the action of $GL(2,\mathbb{Z})$ on the initial configuration. Equations (2.5) and (2.6) describe the action of the global symmetry group $GL(2,\mathbb{Z})$ on the configurational space $\mathcal{B}$ of basis vectors (4D space of linearly-independent 2D vectors) and on the space $\mathcal{Q}_2^+$ of lattices metrics (the 3D space of positive definite symmetric second order tensors $\in \mathbb{R}^2$). In what follows we will mostly refer to the invariance with respect to configurational space $\mathcal{Q}_2^+$, which naturally accounts for frame indifference.

The notion of global lattice symmetry based on $G(\mathbf{e}_I)$ may seem in contradiction with the classical notion of *crystallographic point group* $P(\mathbf{e}_I)$. This is the set of all the orthogonal transformations that leave the crystal invariant:

$$\begin{aligned} P(\mathbf{e}_I) &:= G(\mathbf{e}_I) \cap \mathcal{O} \\ &= \{\mathbf{Q} \in \mathcal{O} : \mathbf{Q}\mathbf{e}_I = m_{JI}\mathbf{e}_J, \quad \mathbf{m} \in GL(2,\mathbb{Z})\}\,, \end{aligned} \tag{2.7}$$

where $\mathcal{O}$ is the set of all orthogonal matrices $\mathbf{Q}^T\mathbf{Q} = 1$. The operations $\mathbf{Q} \in P(\mathbf{e}_I)$ are rotations and reflections (orthogonal transformations) mapping the lattice $\mathcal{L}(\mathbf{e}_I)$ in itself. In other words, $P(\mathbf{e}_I)$ is the orthogonal subset of $G(\mathbf{e}_I)$. We mention that both $P(\mathbf{e}_I)$ and $G(\mathbf{e}_I)$ are independent of the specific basis $\mathbf{e}_I$, but depend only on the lattice $\mathcal{L}$. Indeed the following is easily proved [PZ02]:

$$G(\mathbf{e}_I) := G(m_{JI}\mathbf{e}_J) \quad \forall \mathbf{m} \in GL(2,\mathbb{Z}) \tag{2.8}$$

$$P(\mathbf{e}_I) := P(m_{JI}\mathbf{e}_J) \quad \forall \mathbf{m} \in GL(2,\mathbb{Z})\,. \tag{2.9}$$

However, while $G(\mathbf{e}_I)$ is an infinite group, $P(\mathbf{e}_I)$ is not. Indeed, given a certain lattice

basis:

$$m_{JI} = \mathbf{e}_J \cdot \mathbf{Q}\mathbf{e}_I \quad \Rightarrow \quad |m_{JI}| \leq \|\mathbf{e}_J\|\|\mathbf{Q}\mathbf{e}_I\| = \|\mathbf{e}_J\|\|\mathbf{e}_I\| \tag{2.10}$$

which admits only finite integral solutions ($\|\mathbf{v}\|$ euclidean norm of vector $\mathbf{v}$).

In some sense, the size of the point group $P(\mathbf{e}_I)$ of a certain lattice is indicative of the "amount of symmetry" of that lattice. This concept does not apply to $G(\mathbf{e}_I)$, which contains the infinite number of non-rigid mappings associated with the arbitrariness of the chosen lattice basis. The implied deformations are simple shears leaving the crystal invariant and can be written as:

$$\boldsymbol{S}\mathbf{e}_I = s_{IJ}\mathbf{e}_J, \qquad \boldsymbol{S} = \mathbf{I} + \hat{\mathbf{a}} \otimes \hat{\mathbf{n}} \qquad (s_{IJ}) \in GL(2,\mathbb{Z}), \tag{2.11}$$

where $\hat{\mathbf{a}}$ and $\hat{\mathbf{n}}$ are two orthogonal unit vectors; $\mathbf{I}$ is the identity matrix. A detailed proof of this claim can be found in [Eri05].

Since it is desirable to treat in the same manner lattices that are equivalent, one needs a suitable criterion for a classification of lattices with equivalent properties. The classical subdivision of lattices in *crystal systems* is based on conjugacy relations among their point groups. Indeed, when an orthogonal transformation $\mathbf{Q} \in \mathcal{O}$ is applied to basis $\{\mathbf{e}_I\}$, the associated point group is transformed to the $\mathcal{O}$-conjugate of itself:

$$P(\mathbf{Q}\mathbf{e}_I) = \mathbf{Q}P(\mathbf{e}_I)\mathbf{Q}^T. \tag{2.12}$$

Then, the two lattices $\mathcal{L}$ and $\mathcal{L}'$ are said belong to the same crystal system when their respective point groups are orthogonally conjugate. In 2D there are 4 different crystal systems: *oblique, rectangular, square* and *triangular*.

A finer classification is offered by the subdivision of lattices in *Bravais types* (also called *lattice types* in literature). This classification is based on conjugacy in $GL(2,\mathbb{Z})$, that is more restrictive condition that conjugacy in $\mathcal{O}$ [PZ02]. To explain how this classification is obtained, it is necessary to introduce the *lattice groups* $L(\mathbf{e}_I)$, that are integral representations of the point groups $P(\mathbf{e}_I)$:

$$L(\mathbf{e}_I) := \{\mathbf{m} \in GL(2,\mathbb{Z}) : m_{IJ}\mathbf{e}_J = \mathbf{Q}\mathbf{e}_I, \mathbf{Q} \in P(\mathbf{e}_I)\}. \tag{2.13}$$

Notice that, differently from $P(\mathbf{e}_I)$ and $G(\mathbf{e}_I)$, lattice group $L(\mathbf{e}_I)$ of a given lattice depends on the specific basis $\{\mathbf{e}_I\}$ chosen to describe that lattice. They are finite and coincide with the maximal subgroups of $GL(2,\mathbb{Z})$ acting orthogonally on a certain lattice. When a basis $\mathbf{e}_I$ is transformed into an equivalent one $\mathbf{e}'_I = m_{JI}\mathbf{e}_J$ by the application of an integer matrix $\mathbf{m} \in GL(2,\mathbb{Z})$, the associated lattice group changes into a $GL(2,\mathbb{Z})$-conjugate:

$$L(\mathbf{e}'_I) = \mathbf{m}^{-1}L(\mathbf{e}_I)\mathbf{m}. \tag{2.14}$$

We say that two lattices $\mathcal{L}$ and $\mathcal{L}'$ belong to the same Bravais type if their respective lattice groups $L(\mathbf{e}_I)$ and $L(\mathbf{e}'_I)$ are conjugate in $GL(2,\mathbb{Z})$, i.e. (2.14) holds for some $\mathbf{m} \in GL(2,\mathbb{Z})$. Also, when $\mathcal{L}$ and $\mathcal{L}'$ have the same Bravais type, there will be a certain choice for basis $\{\mathbf{e}'_I\}$ such that $L'(\mathbf{e}'_I)$ will be equivalent to $L(\mathbf{e}_I)$. Notice also that lattice group is not affected by orthogonal transformations, in the sense that:

$$L(\mathbf{Q}\mathbf{e}_I) = L(\mathbf{e}_I). \tag{2.15}$$

The concept of lattice group can be reformulated in terms of the correspondent metric tensor $\mathbf{C}$:

$$L(\mathbf{e}_I) = \left\{\mathbf{m} \in GL(2,\mathbb{Z}) : \mathbf{m}^T\mathbf{C}\mathbf{m}\right\} := L(\mathbf{C})\,. \tag{2.16}$$

In 2D, there are 5 Bravais types, *oblique, rectangular, rhombic, square* and *triangular* (the latter indicating an equilateral triangle with hexagonal symmetry). The corresponding groups, along with the classification of crystal systems, are reported in Table 2.1, taken from [CZ04]. Note that the action (2.6) defines the relation between metric tensors of the same Bravais type. Then, it divides the configurational space of metric tensors $\mathcal{Q}_2^+$ in 5 orbits, each corresponding to a particular Bravais type.
Summarizing, there are two different criteria for the classification of simple lattices:

- Conjugacy of point groups $P(\mathbf{e}_I)$ in $\mathcal{O}$, resulting in the classifications of lattices in *crystal systems*. This classification is also known as *geometric symmetry* of simple lattices.

- Conjugacy of lattice groups $L(\mathbf{e}_I)$ in $GL(2,\mathbb{Z})$, resulting in the classifications of lattices in *Bravais types* (also *lattices types*), also called *arithmetic symmetry* of simple lattices.

Both of these classifications are based on the notion of crystallographic point group $P(\mathbf{e}_I)$, however the second is more suitable for the purpose of this Thesis, being directly compatible with $GL(2,\mathbb{Z})$ invariance. Indeed, it can be seen as the restriction of actions (2.5) and (2.6) to a suitable neighborhood of "small but finite" deformations, the so called Ericksen-Pitteri Neighborhood (EPN) (see [Pit84] and chapter 4 of [PZ02] for more details).

2.1.1 Bravais Lattices in C Space

Since the tensor $\mathbf{C}$ is symmetric, we may represent all possible 2D Bravais lattices in the three dimensional space given by C_{11}, C_{22}, C_{12}. This configurational space is very useful for visualizing the different lattice types and will be important for the understanding of the energy construction.
We remark that, because $\mathbf{C} \in \mathcal{Q}_2^+$ by definition, every admissible lattice metric $\mathbf{C}$ belongs to the subspace limited by condition $\det(\mathbf{C}) > \mathbf{0}$, that is, the upper part of the 3D surface limited by the hyperbolic surface $\det(\mathbf{C}) = \mathbf{C_{11}C_{22} - C_{12}^2 = 0}$. By restricting the

Crystal system (International Symbol)	Lattice type (International Symbol)	Fixed set	Lattice group (up to inversion)
oblique (2)	oblique ($p2$)	$0 < C_{11} < C_{22}$ $0 < C_{12} < \frac{C_{11}}{2}$	$\begin{pmatrix} 1 & 0 \\ 0 & 1 \end{pmatrix}$
rectangular ($2mm$)	rectangular ($p2mm$)	$0 < C_{11} < C_{22}$ $C_{12} = 0$	$\begin{pmatrix} 1 & 0 \\ 0 & 1 \end{pmatrix}, \begin{pmatrix} -1 & 0 \\ 0 & 1 \end{pmatrix}$
	rhombic or centered–rectangular ($c2mm$)	Fixed set I $0 < C_{11} = C_{22}$ $0 < C_{12} < \frac{C_{11}}{2}$	$\begin{pmatrix} 1 & 0 \\ 0 & 1 \end{pmatrix}, \begin{pmatrix} 0 & 1 \\ 1 & 0 \end{pmatrix}$
		Fixed set II $0 < C_{11} < C_{22}$ $0 < C_{12} = \frac{C_{11}}{2}$	$\begin{pmatrix} 1 & 0 \\ 0 & 1 \end{pmatrix}, \begin{pmatrix} 1 & 1 \\ 0 & -1 \end{pmatrix}$
square ($4mm$)	square ($p4mm$)	$0 < C_{11} = C_{22}$ $C_{12} = 0$	$\begin{pmatrix} 1 & 0 \\ 0 & 1 \end{pmatrix}, \begin{pmatrix} 0 & -1 \\ 1 & 0 \end{pmatrix}$ $\begin{pmatrix} -1 & 0 \\ 0 & 1 \end{pmatrix}, \begin{pmatrix} 0 & 1 \\ 1 & 0 \end{pmatrix}$
triangular ($6mm$)	triangular ($p6mm$)	$0 < C_{11} = C_{22}$ $0 < C_{12} = \frac{C_{11}}{2}$	$\begin{pmatrix} 1 & 0 \\ 0 & 1 \end{pmatrix}, \begin{pmatrix} 0 & -1 \\ 1 & 1 \end{pmatrix}$ $\begin{pmatrix} 1 & 1 \\ -1 & 0 \end{pmatrix}, \begin{pmatrix} -1 & 0 \\ 1 & 1 \end{pmatrix}$ $\begin{pmatrix} 1 & 1 \\ 0 & -1 \end{pmatrix}, \begin{pmatrix} 0 & 1 \\ 1 & 0 \end{pmatrix}$

Table 2.1: The five Bravais types of simple lattices in 2D, and the fixed sets (sets of metrics with given lattice group) intersecting the fundamental domain D in (2.21), with the corresponding lattice groups (only one element of each pair $(m, -m)$ is tabulated). See also Figure 2.4.

description to the hyperbolic surface $\det(\mathbf{C}) = \mathbf{C_{11}C_{22} - C_{12}^2 = 1}$, we limit the analysis to lattices with the volume of a unit cell, chosen as reference (see Figure 2.4). This can be done without loosing generality since all the other hyperbolic surfaces are related homotetically. A particular unit lattice has infinite representations on the $\det \mathbf{C} = 1$ surface, all in relation through action (2.6). As a consequence, the invariance subdivides the surface $\det \mathbf{C} = 1$ into a series of subdomains related by trivial symmetry operations. Each

of these subdomains is a *fundamental domain* for the action (2.6), i.e. a subset of $\mathcal{Q}_2^+$ such that every $GL(2,\mathbb{Z})$ orbit, and then every Bravais lattice type, has one and just one element contained in it. In Figure 2.4 (on top) this subdivision of the $\det \mathbf{C} = 1$ space is illustrated, with the focus on one of these fundamental domains, denoted by D. Notice as higher symmetry lattices, triangular and square, are identified by points, rhombic and rectangular lattices by lines, while generic oblique lattice occupy all the remaining points of the $\det \mathbf{C} = 1$ surface.

In Figure 2.4 (on bottom) we illustrate schematically how these equivalent configurations can be distinguished through:

- A different choice for the reference basis vectors $\mathbf{e}_I$.
- Application of a lattice invariant shear (2.28) on the reference basis $\mathbf{e}_I$.

Once a fundamental domain D fixing the tessellation has been chosen, the energy can be defined on it only and its action will be automatically extended to the entire $\det \mathbf{C} = 1$ space, by the mapping (2.6). This implies that the ensuing energy landscape must be periodic.
As already remarked, the configurational space $\det \mathbf{C} = 1$ is a hyperbolic surface. A representation of this space can be obtained using one of the available models of hyperbolic geometry. In Figure 2.5 the space $\det \mathbf{C} = 1$ and its tessellation in invariant subdomains is showed using the Poincaré disk, in which the infinite hyperbolic surface is projected to a circle of unit radius. This representation is particularly useful as it allows to have a global representation of the infinite configurational space. In this projection, the points at infinity are represented by the external circumference of the disk. The mapping linking a point (x, y) on the disk with the point $(\widehat{x}, \widehat{y}) = (\frac{C_{12}}{C_{22}}, \frac{\sqrt{\det \mathbf{C}}}{C_{22}})$ on a generic hyperbolic surface of determinant $\det \mathbf{C}$ [3] is given by the formulas:

$$x = \frac{\widehat{x}^2 + \widehat{y}^2 - 1}{\widehat{x}^2 + (\widehat{y}+1)^2} \tag{2.17}$$

$$y = \frac{2\widehat{x}}{\widehat{x}^2 + (\widehat{y}+1)^2} \tag{2.18}$$

Note that the boundaries of the subdomains of periodicity correspond, on the Poincaré disk, to diameters or to the arcs of circle intersecting the disk perpendicularly, which are geodesics in this representation of the hyperbolic surface [And06].

[3] on this surface, once that $\det \mathbf{C}$, C_{22} and C_{12} are given, component C_{11} is determined by condition $\det \mathbf{C} = C_{11}C_{22} - C_{12}^2 = 1$.

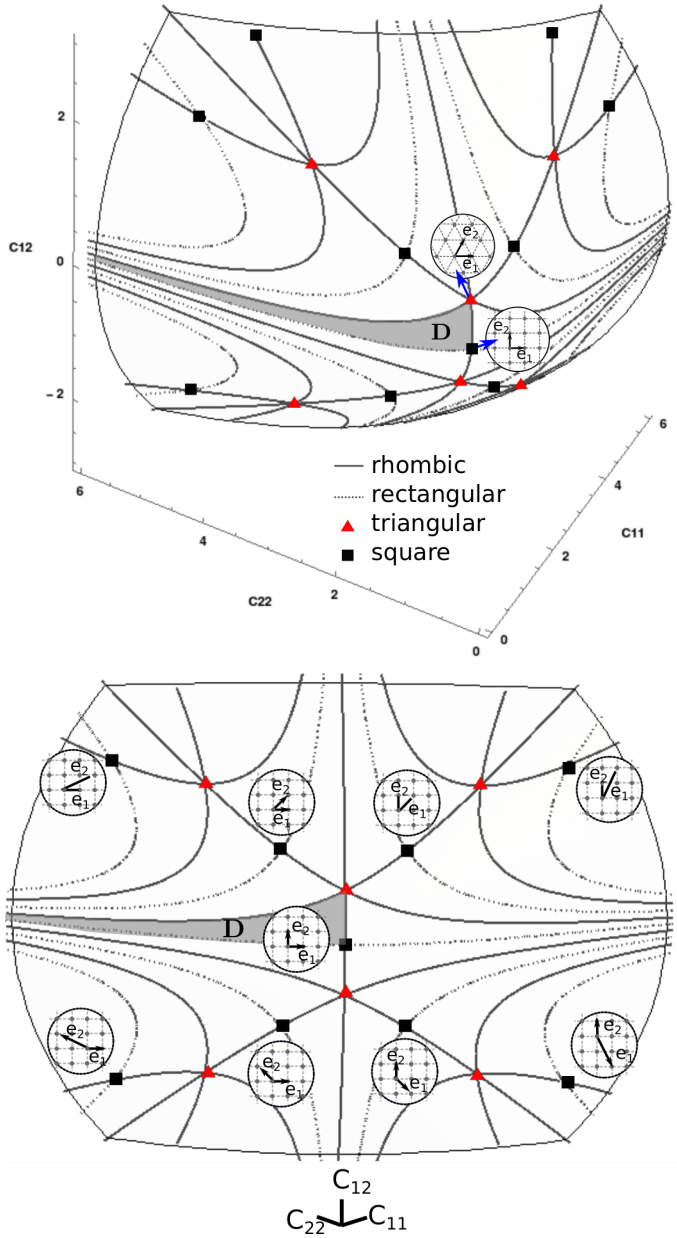

Figure 2.4: **Configurational Space:** a) Illustration of strain space C_{11},C_{12},C_{22}. Admissible metric tensors should satisfy condition $\det \mathbf{C} > 0$, which corresponds to a hyperboloid in the C_{11},C_{12},C_{22} space. A portion of the infinite hyperbolic surface $\det \mathbf{C} = 1$, containing all simple lattices of unit volume, is shown as reference. b) Relation between different square symmetry metric points is illustrated schematically. These lattices are equivalent but characterized by a different choice of the lattice basis vectors $\{\mathbf{e}_I\}$.

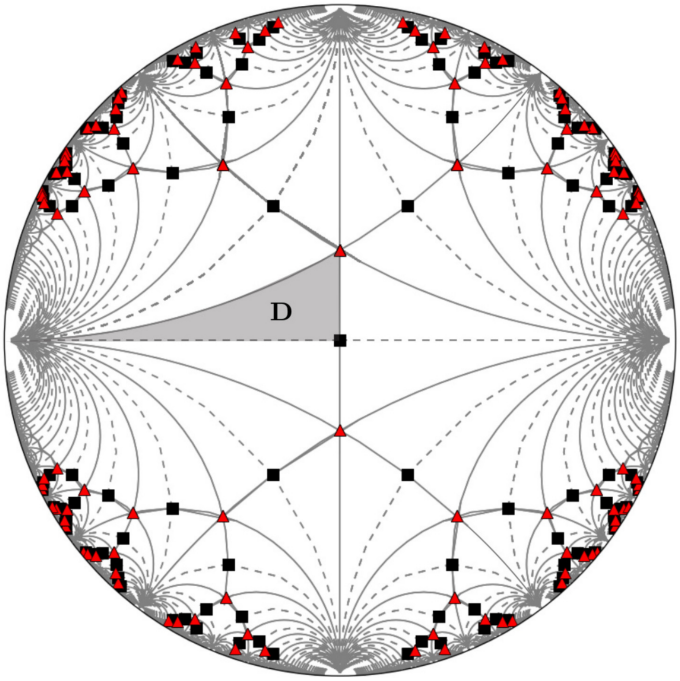

Figure 2.5: **Poincaré Representation of the Configurational Space:** space $\det \mathbf{C} = 1$ in the Poincaré disk representation. For the sake of clarity, only some of the infinite square and triangular lattices are illustrated explicitly. Full and dashed lines, corresponding to rhombic and rectangular lattices, respectively, are geodesics in the hyperbolic space.

2.2 Energy Construction

Our model is based on the assumption, due to J. Ericksen [Eri97], that a strain energy density φ for the crystalline lattice exists, and that it depends only on the current configuration of the basis vectors [4] $\mathbf{e}_i$.

We already remarked that the crystal behavior has to be independent from the choice of the observer. This means that the lattice energy φ must satisfy the condition of frame indifference [Sal09, FLBGS10, Bha03, SMF19]. Therefore, we build strain energy density directly as a function of $\mathbf{C}$ rather than as a function of the basis vectors $[\mathbf{e}_I]$, thus eliminating rigid rotations in the actual (Eulerian) space. To satisfy material symmetry of the lattice, which we discussed above, the function $\varphi(\mathbf{C})$ must also be invariant under the

[4] Here we limit the discussion to simple lattices, however we remark that this approach can be extended, with some additional complexity, to multi-lattices as well (see for instance chapter 11 of [PZ02] or chapter 11 of [TM11].

action of the global symmetry group $GL(2,\mathbb{Z})$:

$$\varphi(\mathbf{C}) = \varphi(\mathbf{m}^T\mathbf{C}\mathbf{m})\,. \tag{2.19}$$

Definition of an energy with the required symmetry (2.19) may not seem straightforward, however one can notice that φ does not need to be defined on the entire surface $\det\mathbf{C} = 1$. Instead, a reference energy φ_0 can be constructed on a fundamental domain only, a subdomain of $\mathcal{Q}_2^+$ where every Bravais type has one and only one representative metric. Once a fundamental domain D has been chosen and the reference energy φ_0 defined, an extension φ invariant under $GL(2,\mathbb{Z})$ and defined on to the entire surface $\det\mathbf{C} = 1$ can be obtained simply by setting:

$$\varphi(\mathbf{C}) = \varphi(\mathbf{m}^T\mathbf{C}\mathbf{m}) = \varphi_0(\tilde{\mathbf{C}})\,. \tag{2.20}$$

In order to exploit the property (2.20), one has to have a general procedure which, for a general metric tensor $\mathbf{C}$, generates the matrix $\mathbf{m}$ which maps it back on the corresponding reference metric $\tilde{\mathbf{C}} \in D$. For the reasons that will be explained shortly, it is convenient to chose the fundamental domain D in the form:

$$D = \left\{ C \in \mathcal{Q}_2^+, \quad 0 < C_{11} \leq C_{22}, \quad 0 \leq C_{12} \leq \frac{C_{11}}{2} \right\}. \tag{2.21}$$

It is easy to see that D contains only one representative of every Bravais type. More specifically, the square symmetry is represented by point $C_{11} = C_{22} = 1$, $C_{12} = 0$, triangular lattice symmetry by point $C_{11} = C_{22} = \gamma^2$, $C_{12} = \frac{\gamma^2}{2}$, where $\gamma = \sqrt[4]{\frac{4}{3}}$ is the length of basis vectors of a unit area triangular lattice. Descending to lower symmetries, rectangular and rhombic lattices are located along lines, coinciding with the boundaries of D. The $C_{12} = 0$ boundary is the one corresponding to rectangular lattices configurations while the other two boundaries correspond to two different type of rhombic lattices: the "skinny rhombi" and the "fat rhombi". Along the $C_{12} = \frac{C_{11}}{2}$ boundary we find "skinny rhombi" configurations, i.e. configurations in which one of the angles is smaller than 60 degrees, so that a diagonal is shorter than the side, while on the remaining boundary $C_{11} = C_{22}$ one has the "fat rhombi", whose angles are all between 60° and 120°, and both diagonals longer than the side (see also [CZ04]). Generic obliquous lattices cover the interior of D.
The importance of this choice of D is given by the particular form of the metrics $\tilde{\mathbf{C}} \in D$. They have what is called the *reduced form of Lagrange*, characterized by the conditions:

- $\tilde{\mathbf{e}}_1$ is the shortest lattice vector.
- $\tilde{\mathbf{e}}_2$ is the shortest lattice vector not collinear with $\tilde{\mathbf{e}}_1$ and for which the sign is chosen in such a way that the angle between the two is acute.

For this choice of the reference domain, the needed mapping between a general $\mathbf{C}$ and its corresponding analogue $\tilde{\mathbf{C}} \in D$ is known. It is given by the iterative procedure known as *Lagrange reduction*. Given an arbitrary lattice basis $\mathbf{e}_I$, the corresponding Lagrange reduced basis $\tilde{\mathbf{e}}_I$ can be obtained by applying the finite iterative procedure:

- if $|\mathbf{e}_1| \geq |\mathbf{e}_2|$, swap the two vectors;
- if $\mathbf{e}_1 \cdot \mathbf{e}_2 \leq 0$, change sign to $\mathbf{e}_2$;
- if $\mathbf{f} = \mathbf{e}_1 - \mathbf{e}_2$ is shorter than $\mathbf{e}_2$, replace $\mathbf{e}_2$ with $\mathbf{f}$. ...

The same procedure can be also expressed in terms of the components of $\mathbf{C}$:

- if $C_{12} < 0$, change sign to C_{12};
- if $C_{22} < C_{11}$, swap the two components;
- if $2C_{12} > C_{11}$ set $C_{12} = C_{12} - C_{11}$ and $C_{22} = C_{22} + C_{11} - 2C_{12}$. ...

Now that the fundamental domain D and the reduction mapping are given, only the reference energy φ_0 is missing. It may be parameterized in many different ways, (using polynomials expressions, Fourier coefficients, spline interpolations, ...) but it has to respect a suitable regularity at the boundaries. We will require φ_0 to satisfy $\mathcal{C}^2$ smoothness, which ensures the continuity of the elastic moduli.

Moreover, φ_0 must have a minimum which corresponds to the chosen crystal symmetry. For instance, when modeling a square lattice, φ_0 will be constructed in such a way that minimum coincides with the square symmetry lattice (that is point $C_{11} = C_{22} = 1$, $C_{12} = 0$). Once this requirement is satisfied, the extended energy φ has the desired symmetry and is indefinitely periodic in tensorial space.

Up to now we considered only volume-invariant metrics which evolve on surface $\det \mathbf{C} = 1$ only. However, one needs to consider also the reference lattices outside of this surface, exploring configurations which allows for a volume change (the system will have $\det \mathbf{C} < 1$ when compressed and $\det \mathbf{C} > 1$ when extended). This poses no particular problem since $\det \mathbf{C}$ is invariant under $GL(2, \mathbb{Z})$. Therefore, by defining φ_0 as a function of scaled variables $C_{IJ}/(\det \mathbf{C})^{1/2}$ and of $\det \mathbf{C}$ one can decouple the *isochoric* contribution to the energy from the *volumetric* one.

2.2.1 Polynomial Energy

In [CZ04] Conti and Zanzotto, following Parry [Par76] who formulated the smoothness conditions and considered various special examples, introduced a general 6-th order polynomial $GL(2, \mathbb{Z})$ invariant energy with the objective of modelling irreversible martensitic transformations. This energy depends, in addition to $\mathbf{C}$, on a thermal parameter β which allows, when increased, to pass from a square symmetry to an hexagonal one. Here we

adopt this energy for the modelling of plastic deformation without considering phase transitions, i.e. keeping the parameter β fixed.

The proposed polynomial energy function φ has to be $\mathcal{C}^2$ smooth across the boundaries of D. The application of this condition is simplified significantly when one uses polynomials that are invariants of a certain point group. To better explain this fact we need to explain better the concept of *Ericksen-Pitteri neighborhood (EPN)*.
The concept of EPN where firstly introduced by Ericksen and Pitteri [Eri79, Pit84]. It is widely used to distinguish reversible and irreversible martensitic transformations (see also [Bha98, BCZZ04]). An EPN is a subspace of $\mathcal{Q}_2^+$ which contains transformations with the property that the initial, the final and all the intermediate configurations have a common finite symmetry subgroup. Consider, for instance, a deformation represented by the reference point $\mathbf{C_0}$ coinciding with the symmetry point $\mathbf{T}$ in Figure 2.6. During the deformation we will change the Bravais type of the lattice going, for instance, to an oblique final configuration $\mathbf{C_1}$. The corresponding lattice group $L(\mathbf{C_0})$ will change but, as long as the corresponding metric stays in the EPN, it will be a subgroup of $L(\mathbf{T})$. If, instead, the final configuration ends up located outside the EPN, $L(\mathbf{C_1})$ will be no more a subgroup of $L(\mathbf{T})$, but of an other lattice group centered on an other higher symmetry point that is "nearer" to the final configuration. As a consequence of this, it will be no more possible to describe the entire deformation process (which contains all intermediate configurations) using a finite subgroup of $GL(2,\mathbb{Z})$.

More formally, given any lattice metric $L(\mathbf{C_0})$, an open neighborhood $\mathcal{N}(\mathbf{C_0})$ of $\mathbf{C_0}$ in $\mathcal{Q}_2^+$ is an EPN if the following properties are satisfied:

(i) $m^t \mathcal{N} m = \mathcal{N}$ for all $m \in L(C_0)$;

(ii) $m^t \mathcal{N} m \cap \mathcal{N} = \emptyset$ for all $m \in GL(2,\mathbb{Z}) \setminus L(C_0)$.

The maximal EPNs for the reference square and triangular lattices are shown in Figure 2.6. For instance, the maximal EPN associated with the square lattice $\mathbf{S}$ is given by the four copies of fundamental domain D converging on square symmetry point $\mathbf{S}$ and obtained trough the action of the lattice group $L(\mathbf{S})$. Similarly, the maximal EPN for the triangular symmetry is given by the six copies of D converging on hexagonal symmetry point $\mathbf{T}$. For a generic obliquous lattice, the maximal EPN coincides simply with D itself. Intuitively, we can say that the maximal EPN associated with a certain symmetry correspond to its "elastic" subdomain, meaning, the "area of pertinence" of the corresponding energy well.

Once shapes of the maximal EPNs are found, we can use polynomials that are continuous in the maximal $\mathcal{N}(\mathbf{T})$. In this case continuity requirements are automatically satisfied on two of the three boundaries of the fundamental domain D. Then, we know from [SR97], that if we use linear combinations of hexagonal invariants I_i the continuity of the corresponding polynomials is ensured under $L(\mathbf{T})$ and therefore along all the maximal $\mathcal{N}(\mathbf{T})$.

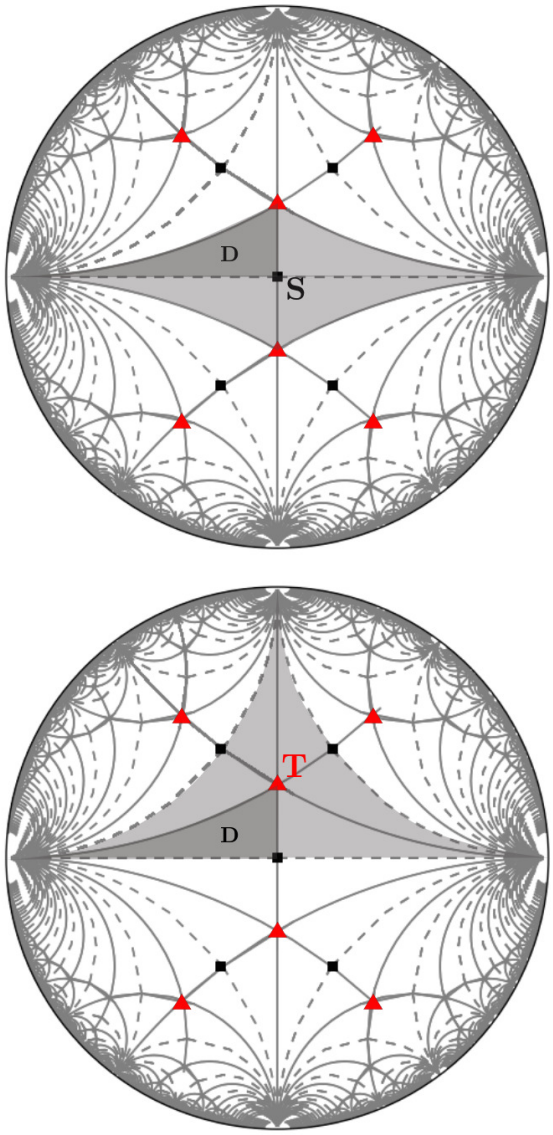

Figure 2.6: **Maximal EPNs:** Examples of maximal EPNs in $\mathcal{Q}_2^+$, indicated as dashed areas (fundamental domain D is also shown). Maximal EPN for a square lattice metric (on top), and for a triangular lattice metric (on bottom). In both cases, the boundary does not belong to the (open) maximal EPN.

These invariants can be expressed as functions of the corresponding metric tensors:

$$\begin{aligned} I_1 &= \frac{1}{3}(C_{11}+C_{22}-C_{12}), \\ I_2 &= \frac{1}{4}(C_{11}-C_{22})^2+\frac{1}{12}(C_{11}+C_{22}-4C_{12})^2, \\ I_3 &= (C_{11}-C_{22})^2(C_{11}+C_{22}-4C_{12})-\frac{1}{9}(C_{11}+C_{22}-4C_{12})^3\,. \end{aligned} \tag{2.22}$$

We can now consider sixth-order polynomial functions $\hat{\varphi}_0$ of $(C_{11},\ C_{12},\ C_{22})$, with restrictions $C_{12}^2 < C_{11}C_{22}$, that can be written as linear combination of the invariants I_i. It can be proved [CZ04] that $\mathcal{C}^2$ continuity on the boundary $C_{12}=0$ of D is ensured by setting:

$$\left.\frac{\partial\hat{\varphi}_0}{\partial C_{12}}\right|_{C_{12}=0} = 0. \tag{2.23}$$

By considering all the sixth order polynomial of this type, we obtain a 10-dimensional linear space and therefore 10 linearly independent vectors ψ_i are needed to define the most general potential φ_0. Since $\det\mathbf{C}$ is invariant, three basis vectors may be respectively $\det\mathbf{C}$, its square and its cube, the others can be chosen as functions of invariants I_i. A suitable choice for the vectors ψ_i is:

$$\begin{aligned} \psi_1 &= {I_1}^4\, I_2 - \frac{41\,{I_2}^3}{99} + \frac{7\,I_1\,I_2\,I_3}{66} + \frac{{I_3}^2}{1056}, \\ \psi_2 &= {I_1}^2\,{I_2}^2 - \frac{65\,{I_2}^3}{99} + \frac{I_1\,I_2\,I_3}{11} + \frac{{I_3}^2}{264}, \\ \psi_3 &= \frac{4\,{I_2}^3}{11} + {I_1}^3\,I_3 - \frac{8\,I_1\,I_2\,I_3}{11} + \frac{17\,{I_3}^2}{528}, \\ \psi_4 &= \frac{9\,{I_1}^5}{2} - 4\,{I_1}^3\,I_2 + I_1\,{I_2}^2 - \frac{I_2\,I_3}{48}, \\ \psi_5 &= 48\,{I_1}^5 - 24\,{I_1}^3\,I_2 + {I_1}^2\,I_3, \\ \psi_6 &= 21\,{I_1}^4 - 5\,{I_2}^2 + I_1\,I_3, \\ \psi_7 &= -\frac{5\,{I_1}^3}{2} + I_1\,I_2 - \frac{I_3}{48}, \\ \psi_8 &= \det\mathbf{C} \\ \psi_9 &= (\det\mathbf{C})^2 \\ \psi_{10} &= (\det\mathbf{C})^3 \end{aligned} \tag{2.24}$$

The general sixth order polynomial $\hat{\varphi}_0$, satisfying the required continuity conditions, can be obtained by linear combinations of the functions ψ_i listed above. To decouple the isochoric and the volumetric contributions, we define the energy φ_0 in terms of scaled variables $\mathbf{C}/\det^{1/2}\mathbf{C}$:

$$\varphi_0(\mathbf{C}) = \varphi_0\left(\det\mathbf{C}, \frac{\mathbf{C}}{\det^{1/2}\mathbf{C}}\right)\,. \tag{2.25}$$

The functions ψ_i are homogeneous and the scaling $\frac{\mathbf{C}}{(det\mathbf{C})^{1/2}}$ can be incorporated easily. The decoupled φ_0 can be written as:

$$\varphi_0(\mathbf{C}) = h(\det \mathbf{C}) + \sum_{i=1}^{7} \beta_i \psi_i \left(\frac{\mathbf{C}}{\det^{1/2} \mathbf{C}} \right) , \tag{2.26}$$

where β_i are constant coefficients whose values of β_i must be chosen to ensure that the minimum of $\varphi_0(\mathbf{C})$ has the desired symmetry. For instance, we can make choices:

- $\beta_1 = -\frac{1}{4}$ $\beta_3 = 1$ $\beta_2 = \beta_4 = \beta_5 = \beta_6 = \beta_7 = 0$ to ensure square symmetry.
- $\beta_1 = 4$ $\beta_3 = 1$ $\beta_2 = \beta_4 = \beta_5 = \beta_6 = \beta_7 = 0$ to ensure hexagonal symmetry.

To cover both possibilities we can set:

$$\varphi_0(\mathbf{C}) = \beta_1 \psi_1 \left(\frac{\mathbf{C}}{\det^{1/2} \mathbf{C}} \right) + \psi_3 \left(\frac{\mathbf{C}}{\det^{1/2} \mathbf{C}} \right) - K(\ln \det \mathbf{C} - \det \mathbf{C}) , \tag{2.27}$$

where the volumetric part has been taken in the logarithmic form to exclude configurations with infinite compression. The coefficient K plays the role of a bulk modulus.

In Figure 2.7 energy contours for the square ($\beta = -1/4$) and triangular ($\beta = 4$) lattices are illustrated on the Poincaré disk (a cut-off value of 4.15 has been used for visualizing better the shape of the low energy valleys).

It is important to remember that the chosen configurational space does not tell apart configurations which differs only by a rigid rotation. Therefore, every energy well in our energy landscape represent an infinite number of configurations, that are indeed energetically equivalent, an "orbit", see [Bha98] for more details.

2.2.2 Energy Landscape

In this section we illustrate some important features of the obtained energy landscape. While our observations will be based on the energy potential (2.27), the discussed features are general and are related directly to the $GL(2, \mathbb{Z})$ invariance.

We begin with the case when the energy minimizer is the square symmetry lattice. Then, the discussion will be extended to the case of the triangular lattice. In both cases, the periodic behavior of the energy emerges automatically from the use of $GL(2, \mathbb{Z})$ invariance.

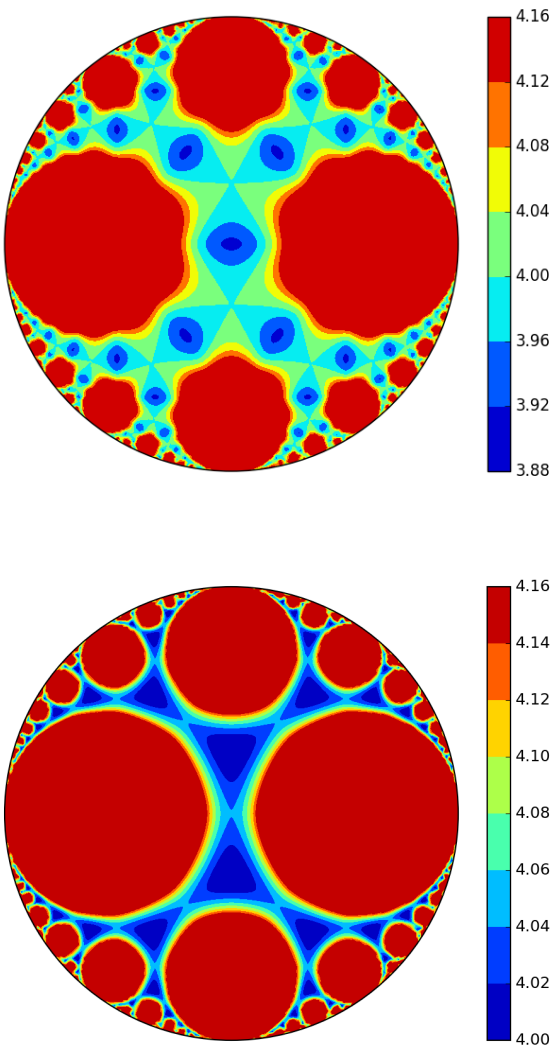

Figure 2.7: **Energy Landscape:** Energy landscape corresponding to energy density (2.27) for square symmetry $\beta = -\frac{1}{4}$ (on top) and hexagonal symmetry $\beta = 4$ (on bottom) is illustrated on the Poincaré disk. Color indicates the energy level, blue-low, red-high. An upper cut-off of 4.15 has been used for the highest-energy values for an improved visualization of low-energy barriers and wells.

Square Lattice

We now focus on the periodic energy anchored at a square lattice. The reference metric $\mathbf{S}$ written in the reference basis $\mathbf{e}_1^T = \{1 \quad 0\}$, $\mathbf{e}_2^T = \{0 \quad 1\}$ and has components $C_{11} = C_{22} = 1, C_{12} = 0$. To visualize the infinite periodicity of our polynomial energy, consider three simple shears of the type:

$$\boldsymbol{S} = \mathbf{I} + \alpha \mathbf{a} \otimes \mathbf{n} \tag{2.28}$$

where $\mathbf{a}$ and $\mathbf{n}$ are two orthogonal unit vectors indicating, respectively, the shear direction and its normal. The remaining parameter α represents the amount of shear. Notice that if we assume $\mathbf{a} = \mathbf{e}_1$ and $\mathbf{n} = \mathbf{e}_2$ in (2.28), we obtain, for integer values of α, a lattice invariant shear of the type (2.11).

Suppose that the shearing direction $\mathbf{a}$ is inclined by $\theta = 0°$ (that is the case we just mentioned), $\arctan(\frac{1}{2})$ and $45°$ with respect to the horizontal direction. Matrix $\mathbf{F}$, expressing the corresponding deformation of the reference undeformed basis vectors $\{\mathbf{e}_I\}$, (such that $\mathbf{e}_\mathbf{i}^* = \mathbf{F}\mathbf{e}_\mathbf{I}$ [5]) is given by:

$$\mathbf{F} = \begin{bmatrix} 1 - \alpha \cos\theta \sin\theta & \alpha \sin^2\theta \\ \alpha \cos^2\theta & 1 + \alpha \cos\theta \sin\theta \end{bmatrix} \quad . \tag{2.29}$$

For our three values of the angle θ, we obtain accordingly:

$$\begin{aligned} \mathbf{F}_{0°} = \begin{bmatrix} 1 & \alpha \\ 0 & 1 \end{bmatrix} \qquad \mathbf{F}_{\arctan(\frac{1}{2})} = \begin{bmatrix} 1 - \frac{2}{5}\alpha & \frac{1}{5}\alpha \\ -\frac{1}{5}\alpha & 1 + \frac{2}{5}\alpha \end{bmatrix} \\ \mathbf{F}_{45°} = \begin{bmatrix} 1 - \frac{1}{2}\alpha & \frac{1}{2}\alpha \\ -\frac{1}{2}\alpha & 1 + \frac{1}{2}\alpha \end{bmatrix} \quad . \end{aligned} \tag{2.30}$$

When a homogeneous deformation $\mathbf{F}$ parametrized by α is applied to the reference basis we obtain a *loading path* in the configurational space C_{11}, C_{22}, C_{12}. The deformed basis $\{\mathbf{e}_i^*\}$ reproduces a square lattice every time that the corresponding matrix $\mathbf{F}$ in (2.29) acquires all integer entries, i.e. every time that it describes a lattice-invariant shear (2.11). It is easy to see that the three shears in (2.30) have, respectively, periods of $\alpha = 1$, 5 and 2. Note that the implied periodicity is not necessarily symmetric with respect of the original state $\{\mathbf{e}_I\}$, as we observe for $\theta = \arctan(\frac{1}{2})$ in Figure 2.7, where we show energy profiles (a) and the evolution of the shearing paths on the configurational space (b). As expected, the energy barriers are significantly lower along the direction $\theta = 0°$, which, being aligned with a crystallographic plane, represents a natural shearing direction for the crystal. As a consequence of the square lattice symmetry, shear paths characterized by angles θ inclined by $\pm 90°$ with respect to each other are energetically equivalent, i.e. they generate the same

[5] Distinction between low-case and capital indexes will be introduced more systematically in the next Chapter. For now we anticipate the fact that capital letters refers to quantities in the undeformed, reference state while low-case indexes refers to the same quantities after a deformation process.

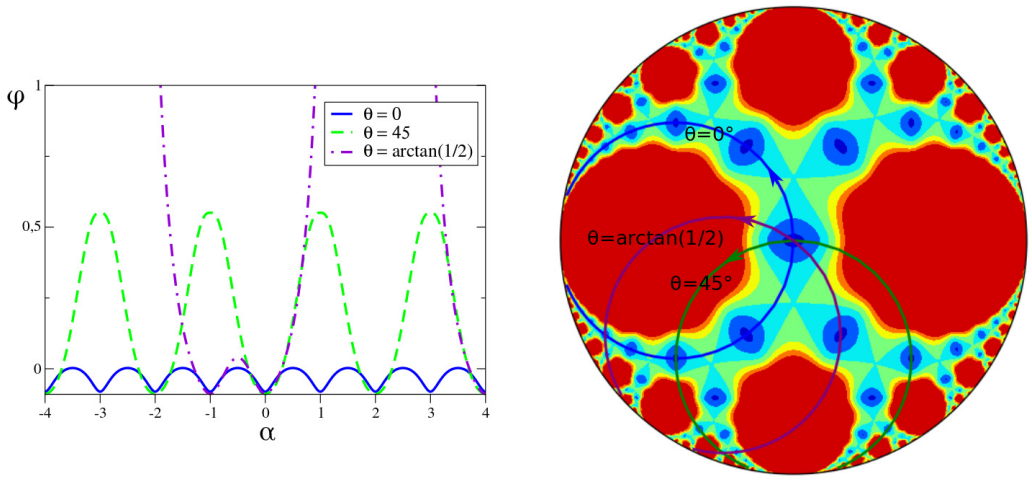

(a) (b)

Figure 2.8: **Shear Loading Paths:** Energy landscape for different shearing paths $\theta = 0°$, $\theta = \arctan(1/2)$ and $\theta = 45°$ is shown. Shear asymmetry and different periodic behavior along general shearing directions are fully described.

energy landscape. An interesting feature, revealed by the Poincaré disk representation is that all simple shear paths are tangent to the boundary at infinity. Notice also that the obtained landscape is way more generic than the one resulting from the periodic energies proposed in [MO07, Onu03, CB05].

While simple shears allow one to explore the energy landscape by probing it along the circular trajectories, other interesting loading paths are the ones corresponding to the boundaries of the fundamental domain D. As we have already mentioned, those correspond to rhombic and rectangular lattices and are also geodesics on the Poincaré disk. By symmetry, the points belonging to these paths are local maxima or minima of the energy. In the case of the landscape centered at a square lattice the rectangular and the fat rhombic path, originating at the point **S**, are both at the bottom of energy valleys. Observe also that the fat rhombic path is directed towards a local maximum, the triangular lattice point **T**, while the rectangular path evolves towards infinity spanning an increasingly higher energy barrier without encountering any other square lattice configurations.
In the case of a fat rhombic path the deforming directions are the diagonals of the square. The corresponding pure shear deformation is given by the matrix (see also [DMS12, TVMN19]):

$$\mathbf{F} = \frac{1}{\sqrt{\cosh\alpha}} \begin{bmatrix} \cosh\alpha & \sinh\alpha \\ 0 & 1 \end{bmatrix}. \tag{2.31}$$

The energy barrier along this path is lower with respect to the previously mentioned $\theta = 0°$ simple shear. The point **T** is a local maximum along the fat rhombic direction, but is a minimum along the skinny rhombic one, as we illustrate schematically in Figure 2.9. The

triangular point **T** is therefore a saddle point in which three low energy valleys converge. Since in our model the low-energy valleys define available slip systems, this position of **T** makes it particularly important in determining non-trivial coupling between the activated slips.
The rectangular path also corresponds to a pure shear, in which the vertical direction is extended and the horizontal shortened. The associated deformation gradient is:

$$\mathbf{F} = \begin{bmatrix} \sqrt{1-\alpha} & 0 \\ 0 & \frac{1}{\sqrt{1-\alpha}} \end{bmatrix}. \tag{2.32}$$

As we have already remarked, this paths evolves towards infinity without crossing any other shear invariant minimizer of our square lattice centered energy landscape.

While simple and pure shears are distinguished just by a rigid rotation in a linear strain description, the relation is more complex in a geometrically non-linear strain formulation [DMS12, TVMN19]. Indeed, these two deformations define two different paths in the configurational space, which are not at all rotation-related.
The overlap of pure and simple shears trajectories it is not the only approximation implied by linearized small strains assumption. Indeed, consider the two symmetry related shears with $\theta = 0°$ and $\theta = 90°$, that are given by the matrices:

$$\mathbf{F}_{0°} = \begin{bmatrix} 1 & \alpha \\ 0 & 1 \end{bmatrix} \qquad \mathbf{F}_{90°} = \begin{bmatrix} 1 & 0 \\ -\alpha & 1 \end{bmatrix} \tag{2.33}$$

These are the most natural simple shears for the crystal since they are oriented along crystallographic directions. They have period 1 and relatively low energy barriers. As previously remarked, these two paths are equivalent energetically, however they are distinguished in terms of the associated strains. In a linear description, the components of the linearized strain tensor ϵ are the same for these two trajectories:

$$\epsilon = \frac{1}{2}\begin{bmatrix} 0 & \alpha \\ \alpha & 0 \end{bmatrix}. \tag{2.34}$$

Instead, they are different when considering the nonlinear strain tensor $2\mathbf{E} = (\mathbf{C} - \mathbf{I})$:

$$\mathbf{E}_{0°} = \frac{1}{2}\begin{bmatrix} 0 & \alpha \\ \alpha & \alpha^2 \end{bmatrix} \qquad \mathbf{E}_{90°} = \frac{1}{2}\begin{bmatrix} \alpha^2 & \alpha \\ \alpha & 0 \end{bmatrix}. \tag{2.35}$$

A nonlinear term $\propto \alpha^2$ appears along one of the diagonal entries E_{11} and E_{22}, which are proportional to the stretch along the initial lattice vectors $\mathbf{e}_1$ and $\mathbf{e}_2$. In the small strain limit, the condition of constant volume is expressed by the requirement that the trace of the deformed cell remains constant. Then, the linearized configurations are located on the plane $tr(\mathbf{C}) = 2$, which is tangent to the hyperboloid $\det \mathbf{C} = 1$ in the initial undeformed square state **S** (as schematized in Figure 2.10). One may easily verify from

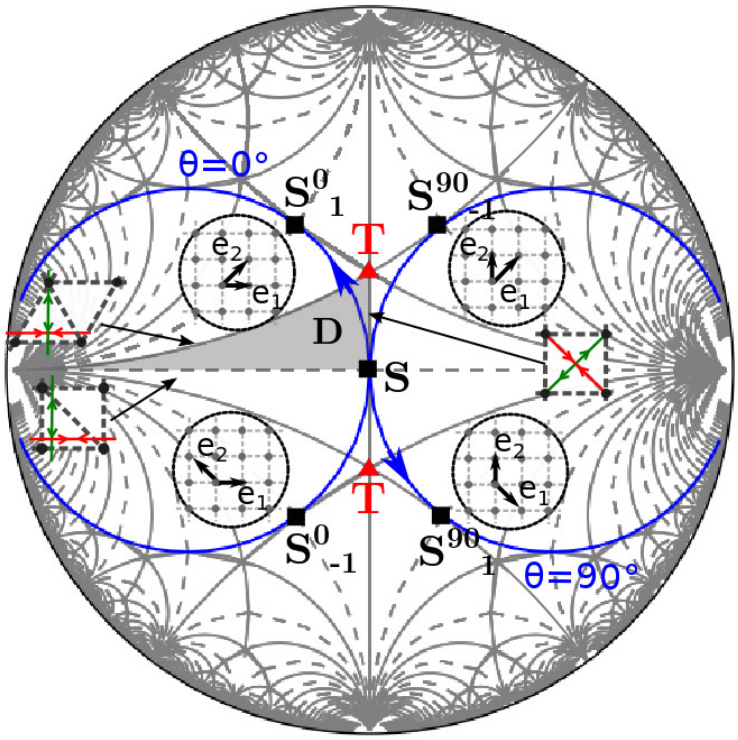

(a)

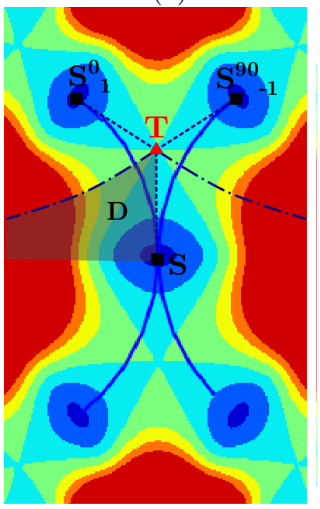

(b)

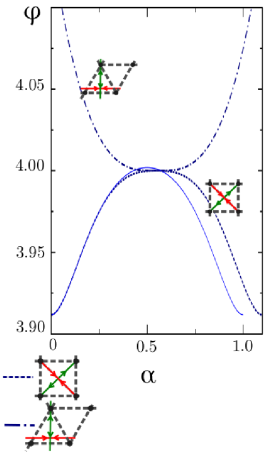

(c)

Figure 2.9: **Square Symmetry Reference Well:** Configuration of square wells near reference well **S**, the simple shears $\theta = 0°$ and $\theta = 90°$ are showed with continue blue lines while pure shear paths are showed with differently dashed blue lines (b). Energy landscape along these low energy barriers is illustrated with evidence of triangular lattice point **T**, located in the upper vertex of the fundamental domain. In (c) the graphs of energy profiles corresponding to skinny and fat rhombic paths are shown, together with the $\theta = 0°$ shear path.

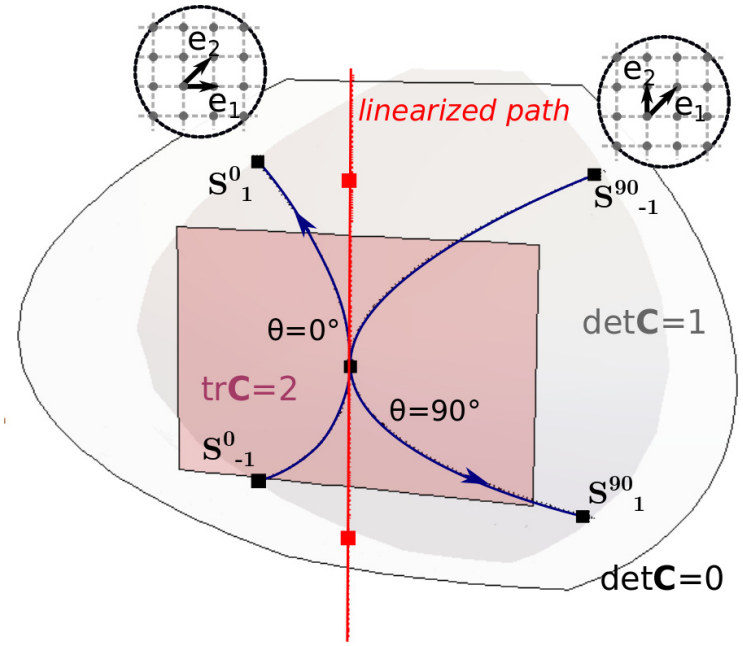

Figure 2.10: **Linear and Nonlinear Configurational Spaces:** Representation of nonlinear and linear $\theta = 0°$, $\theta = 90°$ shearing paths. Linearized strain components are situated on plane $tr(\mathbf{C}) = 2$, tangent to the initial undeformed configuration $\mathbf{S}$. As the square configurations $\mathbf{S}_0^{+1}$ and $\mathbf{S}_{90}^{-1}$ differ for a nonlinear component, they result merged in one point the linearized strain space.

(2.34) that in such approximate theory the paths $\theta = 0°$ and $\theta = 90°$ merge along the line $C_{11} = C_{22} = 1$. Therefore the two different minima $\mathbf{S}_0^{+1}$ and $\mathbf{S}_{90}^{-1}$ collapse, in a linear theory, on the same point. This causes a degeneracy since it is no longer possible to distinguish between the two cases. For instance, when the system is forced through instability, it may choose to restore its square structure in one way or another depending on which basis vector is more prone to stretch. The same superimposition phenomenon takes place for the trajectories $\theta = 45°$, $\theta = 135°$. More generally, the further is the position of the minima from the original undeformed state, the more relevant are the nonlinear components for their description in the space C_{11}, C_{22}, C_{12}. The above examples show the importance of using the geometrically non-linear strain in any tensorial description of plastic slip. In other words, a fully coherent use of the $GL(2, \mathbb{Z})$ invariance requires the formulation in terms of geometrical non-linear strains.

Triangular Lattice

We now turn to the case of the triangular symmetry crystal. In this case the reference state is given by the point $\mathbf{T}$, the upper vertex of the fundamental domain D, with coordinates

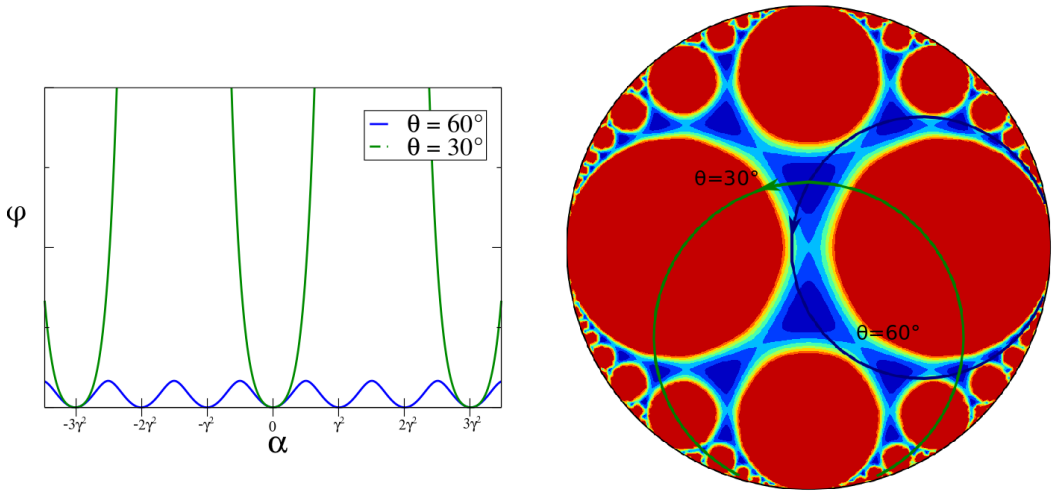

(a) (b)

Figure 2.11: **Shear Loading Paths in the Triangular Lattice:** Energy landscape for shearing paths $\theta = 30°$ and $\theta = 60°$ is shown. The different periodic behaviors along general shearing directions are fully described.

$C_{11} = C_{22} = \gamma^2$, $C_{12} = \frac{\gamma^2}{2}$. Now the lattice cell is indeed described by the basis vectors:

$$\mathbf{e}_1 = \left\{ \begin{array}{c} \gamma \\ 0 \end{array} \right\} \quad \mathbf{e}_2 = \left\{ \begin{array}{c} \frac{1}{2}\gamma \\ \frac{\sqrt{3}}{2}\gamma \end{array} \right\} \quad , \tag{2.36}$$

where $\gamma = \sqrt[4]{\frac{4}{3}}$. In the triangular lattice, there are three axes of symmetry, inclined respectively at $\theta = 0°$, $60°$ and $120°$. This higher symmetry manifests itself also in the fact that more copies of the fundamental domain (six) are converging in $\mathbf{T}$. The energy barriers corresponding to simple shears with $\theta = 60°$, oriented along lattice directions, and with a general inclination $\theta = 30°$ are illustrated in Figure 2.11. Such paths will pass through energy minima every time the deformed vectors become integer multiples of the basis (2.36). This takes place at every $\alpha = \gamma^2$ for $\theta = 60°$ (or, analogously $\theta = 0°$, $\theta = 120°$) and at every $\alpha = 3\gamma^2$ for $\theta = 30°$ (or $\theta = 90°$, $150°$). As in the square lattice, barriers are significantly lower in shearing directions that are aligned with crystallographic planes. An interesting feature of the triangular lattice is that symmetry related shear paths with $\theta = 0°$, $\theta = 60°$ and $\theta = 120°$ pass through the same energy wells, (see Figure 2.12). Matrices of these shears are given by:

$$\begin{array}{c} \mathbf{F}_{0°} = \left[\begin{array}{cc} \gamma & \frac{\gamma}{2} + \alpha\frac{\sqrt{3}}{2}\gamma \\ 0 & \frac{\sqrt{3}}{2}\gamma \end{array} \right], \qquad \mathbf{F}_{60°} = \left[\begin{array}{cc} \gamma - \alpha\frac{\sqrt{3}}{4}\gamma & \frac{\gamma}{2} \\ -\frac{\gamma}{4}\alpha & \frac{\sqrt{3}}{2}\gamma \end{array} \right], \\ \mathbf{F}_{120°} = \left[\begin{array}{cc} \gamma + \alpha\frac{\sqrt{3}}{4}\gamma^3 & \frac{1}{8}\gamma(4 + \alpha(2 + \sqrt{3}\gamma^2)) \\ -\alpha\frac{\sqrt{3}}{2}\gamma & \frac{\sqrt{3}}{2}\gamma - \alpha\frac{(2+\sqrt{3}\gamma^2)}{4\gamma} \end{array} \right]. \end{array} \tag{2.37}$$

It is easy to verify that the strain configurations associated with the wells $\{\mathbf{T}_1^{0^\circ}, \mathbf{T}_{-1}^{120^\circ}\}$, $\{\mathbf{T}_1^{60^\circ}, \mathbf{T}_{-1}^{0^\circ}\}$ and $\{\mathbf{T}_1^{120^\circ}, \mathbf{T}_{-1}^{60^\circ}\}$ coincide. The associated deformed lattices are related by a 60° rigid rotation, see Figure (2.12). Then, differently from what is observed in the square lattice, symmetry related shears result in strain-equivalent lattices configurations, and the corresponding deformation gradients are distinguished just by a rigid rotation. However, the related simple shear paths are different and cross only on the **C** space.

Pure shears corresponding to the boundary of D deserve special attention. In the point **T**, one observes the crossing of the skinny and the fat rhombic path, the first evolve at infinity towards an increasingly higher energy barriers (as the rectangular path in the square lattice), the second one is directed towards the square symmetry point **S**, which is a local maximum inside the associated energy valley. The energy level is significantly lower along this pure shear path comparing to the paths describing simple shears, in a way far more pronounced than what is observed in the square lattice case, see Figure 2.12. In view of this, the point **S** is likely to play a very important role in the mechanism of dislocation nucleation.

The fat rhombic path is again described by matrix (2.31), which for $\alpha = 0.5493$ corresponds to the triangular lattice. Starting from this value, it is possible to span the path towards the square configuration **S** by decreasing α. The skinny rhombic path is obtained by applying to the reference basis the matrix (2.32):

$$\mathbf{F} = \begin{bmatrix} \gamma\sqrt{1-\alpha} & 0 \\ 0 & \frac{\sqrt{3}}{2}\gamma\frac{1}{\sqrt{1-\alpha}} \end{bmatrix} \tag{2.38}$$

In Figure 2.12 we schematically depict the elongated and shortened directions associated with such pure shears. Finally, we remark that the difference between simple and pure shears will be lost in a linear strain description.

2.2.3 Additional Remarks

In this Chapter, we discussed the importance of adopting $GL(2,\mathbb{Z})$ invariance in the construction of an energy density suitable for the description of plastic deformation in crystals. Differently from the point group based material symmetry, $GL(2,\mathbb{Z})$ invariance takes into account lattice-invariant shears ensuring that the energy landscape is periodic. We showed a way to effectively construct an energy possessing the desired invariance. Despite the fact that the quantitative values of the energy barriers are controlled by the particular polynomial form we use, the general properties of the system and the overall form of the energy landscape depend exclusively on the imposed invariance. In particular, the behavior of the system in simple shear and the very peculiar role of the high symmetry points **T** and **S**, are the general consequence of the $GL(2,\mathbb{Z})$ invariance, unrelated to the specific representation

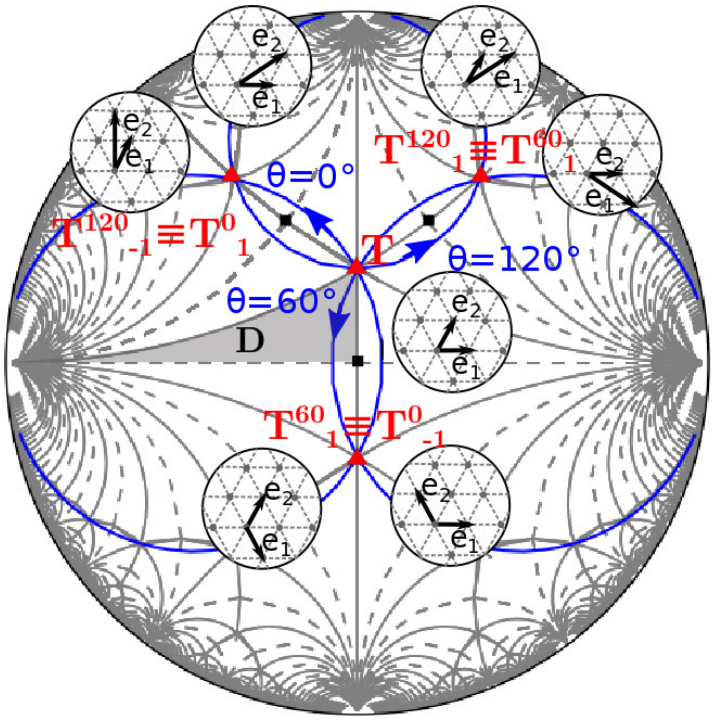

(a)

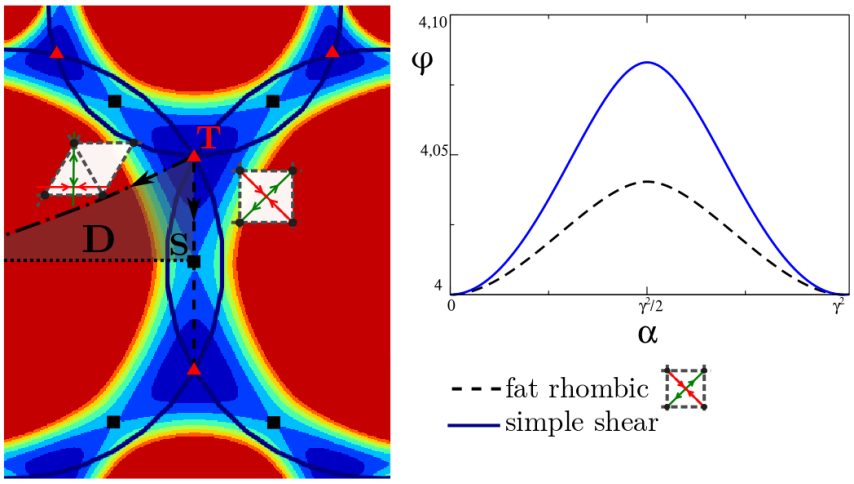

(b)

Figure 2.12: **Hexagonal Symmetry Reference Well:** Configuration of triangular wells near the reference well **T**. Simple shears $\theta = 0°$, $60°$ and $120°$ are showed with continue blue lines while pure shear paths are showed with differently dashed lines (a). Energy landscape near the reference well, with evidence on the fact that energy is significantly lower along the fat rhombic path (b).

of the potential within the fundamental domain D. This will become even clearer when we present the $GL(2,\mathbb{Z})$-invariant energy obtained from pair-potential in Chapter 6.

Chapter 3

Continuum Formulation and Numerical Implementation

In the previous Chapter we showed how to construct a strain energy density with symmetry properties derived directly from the global symmetry group $GL(2,\mathbb{Z})$. This allowed us to describe the energy landscape associated with lattice invariant-shears, which are essential for the description of crystal plasticity. In this Chapter we illustrate how to include the presented energy in the continuum framework accounting for finite deformations. By constructing a strain energy density function for the crystal lattice, we implicitly assumed that this energy represents the potential energy of a unit cell. In order to link continuum and discrete, lattice-based, descriptions one needs to make another fundamental assumption, known as *Cauchy-Born rule*. This will allow us to connect the two formulations in a straightforward manner, but with some drawbacks. From one point of view, the possibility to exploit a fully continuum formulation is advantageous. Macroscopic quantities such as stresses and strains are defined directly and the energy minimization can be treated in full generality as a boundary value problem. Moreover, such continuum setting allows one to exploit the well-known techniques available for the numerical solution of PDEs, such as the finite differences and the finite elements methods. On the other hand, by assuming the Cauchy-Born hypothesis, truly atomisitc non-local interactions are lost and replaced by the study of slowly varying fields. Another drawback is due to the fact that $GL(2,\mathbb{Z})$ invariant, purely continuum approaches suffer from the lack of convergence, the obtained solution is dependent on the adopted discretization and tends to a totally-relaxed, fluid like state in the limit of infinite fineness of the discretization [Fon87].

To deal with these issues we introduce explicitly a length scale into the theory making the approach not fully continuum. We recall that purely continuum $GL(2,\mathbb{Z})$ invariant theories have been studied before ([BJ89, Fon87, Kin87b, Kin87a, CK88]), and that $GL(2,\mathbb{Z})$ invariant continuum energies derived by using the Cauchy-Born rule are important ele-

ments of local formulation of the QC method [TPO96]. In [OP98] Ortiz refers explicitly to such approach as *Cauchy-Born Theory of Crystal Elasticity*. Here we deviate from these purely-continuum models by incorporating the inherent length scale explicitly. Moreover, our construction of the energy density is based directly on the requirement that $GL(2,\mathbb{Z})$ invariance is satisfied exactly instead of being gradually lost with deformations, as in the case of the local QC method.

We start with introducing the boundary value problem used for elasto-static problems, in their general, finite-displacement formulation.Then we discuss how to coherently include the lattice-based energy in such continuum framework using the Cauchy-Born rule. We address some peculiar aspects involved in the mathematical formulation of $GL(2,\mathbb{Z})$ invariant energies and then address explicitly the introduction of the internal length scale. Numerical implementation of the model is also presented. We conclude the Chapter showing some initial validation tests for the proposed model: the visualization of a dislocation core and an illustration of the simplest interactions between two dislocations.

3.1 The Hyperelastic Boundary Value Problem

Consider a hyperelastic[1] medium subjected to prescribed boundary conditions. The problem incorporates finite deformations and it is therefore necessary to distinguish the initial undeformed state, the *Lagrangian configuration* from the final deformed one, the *Eulerian configuration*, each of them characterized by their respective coordinate systems.

In what follows, when not explicitly stated otherwise, the convention will be used where the capital letters refer to Lagrangian quantities and low-case letters to Eulerian variables. Let's Ω be a body in the Lagrangian, undeformed reference state and define $\partial\Omega$ as its boundary. Suppose that assigned tractions $\mathbf{T}^*$ and displacements $\mathbf{u}^*$ are given on separate subdomains of the boundary $\partial\Omega_T$ and $\partial\Omega_u$, such that $\partial\Omega_T \cup \partial\Omega_u = \partial\Omega$ and $\partial\Omega_T \cap \partial\Omega_u = \emptyset$. After deformation, the body is represented by the domain ω with boundary $\partial\omega$ (see Figure 3.1). We further assume that a material point $\mathbf{X}$ in the undeformed configuration is mapped on the point $\mathbf{x}$ in the deformed configuration. For simplicity, both Lagrangian and Eulerian reference systems are assumed to be Cartesian. These two systems of basis vectors will be denoted by $[\mathbf{I}_I]$ and $[\mathbf{i}_i]$ respectively. Position vectors in the undeformed and deformed configurations can be represented in their Cartesian components:

$$\mathbf{X} = X_I \mathbf{I}_I \tag{3.1}$$

$$\mathbf{x} = x_i \mathbf{i}_i \,, \tag{3.2}$$

[1] A *hyperelastic material*, or *Green Elastic*, is an elastic material, not necessarely linear-elastic, which admits an energy density function [Ogd97]

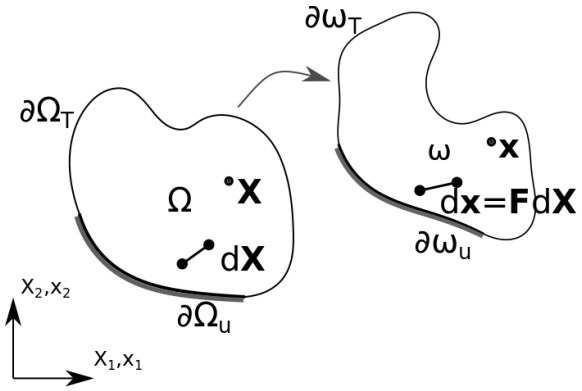

Figure 3.1: **Finite Deformation:** Schematic representation of the Lagrangian undeformed configuration and of the Eulerian deformed configuration in a finite deformation problem.

where we recall that the capital and low-case indices refers to Lagrangian and Eulerian configurations respectively (Einstein convention $x_i\mathbf{i}_i = \sum_i x_i\mathbf{i}_i$ is implied). Indexes vary between $1, \ldots, n_d$ where n_d is the dimension of the system ($n_d = 2$ in 2D).
With the choice that the vector bases $[\mathbf{I}_I]$ and $[\mathbf{i}_i]$ coincide, we can write:

$$x_i = \delta_{iJ}(X_J + U_J)\,, \tag{3.3}$$

where δ_{iJ} is the Kronecker delta, which implies that $U_I = u_i$. The goal is to find a displacement field $\mathbf{u}$ such that the deformed configuration is in equilibrium, meaning that internal stresses due to the deformation are balanced by the externally imposed tractions. It is then necessary to introduce suitable stress and strain measures. We first define the deformation gradient $\mathbf{F}$, a second order tensor whose components are given by:

$$F_{iJ} = \frac{\partial x_i}{\partial X_J}\,. \tag{3.4}$$

The tensor $\mathbf{F}$ can also be expressed in terms of displacements as:

$$F_{iJ} = \delta_{iJ} + \frac{\partial u_i}{\partial X_J}\,, \tag{3.5}$$

and describes the change of length for an infinitesimal line element $d\mathbf{X}$ after the deformation:

$$dx_i = F_{iJ}dX_J\,. \tag{3.6}$$

Its determinant $J = \det \mathbf{F}$ maps an infinitesimal undeformed volume element $d\Omega$ into a deformed Eulerian element $d\omega$, so that:

$$d\omega = Jd\Omega\,. \tag{3.7}$$

The single-valuedness of the deformation requires that the determinant J is positive definite. We note that $\mathbf{F}$ is a two-point tensor, which is defined in Lagrangian and Eulerian configurations simultaneously. Moreover it is not material frame indifferent. A rotation-independent strain measure for the Lagrangian reference system is then the right Cauchy-Green strain tensor:

$$\mathbf{C} = \mathbf{F}^T\mathbf{F}\,, \qquad C_{IJ} = F_{kI}F_{kJ}, \tag{3.8}$$

which is written in matrix form and in components, respectively. Notice that the determinant of $\mathbf{C}$ must be positive definite:

$$\det \mathbf{C} > 0\,. \tag{3.9}$$

To derive the constitutive law relating stress and strains, one needs the strain energy density $\phi(\mathbf{C})$. For hyperelastic materials, stress measures $\mathbf{P}$ and $\mathbf{S}$, the first and the second Piola-Kirchhoff strain tensors, can be defined by the relations:

$$\mathbf{P} = \rho_0 \frac{\partial \phi}{\partial \mathbf{F}}\,, \qquad P_{iJ} = \rho_0 \frac{\partial \phi}{\partial F_{iJ}} \tag{3.10}$$

$$\mathbf{S} = 2\rho_0 \frac{\partial \phi}{\partial \mathbf{C}}\,, \qquad S_{IJ} = 2\rho_0 \frac{\partial \phi}{\partial C_{IJ}} \tag{3.11}$$

where ρ_0 is the density in the Lagrangian, undeformed state. These two stress measures are related by:

$$\mathbf{P} = \mathbf{FS} \qquad P_{iJ} = F_{iK}S_{KJ}\,. \tag{3.12}$$

Mathematical equilibrium condition states that the divergence $(\nabla\cdot)$ of stresses must be balanced by the applied bulk forces. The boundary value problem for an elasto-static solid can be formulated as follows:

$$\nabla \cdot \mathbf{P} + \rho_0\mathbf{B} = 0\,, \qquad P_{iJ,k} + \rho_0 B_k = 0 \qquad on \quad \Omega \tag{3.13}$$

$$\mathbf{PN} = \mathbf{T}^*\,, \qquad P_{iJ}N_j = T_j^* \qquad on \quad \partial\Omega_T \tag{3.14}$$

$$\mathbf{u} = \mathbf{u}^*\,, \qquad u_i = u_i^* \qquad on \quad \partial\Omega_u \tag{3.15}$$

where $\mathbf{B}$ are body forces, $\mathbf{N}$ is the normal unit vector to $\delta\Omega_T$ in the Lagrangian reference system and operator $(\cdot)_{,k}$ is the partial derivative with respect of coordinate k. System (3.13-3.15) is known as the strong form of the elasto-static boundary value problem. This formulation selects a critical point of the total potential energy of the system,

$$\Pi = \int_\Omega \varphi(\mathbf{C}(\mathbf{X}))d\Omega - \int_\Omega \rho_0\mathbf{B}\cdot\mathbf{u}d\Omega - \int_{\partial\Omega_T} \mathbf{T}^*\cdot\mathbf{u}d\partial\Omega\,. \tag{3.16}$$

Solution of the elasto-static problem can be also found through the direct minimization of functional Π with respect to $\mathbf{u}$. The path followed by the Finite Element Method (FEM)

[ZT00a, ZT00b] is to solve the system of PDEs through the discretization of the corresponding weak, integral, formulation. The continuum domain Ω is then made discrete through the design of a numerical grid (the mesh), and solution $\mathbf{u}$ is calculated exactly only on selected points $\mathbf{X}_i$ (mesh nodes). Then, an approximate solution $\mathbf{u}$ is obtained on the entire domain by interpolations of the obtained nodal values $\mathbf{u}_i$, using suitable interpolation functions (shape functions).

Notice that the discretization, necessary for solving numerically the system of continuum PDEs, brings an internal length scale into the problem (3.13-3.15). As we have already mentioned, in $GL(2,\mathbb{Z})$ invariant theories there is a need of a regularization, as the non-regularized solution exhibits a fluid like behavior. In our theory the discretization will then be more than a numerical tool, and will assume a physical meaning, as we will discuss shortly.

Minimization of the discretized form of (3.16) generally leads to a non-linear problem that is solved numerically using usually minimization strategies of the family of the Newton-Raphson method (NR). For the minimization of (3.16) it will be necessary to compute, along with the energy $\varphi(\mathbf{C})$, also its derivatives:

$$S_{IJ} = 2\rho_0 \frac{\partial \phi}{\partial C_{IJ}} \tag{3.17}$$

$$\mathcal{C}_{IJKL} = 2\rho_0 \frac{\partial \phi^2}{\partial C_{IJ} \partial C_{KL}} \,. \tag{3.18}$$

Hessian $\mathcal{C}_{IJKL}$ is a fourth order tensor relating increments of stress $\dot{S}_{IJ}$ to increments of strain $\dot{C}_{KL}$. It is sometimes called the second elasticity tensor, while the first elasticity tensor is:

$$\mathcal{A}_{iJkL} = \frac{\partial^2 \phi}{\partial F_{iJ} \partial F_{kL}} \,, \tag{3.19}$$

We remark that the second Piola-Kirchhoff stress $\mathbf{S}$ is the work-conjugate of $\mathbf{C}$ (as $\mathbf{P}$ is the work-conjugate of $\mathbf{F}$) and therefore is the stress measure to be used in the problem. Once $\mathbf{S}$ is calculated, it is desirable to evaluate also the Cauchy stress tensor $\boldsymbol{\sigma}$, whose components give the stresses in the current, deformed configuration. This Eulerian stress measure can be obtained from $\mathbf{S}$ using the relations:

$$\boldsymbol{\sigma} = \frac{1}{J}\mathbf{F}\mathbf{S}\mathbf{F}^T \,, \qquad \sigma_{ij} = \frac{1}{J} F_{iI} S_{IJ} F_{jJ} \,, \tag{3.20}$$

where $J = \det \mathbf{F}$ is the jacobian of the transformation. Operation $f^*(\mathbf{x}) = \mathbf{F}\mathbf{x}\mathbf{F}^T$, appearing in (3.20) is called *push forward*. It allows one to map forward to the deformed configuration second order tensors defined in the Lagrangian (undeformed) one. Its inverse $f_*(\mathbf{x}) = \mathbf{F}^{-1}\mathbf{x}\mathbf{F}^{-T}$, the *pull back*, allows one to map back Eulerian tensors in the Lagrangian configuration.

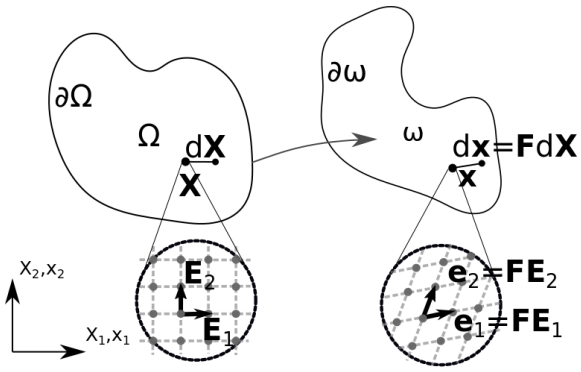

Figure 3.2: **Cauchy-Born Rule:** Representation of the Cauchy-Born assumption. The continuum formulation is linked to the lattice based one by assuming the lattice vectors $\{\mathbf{e}_I\}$ to behave like the element of infinitesimal lenght $d\mathbf{X}$ in the continuum formulation.

3.2 The Energy φ in the Continuum Formulation

To use the lattice -based energy density in the continuum framework one has to establish a link between discrete lattice description and the continuum one. This is usually done through the assumption of the Cauchy-Born rule (CBR), introduced by Cauchy [Cau28] and subsequently improved by Born[Bor15]. It states that material vectors $d\mathbf{X}$ in the continuum description deform in agreement with lattice vectors $\mathbf{e}_I$, underlying the continuum at point $\mathbf{X}$ [Eri05, Eri08, Zan96]. It implies that the local deformation gradient $\mathbf{F}(\mathbf{x})$ actually describes the deformation of the underlying lattice:

$$\mathbf{e}_i = F_{iJ}\mathbf{e}_J. \tag{3.21}$$

Therefore, once (3.21) is assumed to hold, one may compute the energy density ϕ for unit volume of the crystal viewed as a continuum using the lattice energy φ

$$\phi(\mathbf{F}) := \varphi(\mathbf{F}\mathbf{e}_I) = \varphi(\mathbf{e}_i), \tag{3.22}$$

where the reference lattice vectors $\mathbf{e}_I$ are understood as fixed. Since material frame indifference must hold, that is, the material constitutive response has to be independent of the chosen frame of reference, the continuum energy depends on $\mathbf{F}$ only through the right Cauchy-Green strain tensor $\mathbf{C} = \mathbf{F}^T\mathbf{F}$. In the reference basis $\mathbf{I}_I = \mathbf{e}_I$, This strain tensor is represented by the metric tensor of the lattice:

$$C_{IJ} = \mathbf{e}_I \cdot \mathbf{C}\mathbf{e}_J\,. \tag{3.23}$$

Then, we can directly define the continuum energy density ϕ as dependent on $\mathbf{C}$:

$$\phi(\mathbf{C}) = \varphi(\mathbf{e}_I \cdot \mathbf{C}\mathbf{e}_J) \tag{3.24}$$

Notice that, since $\mathbf{F}$ and $\mathbf{C}$ are referred to a certain reference basis $\mathbf{e}_I$, the function ϕ actually depends on this choice. Also matrices $\mathbf{m} \in GL(2,\mathbb{Z})$ are implicitly referred to $\mathbf{e}_I$. Therefore, when reference state is changed, also ϕ and $\mathbf{m}$ change accordingly. In this Thesis work we always keep as reference basis $\mathbf{e}_I$ the unit square lattice aligned with Cartesian reference system $\mathbf{I}_I$ (i.e: $\mathbf{e}_1^T = \{1 \quad 0\}$, $\mathbf{e}_2^T = \{0 \quad 1\}$).

One has to keep in mind that the CBR may break in some conditions [Eri08, Zan96]. However, in the case of simple Bravais lattices CBR can be always used to obtain suitable energy densities representing the correct symmetry group [Zan96]. The main consequence of CBR is that the energy $\varphi(\mathbf{C})$ is inherently local[2]. This means that only slowly varying fields can be handled. As a consequence, the obtained description will produce a somewhat blurred picture with respect to a truly atomistic approach. Locality is an intrinsic consequence of the continuum formulation, as the principle of local action (see footnote 2) is implicit in the formulation of the classical nonlinear elasticity [MH94, TN04]. This means that our discrete elements will not be truly atomistic, but rather will be representative of a meso-scale block of atoms. Therefore, there is an inherent length-scale associated with the Cauchy-Born assumption. We assume that it is the smallest atomistic size for which the energy landscape can be viewed as periodic in the range of strains of interest. This aspect has to be kept in mind as there is no other internal length scale in the theory.

Now that a continuum form of the energy density function ϕ is obtained, we can use it in the hyperelastic problem (3.13-3.15). To this end we need to first find the dependence of the density function ϕ on the reference energy density ϕ_0, defined on the fundamental domain D. Every time that partial derivatives of ϕ are computed, this dependence must be used. Indeed, employing the chain rule, we have for the first and second derivatives of ϕ respectively:

$$\frac{\partial \phi}{\partial C}_{KL} = \frac{\partial \phi_0}{\partial \bar{C}_{IJ}} \frac{\partial \bar{C}_{IJ}}{\partial C_{KL}}\,, \tag{3.25}$$

$$\frac{\partial^2 \phi}{\partial C_{IJ} \partial C_{KL}} = \frac{\partial}{\partial C_{KL}} \left[\frac{\partial \phi_0}{\partial \bar{C}_{OZ}} \frac{\partial \bar{C}_{OZ}}{\partial C_{IJ}} \right] = \frac{\partial^2 \phi_0}{\partial \bar{C}_{RS} \bar{C}_{OZ}} \frac{\partial \bar{C}_{OZ}}{\partial C_{IJ}} \frac{\partial \bar{C}_{RS}}{\partial C_{KL}}\,. \tag{3.26}$$

The Lagrange-reduced, reference metric $\bar{\mathbf{C}}$ is related to the unreduced one by action (2.6), i.e. in components:

$$\bar{C}_{KL} = m_{IK} C_{IJ} m_{JL}\,. \tag{3.27}$$

Then the partial derivatives of the reference metric $\bar{\mathbf{C}}$ are given by:

$$\frac{\partial \bar{C}_{KL}}{\partial C_{IJ}} = m_{IK} m_{JL}\,. \tag{3.28}$$

[2] We consider as *local* approach a continuum theory for which holds the principle of local action, i.e. such that response at a certain point is given by the value of model variables at that point only. In a *non-local* material formulation instead, properties at a certain point depend also on values of variables in other distinguished material points.

The expressions for the second Piola-Kirchhoff $\mathbf{S}$ stress (3.17) and second elasticity tensor $\mathcal{C}$ (3.18) are then:

$$S_{IJ} = 2m_{IO}m_{JZ}\frac{\partial \phi_0}{\partial \bar{C}_{0Z}}\,, \tag{3.29}$$

$$\mathcal{C}_{IJKL} = 2m_{KW}m_{LU}m_{IR}m_{JS}\frac{\partial^2 \phi_0}{\partial \bar{C}_{RS}\bar{C}_{WU}}\,. \tag{3.30}$$

Since C_{IJ} is symmetric, the matrix forms of $[\frac{\partial \phi_0}{\partial \bar{\mathbf{C}}}]$ and $[\frac{\partial^2 \phi_0}{\partial \bar{\mathbf{C}}\partial \bar{\mathbf{C}}}]$ are given by:

$$\left[\frac{\partial \phi_0}{\partial \bar{\mathbf{C}}}\right] = \begin{bmatrix} \frac{\partial \phi_0}{\partial \bar{C}_{11}} & \frac{1}{2}\frac{\partial \phi_0}{\partial \bar{C}_{12}} \\ \frac{1}{2}\frac{\partial \phi_0}{\partial \bar{C}_{12}} & \frac{\partial \phi_0}{\partial \bar{C}_{22}} \end{bmatrix} \tag{3.31}$$

$$\left[\frac{\partial^2 \phi_0}{\partial \bar{\mathbf{C}}\partial \bar{\mathbf{C}}}\right] = \begin{bmatrix} \begin{bmatrix} \frac{\partial^2 \phi_0}{\partial \bar{C}_{11}^2} & \frac{1}{2}\frac{\partial \phi_0}{\partial \bar{C}_{12}\partial \bar{C}_{11}} \\ \frac{1}{2}\frac{\partial \phi_0}{\partial \bar{C}_{12}\partial \bar{C}_{11}} & \frac{\partial^2 \phi_0}{\partial \bar{C}_{22}\partial \bar{C}_{11}} \end{bmatrix} & \frac{1}{2}\begin{bmatrix} \frac{\partial \phi_0}{\partial \bar{C}_{11}\partial \bar{C}_{12}} & \frac{1}{2}\frac{\partial \phi_0}{\partial \bar{C}_{12}^2} \\ \frac{1}{2}\frac{\partial \phi_0}{\partial \bar{C}_{12}^2} & \frac{\partial \phi_0}{\partial \bar{C}_{22}\partial \bar{C}_{12}} \end{bmatrix} \\ \frac{1}{2}\begin{bmatrix} \frac{\partial \phi_0}{\partial \bar{C}_{11}\partial \bar{C}_{12}} & \frac{1}{2}\frac{\partial \phi_0}{\partial \bar{C}_{12}^2} \\ \frac{1}{2}\frac{\partial \phi_0}{\partial \bar{C}_{12}^2} & \frac{\partial \phi_0}{\partial \bar{C}_{22}\partial \bar{C}_{12}} \end{bmatrix} & \begin{bmatrix} \frac{\partial^2 \phi_0}{\partial \bar{C}_{11}\partial \bar{C}_{22}} & \frac{1}{2}\frac{\partial \phi_0}{\partial \bar{C}_{12}\partial \bar{C}_{11}} \\ \frac{1}{2}\frac{\partial \phi_0}{\partial \bar{C}_{12}\partial \bar{C}_{11}} & \frac{\partial^2 \phi_0}{\partial \bar{C}_{22}^2} \end{bmatrix} \end{bmatrix}. \end{bmatrix}$$

The formulas (3.29) and (3.30) can be written in matrix form as:

$$\mathbf{S} = \mathbf{m}\left[\frac{\partial \phi_0}{\partial \bar{\mathbf{C}}}\right]\mathbf{m}^T\,. \tag{3.32}$$

$$\mathcal{C} = \mathbf{m}\mathbf{m}\left[\frac{\partial^2 \phi_0}{\partial \bar{\mathbf{C}}\partial \bar{\mathbf{C}}}\right]\mathbf{m}^T\mathbf{m}^T\,. \tag{3.33}$$

In this way, all the elements for the solution of PDEs system (3.13-3.15) in terms of the $GL(2,\mathbb{Z})$-invariant energy are in place.

3.3 Regularization

We have already mentioned that, as a consequence of its local nature, the continuum Cauchy-Born theory of elasticity lacks an intrinsic length scale [OP98]. This is not a realistic limit since in a scale-free setting, $GL(2,\mathbb{Z})$ invariant energies inevitably produce zero deviatoric stresses. The refinement of the discretization mesh produces in such systems increasingly fine oscillations, with solid reaching a "fluid like" liquid state in the limit [Eri73, Fon87]. This means that in a purely continuum framework this theory is not suitable for the description of crystals and that a regularized length scale needs to be introduced. Intuitively, this internal length scale has to be somewhere in between a fully atomistic scale and a coarse continuum macroscale.

To better illustrate this point, we propose a simple thought experiment, illustrated in Figure 3.3. We take a simple regular box of $N \times N$ atoms interacting with each other

through a Lennard-Jones pair potential and deform it homogeneously in simple shear. Then the total potential energy of the box Π is computed and divided by the box volume to obtain the energy density φ. For an increasing value of N the obtained landscape becomes almost perfectly periodic. Moreover, periodicity manifests itself already in atomic domains whose size is relatively small. For instance, at $N = 10$ the second and the first wells differ one another for less than 10%, at $N = 50$ the second well is captured almost exactly. This simple experiment suggests that $GL(2, \mathbb{Z})$-invariant energies do actually represent a small set of atoms deforming homogeneously. Therefore, the inherent length scale implied in the CBR assumption, can be taken as the smallest volume where a periodic energy can be reasonably assigned inside the strain domain of interest in the particular problem.

We recall that the numerical solution of the hyperelastic problem (3.13-3.15) is obtained using a discrete grid. We can therefore associate a physical meaning with the adopted discretization, i.e. we make the assumption that the meso-scale $GL(2, \mathbb{Z})$ invariant elements are at the same time:

- large enough to effectively exhibit a periodic energy landscape.
- small enough to capture the phenomena of interest, for instance the nucleation of dislocations.

As a consequence of the inherent locality of the ensuing mesoscopic description, some aspects of a truly atomistic description will be necessarily lost, for instance, dislocations cores will be represented in a coarse-grained, blurred way. However, the main features of the dislocation cores are still well captured and the main dislocation interactions, responsible for instance, for their annihilation, will be accounted without any ad hoc assumptions.

3.4 Numerical Implementation

To find the the numerical solution of the hyperelastic problem (3.13-3.15) we wrote our FEM code using the C++ programming language [Str00]. We used the weak form of the PDEs, and looked for a displacement field $\mathbf{u}$ such that the total potential energy $\Pi(\mathbf{u})$ (3.16) is minimized. Stationary points of the functional $\Pi(\mathbf{u})$ are given by the condition:

$$\frac{\partial \Pi}{\partial \mathbf{u}} = 0\,. \tag{3.34}$$

For simplicity, we do not consider external applied tractions $\mathbf{T}^*$ and volume forces $\mathbf{B}$. Instead, we prescribe displacements of the boundary $\partial\Omega = \partial\Omega_u$.

The continuum reference domain Ω is discretized using a regular grid of triangular elements, coherent with the lattice structure. With each node we associate a deformed cell defined by the basis vectors $\mathbf{e}_i$ aligned with the element sides. Displacements are

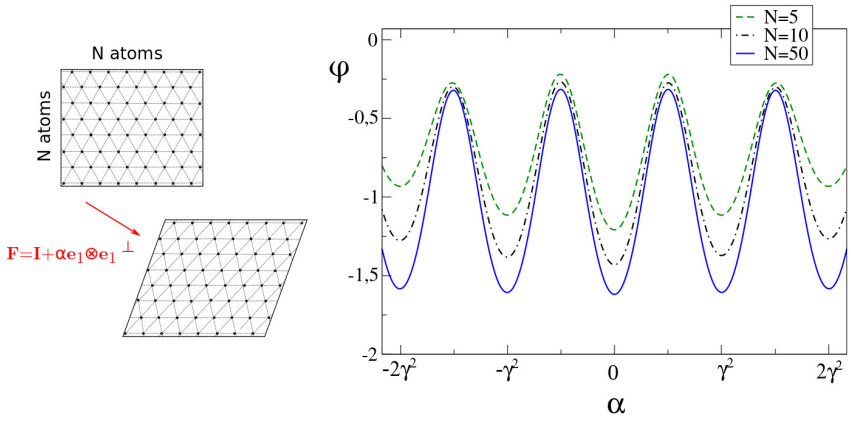

Figure 3.3: **Periodic Behavior and Length Scale:** Construction of a periodic energy density function $\phi(\mathbf{C})$ implies that the fundamental element of the model is given by a certain number of atoms deforming homogeneously. Here, MS energy profile corresponding to a domain of $N \times N$ atoms interacting with a Lennard-Jones potential is shown in correspondence of a simple shear deformation. Note that periodicity manifests already in correspondence of small sizes N.

then approximated by the interpolation of nodal values $\mathbf{u}^a$ (the effective unknowns of the discretized problem):

$$\mathbf{u} \approx \widehat{\mathbf{u}} = \sum_{a}^{n_n} \mathbf{N}^a(\mathbf{X})\mathbf{u}^a \,. \tag{3.35}$$

Here upper index a indicates the corresponding node and n_n is the total number of nodes in the discretization of Ω. Interpolation functions $\mathbf{N}^a(\mathbf{X}) = \{N^a_{x1}(\mathbf{X}), N^a_{x2}(\mathbf{X})\}$ satisfy condition $\mathbf{N}^a(\mathbf{X}^b) = \delta_{ab}$. They are chosen linear piecewise, with nonzero values only on elements containing node a. The local definition of the shape functions simplifies noticeably implementation of the approximate displacement (3.35). We use classical triangular elements (see also Chapter 8 in [ZT00a]). The same interpolation is used along the two directions $X_1 = X$ and $X_2 = Y$, $(N^a_X = N^a_Y)$. More specifically, both the horizontal and the vertical components of the displacement field $\mathbf{u}$ are interpolated using the shape functions of the type:

$$N^a = \frac{a_a + b_a X + c_a Y}{2\Delta} \tag{3.36}$$

where Δ is the area of the triangular element while the coefficients a_a, b_a and c_a depends only on nodal Lagrangian coordinates:

$$a_a = X_b Y_c - X_c Y_b \qquad b_a = Y_b - Y_c \qquad c_a = X_c - X_b \,. \tag{3.37}$$

Indices $[\cdot]_{a,b,c}$ refer to the three nodes belonging to the same element. The discrete defor-

mation gradient is then given by (in components):

$$F_{iJ} = \delta_{iJ} + \sum_{a}^{n} N_J^a u_i^a \,, \tag{3.38}$$

where $N_{,J}^a$ are the derivatives of nodal function N^a with respect to coordinate J. By replacing displacement $\mathbf{u}$ with the approximate interpolation of nodal values $\widehat{\mathbf{u}} = \sum_a^{n_n} \mathbf{N}^a \mathbf{u}^a$, we effectively replace (3.34) by the system of $n_n n_{dim}$ equations:

$$\frac{\partial \Pi}{\partial u_i^a} = \int_\Omega \frac{\partial \phi}{\partial F_{iJ}} \frac{\partial F_{iJ}}{\partial u_i^a} d\Omega = \int_\Omega P_{iJ}(\mathbf{F}) N_J^a d\Omega \,, \tag{3.39}$$

Note that only derivatives of the shape functions $\mathbf{N}$ enter the integral (3.39). Those depend only on nodal values $\mathbf{X}^a$ of the Lagrangian coordinates $\mathbf{X}$:

$$N_{,X}^a = \frac{Y_b - Y_c}{2\Delta} \,, \qquad N_{,Y}^a = \frac{X_c - X_b}{2\Delta} \,. \tag{3.40}$$

Therefore, all terms of the integrand can be extracted from under the integral making the integration of (3.39) straightforward ($\int_{\Omega_e} d\Omega = \Omega_e$).

Every time an out of balance displacement field is imposed on the boundaries $\partial\Omega$, the residual forces $\mathbf{f}^a$ appear at nodes:

$$f_i^a = -\frac{\partial \Pi}{\partial u_i^a} = -\int_\Omega P_{iJ}(\mathbf{F}) N_J^a d\Omega. \tag{3.41}$$

These forces need to be equated to zero in order to satisfy (3.39). Since these residual forces depend on the displacement field $\mathbf{u}$ through $\mathbf{P}$, the problem is non-linear and the minimization of $\Pi(\mathbf{u})$ requires an iterative procedure. Here we utilize the L-BFGS strategy (Limited-memory Broyden Fletcher Goldfarb Shanno algorithm) [LN89], which belongs to the family of the Newton-Raphson methods. More specifically, we integrated into our code the L-BFGS solver available with the dlib C++ library [Kin09]. This strategy allows one to converge to a local energy minimum even in the strongly non-convex case considered here.

The L-BFGS routine takes as an input the total energy of the system $\Pi = \int_\omega \phi(\widehat{\mathbf{u}}) d\Omega$ and the vector of nodal residual forces $\mathbf{f}$ whose components are given by (3.41). Then it evaluates an approximated form of the hessian matrix that is used in the construction of a tangent matrix $\mathbf{K}$. Finally, an iterative solution of the discrete system

$$\mathbf{K}^k \Delta \mathbf{u}^{k+1} - \mathbf{f}^k = 0 \,, \tag{3.42}$$

is attempted iterating on k for as long as the residual falls beyond the specified tolerance threshold. The resulting solution is a vector of nodal displacements $\mathbf{u}$ given by $\mathbf{u}^{k+1} = \mathbf{u}^k + \Delta \mathbf{u}^{k+1}$. An iterative system of the type (3.42) is solved for every applied

load increment.

We now summarize the implemented numerical procedure. For a given loading step, strain tensors $\mathbf{F}^e$ and $\mathbf{C}^e$ are evaluated in every element of the mesh. These tensors are assumed to represent the deformation of the underlying lattice basis $[\mathbf{e}_i]$. Then, Lagrange reduction procedure is applied element-wise thus allowing evaluation of the corresponding reduced basis $\bar{\mathbf{e}}_i$ and therefore of matrices $\mathbf{m}^e$ (using equation 2.5). Obviously, when $\mathbf{C}^e$ is located within fundamental domain D, Lagrange reduction gives simply $\mathbf{m}^e = \mathbf{I}$. Once $\mathbf{m}^e$ are found, the second Piola-Kirchhoff stress is evaluated using (3.29) and the first Piola-Kirchhoff is computed from it (3.12). In this way, all the elements for the calculation of the total energy $\Pi = \sum_e \int_{\Omega^e} \phi(\mathbf{C}^e)$ and of the vector of residual forces $\mathbf{f}$ (3.41) are in place and the iterative solution of (3.42) can be sought. The Cauchy stress tensor $\boldsymbol{\sigma}^e$ can be evaluated by post-processing the results obtained for $\mathbf{F}^e$ and $\mathbf{S}^e$ using relation (3.20).

3.5 Model Validation

Now that the strain energy and the associated boundary value problem have been formulated and implemented in a numerical code, we can perform some validation tests. One of the main advantages of the proposed model is in its capability to describe dislocations and their main interactions without the need of any phenomenological rules. To show that this is indeed the case, we discuss here some simple tests. We start by showing a single edge dislocation and discussing the corresponding stress field. We continue with two simple examples in which two edge dislocations are placed at close distance and allowed to interact. The observed interaction process is presented as a sequence of non-equilibrium states with evolution described by the minimization procedure which we interpret physically as an over-damped athermal dynamics.

3.5.1 Dislocation Core Sructure

To create a single dislocation in an otherwise perfect crystal, we prescribe a displacement field corresponding to Volterra for the edge dislocation (1.3), which we use as initial condition for the relaxation process under free boundary conditions. More specifically, the imposed displacement field is (see also [HL06])

$$u_x = \frac{b}{2\pi}\left[\arctan\frac{y}{x} + \frac{xy}{2(1-\nu)(x^2+y^2)}\right], \tag{3.43}$$

$$u_y = \frac{b}{2\pi}\left[\frac{1-2\nu}{4(1-\nu)}\ln(x^2+y^2) + \frac{x^2-y^2}{4(1-\nu)(x^2+y^2)}\right], \tag{3.44}$$

where b is the Burgers vector magnitude and ν the Poisson's ratio. This implemented displacement field corresponds to an edge dislocation centered at point $X = Y = 0$, and

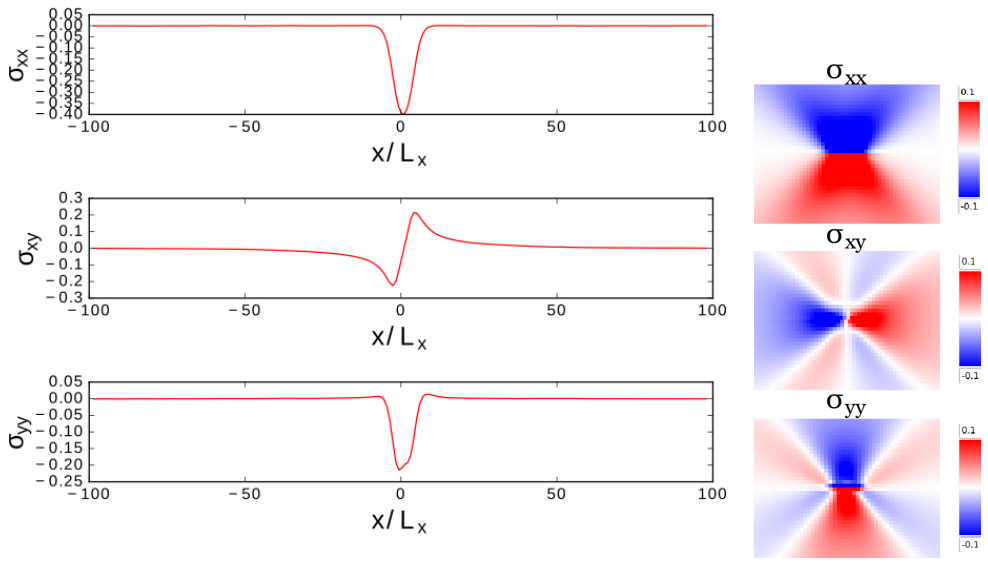

Figure 3.4: **Dislocation Stress Field in the Square Lattice:** On the left: Cauchy stresses along an horizontal middle section of the analyzed domain. On the right: stress fields corresponding to the three stress components σ_{xx}, σ_{xy} and σ_{yy} (values showed are in between -0.1 and 0.1.)

we choose an unit Burgers vector aligned with the X direction.

We now discuss the results obtained for a square domain with $N = 200 \times 200$ nodes, however, the obtained solution does not depend significantly on the domain size, provided that we have enough elements to resolve the dislocation core (the lower limit is $N \approx 10$). The resulting equilibrium solution indeed corresponds to a single edge dislocation in the middle of the domain with a step appearing in the left side of the crystal (see also Figure 3.5).

In Figure 3.4 we illustrate the obtained Cauchy stress field along the horizontal section in the middle of the domain and stress contours near the dislocation core. Note the qualitative agreement with the solution of Volterra illustrated in Chapter 1. However, now the dislocation core is resolved. Clearly, the finer is the discretization, the narrower will be the obtained dislocation core.

In Figure 3.5 we show how the metric tensors of the finite elements composing the discretized domain are arranged on Poincaré disk representing the configurational space C_{11}, C_{22} and C_{12}. Clearly, the two energy wells S and S_0^{+1} are involved simultaneously and elements in between, distributed along the low-energy valley, actually form the dislocation core. On the same figure, we illustrate the full domain, showing the Cauchy stress σ_{xy} profiles, and a detail of the element triangulation inside the dislocation core.

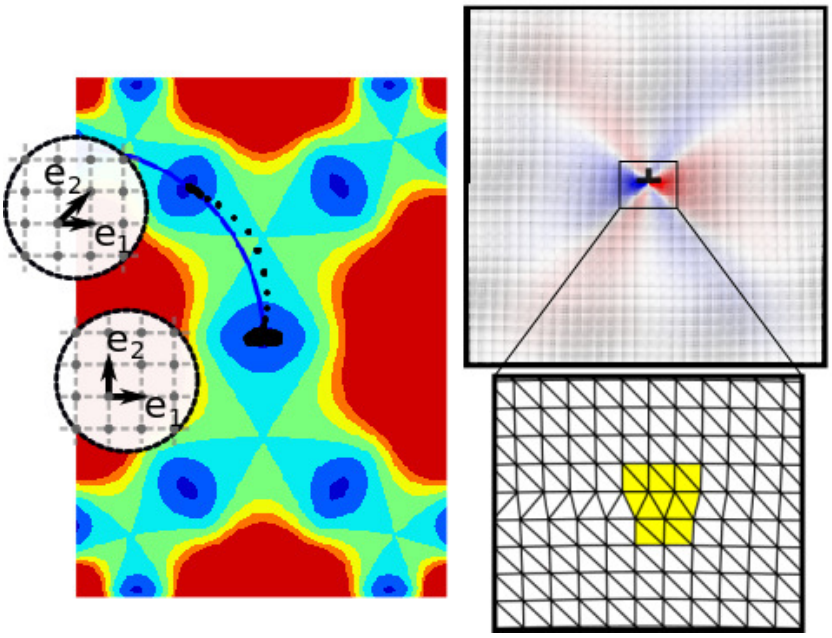

Figure 3.5: **Dislocation Structure in the Square Lattice:** On the left: distribution of metrics associated with discrete elements on configurational space C_{11}, C_{22}, C_{12}, with evidence on engaged wells S and S_0^{+1}. On the right: A picture of the full domain is showed along with a detail of the triangulation in correspondence of the dislocation core, showing the presence of sheared element configurations.

The same test was performed for the triangular lattice. In this case the value of the Burgers vector magnitude b in the initial displacement field equals the triangular lattice spacing γ. Equilibrium solution is, as in the square lattice case, given by a single dislocation centered in the middle of the domain with an extra step appearing in the left surface of the crystal. Stress profiles are also in qualitative agreement with linear elastic solution (1.3), even if the core structure is somehow different of what was observed in the case of the square crystal, most prominently the computed stress peak values are lower.

In Figure 3.7 we show the corresponding distribution of the values of the metric tensor in configurational space, with the clear evidence of the engagement of two energy wells $\mathbf{T}$ and $\mathbf{T}_0^{+1}$. Elements forming the the dislocation core are well aligned with the $\theta = 0°$ shear trajectory. In Figure 3.7 we illustrate a detail of the grid triangulation around the dislocation core.

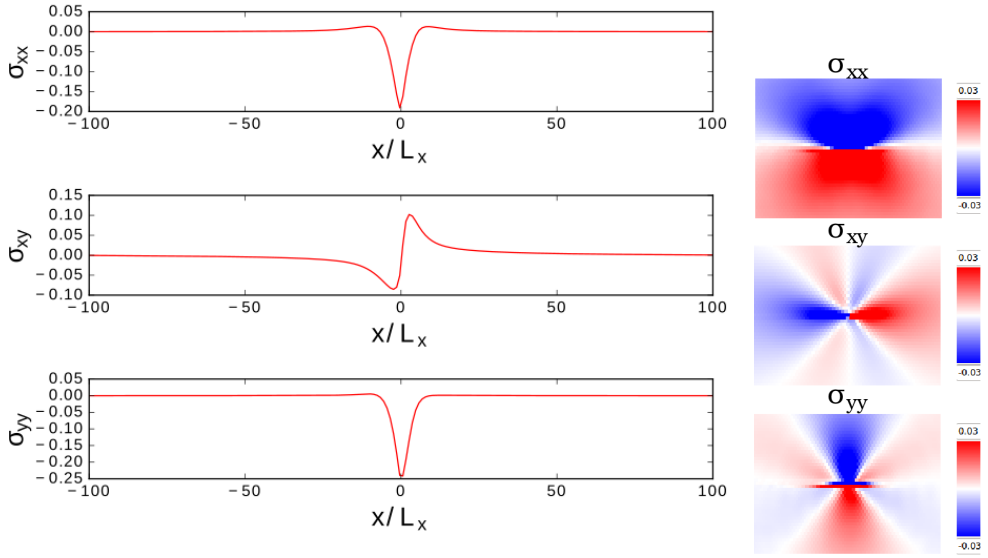

Figure 3.6: **Dislocation Stress Field in the Triangular Lattice:** On the left: Cauchy stresses along an horizontal middle section of the analyzed domain. On the right: stress fields corresponding to the three stress components σ_{xx}, σ_{xy} and σ_{yy} (values showed are in between -0.03 and 0.03).

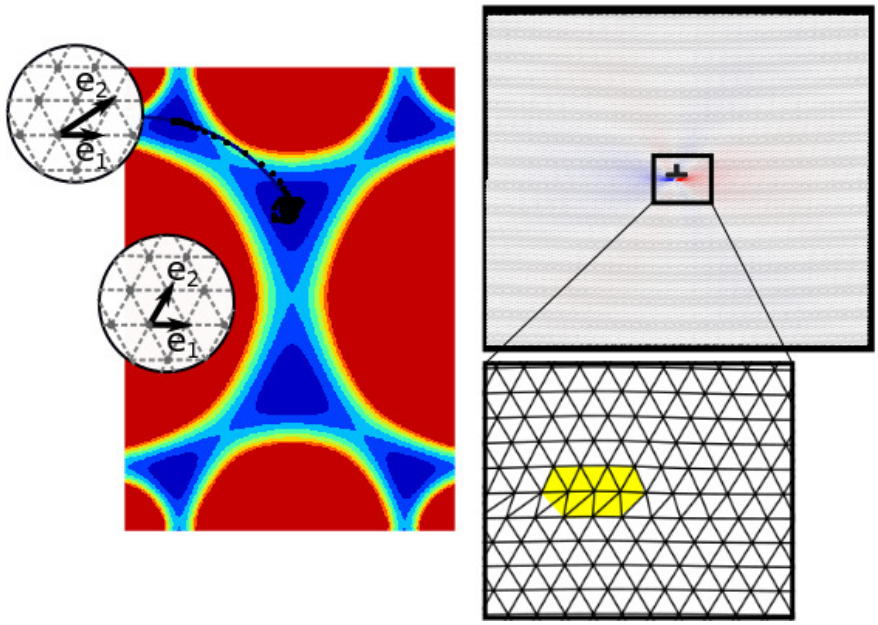

Figure 3.7: **Dislocation Structure in the Triangular Lattice:** On the left: finite element distribution on configurational space C_{11}, C_{22}, C_{12} with evidence on engaged wells T and T_0^{+1}. On the right: A picture of the full domain is showed along with a detail of the triangulation in correspondence of the dislocation core, showing the presence of sheared element configurations.

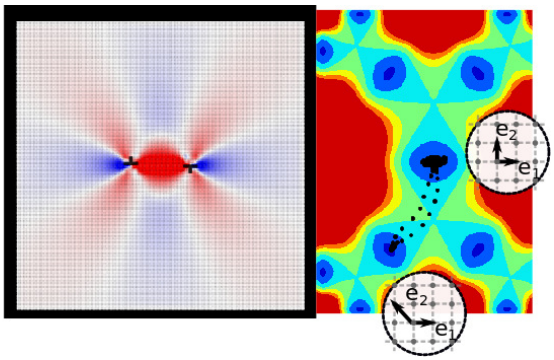

Figure 3.8: **Dislocation Annihilation:** Initial configuration imposed to the system which ends with annihilation of the two dislocations of opposite sign. On the left, we show the analyzed domain with colors corresponding to the Cauchy stress σ_{xy} field. On the right, the elements distribution in the configurational space is shown.

3.5.2 Dislocation Interactions

We now discuss two simple examples of dislocation interactions. In a first example, two edge dislocations of opposite sign are introduced in the domain with a relatively small distance between each other. In the second example, we consider an analogous configuration but in which dislocations have the same sign. In the first example, dislocations attract each other up to a point at which the two cores merge, thus restoring the perfect crystal configuration. In the second example the two cores repel up to a point when the two dislocations become lattice trapped. The first example is of particular importance as annihilation is a typical example of short-range interaction, which in our model is accounted for automatically. We recall that the initial configurations are not static equilibria and that the observed "dynamics" corresponds to minimization steps of the L-BFGS algorithm. In both examples we used a regular $N = 200 \times 200$ grid.

In Figure 3.8 we show the initial configuration in the annihilation test, characterized by the presence of a dislocation dipole involving energy wells $\mathbf{S}_0^{-1}$ and $\mathbf{S}$. Due to the reciprocal attraction between the two dislocations, this initial configuration is out of equilibrium. Dislocations are observed to approach towards each other up to the point in which the two cores annihilate restoring a perfect crystal which is the final equilibrium state. In Figure 3.9 we illustrate different phases of this process in terms of Cauchy stress σ_{xy} profiles and show the corresponding element distribution in the configurational space. As the two dislocations approach each other, elements migrate gradually from $\mathbf{S}_0^{-1}$ to the neighboring well $\mathbf{S}$. In the final configuration all the elements are centered in point $\mathbf{S}$, and we recover a perfect crystal.

In the second example the two dislocations repel each other. They are observed to migrate in the direction of the external boundaries up to the point in which they reach

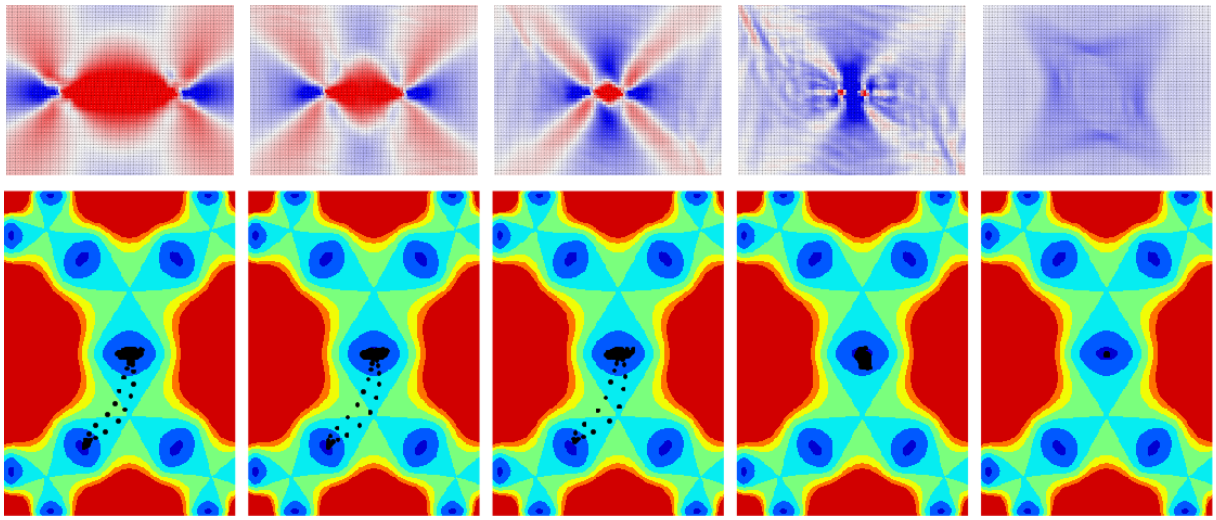

Figure 3.9: **Dislocation Annihilation Process:** Some steps of the minimization procedure are shown, in correspondence of which the gradual approaching of dislocations is observed, up to the point in which the two dislocations annihilate originating a perfect crystal. On the top, Cauchy stress σ_{xy} field is shown, along with the corresponding elements distribution in the configurational space (on bottom).

an equilibrium. In Figure 3.10 we illustrate the initial and final configurations in terms of Cauchy stress σ_{xy} contours and show the element distribution in the configurational space.

These examples are simple, however they allow us to illustrate the inner working of the proposed model. Despite the fact that we are dealing with a local formulation, our examples show that the model can effectively describe the main features of dislocation interaction.

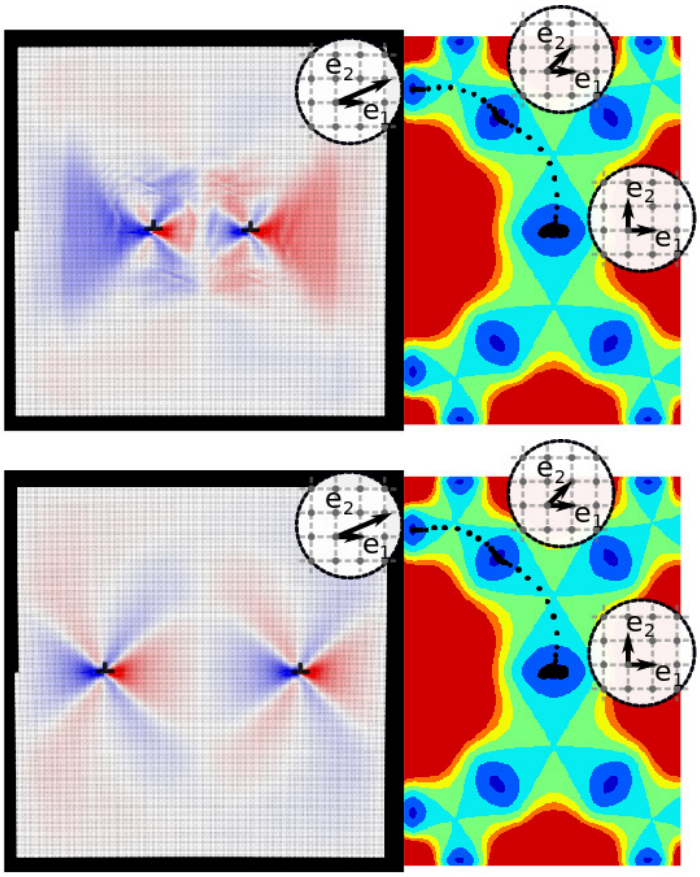

Figure 3.10: **Initial (top) Configuration and Final Equilibrium State (bottom) for the Case of the Two Dislocations of the Same Sign.** The two dislocation repel each other up to an equilibrium distance in which attractive and repulsive forces are balanced. In this case the engaged wells are $\mathbf{S}$, $\mathbf{S}_0^{+1}$ and $\mathbf{S}_0^{+2}$. Some readjustments of the elements occupying the low-energy valleys between the wells is observed between initial and final configuration.

Chapter 4

Homogeneous Nucleation

As a proof of principle, we apply the proposed model to the study of nucleation of dislocations in a perfect crystal, also called *homogeneous nucleation of dislocations*. The homogeneous, defectless crystal is loaded quasi-statically up to a critical load for which it becomes unstable. This loss of stability drives the evolution of the crystal towards a new equilibrium configuration in which crystalline defects are present. We study systematically this elastic instability and the ensuing defect patterns. Our particular focus is on the role of crystal symmetry (square and triangular crystals) and of crystal orientation inside the loading device. Before performing simulations, we characterized analytically the stability condition for the system, thus obtaining reference values for the critical loads and the related unstable modes. The presence of an analytical criterion will allow us to better interpret the obtained numerical results.

Despite the fact that defect-free crystals are uncommon in nature, the study of homogeneous nucleation phenomena has become more important with the increasing miniaturization of technological devices, containing only very few initial dislocations. Homogeneous dislocation nucleation under mechanical probing tests, such as nanoindentation, has been widely investigated with both experiments [dlFZG$^+$02, GVVS01] and simulations [ZLVV$^+$04, MR08, GM16]. This phenomena plays a fundamental role also in different experimental conditions, such as, for instance, the homogeneous compression of nano-pillars [RNS07]. Moreover, dislocations have been observed to nucleate homogeneously also at the interior of grains in polycrystals [GO08]. Here we are more interested in a theoretical investigation of the homogeneous nucleation phenomena, which allows one to identify and characterize various relevant mechanisms in a fundamental manner.

We begin with the theory leading to the Legendre-Hadamard stability condition [Had03], which was used, for instance, by Hill in his analysis of stability of crystals [Hil58, Hil62]. Then, we will discuss our numerical results obtained for square and triangular crystals,

dedicating a subsection to each crystal symmetry. We start with the analytical predictions for the bifurcation point and then present the study of the post-bifurcation behavior in detail. In this Chapter we limit our analysis to the case of the polynomial energy (2.27), while the following Chapter we will study the same physical phenomenon using the pair-potential based energy.

4.1 Stability Criterion

It is known that the solution of the problem (3.13-3.15) with displacements controlled at the whole boundary is stable with respect to small perturbations as long as the energy function ϕ is strongly elliptic [Hil62, Ogd97]. Consider a homogeneous, slowly increasing deformation described by the deformation gradient $\mathbf{F}$. Along the loading path, the corresponding energy $\phi(\mathbf{F})$ will be strongly elliptic up to a certain critical value of the imposed load $\mathbf{F}^c$. This value is a bifurcation point in the solution path and for $\mathbf{F} > \mathbf{F}^c$ the homogeneous solution will cease to be stable. The strong ellipticity condition can be formulated in terms of the *acoustic tensor* $\mathbf{Q}$, defined by the condition:

$$\mathcal{Q}_{ik}(N) = N_J \mathcal{A}_{iJkL} N_L \,, \tag{4.1}$$

where $\mathbf{N}$ is an arbitrary unit vector in the Lagrangian configuration and $\mathcal{A}_{iJkL}$ the linearized elastic moduli (3.19).

Tensor Q_{ik} is called acoustic tensor since it is related to the propagation infinitesimal waves superimposed on a finite deformation [Eri53]. We recall that, since stability can be understood by studying the system's response to a perturbation, the theory of infinitesimal waves and stability analysis of the incremental boundary problem are closely connected (see for instance section 6.4 of [Ogd97]).
The strong ellipticity condition is then expressed as:

$$Q_{ik}(\mathbf{N}) m_i m_k > 0 \,, \tag{4.2}$$

with $\mathbf{m}$ being an arbitrary unit vector in the Eulerian configuration. Stability of the solution is lost when the inequality (4.2) is no longer strict, with equality emerging for some non-trivial $\mathbf{N}$ and $\mathbf{m}$.
Consider the incremental version of equilibrium equation (3.13) (with no body forces):

$$(\mathcal{A}_{iJkL} \dot{u}_{k,L})_{,J} = 0 \,, \tag{4.3}$$

The analogy with the theory of infinitesimal waves becomes apparent when we consider the dynamic counterpart of (4.3):

$$(\mathcal{A}_{iJkL} \dot{u}_{k,L})_{,J} = \varrho \frac{\partial^2 \dot{u}_i}{\partial t^2} \,, \tag{4.4}$$

and take as incremental displacement $\mathbf{u}$ a form of a plane wave

$$\mathbf{u} = \mathbf{m} f(\mathbf{N} \cdot \mathbf{X} - ct)\,, \tag{4.5}$$

where unit vectors $\mathbf{N}$ and $\mathbf{m}$ are, respectively, the wave direction and the wave polarization, f is a double differentiable function and c represents the wave velocity. By substituting (4.5) in (4.4) we obtains:

$$Q_{ik}(\mathbf{N}) m_k = \mathcal{A}_{iJkL} N_J N_L m_k = \varrho c^2 m_i\,, \tag{4.6}$$

which is known as the propagation condition. As long as $\mathbf{Q}$ is positive definite (i.e. as long as the incremental equations are strongly elliptic) the eigenproblem (4.6) has two real eigenvalues (three in the three-dimensional case) corresponding to a longitudinal and a transversal wave [Hil62]. Instead, when $\mathbf{Q}$ is positive semi-definite, equation (4.6) admits solution with $c = 0$ for some non-zero $\mathbf{N}$ and $\mathbf{m}$, thus implying the existence of a stationary wave, and therefore an incipient instability. When (4.6) admits negative eigenvalues, the homogeneous configuration is unstable. This indicates the emergence of a new equilibrium and implies inhomogeneity and pattern formation.

The direction $\mathbf{N}$ and the polarization $\mathbf{m}$ of the corresponding wave can be interpreted as the characteristics of the nucleated defects. Indeed, the same acoustic tensor based instability criterion is used for the prediction of shear bands [Ric76], with the Eulerian counterpart $\mathbf{n}$ of $\mathbf{N}$ being the normal to the plane in which the shear band develops.

In our mesoscopic setting, if $\mathbf{n}$ turns out to be approximately perpendicular to $\mathbf{m}$, we expect the nucleating defects to be dislocations with slip plane normal to $\mathbf{n}$ and Burgers vector aligned with $\mathbf{m}$.

For hyperelastic materials condition (4.4) implies:

$$\det(\mathcal{Q}(\mathbf{N})) \geqq 0\,. \tag{4.7}$$

It is possible to reformulate this condition in a way that the associated wave direction and polarization are both in the Eulerian configuration. Consider the Eulerian moduli a_{ijkl} obtained from $\mathcal{A}_{iJkL}$ applying the push-forward operator (already mentioned in Chapter 3):

$$\mathsf{a}_{ijkl} = F_{jR} F_{lS} \mathcal{A}_{iRkS}\,, \tag{4.8}$$

The expression in the Eulerian configuration for the acoustic tensor q_{ik} is then:

$$q_{ik} = n_j n_k \mathsf{a}_{ijkl}\,, \tag{4.9}$$

which leads to a fully Eulerian formulation of the stability criterion:

$$\det(q(\mathbf{n})) \geqq 0\,. \tag{4.10}$$

That is the condition that we will be using in what follows.

Since the energy density ϕ is defined directly in terms of $\mathbf{C}$, it is convenient to compute acoustic tensor $\mathcal{A}_{iJkL} = \frac{\partial^2 \phi}{\partial F_{iJ} \partial F_{kL}}$ (or $\mathtt{a}_{ijkl}$) in terms of $\mathcal{C}_{IJKL} = 2\rho_0 \frac{\partial \phi^2}{\partial C_{IJ} \partial C_{KL}}$. This is done by the relation:

$$\mathcal{A}_{iJkL} = 2\mathcal{C}_{RJSL} F_{kR} F_{iS} + S_{JL}\delta_{ik}\,. \tag{4.11}$$

Moreover, in the computation of (4.2), one has to take in consideration the relations (3.29-3.30). The expression of the acoustic tensor in terms of the reference energy ϕ_0 takes the following form:

$$\mathcal{Q}_{ik} = N_J N_L (4 m_{XW} m_{JU} m_{YR} m_{LS} \tfrac{\partial^2 \phi_0}{\partial \widetilde{C}_{RS} \widetilde{C}_{WU}} F_{kY} F_{iX} + \delta_{ik} 2 m_{JO} m_{LZ} \tfrac{\partial \phi_0}{\partial \widetilde{C}_{0Z}})\,. \tag{4.12}$$

The use of condition (4.7) in continuum elasticity is rather common [Big12], however it has been also used to predict nucleation of microscale defects (see for instance the "Λ *criterion*" proposed in [VVLZ$^+$03, ZLVV$^+$04, ZZ08]). The adequacy of this criterion to characterize microscale instabilities is still debated. In [MR08] the authors contest its validity for prediction of dislocation nucleation under nanoindentation, a situation characterized by a strongly heterogeneous strain field. This statement is partly confuted in [GM16], where the authors found this criterion adequate for the analysis of nucleation under nanoindentation. In our work the use of this criterion is fully justified as we are studying instability of an homogeneously deformed body loaded in a hard device.

4.2 Square Lattice

In this Section, we report the homogeneous nucleation results obtained for the square lattice, which is simulated numerically using the polynomial energy (2.27). First, we discuss the analytical results obtained from the stability analysis, with focus on the value of the critical load α_c and the related orientation $\mathbf{n}$. Then, we discuss the post-bifurcation patterns obtained through numerical minimization of the energy functional (3.16).

4.2.1 Stability analysis

Starting from the undeformed configuration, we used condition (4.10) to identify the domain in the configurational space where the strong ellipticity holds. Within this region, the crystal can deform homogeneously and elastically, however, as soon as the equality in (4.10) can be achieved for some non trivial $\mathbf{n}$, the homogeneous state becomes unstable and defects begin to appear within the crystal. To study the onset of instability in the perfect crystal, we look for the points in configurational space for which the equality $\det q_{ik} = 0$ holds, which distinguish the boundary of homogeneous, elastic regime. With some semantic freedom, we will refer to the surface identified in this way as the *yield surface*.

To find the points belonging to the yield surface, we considered different simple shear deformations of type (2.28) and identified the first value of the loading parameter $\alpha = \alpha_c$ for which the condition $\det q_{ik} = 0$ is satisfied (the bifurcation point). This special state corresponds to a point in the configurational space as we illustrate in Figure 4.2. By spanning the configurational space with many simple shear trajectories, we find a set of bifurcation points and the yield surface is then obtained by interpolation. The points in which the yield surface intersects the boundaries of the fundamental domain are of particular interest, and therefore we considered explicitly also the fat rhombic (2.31) and the rectangular (2.32) pure shears.

The obtained yield surface is illustrated in In Figure 4.2. Observe that the lowest value of α_c corresponds to the case when the energy barrier is the lowest. The corresponding path is the rhombic pure shear, and $\alpha_c = 0.132$. This value increases continuously as we move to the rectangular pure shear, corresponding to the highest energy barrier, where the associated critical load is $\alpha_c = 0.499$. The form of the yield surface is therefore elongated as illustrated in Figure 4.2.

We performed such stability analysis along five different loading paths. These are the two pure shears which, starting from point **S**, travel along the boundary of fundamental domain D (rhombic and rectangular), and three simple shears, with inclinations $\theta = 0°$, $\arctan(\frac{1}{2})$, and $45°$, see (2.30). As we have already remarked, the two pure shears are important as they correspond to two extremal responses of the system. The other paths are representative of three different ways of spanning the energy landscape with a simple shear (see also the corresponding energy landscape in Figure 2.8 of Chapter 2). In Figure 4.2) we show all the analyzed paths on configurational space. They are all characterized by different values of the critical load α_c.

For all these paths, we evaluated the corresponding unstable directions $\mathbf{n}$. Then, solving the eigenproblem (4.6), we obtained the corresponding polarization vectors $\mathbf{m}$, which are always almost perpendicular to $\mathbf{n}$. This suggests that instability will develop with the nucleation of dislocations along the slip plane $\mathbf{n}^{\perp}$, in analogy with the shear-band type instability in a purely continuum problem.

By associating with each unstable mode a unit vector $\mathbf{n} = (\cos\xi, \sin\xi)^T$ we can show the $\det q_{ik}$ profiles as a function of the instability angle ξ, which characterizes the orientation of $\mathbf{n}$ with respect to the reference horizontal axis X. In Figure 4.3 we show such graphs for the rhombic and rectangular paths, while in Figure 4.4 we show the analogous graphs for our three simple shears. In each case, we show two profiles corresponding to the beginning of the loading path ($\alpha = 0.001$) and to the critical load $\alpha = \alpha_c$, where the equality in (4.10) is first reached for some $\mathbf{n}$.

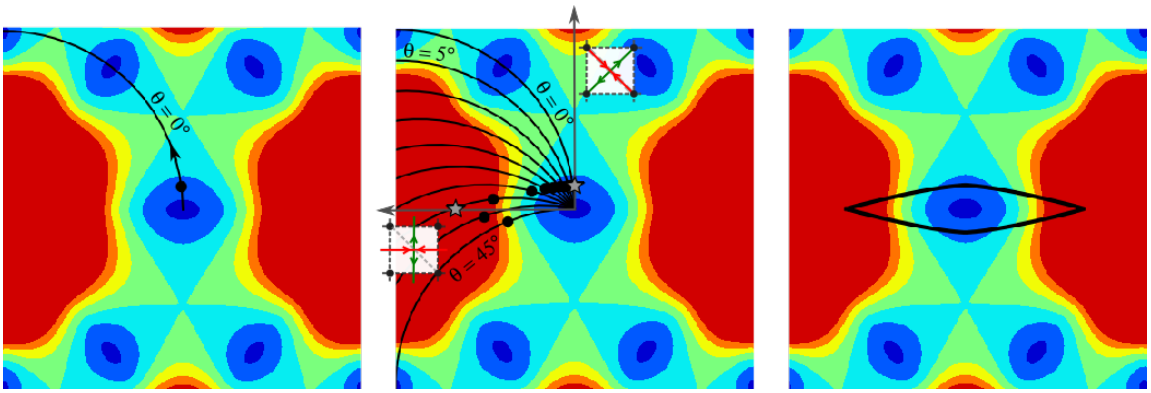

(a) (b) (c)

Figure 4.1: **Yield Surface for the Square Lattice:** a) Simple shear trajectory $\theta = 0°$ is shown, with evidence on the point in which the bifurcation appears. b) Bifurcation points, drawing the yield surface, are showed for different simple shears in which the angle θ is progressively increased of 5°. We show also the bifurcation points corresponding to the fat rhombic and rectangular pure shears (grey stars). c) The yield surface, obtained by interpolation of bifurcation point, is shown.

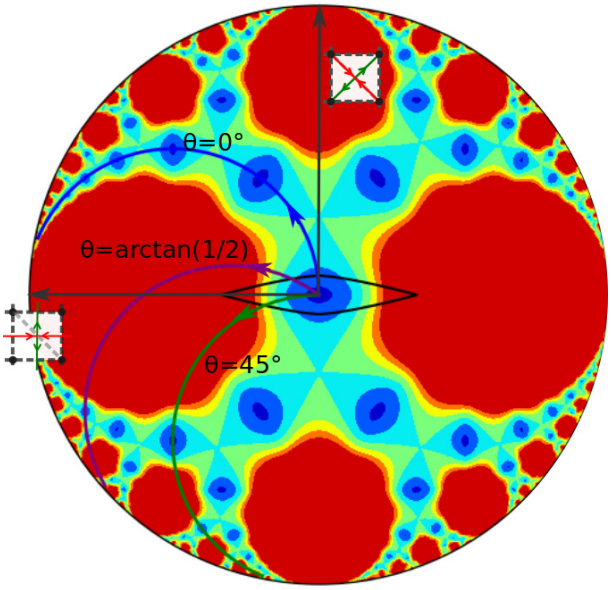

Figure 4.2: **Analyzed Shear Paths on the Configurational Space:** Two pure shears, the rectangular and the rhombic paths coinciding with boundaries of D, and the three simple shears $\theta = 0°$, $\arctan(\frac{1}{2})$, and 45° are analyzed.

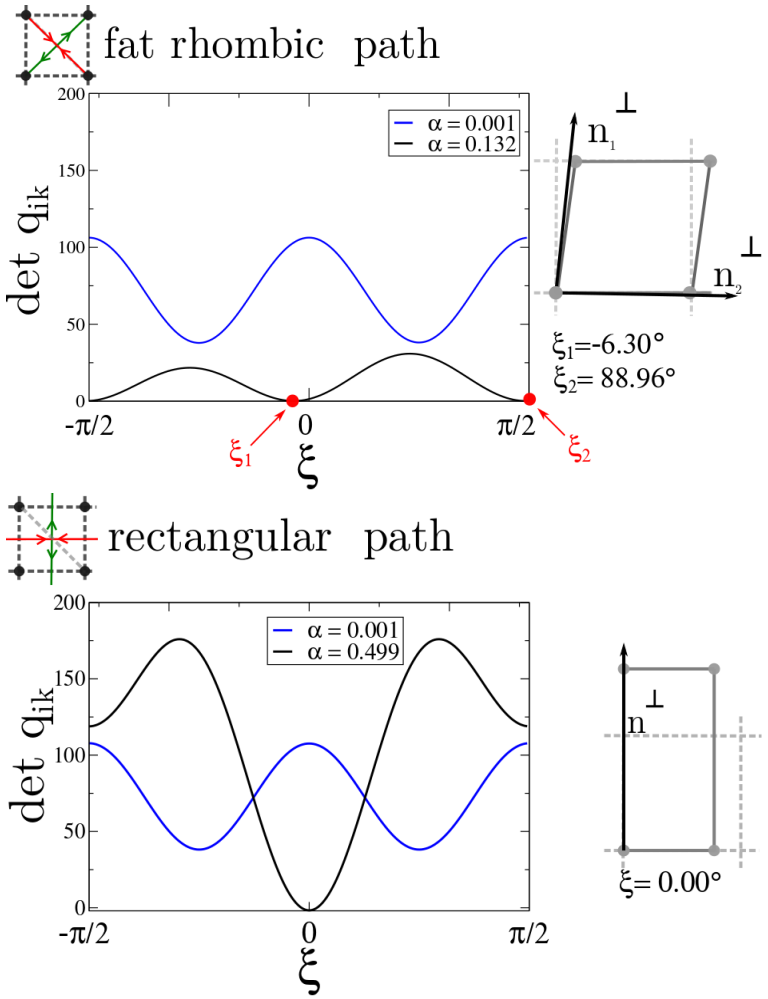

Figure 4.3: $\det q_{ik}$ **Profiles along the Fat Rhombic and the Rectangular Paths**: Evidence on load α_c for which equality in (4.10) is satisfied. The fat rhombic pure shear (on top) shows the simultaneous appearence of two instability directions while just one appears in case of the rhombic path (on bottom). On the side of each graph we show the orientation of wave direction $\mathbf{n}^{\perp}$ with respect of the deformed lattice cell at $\alpha = \alpha_c$.

In the case of the fat rhombic pure shear path (Figure 4.3) we observe the simultaneous appearance of two unstable modes $\mathbf{n}_1(\xi_1)$ and $\mathbf{n}_1(\xi_2)$. Angles ξ_i are respectively $\xi_1 = -6.3°$ and $\xi_2 = 88.74°$. Then, the associated directions $\mathbf{n}_1^\perp$ and $\mathbf{n}_2^\perp$ are almost aligned with the vectors of the lattice cell in the Eulerian configuration at $\alpha = \alpha_c$, inclined respectively by $0.00° \approx \xi_2^\perp$ and $82.40° \approx \xi_1^\perp$ with respect of $\mathbf{X}$ axis (see Figure 4.3). This means that both these two slip directions are likely to be activated and we expect dislocations to nucleate simultaneously along $\mathbf{e}_1$ and $\mathbf{e}_2$.

This simultaneous appearance of the two unstable modes $\mathbf{n}$ is quite remarkable. Indeed, while the appearance of dislocations along $\mathbf{e}_1$ is suggested by the direction of the applied load, the coupling with $\mathbf{e}_2$ is counterintuitive. This coupling is due to the peculiar nature of the saddle point $\mathbf{T}$, already discussed in Chapter 2 (see also Figure 2.9). This will be explained more clearly in the next subsection.

Along the rectangular pure shear path, only one instability direction $\mathbf{n} = (\cos\xi, \sin\xi)^T$ can be activated, with the angle $\xi = 0.00°$. Despite $\mathbf{n}^\perp$ being perfectly aligned with the stretched direction $\mathbf{e}_2$ this instability does not result in the activation of the corresponding slip system, as we are going to see below.

Graphs obtained for the three simple shear paths show behaviors that are in between these two cases. The results of the stability analysis for the simple shear path $\theta = 0°$ are very similar to those of the fat rhombic path, with two unstable modes appearing almost simultaneously at $\alpha_{c\,1} = 0.132$ and $\alpha_{c\,2} = 0.133$. Even in this case, the corresponding unstable modes are approximately aligned with the deformed lattice directions, with $\xi_1^{0°} = -6.03°$, $\xi_2^{0°} = 88.96°$ and current $\mathbf{e_1}$, $\mathbf{e_2}$ inclined by $0.00° \approx \xi_2^{0°\perp}$ and $82.50° \approx \xi_2^{0°\perp}$ respectively.

Instead, for higher values of θ, one observes the predominance of a single unstable mode, with $\xi^{26°} = -3.69°$ and $\xi^{45°} = -14.85°$. The corresponding direction $\mathbf{n}^\perp$ is close to the sheared vertical lattice vector $\mathbf{e}_2$, with a misaligment of about 5° for both $\theta = 26°$ and the $\theta = 45°$ shear paths.

These observations suggest a strong dependence of the post-instability pattern on the loading path, i.e. the orientation of the crystal with respect to loading device. For the paths which evolve in the low energy basin identified by square point $\mathbf{S}$ and triangular point $\mathbf{T}$, instability occurs at relatively low values of the load α. Moreover, two unstable modes appear almost simultaneously suggesting the simultaneous activation of the two plastic mechanisms corresponding to the two low energy valleys associated with $\theta = 0°$ and $\theta = 90°$ simple shears. Instead, paths evolving through higher energy barriers are characterized by higher values of α_c, instability takes place at higher values of energy density ϕ and the associated unstable mode is not aligned with any of the lattice directions.

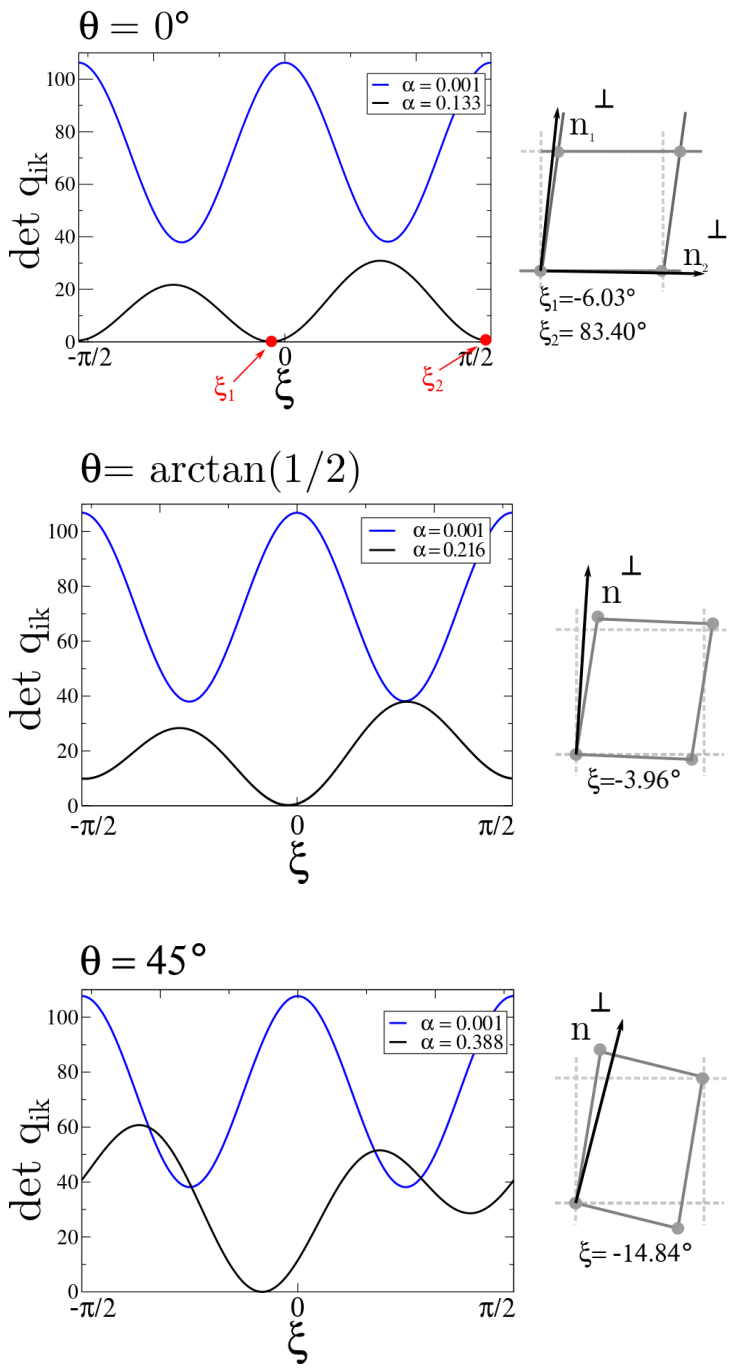

Figure 4.4: $\det q_{ik}$ **Profiles for the Simple Shears** $\theta = 0°$, $\arctan(\frac{1}{2})$, $45°$**:** Evidence on critical load $\alpha = \alpha_c$. Lattice configurations corresponding to $\alpha = \alpha_c$ and associated unstable modes $\mathbf{n}^{\perp}$ are also shown.

4.2.2 Simulations Results

Simulations were performed by loading the system quasi-statically. The system is assumed to evolve slowly through a series of equilibrium configurations, each characterized by a slightly different load. Therefore, dynamic effects can be neglected and the quasi-static problem (3.13-3.15) needs to be solved for each of the applied load steps. Evolution of the system is followed until the value of loading parameter for which stability is lost.

We refer to the numerical counterpart of analytical value α_c as α_c^*. Stability loss manifests itself through a sudden drop in the average stress and the appearance of an inhomogeneous configuration of defects. The emergence of complexity can be also observed in configurational space. Indeed, by assigning a point in the configurational space to the metric $\mathbf{C}^e$ of every individual finite element of the discretization, we observe a perfect overlap for $\alpha < \alpha_c^*$. However, when stability is lost, the homogeneous configuration breaks down and points spread in configurational space, reaching different energy wells (see Figure 4.5). In what follows, we will always associate with the observed patterns the corresponding configuration in the space of metric tensors $\mathbf{C}$, as in Figure 4.5.

In order to ensure independence of the system size, we performed the simulations considering different numbers of nodes, ranging from 10^4 to 10^6. We also used different boundary conditions, experimenting with both fixed and periodic conditions[1]. No significant dependence on these factors was identified in the performed simulations, and the presented results have to be considered robust. The loading step, however, has to be selected with some care. We first loaded the system with a load step of 10^{-3} to ensure an overall agreement between the numerical value α_c^* and the α_c evaluated theoretically. In a second set of tests, we refined the load step to 10^{-4} in the proximity of the critical value of α to capture in more detail the nucleation phenomenon.

For all the considered paths, an excellent agreement between the numerical value α_c^* corresponding to the first instability and the theoretical value of α_c was observed (see Figure 4.6). Connection of the obtained patterns with the evaluated unstable modes $\mathbf{n}$ is more straightforward along some paths than others, as we show below. We begin the discussion with the two pure shear paths. They are particularly revealing as they represent two extremal system responses and they evolve along highly symmetric directions in the

[1]In order to apply periodic boundary conditions, we assign as neighbor to each boundary node the corresponding node on the opposite side. Positions of these periodic neighbors are then adjusted, keeping in mind that they have to be translated by the domain dimension deformed accordingly with the imposed deformation gradient $\mathbf{F}$. In correspondence of every loading step, boundary nodes are moved in agreement with the imposed deformation gradient, but are then let free to relax.

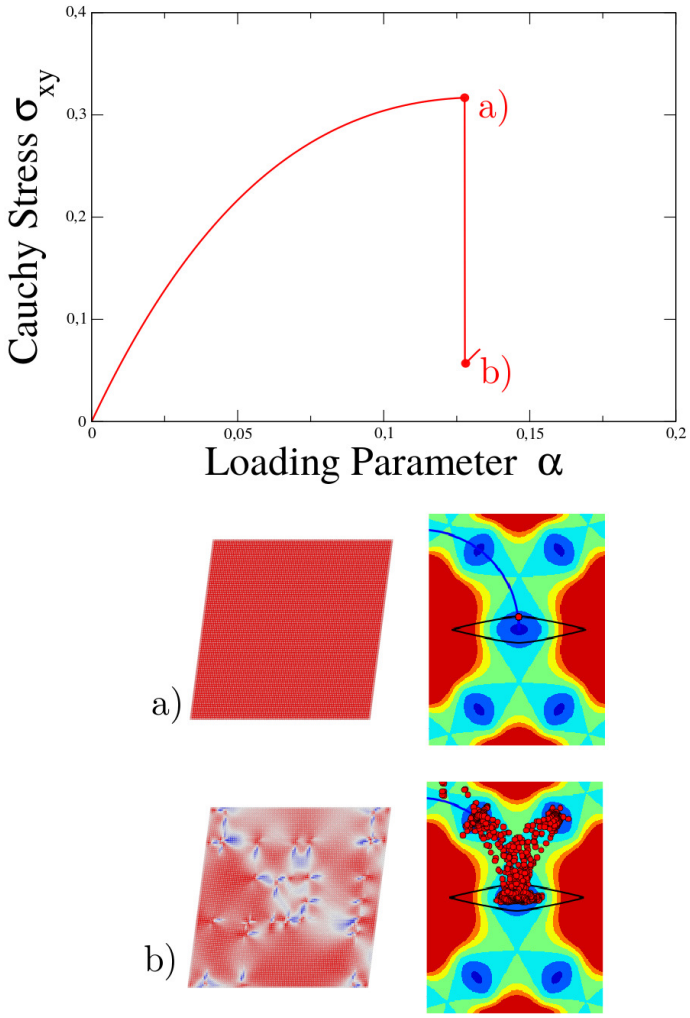

Figure 4.5: **Homogeneous Nucleation:** In this picture, a perfect crystal with fixed boundary conditions is loaded quasistatically up to load value α at which stability of the homogeneous configurations is lost. System deforms homogeneously up to point a), and all the elements are mapped on a single point on configurational space. In the post instability equilibrium, point b), the system show patterning and more than one wells are occupied on configurational space.

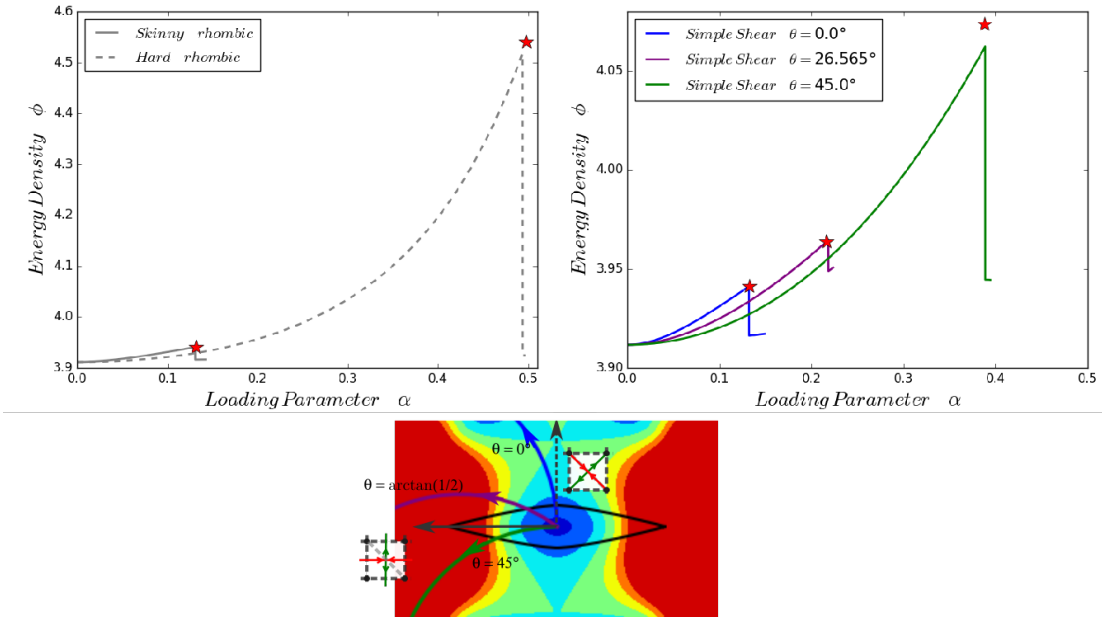

Figure 4.6: **Energy Density up to Nucleation:** Evolution of energy density ϕ along the four considered paths. On the left: the fat rhombic and the rectangular pure shears. On the right: The three simple shears $\theta = 0°, \arctan(\frac{1}{2})$, and $45°$. A good agreement between the analytic value α_c and the numerical α_c^* is observed in all these loading directions. The showed data were obtained from a $N = 10^4$ simulation.

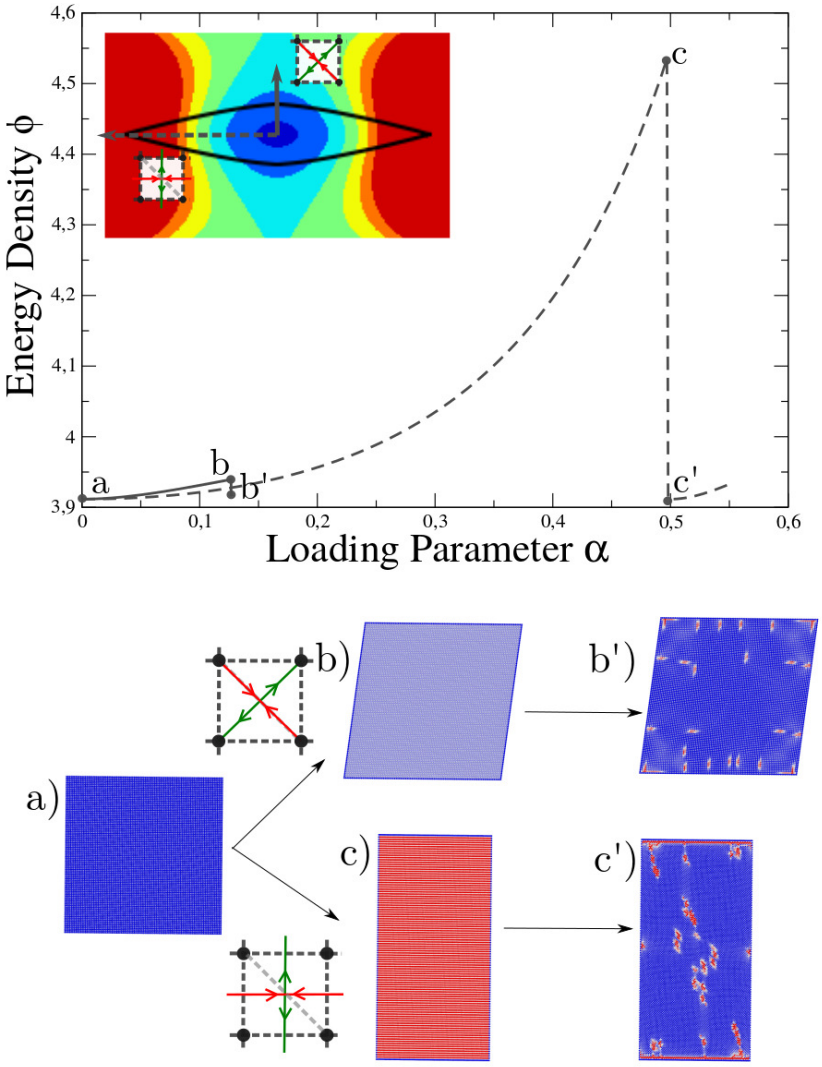

Figure 4.7: **Homogeneous Nucleation along the two Pure Shears:** These loading paths respectively the paths for which instability happens at lowest and higher value of loading parameter α. These two "extremal" paths are representative of two different mechanisms of nucleation.

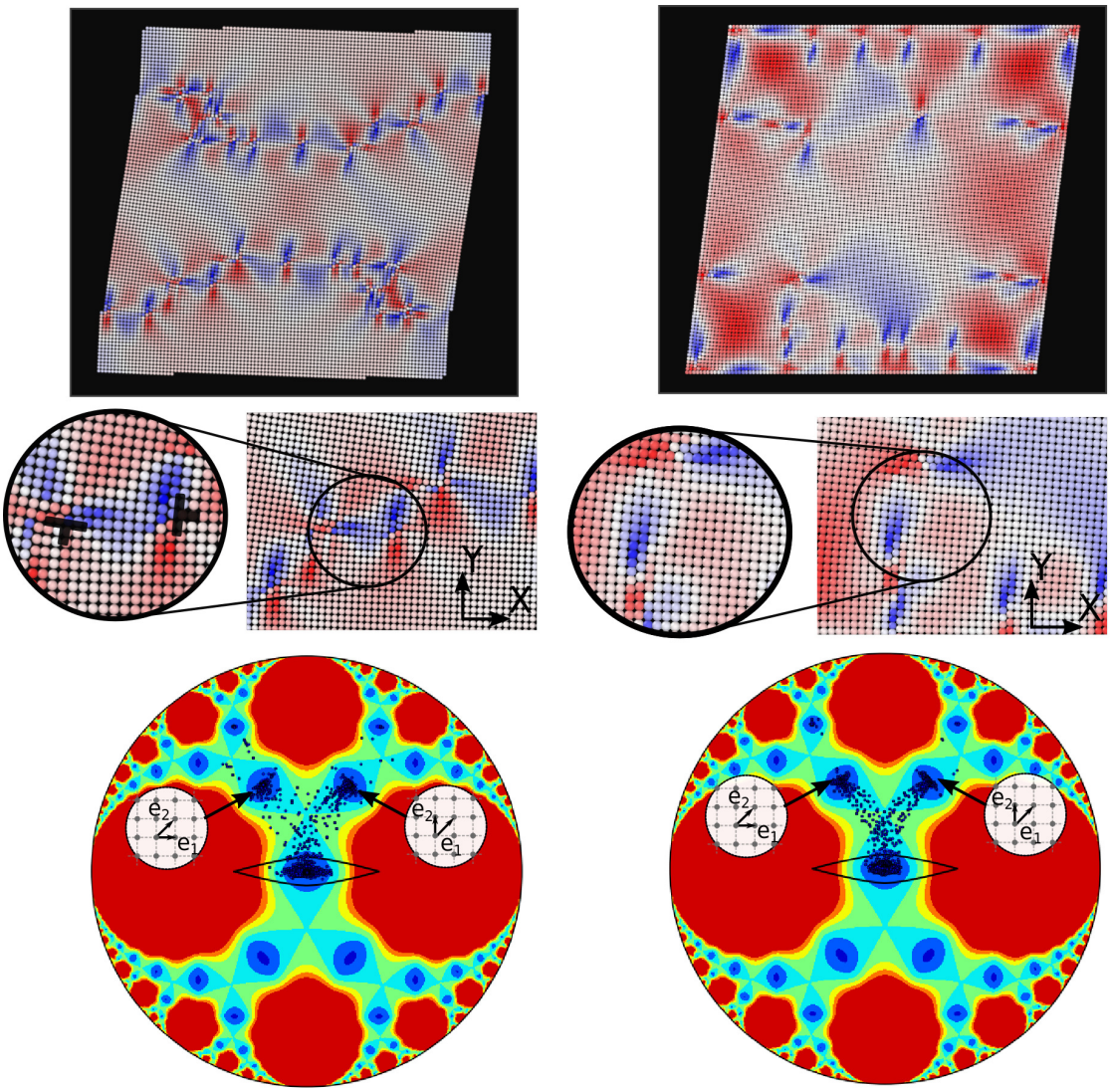

Figure 4.8: **Post-Instability Pattern for the Rhombic Pure Shear:** Results are shown for a $N = 10^4$ domain with both periodic (left) and fixed (right) boundaries. On top: the Cauchy stress σ_{xy} is shown in the full domain with evidence on two edge dislocations. On bottom: The element points in the configurational space. Wells $\mathbf{S}$, $\mathbf{S}_1^{0^\circ}$, and $\mathbf{S}_{-1}^{90^\circ}$ are simultaneously activated. The points on the valleys connecting these wells correspond to the elements in the dislocation core.

energy landscape. The fat rhombic path is the one for which instability takes place at the lowest level of energy and at the smaller value of the critical load, while the rectangular path is the one for which both the energy and the stresses are the highest. In Figure 4.7, we illustrate evolution of energy density ϕ along these loading paths and show the configuration of stress at the loading steps immediately preceding and following instability. The results obtained for rhombic pure shear are summarized in Figure 4.8, where we show the post-instability pattern along with elements distribution in the configurational space. Coloring reflects the value of the Cauchy stress components σ_{xy}.

As predicted by the instability analysis, both vertical and horizontal edge dislocations are present in the post-bucling state. We emphasize that all these dislocations nucleate collectively. We recall that in our model dislocations appear as interfaces between equivalent shear-related phases and that elements located along low-energy valleys connecting the energy wells represent dislocation cores (as illustrated in Figure 3.5). Considering the configuration of dislocation shown in Figure 4.8 one can clearly notice how both plastic slips associated with the two energy valleys are activated. The three wells $\mathbf{S}$, $\mathbf{S}_1^{0^\circ}$, and $\mathbf{S}_{-1}^{90^\circ}$ are simultaneously present in the post-instability equilibrium, and points in between $\mathbf{S}$ and $\mathbf{S}_1^{0^\circ}$ and in between $\mathbf{S}$ and $\mathbf{S}_{-1}^{90^\circ}$ correspond to the horizontal and vertical dislocation cores, respectively. Observing the distribution of points in the configurational space, one can understand the importance of the saddle point $\mathbf{T}$ ensuring the coupling of these two modes.

Along the rectangular pure shear path, the mechanical behavior and the resulting defect pattern are very different. Indeed, the post instability configuration appear as a 45° rotated version of the original configuration. Some elongated configurations of defects are also observed, but they are rather different from the neatly defined edge dislocations found along the fat rhombic pure shear path. Quite interestingly, this rotated configuration is obtained by a fine mixture of shear-equivalent phases, in which the undeformed crystal phase $\mathbf{S}$ is entirely absent. We illustrate this in detail in Figures 4.9 and 4.11. Observe that, the engaged energy wells are 45° rotated versions of the $\mathbf{S}_1^{0^\circ}$ and $\mathbf{S}_{-1}^{0^\circ}$ wells (we recall that each well is the configurational space represent an orbit where the rotation equivalent configurations are indistinguishable). Even if some disorder is present, the rotated configuration emerges as a fine mixture of these two fully compatible phases almost without any presence of interface defects. This is a very different behavior from what is observed along the rhombic pure shear phat, where the sheared phases were confined to some isolated slip planes throughout the crystal. Here the lattice reorganization is global and cooperative.

To summarize, we observe two very different behaviors while loading the crystal along the opposite sides of the fundamental domain. Along the fat rhombic path, which crosses the yield surface at low energy, instability manifests itself as collective nucleation of edge dislocations. The coupling of the vertical and the horizontal slip planes, predicted by the

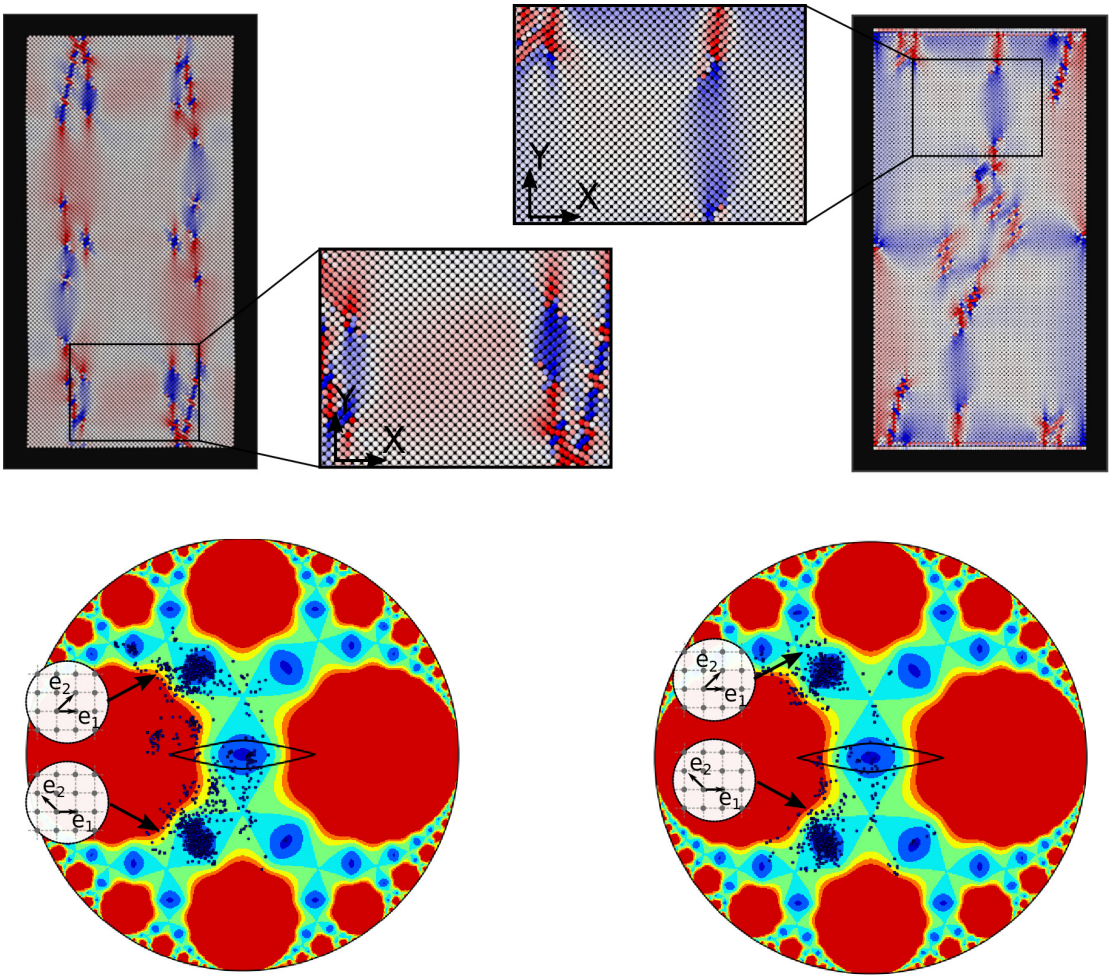

Figure 4.9: **Post-Instability Pattern for the Rectangular Pure Shear:** A $N = 10^4$ domain is considered. Results for a simulation with periodic boundaries (left) and fixed (right). On top: the Cauchy stress σ_{xy} in the full domain with evidence on a region, to better illustrate the final, 45°-rotated cristal lattice structure. On bottom: the elements points in the configurational space show the engagement of the two wells $\mathbf{S}_1^{0^\circ}$, and $\mathbf{S}_{-1}^{0^\circ}$ (or more precisely a 45°-rotated equivalent of these two), with some residual defects variously placed.

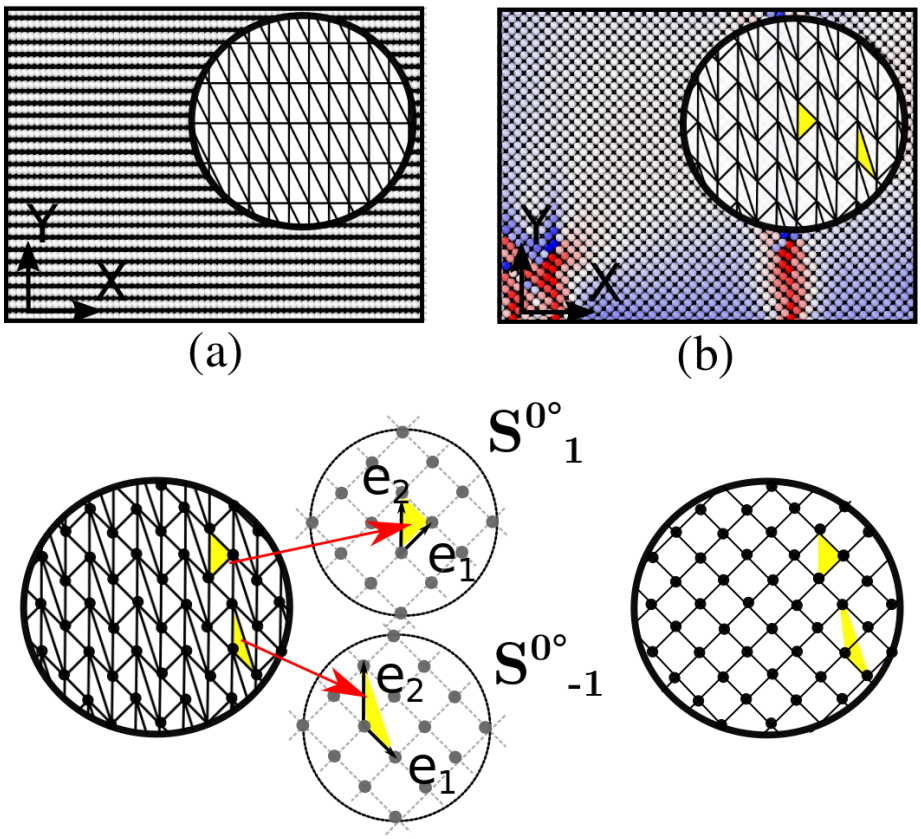

Figure 4.10: **Crystal Rearrangement along the Rectangular Path** On top: details of the crystal structure along the rectangular path before (a), and after (b), nucleation. On the bottom, a detail of the post-instability pattern, where elements of the triangulation are shown. The crystal structure experiences a global rearrangement where the 45° rotated version of wells $\mathbf{S}_1^{0^\circ}$ and $\mathbf{S}_{-1}^{0^\circ}$ are finely mixed. This rearrangement gives again a square lattice, but rotated by 45°.

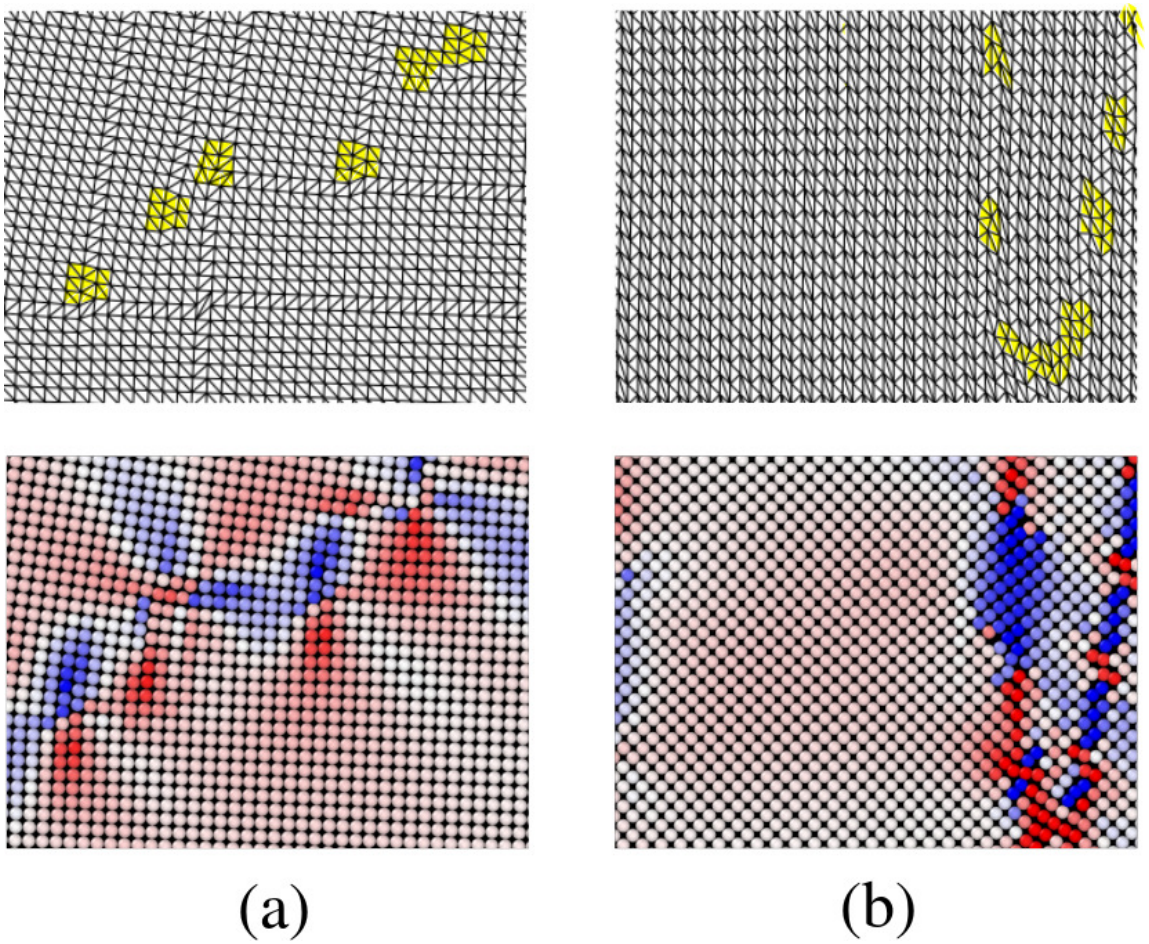

Figure 4.11: **Cauchy Stress σ_{xy} and Lattice Structure for the Rhombic and the Rectangular Paths:**. (a) rhombic, (b) rectangular. In yellow we highlight the dislocation cores and the other observed topological defects. While in (a) the shear is limited to specific lattice planes, in (b) the rearrangement is global.

instability analysis, highlights the importance of point **T** in shaping the energy landscape. On the other hand, along the rectangular path, instability takes place at much higher values of energy density. The path crosses the landscape far away from any low-energy valleys and the energy minimization leads to the global reorganization of the crystal, in which the two compatible sheared configuration $\mathbf{S}_1^{0^\circ}$ and $\mathbf{S}_{-1}^{0^\circ}$ become finely mixed throughout the full crystal volume. In this latter case relation between predicted unstable mode $\mathbf{n}$ and the observed pattern is not really visible. The rectangular path intersects the yield surface in correspondence of its narrow edge and may therefore seem a somewhat extreme type of loading. However, we will illustrate shortly how the corresponding reorganization mechanism appears also in the case of other simple shears crossing the yield surface in correspondence of high energy values.

The simple shear paths show an intermediate behavior between the two extreme cases discussed above. In agreement with what was predicted by the stability analysis, the $\theta = 0^\circ$ shear path shows a response analogous to the one along the rhombic shear path, and a collective nucleation of vertical and horizontal dislocations is observed. The activation of both low energy valleys is clearly visible in the configurational space, where it is possible to notice the simultaneous engagement of the three wells $\mathbf{S}$, $\mathbf{S}_1^{0^\circ}$ and $\mathbf{S}_{-1}^{90^\circ}$ (Figure 4.12.(a)). The $\theta = \arctan(\frac{1}{2})$ shear path also shows nucleation of linear defects identifiable as edge dislocations, but only along the vertical shear plane. This agrees with the stability analysis prediciting that only one mode $\mathbf{n}$ gets activated, even if a certain misaligment between $\mathbf{n}^\perp$ and Eulerian lattice direction $\mathbf{e}_2$ exists. In the configurational space we observe a major stream of points in the valley between the $\mathbf{S}$ and $\mathbf{S}_{-1}^{90^\circ}$ wells. however the final configurations are not centered at the bottoms of these wells, but are slightly shifted towards rectangular lattices, meaning that the system is not fully relaxed (Figure 4.12.(b)). The most interesting scenario is observed for the $\theta = 45^\circ$ simple shear path, which crosses the yield surface far from the low energy valley. In this case, the final pattern is characterized by the presence of grains with different lattice orientation, separated by irregular boundaries. Inside each grain some isolate edge dislocations is present. This added complexity is reflected in the associated configurational space of metric tensors, where one can see that, in addition to the reference well, all the four neighboring wells become also engaged, and few elements even reach more distant wells. In Figure 4.13, we show how the differently oriented crystal regions can be obtained with a combination of shear-invariant phases, similarly to what was observed along the rectangular path. Therefore, in this case both the dislocations-type slip and the global rearrangement mechanism are activated, allowing the system to reach a very complex patterning already during its first instability. in this case, as for the case of the rhombic pure shear, we do not observe a direct connection between the predicted unstable mode $\mathbf{n}$ and the observed pattern. As we have already mentioned, these patterning features are independent of system sizes and of the nature of boundary conditions. In Figures 4.14 and 4.15 we show patterns obtained for a $N = 10^6$ simulations as we apply $\theta = 0^\circ$ and $\theta = 45^\circ$ simple shears. The larger system size allows one to

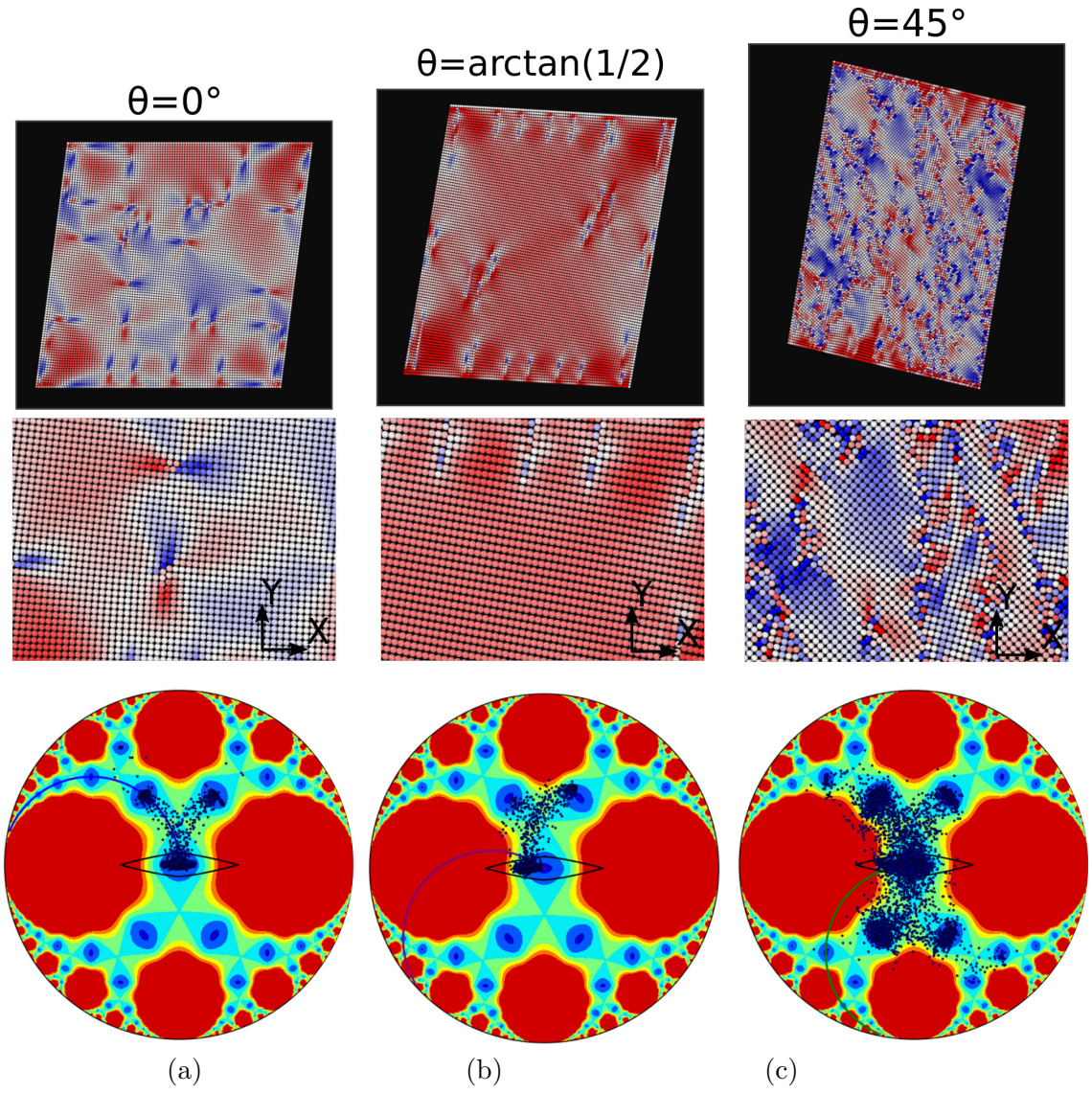

Figure 4.12: **Post-Instability Patterns for the Considered Simple Shears:** A $N = 10^4$ domain is considered. Cauchy stress σ_{xy} is showed on the entire domain and on a blown-up detail, to better appreciate the difference of the obtained patterns. Distribution of the elements points in the configurational space it is also shown.

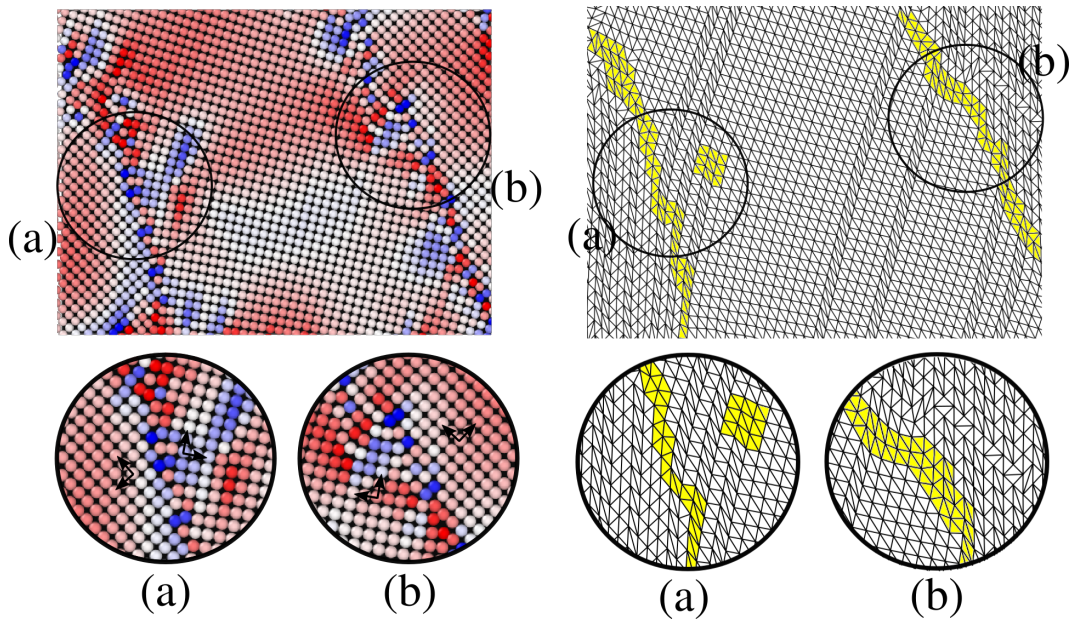

Figure 4.13: **A detail of the Simple Shear $\theta = 45°$ Post-Instability Pattern:** colors indicate the values of σ_{xy} component of Cauchy stress. Regions with different orientations are accorded with various topological defects. As in the rectangular path, the lattice rotation is actually a mixture of compatible sheared phases. Dislocations are also observed.

generate more complex rearrangements in the microstructure, however, the main features of the emerging defect patterns remain the same.

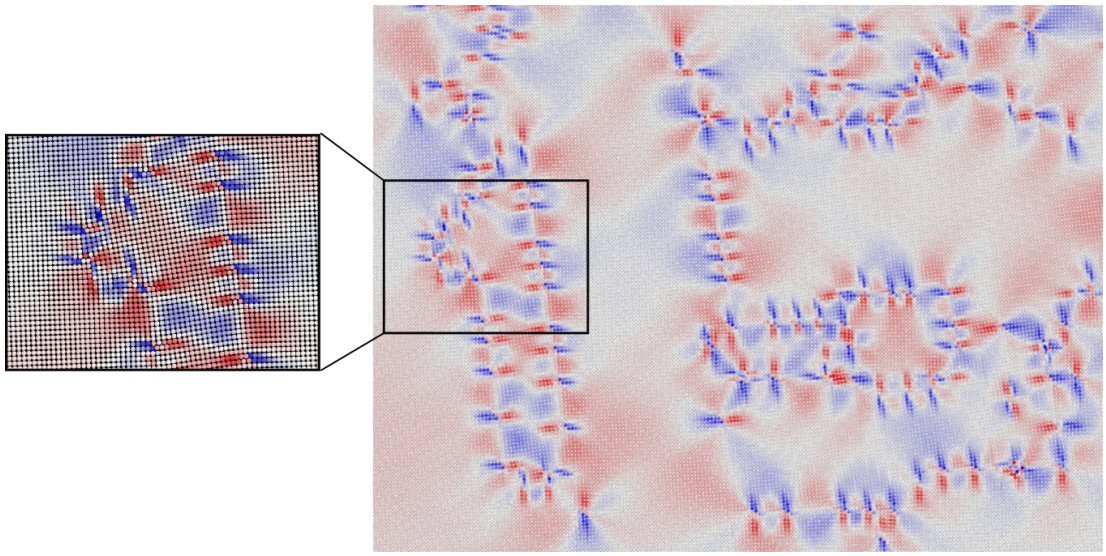

Figure 4.14: **Post-Instability Pattern for a $N = 10^6$ Simulation with Periodic Boundary Conditions for $\theta = 0^\circ$ Simple Shear:** Colors indicate the σ_{xy} stress field.

4.3 Triangular Lattice

In this Section, we apply the same analysis to the triangular lattice with hexagonal symmetry. To this end, we first construct the polynomial energy (2.27) with coefficient $\beta = 4$ and the perform stability analysis based on strong ellipticity condition (4.10). We focus on some representative paths and discuss simulation results, pointing out their relation with the analytical predictions. This allows us to show not only the significant dependence of the nucleated defect pattern on orientation of the sample in the loading device, but also on the symmetry of the lattice.

4.3.1 Stability analysis

Starting from the reference triangular well $\mathbf{T}$, we followed general shearing paths and computed the first critical values of the load $\alpha = \alpha_c$ where the strict inequality in (4.10) first fails. This gives us the yield surface, separating the region of configurational space where homogeneous deformation of the crystal is stable from the region in which one can expect the simultaneous activation of energy wells different from $\mathbf{T}$. In Figure 4.16 we illustrate

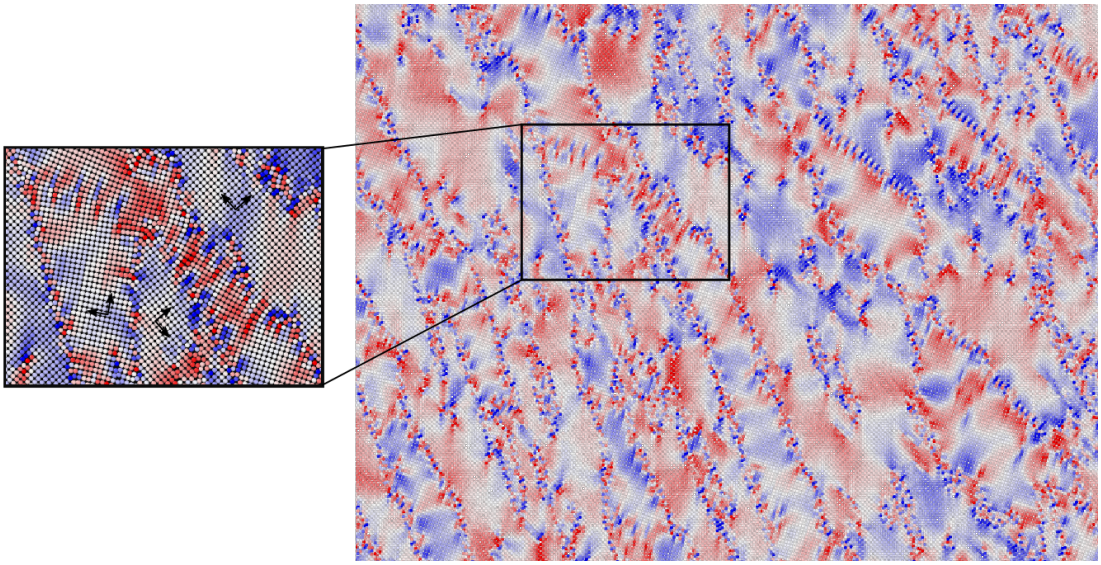

Figure 4.15: **Post-Instability Pattern for a $N = 10^6$ Simulation with Periodic Boundary Conditions for $\theta = 45°$ Simple Shear:** Colors indicate the σ_{xy} stress field.

the computed yield surface. Here, the two extremal paths corresponding to the boundaries of the fundamental domain are two rhombic pure shears: the fat rhombic path and the skinny rhombic path, (the associated deformation gradient is given by (2.31) and (2.38), respectively). Note the difference with the yield surface which we derived for the case of the square lattice (Figure 4.2): in the present case the highest value of α_c, i.e. 0.285, is the one along the low energy fat rhombic path, while the lowest value $\alpha_c = 0.135$ corresponds to the high-energy skinny rhombic path. The value of α_c increases continuously between these two opposite sides of the fundamental domain and the yield surface presents a characteristic triangular shape. Given this symmetry, the difference between the critical values of α_c at the extremes of the yield surface are less pronounced than in the case of square lattice.

In addition to the two rhombic pure shears, we also consider simple shears paths $\theta = 60°$ (equivalent to $\theta = 0°$ and $120°$) and $\theta = 30°$ (equivalent to $\theta = 90°$ and $150°$). These two simple shears are the representatives of an "easy" shearing direction, along a dense crystallographic plane, and a "hard" one, evolving towards higher energy barriers (see also Figure 2.11 in chapter 2). All these mentioned paths are illustrated in Figure 4.16 (b).

We perform the acoustic tensor analysis as before, and report the det q_{ik} profiles in Figure 4.17 and Figure 4.18 for the pure and simple shears, respectively. Similarly to what we have encountered in the case of square symmetry, two instability directions are observed to appear simultaneously along the low energy fat rhombic path. Then, even in the triangular

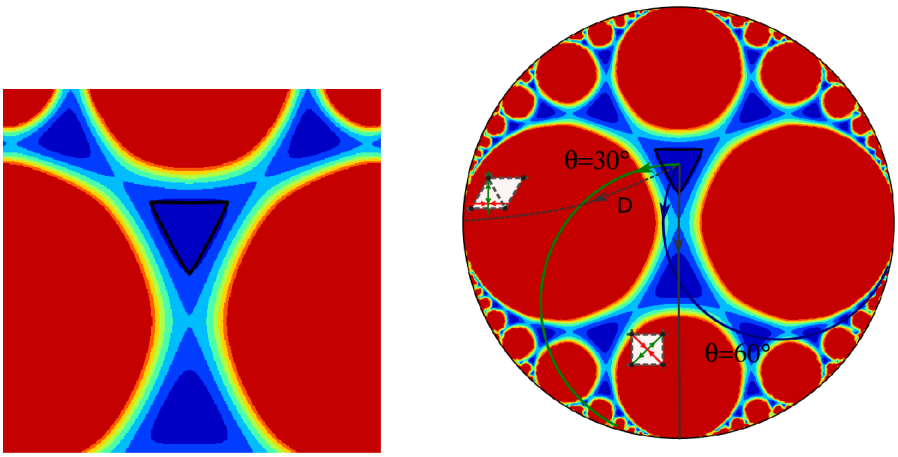

(a) (b)

Figure 4.16: **Yield Surface for the Triangular Lattice:** a) The *yield surface* enclosing the region surrounding the reference triangular well **T** is illustrated with a thick black line. b) The analyzed shear paths and their relation with the yield surface are shown.

lattice, there exists a non trivial coupling between various plastic mechanisms. However, while in the case of square symmetry wave directions were aligned with crystallographic planes, in the present case the corresponding directions $\mathbf{n}^{\perp}$ are not particularly aligned with any of the deformed lattice vectors. Indeed, one has for the two directions $\xi_1^{\perp} = 82.98°$ and $\xi_2^{\perp} = -7.97$, while the crystallographic planes are oriented at 0.00° and 75.01° respectively (see Figure 4.17). Along the skinny rhombic path, just one instability direction is observed and, similarly to what we have encountered in the case of square symmetry, this direction is exactly perpendicular to the compressed axis. The analyzed simple shears paths are characterized by the presence of one unstable mode only, not aligned with the deformed crystallographic directions. In the "easy" simple shear $\theta = 60°$ direction, the misalignment with the closest direction $\mathbf{e}_2$ is of about 18°, and is even more pronounced in the more generic shear direction $\theta = 30°$, where the misalignment exceeds 30°. We summarize all these results in Figure 4.18. The critical loadings are $\alpha_c = 0.179$ and $\alpha_c = 0.162$ for $\theta = 60°$ and $\theta = 30°$, respectively.

We remark that also for the triangular symmetry the polarization vector **m** is always perpendicular to **n**, thus indicating a "shear-band" type of instability. However, the misalignment with the crystallographic directions makes the prediction of the activated slip planes less straightforward.

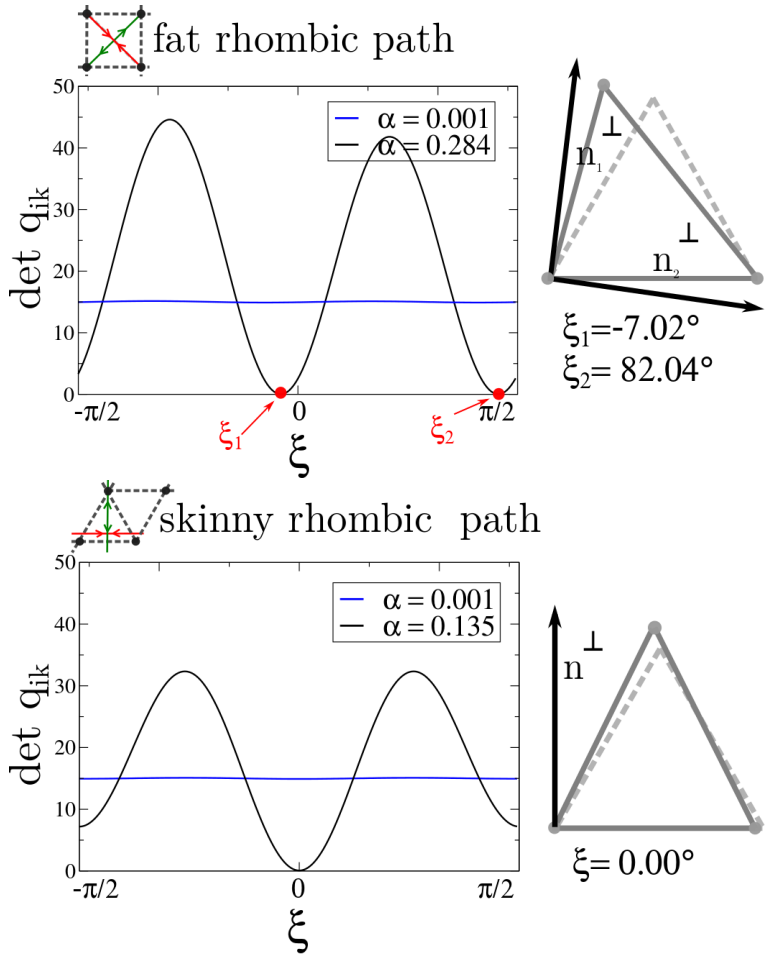

Figure 4.17: $\det q_{ik}$ **Profiles along the Fat Rhombic and the Skinny Rhombic Paths:** Evidence on the load α_c for which equality in (4.10) is satisfied. the fat rhombic pure shear (a) shows the simultaneous appearence of two instability directions, while just one appears in case of fat rhombic path (b). On the side of each graph, we show the orientation of wave direction $\mathbf{n}^{\perp}$ with respect of the deformed lattice cell at $\alpha = \alpha_c$.

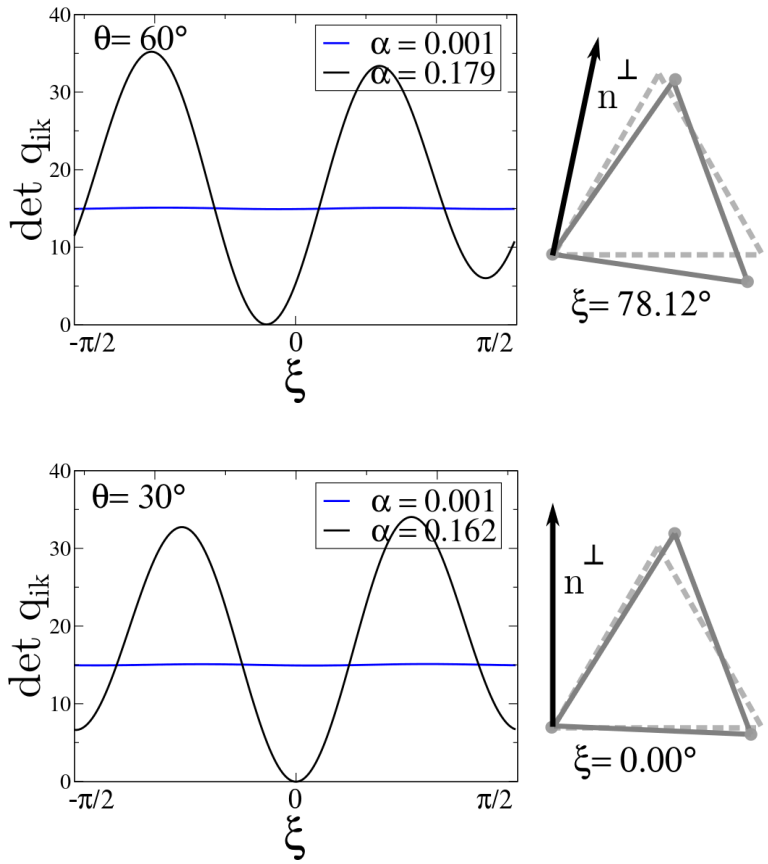

Figure 4.18: $\det q_{ik}$ **Profiles along The Considered Simple Shears:** Profiles for $\theta = 60°$ and $\theta = 30°$ loading paths are shown, with evidence on load α_c for which equality in (4.10) is satisfied. Both these simple shears are characterized by the presence of one unstable mode only, not aligned with crystallographic directions.

4.3.2 Simulations Results

As in the case of the square symmetry, numerical simulations were performed for different system sizes (varying between 10^4 and 10^6) and boundary conditions (fixed and periodic). While these factors do not influence the observed mechanisms of homogeneous nucleation, a certain care has to be taken when considering another factor, the applied loading step.

Our loading protocol will be the same as the one adopted previously for the square symmetry case. In a first set of experiments, to verify the overall agreement with the analytic instability criterion, it is used with a loading increment of 10^{-3}. Then, a refinement to 10^{-4} is adopted near the first instability in order to capture in detail the inherent homogeneous nucleation pattern.

Precursors of Instability and Nucleation Mechanism

In the performed simulations, an overall agreement with the analytical yield surface is observed, however, differently from what we saw in the square symmetry case, nucleation occurs for values α_c^* which are of about a 10% higher than the corresponding analytical predictions α_c. However, when $\det q_{ik}$ is already negative and in proximity of the nucleation event, the system stops being perfectly homogeneous and instead develops periodically-spaced modulations (see Figure 4.19).

For all the considered loading paths, orientation of these inhomogeneous bands agrees with the direction $\mathbf{n}^\perp$ obtained from the strong ellipticity condition (4.10). These bands are observed more clearly when fixed boundary conditions are used. However, the mechanism leading to instability is independent from the particular type of boundary conditions. The non-equilibrium configurations found by the minimization algorithm show the growth of the observed bands that, first become more pronounced and end up being the sources for the nucleation of dislocations. The dislocations appear as dipoles, originating at the center of the bands themselves, where the lattice is more distorted.

To better understand this process, consider Figure 4.21 where the main phases of the evolution are illustrated for simple shear directions $\theta = 60°$ and $\theta = 30°$. The observed bands represent lattice modulations which carry a relative rotation centered in the middle of the bands (phase 1 in Figure 4.21). As the amplitude of the modulation grows, leading to higher relative rotations, the system gets ready for the formation of dislocation dipoles (phase 3). In Figure 4.23, we illustrate specifically the relative rotation that are already observable from the early, pre-instability stage of the bands formation. Starting from an homogeneous state characterized by a particular value of rotation $\mathbf{R} = \mathbf{U}^{-1}\mathbf{F}$, further rotations start to spread around this value, spanning a certain interval and thus shaping the banded structure. The reason for which the instability direction, driving the

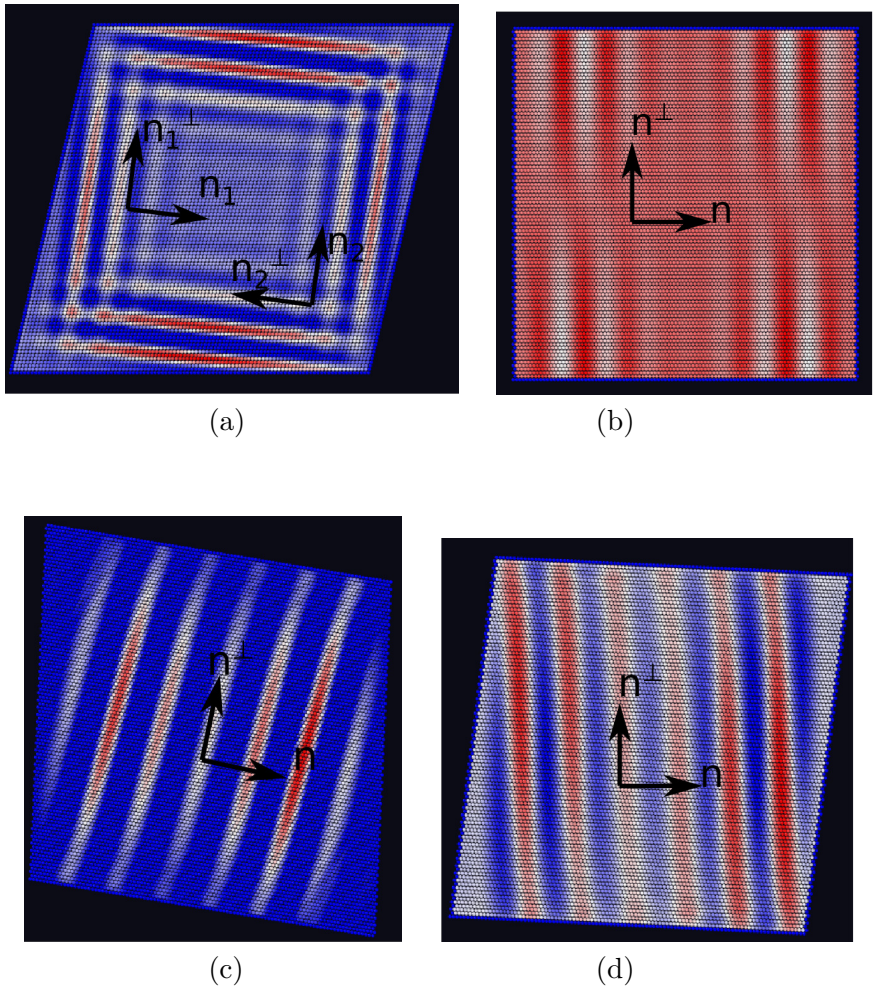

Figure 4.19: **Precursors of the Incipient Instability:** Inhomogeneous states, precursors of the incipient dislocation nucleation, for the considered loading paths. These precursors are characterized by the appearence of higher energy bands, periodically spaced, and whose orientation match the direction of the unstable mode $\mathbf{n}^\perp$ predicted analytically.

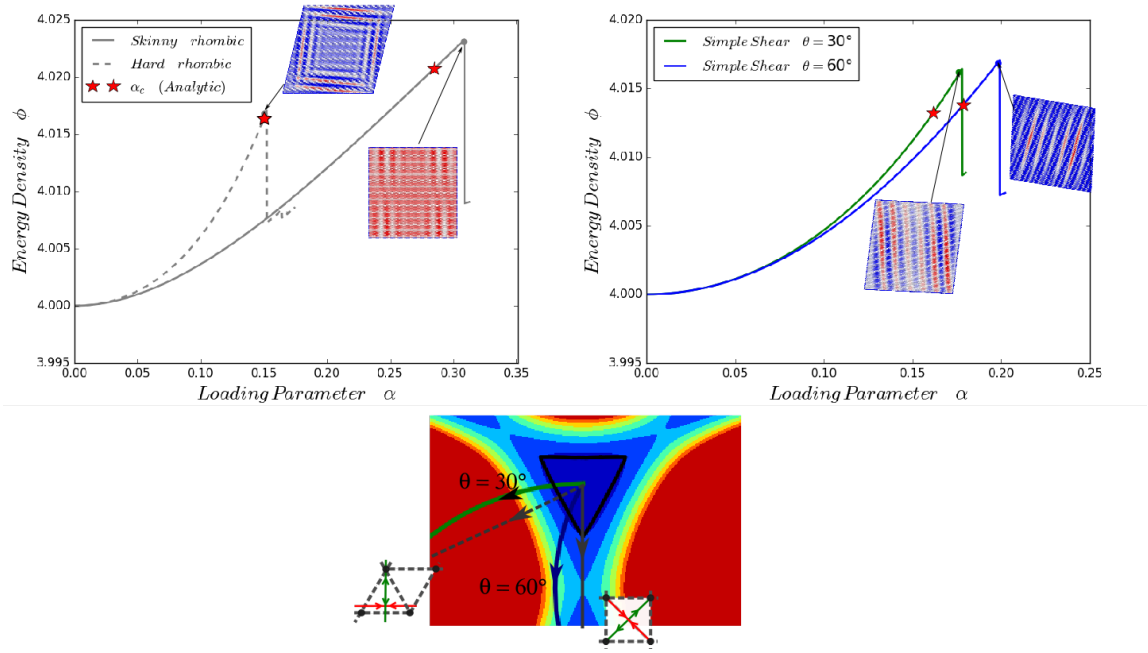

Figure 4.20: **Energy Density up to Nucleation for the Triangular Lattice:** Evolution of the energy density ϕ along the four considered trajectories. On the left: the fat rhombic and the skinny rhombic pure shears. On the right: the two simple shears $\theta = 60°$, and $30°$. Instability happens systematically later than what predicted analytically, and we observe $\alpha*_c \approx 1.1\alpha_c$

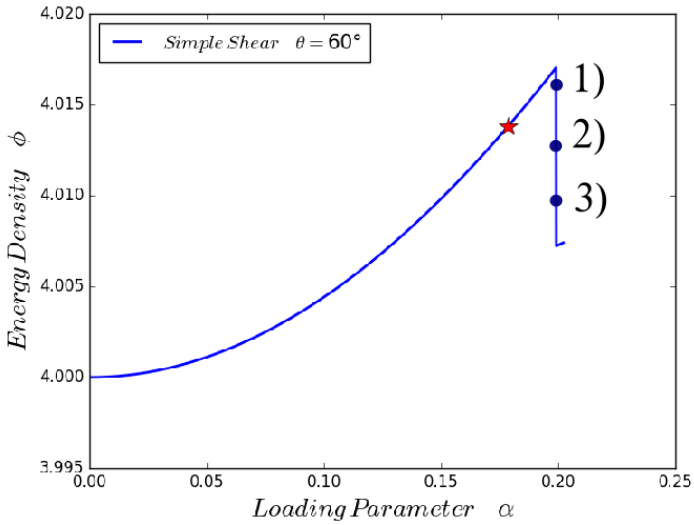

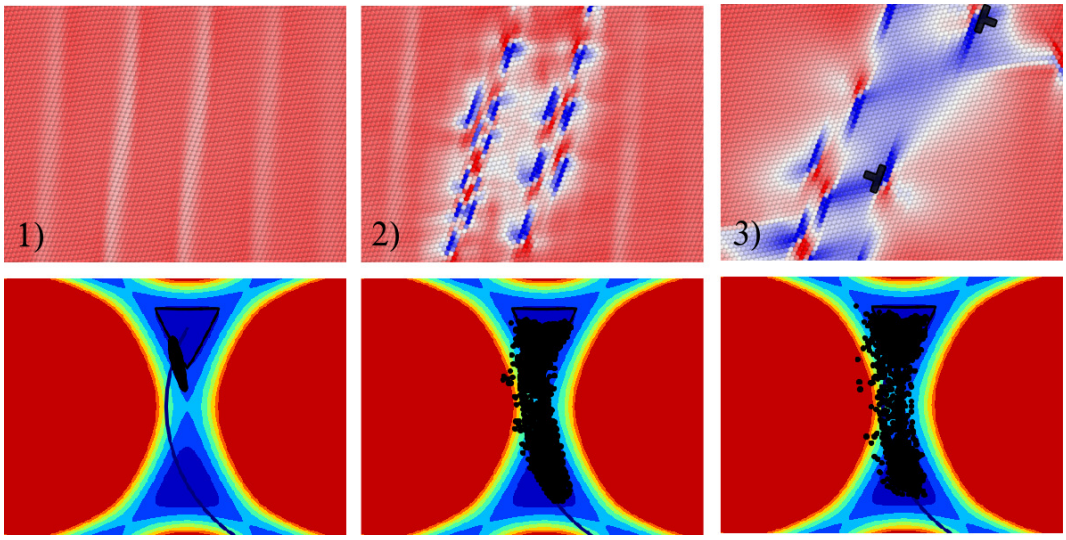

Figure 4.21: **Dislocation Nucleation in the Triangular Lattice along $\theta = 60^\circ$ Simple Shear:** Evolution of the energy density and the Cauchy stress σ_{xy} field representing three different phases of the instability which leads, from the first appearence of inhomogeneous bands, to the formation of dislocations. These are not equilibrium states, but are part of the overdamped dynamics implicit in the minimization procedure. The sequence shows nucleation in the $\theta = 60^\circ$ simple shear. On bottom we show the corresponding distribution of the elements in the configurational space, which highlights the importance of the square point in driving the development of the banded precursors.

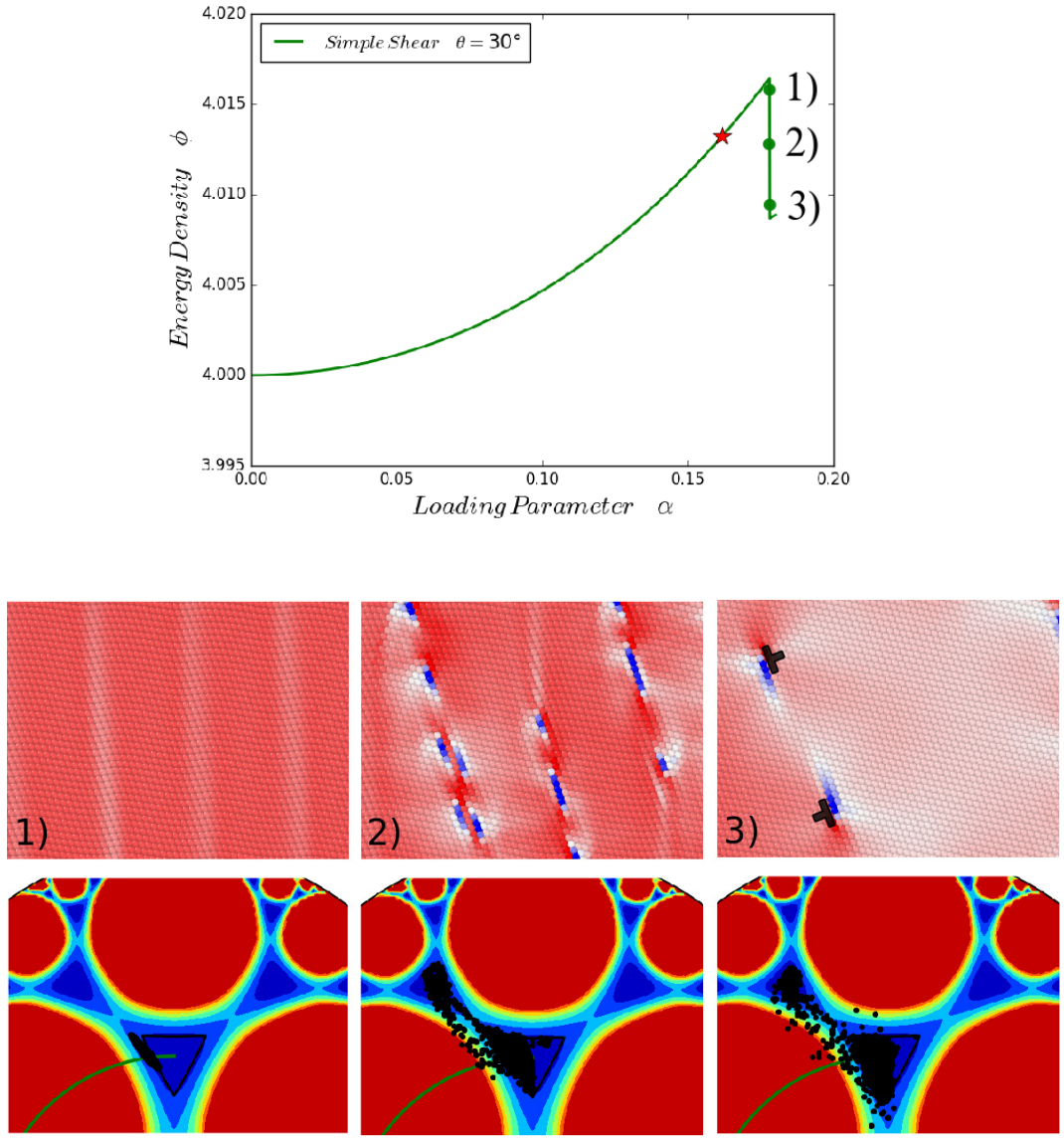

Figure 4.22: **Dislocation Nucleation in the Triangular Lattice along $\theta = 30^\circ$ Simple Shear:** Evolution of the energy density and the Cauchy stress σ_{xy} field representing three different phases of the instability which leads, from the first appearence of inhomogeneous bands, to the formation of dislocations. These are not equilibrium states, but are part of the overdamped dynamics implicit in the minimization procedure. The sequence shows nucleation in the $\theta = 30^\circ$ simple shear. On bottom we show the corresponding distribution of the elements in the configurational space, which highlights the importance of the square point in driving the development of the banded precursors.

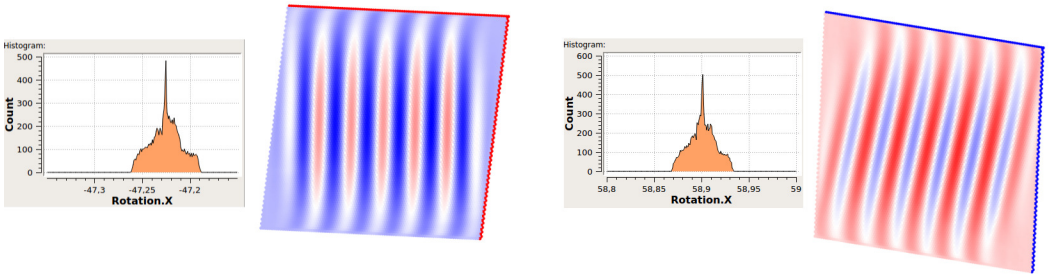

Figure 4.23: **Rotation Distribution in the Band Patterning:** $\theta = 30°$ (left) and $\theta = 60°$ (right) simple shears. This inhomogeneous equilibrium configuration immediately preceeds the instability process described in Figure 4.21, where the interval of observed rotations furter increases, up to the formation of dislocation dipoles.

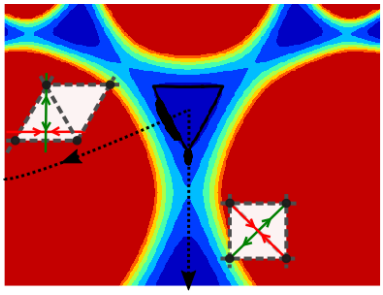

Figure 4.24: **Bands Patterning in configurational space:** Dispersion of elements in configurational space corresponding to the first instants of instability, when bands spread originating a new inhomogeneous pattern. The two case of the skinny and the fat rhombic paths are shown. Here the Dispersion is originated by the bands which are respectively tangential and perpendicular to the yield surface.

band formation, is not oriented along the crystallographic planes, can be seen clearly if we observe how elements evolve in the configurational space. As we illustrate in Figures 4.21 and 4.22, the early configurations of these bands are clearly influenced by the presence of the low energy square saddle point. More specifically, the band formation corresponds, in the configurational space, to the spreading of the configuration points that were originally superimposed on a single point along the imposed shearing path. The spreading cloud of the configurational points evolves towards an elongated structure clearly pointing towards the square symmetry saddles in the middle of low energy valleys (phase 1 of Figures 4.21 and 4.22). This phenomenon takes place generally for all shear directions, with two particular cases. Those are the two rhombic paths, where the spreading associated with bands formation is in the direction either tangential or perpendicular to the yield surface, see Figure 4.24.

In the case of the fat rhombic, low energy, path two types of bands appear simulta-

neously, in agreement of what we learn from the stability analysis where two unstable directions $\mathbf{n}_i^{\perp}$ are found. However these two trajectories are exactly superimposed in the configurational space which makes the visualization of this effect less straightforward than in the square lattice. The skinny rhombic path it is also peculiar in the way that the orientation of $\mathbf{n}_i^{\perp}$ lays exactly in the middle of the two deformed crystallographic planes $\theta = 60°$ and $\theta = 120°$. As we will show below, this also results in the simultaneous activation of two slip systems.

Post-Instability Patterns

We discuss now more in detail how the dislocation patterns emerge from the band structures using the fat rhombic pure shear as our first example. For this type of loading, the presence of two activated slip system is clearly visible in the post-instability equilibrium configurations, shown in Figure 4.25) (where we report the results obtained under both fixed and periodic boundary conditions). The simultaneous presence of well-distinguished triangular lattices $\mathbf{T}_1^{60°}$ and $\mathbf{T}_{-1}^{0°}$ is also clearly visible. We remark that these energy wells, that are distinguished in term of relative slip system, are superimposed in the configurational space, as they are equivalent in term of strain and are different only in terms of a rigid rotation (see also Figure 2.12 in chapter 2). The high symmetry square lattices represent, in this case, degenerate saddles which allow the system to activate two slip systems simultaneously. In view of the fact that space does not distinguish rotations, the actual landscape driving the evolution of the system is more complex than what we see in $\mathbf{C}$ space and higher dimensions must be involved.

Activation of two slip systems is observed also in the case of the skinny rhombic path, but is associated here with a different mechanism. Indeed, when we load the system with periodic boundary conditions, the vertical bands tangential to the yield surface create twins. We illustrate this stable equilibrium phase in Figure 4.26. These twins evolve, under further loading, up to the point of formation of dislocations along the two slip systems connecting the reference configuration $\mathbf{T}$ with the sheared configurations $\mathbf{T}_{-1}^{120°}$ and $\mathbf{T}_1^{60°}$ respectively. The evolution of the system in configurational space shows the activation of both valleys and the two type of dislocations are clearly visible (see Figure 4.26). Some more distant wells are also getting engaged, due to the interaction of the nucleated dislocations. Whe the fixed boundary conditions are applied, the twins do not form, due to the higher impediment to shape change, and the system evolves directly towards the double dislocation type configuration.

As we have already observed in the case of the square lattice, simple shears show an intermediate behavior with respect to what we see along the rhombic pure shear paths. In those cases, just one slip system is activated as a direct consequence of the banded modulation that precede dislocation nucleation, as only one type of dipoles forms when the bands

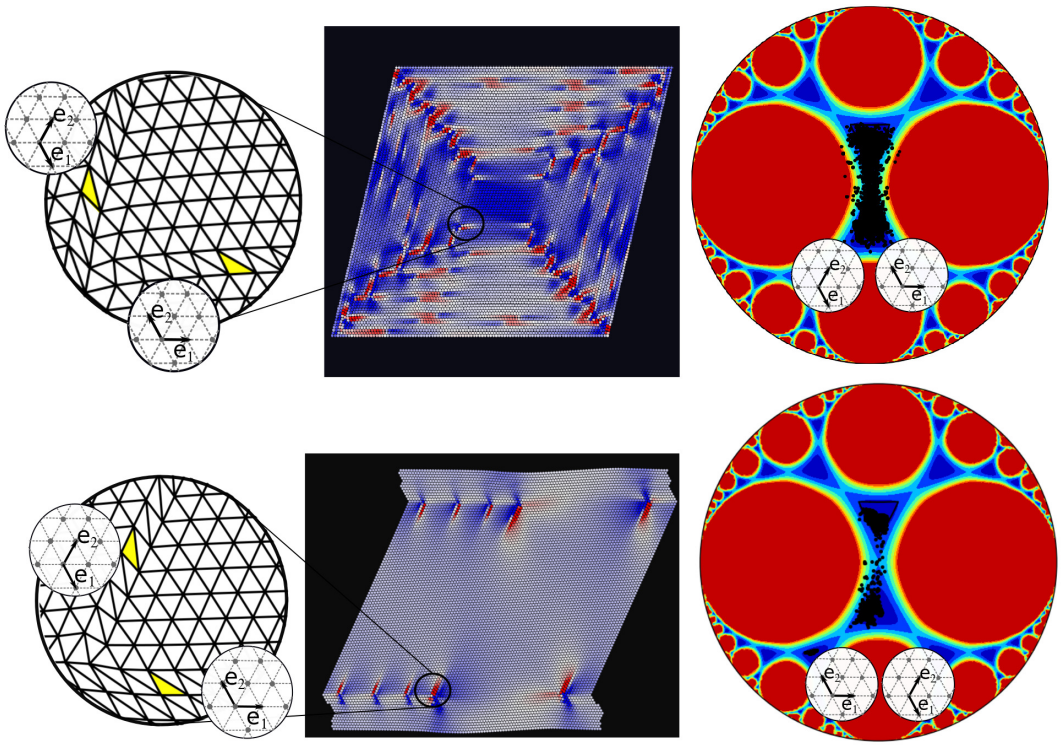

Figure 4.25: **Post-Instability Pattern along the Fat Rhombic Pure Shear:** A $N = 10^4$ domain is considered. On top and bottom, results from simulations with fixed and periodic boundary conditions are shown, respectively.(b) Cauchy stress σ_{xy} field is shown in the full domain. (c) The distribution of elements points in configurational space. The simultaneous presence of the three wells $\mathbf{T}$, $\mathbf{T}_1^{60^\circ}$, and $\mathbf{T}_{-1}^{0^\circ}$ is evident when one considers the corresponding triangulation in which we show a detail in (a).

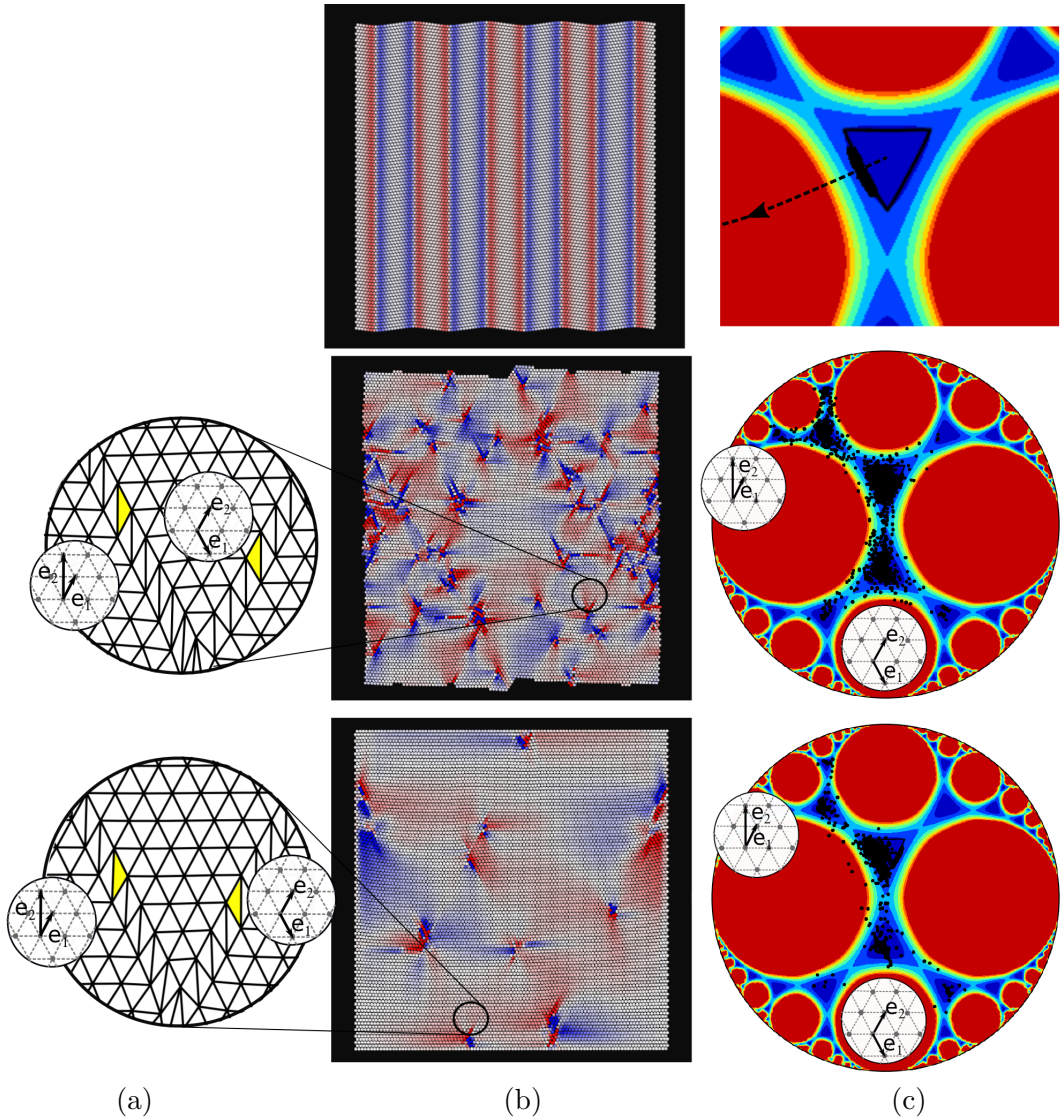

Figure 4.26: **Post-Instability Pattern along the Skinny Rhombic Pure Shear:** A $N = 10^4$ domain is considered. On top, the intermediate stable twin obtained with periodic boundary conditions is shown, followed by the dislocation pattern obtained under further loading. On bottom, results of a simulation with fixed boundary conditions are showed. In this case, the twin cannot form and dislocations nucleate without an intermediate equilibrium phase. On the left (a), a detail of the triangulation is showed to highlight the simultaneous presence of the three wells $\mathbf{T}$, $\mathbf{T}_{-1}^{120^\circ}$ and $\mathbf{T}_{1}^{60^\circ}$. (b) Cauchy stress σ_{xy} field is shown in the full domain. (c) Elements points in the configurational space.

start to grow. However, due to the fact that these bands are periodically distributed and not aligned with the activated planes, the nucleated dislocations subsequently interact with each other and with the boundaries causing the secondary activation of other slip systems. The secondary activation is more present when the misaligment is more pronounced. In Figure 4.27 we illustrate the patterns obtained for the $\theta = 60^\circ$ shear path, where just one type of dislocation, the one between wells $\mathbf{T}$ and $\mathbf{T}_1^{60^\circ}$, is present. The pattern associated with the $\theta = 30^\circ$ shear path is characterized by the involvement of multiple wells, a fact observed for both fixed and periodic boundary conditions.

It is interesting to notice that, while in the square symmetry case there was no significant difference between the instability behavior resulting from simple $\theta = 0^\circ$ shear path and the neighboring pure shear path pointing straight to the energy valleys, in the triangular lattice the behavior differs along such two paths. In particular the double slip activation is not observed for the $\theta = 0^\circ$ (or equivalently $\theta = 60^\circ$) simple shear. This is related to the fact that, while in the square symmetry case these deformations cross the yield surface in relatively close points, this does not happen in the case of triangular symmetry. Of course, when crossing the yield surface along other shearing paths intersecting the yield surface near the fat rhombic pure shear, the same double activation is observed (this happens for instance when using $\theta = 10^\circ$ path and other symmetry related paths).

4.3.3 Beyond the First Instability: Some Perspectives

The mechanisms described above are not limited to homogeneous nucleation and are not operating only at the first instability, but also play a role in the subsequent evolution of the system. Some preliminary results show that the appearance of grains in square lattices may take place at larger strains, in particular, during a second pronounced stress drop. This second rearrangement, however, strongly depends on the system dimension and on the applied boundary conditions. In Figure 4.29 we show a $N = 4 \cdot 10^4$ simulation of a square lattice with periodic boundary conditions where a $\theta = 0^\circ$ simple shear path is continued after the first nucleation event. The initial pattern, constituted by edge dislocations, becomes more complex by the formation of grains, that appear after a second, sharp, stress drop. These grains, initially small, gradually grow without significant hardening. Formation of grains however, is never observed in the triangular lattice, that responds to further loading with activation of additional slips. In Figure 4.30 an hexagonal crystal with periodic boundaries is loaded along simple shear $\theta = 0^\circ$. Here the second stress drop corresponds to a second nucleation of edge dislocations. Also in this case, deformation proceeds without additional hardening over a certain value of the loading parameter α, however, here this is associated with the localization of dislocations along a shear band in the upper part of the domain (see (c) in Figure 4.30).

These studies are still in the initial stage, however, even if a systematic investigation

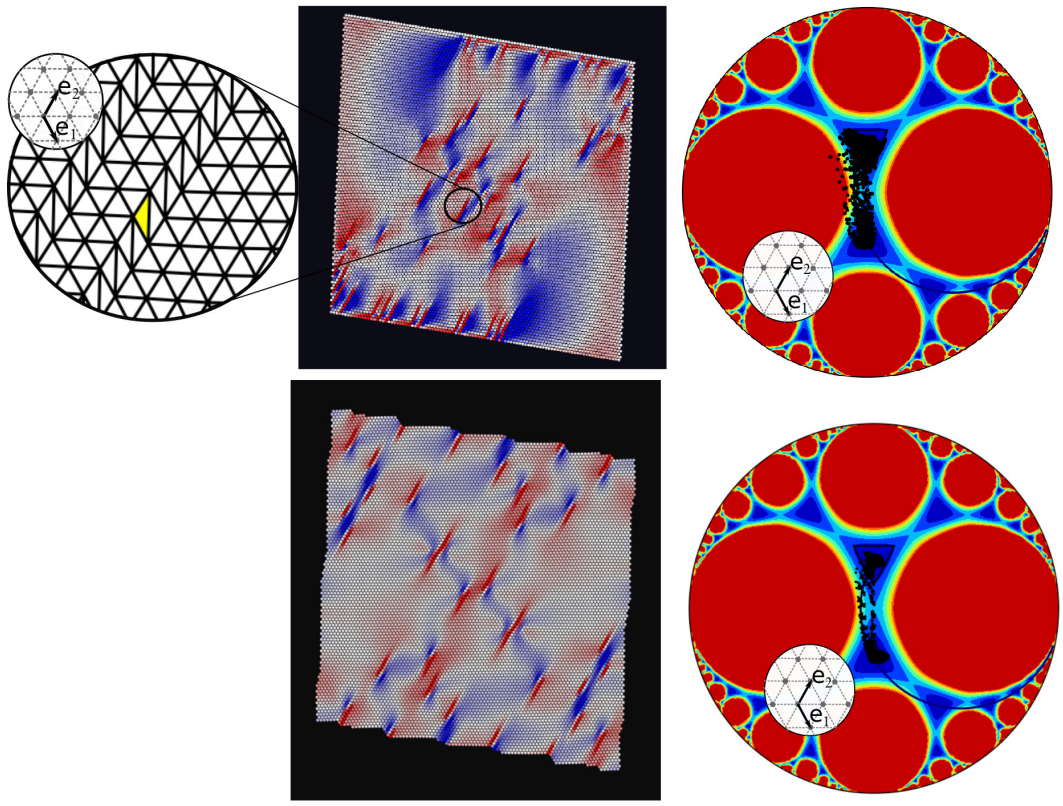

Figure 4.27: **Post-Instability Pattern for Simple Shear $\theta = 60°$:** A $N = 10^4$ domain is considered. On top, the configuration obtained for fixed boundary conditions is shown, while on bottom, results for an analogous simulation with periodic boundaries are illustrated. (a) a detail of the domain triangulation, (b) Cauchy stress σ_{xy} field on the full domain, (c) corresponding elements distribution in the configurational space.

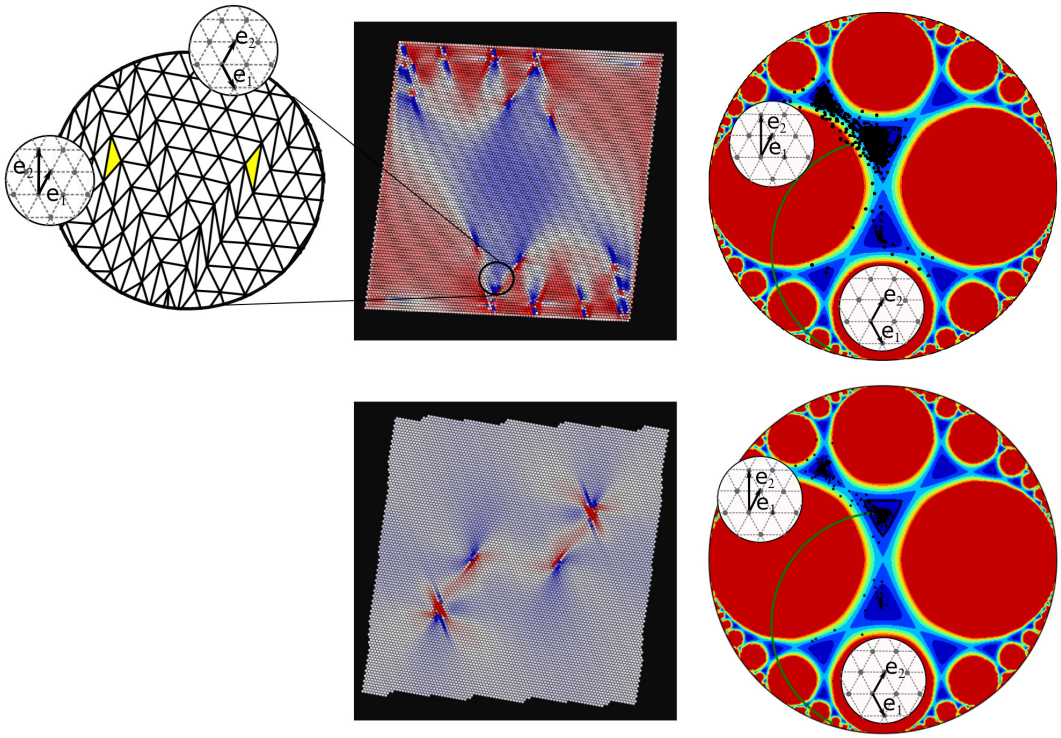

Figure 4.28: **Post-Instability Pattern for Simple Shear $\theta = 30°$:** A $N = 10^4$ domain is considerd. On top, the configuration obtained for fixed boundary conditions is shown, while on bottom results for an analogous simulation with periodic boundaries are illustrated. (a) a detail of the domain triangulation, (b) Cauchy stress σ_{xy} field on the full domain, (c) corresponding elements distribution in the configurational space.

is still missing, the influence of the mechanisms discussed in this section is clearly visible even after the first nucleation event.

4.4 Conclusive Remarks

The obtained results show how the very structure of the energy landscape, whose main features are imposed by the symmetry requirements, fundamentally affects the homogeneous dislocation nucleation phenomenon. For both considered lattice symmetries, when a quasi-static load is applied slowly enough, the strain localization associated with the ellipticity loss appears diffusely throughout the crystal volume. Defects nucleate collectively thus creating a complex pattern already during the first major avalanche.

The main mechanisms of dislocation nucleation can be identified considering two loading paths only. These are the pure shears associated with the sides of the fundamental domain D that both originate in the reference energy well (points **S** or **T**). One of these paths points straight to the lowest energy barrier, on the way to the other high symmetry point. The other evolves towards the infinity without intersecting any other minimizer along the way. While the square lattice is characterized by an elongated yield surface with two corners enclosed between high energy barriers, this does not happen for the triangular lattice, whose yield surface has less sharp corners all pointing towards low energy valleys. As a result, in the square lattice one observes post-instability patterns that are not edge dislocations, but are instead characterized by the global, energetically-costly crystal rearrangements involving combinations of both rotations and shears. This does not happen in the triangular lattice where, due to the different shape of the wells themselves, the formation of dislocation dipoles is always a dominant feature. In both symmetries, orientation of the applied load affects significantly the observed post-instability patterns. Most importantly, in both cases the other high symmetry phases are responsible for the non-trivial coupling of the activated slip systems. This interesting feature shows that these peculiar points of the energy landscape have a fundamental role in the development of complexity in the system. Our findings hint toward a scenario in which location of wells, together with the corresponding saddle points between them, is what controls the post-instability pattern. In this sense, our minimal model provides a useful tool for understanding the link between the structure of defect patterns and the energy landscape characterizing the crystal.

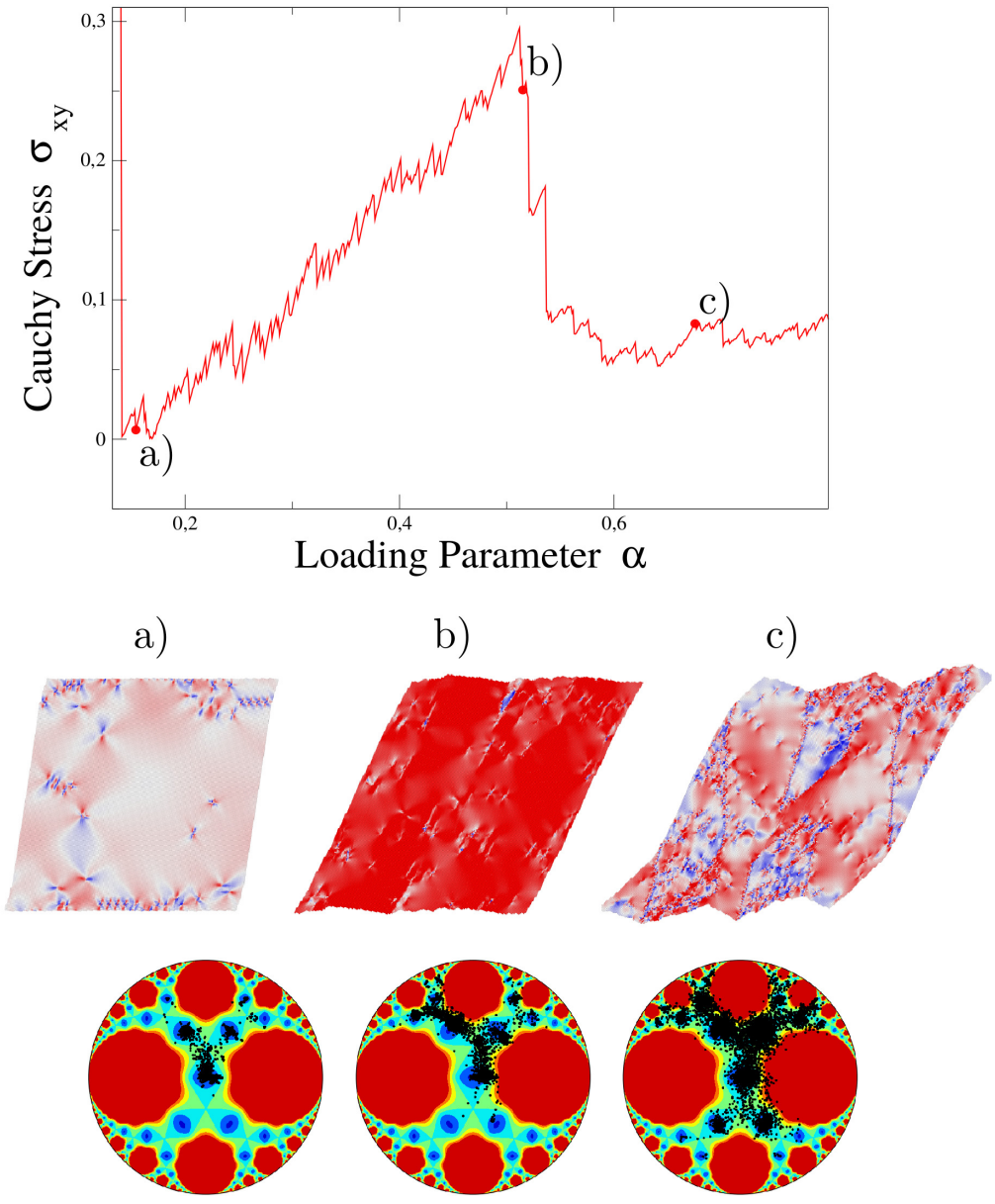

Figure 4.29: **Pattern Evolution in the Square Lattice:** A $N = 4 \cdot 10^4$ square lattice domain with periodic boundaries is loaded along the simple shear path $\theta = 0°$. The system present hardening up to a second stress drop where some grains, initially small, appears. These grains gradually increase allowing the system to deform almost without additional hardening. Notice how the configurational space show the development of increasing complexity.

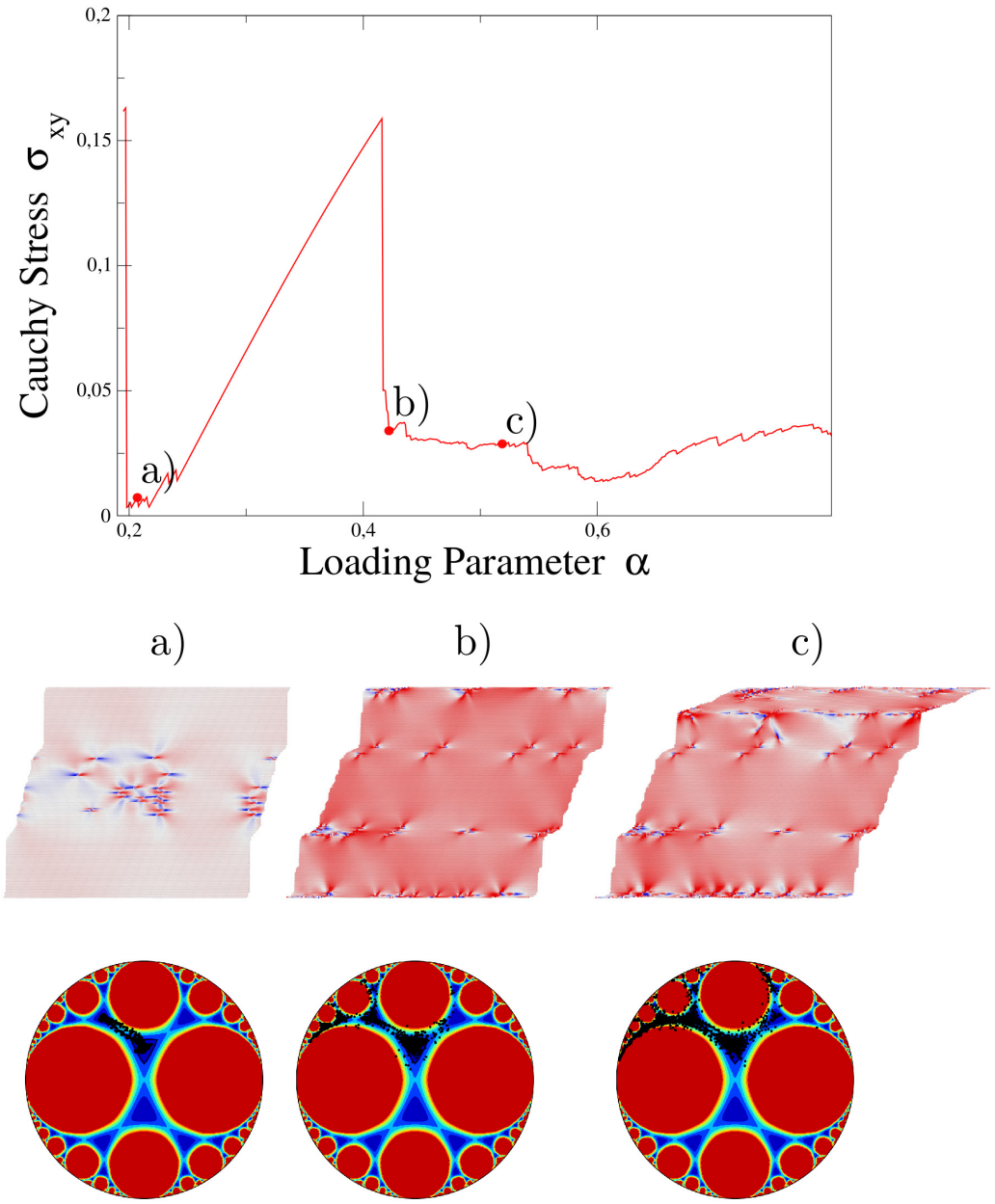

Figure 4.30: **Pattern Evolution in the Triangular Lattice:** A $N = 4 \cdot 10^4$ triangular lattice domain with periodic boundaries is loaded along the simple shear path $\theta = 0°$. The system present hardening up to a second stress drop where additional dislocations are activated. Then, deformation localize along a shear band in the upper region of the periodic domain.

Chapter 5

GL(2,$\mathbb{Z}$) Invariant Energy based on Interatomic Potentials

In the previous Chapters, discussion and simulations were based on the polynomial $GL(2,\mathbb{Z})$ invariant energy proposed in [CZ04]. This allowed us to highlight the important properties originating in this type of symmetry, in particular related to the presence of an infinite number of equivalent energy wells. This property makes the energy landscape rugged and non-convex, thus allowing one to incorporate plasticity and microstructure formation in a fully hyperelastic formulation. One important advantage of the polynomial energy is that it is available in explicit form for the energy is actually needed only within the fundamental domain D. However, this polynomial energy potential does not attempt to match quantitatively the behavior of any specific crystal, because no physical information was used apart from the imposed symmetry. In addition, the complex polynomial form of the energy (2.27) does not allow a straightforward identification of elastic constants, thus making it difficult to calibrate this model using experimental measurements. In view of these drawbacks, we decided to construct the reference energy ϕ_0 within D using a different procedure also relying on the Cauchy-Born rule (CBR). More specifically, in this Chapter we illustrate how to construct the reference energy ϕ_0 directly from interatomic pair potentials $\varphi_p(\mathbf{r}_{ij})$ provided by atomistic modeling. The chosen procedure is analogous to the one used in [OP98] and in the local QC method [MT02, TM11] with the only added feature that construction needs to be done explicitly only within D.

We begin the Chapter discussing such construction in full detail. Then, we illustrate the obtained energy landscape. Interestingly, we find that the isochoric part of the energy is qualitatively similar to the one described by the polynomial potential. Instead, the volumetric response is found to be fundamentally different. Its importance in defining the post-instability behavior of a dislocated crystal is one of the most important findings of this Thesis

A considerable part of this Chapter is devoted to the discussion of the homogeneous nucleation of dislocations. We consider the same loading paths as before for the triangular crystal and repeat for the new potential the analytic study of the acoustic tensor. We discuss the numerical results obtained in our nucleation tests and conclude that the non-trivial coupling between slip systems is still present if we use this empirical potential.

Then, we turn to a direct comparison of the results based on the atomistically informed strain energy density with those obtained with Molecular Statics (MS)[1]. Indeed, we know that Cauchy-Born based continuum methods can represent dislocation cores, but only in a coarse manner. The debate concerning their capability to give a reliable approximation of atomic-scale phenomena is still open.

We begin our comparison by juxtaposing dislocation cores structures as they appear in the two models. Then, we discuss the homogeneous nucleation phenomenon. We first test the validity of the analytical predictions based on (4.10) and then compare qualitatively post-instability patterns. We conclude by showing some simulations of nano-indentation. In contrast to other cases discussed in this Thesis, indentation induces nucleation under a strongly inhomogeneous strain field.

5.1 Energy Construction

We have already emphasized that CBR is crucial for including lattice features in to the hyperelastic boundary value problem. As we discussed in Chapter 3, to link macroscopic continuum deformation tensor $\mathbf{F}$ to the deformation of the lattice, one has to assume that (3.21) holds. Then, CBR allows one to derive a continuous energy density from interatomic potentials in a straightforward manner.

The idea of constructing continuum energy density functions directly from interatomic potentials exploiting CBR is not new. However here, instead of using CBR for finding the potential ϕ directly, we apply the CBR procedure on the fundamental domain D and obtain only ϕ_0. Then, by using (2.20), we automatically extend the obtained potential from D into the infinite configurational space. This allow us to preserve $GL(2,\mathbb{Z})$ invariance for general deformations including the neighborhoods of "far-away" wells. Instead, in the commonly used CBR-hyperelastic approach, the periodicity is limited by the cut-off radius r_c used to compute the interatomic potential (see Figure 5.1).

An accurate modeling of metals would require the use of interaction potentials more

[1]This is the static counterpart of Molecular Dynamics, discussed in chapter 1 and can be seen as the atomistic counterpart of the quasi-static continuum simulations performed in this thesis.

sophisticated than a simple pair interaction potential, as, for instance, the previously mentioned EAM (1.10). However, the fact that we are operating in a two-dimensional setting makes the choice of a simple Lennard-Jones potential (1.8) rather convenient for the purpose of this comparison, as it is known to describe a stable triangular lattice in 2D. It is appreciated that the extension of the model to 3D would probably make the choice of EAM more adequate. This is not a major issue as the discussed procedure is general and can be implemented also in a fully 3D setting. Any potential admitting a site energy of the type (1.12) could be used as well.

More specifically, we consider the 2D Lennard-Jones potential introduced in [Pli95a, WSS87], which describes a stable 2D triangular lattice with interatomic distance $a = 0.687204444$. This Lennard Jones potential has been slightly modified from its standard form (1.8) in a way that it becomes a twice continuously differentiable function, which is necessary to ensure continuity of the stresses. We can write it explicitly

$$\varphi_p(r_{ij}) = \begin{cases} 4\varepsilon\left(\left(\frac{\sigma}{r_{ij}}\right)^{12} - \left(\frac{\sigma}{r_{ij}}\right)^{6}\right) + A, & for \quad r_{ij} < r_{in} \\ \sum_{k=0}^{4} g_k (r_{ij} - r_{in})^k, & for \quad r_{in} < r_{ij} < r_c \\ 0 & for \quad r_{ij} > r_c \end{cases} \tag{5.1}$$

where

$$\begin{aligned} A &= g_0 - 4\varepsilon\left(\left(\frac{\sigma}{r_{in}}\right)^{12} - \left(\frac{\sigma}{r_{in}}\right)^{6}\right) \\ g_0 &= -\frac{1}{6}(r_c - r_{in})(3g_1 + g_2(r_c - r_{in})) \\ g_1 &= \frac{24\varepsilon\sigma^6}{r_{in}^{13}}(r_{in}^6 - 2\sigma^6) \\ g_2 &= \frac{12\varepsilon\sigma^6}{r_{in}^{14}}(26\sigma^6 - 7r_{in}^6) \\ g_3 &= -\frac{(3g_1 + 4g_2(r_c - r_{in}))}{3(r_c - r_{in})^2} \\ g_4 &= \frac{(g_1 + g_2(r_c - r_{in}))}{2(r_c - r_{in})^3}\,. \end{aligned}$$

Parameters have value $\sigma = 2\sin(\pi/10)$, $\varepsilon = 0.5$, $r_c = 2.5$ and $r_{in} = 2$. Modifications, added to ensure continuity of derivatives, do not affect the overall form of the potential, illustrated in Figure 1.3.

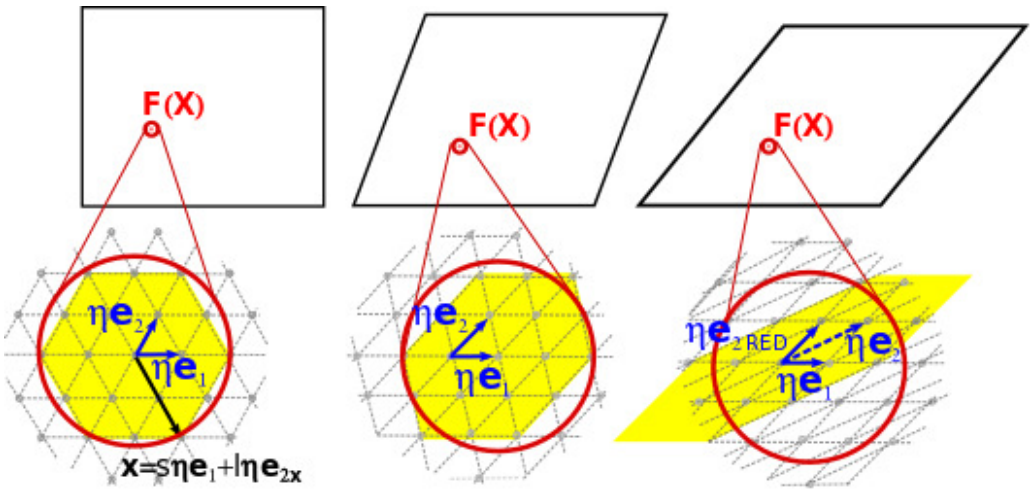

Figure 5.1: **Energy Construction based on Cauchy-Born Rule:** If the atomic lattice is assumed to follow the macroscopic deformation $\mathbf{F}$, the position of all atoms can be determined starting from the deformation of an atomic cell only, described by vectors $\mathbf{e}_1$ and $\mathbf{e}_2$. All the needed distances entering the computation of ϕ can then be evaluated as linear combinations of these vectors. The advantage of using the reduced vectors consist in the fact that one may consider the same atomic cell during the entire deformation, without changing the cut-off radius. If reduction is not used, distances of the sampled atoms starts to exceed the cut-off and the periodic behavior is gradually lost.

We can now obtain the lattice energy density starting from (1.12), and in the case of the Lennard-Jones crystal we need to compute:

$$\varphi = \frac{1}{\Omega_a} E_i = \frac{1}{\Omega_a} \frac{1}{2} \sum_j \varphi_p(r_{ij}), \tag{5.2}$$

where Ω_a is the volume of the atomic cell in the undeformed reference state and $\phi_p(r_{ij})$ is the pair potential (5.1). We recall that only atoms such that $r_{ij} = |\mathbf{x}_j - \mathbf{x}_i| \leq r_c$ contribute to (5.2). Now we adopt the CBR to derive a continuum energy density ϕ as in (3.22). Since the deformation of atomic positions follows local $\mathbf{F}$ homogeneously, positions $\mathbf{x}_j - \mathbf{x}_i$ of all the j atoms in (5.2) are known and can be written as a linear combinations of the the unit basis $\mathbf{e}_I$ (2.36) describing the triangular lattice:

$$\mathbf{x}_j - \mathbf{x}_i = s\mathbf{F}\eta\mathbf{e}_1 + l\mathbf{F}\eta\mathbf{e}_2 \qquad l, s \in \mathbb{Z} \quad l\eta\mathbf{e}_1 + s\eta\mathbf{e}_2 < r_c\,. \tag{5.3}$$

where η is a factor accounting for the actual dimensions of the atomic cell. Considering that distances can be written as a function of metric components:

$$r_{ij} = \sqrt{(\mathbf{x}_j - \mathbf{x}_i) \cdot (\mathbf{x}_j - \mathbf{x}_i)} = \sqrt{\eta^2 s^2 C_{11} + 2\eta^2 sl C_{12} + \eta^2 l^2 C_{22}}\,. \tag{5.4}$$

we can derive a continuous energy $\phi(\mathbf{C})$ in a straightforward manner, simply replacing expressions (5.4) for r_{ij} in (5.2). At this point, we deviate from the more conventional

Cauchy-Born approaches (as the local QC) by focusing on the reference energy ϕ_0 rather that ϕ directly. This is achieved simply by using reduced metrics $\bar{C}_{IJ}$ in (5.4), thus obtaining:

$$\phi_0 = \frac{1}{\Omega_a}\frac{1}{2}\sum_{s}^{r^*}\sum_{l}^{r^*}\varphi_p(\sqrt{\eta^2 s^2\bar{C}_{11} + 2\eta^2 sl\bar{C}_{12} + \eta^2 l^2\bar{C}_{22}})\,, \tag{5.5}$$

where $\bar{C}_{IJ}$ are the reduced metrics and r^* is an integer such that $r^*\eta\mathbf{e}_1 = r_c$. Since we use reduced metrics, the obtained energy is defined in the fundamental domain D.

The $\mathcal{C}^2$ continuity of the pair interactions potential $\varphi_p(r_{ij})$ ensures that the reference energy ϕ_0 is $\mathcal{C}^2$ continuous as well. Then, the energy can extended to the entire space of metric tensors $\mathcal{Q}_2^+$ by means of (2.20). We remark that, since $GL(2,\mathbb{Z})$ operates only for isochoric transformations, Lagrange reduction does not interfere with the volumetric part of the energy that becomes automatically accounted for in the illustrated procedure. Therefore, it does not need to be added explicitly as a separate term.

We recall that the derivatives $\frac{\partial\phi_0}{\partial\bar{C}_{IJ}}$ and $\frac{\partial^2\phi_0}{\bar{C}_{IJ}\bar{C}_{IK}}$ are needed for the evaluation of the second Piola-Kirchhoff stress tensor $\mathbf{S}$ given by equation (3.29) and of the elastic moduli $\boldsymbol{\mathcal{C}}$ (3.30). They are also obtained in a straightforward manner:

$$\frac{\partial\phi_0}{\partial\bar{C}_{IJ}} = \frac{1}{\Omega_a}\frac{1}{2}\sum_{s}^{r*}\sum_{l}^{r*}\frac{\partial\varphi_p}{\partial r}\frac{\partial r}{\partial\bar{C}_{IJ}}\,, \tag{5.6}$$

$$\frac{\partial\phi_0}{\partial\bar{C}_{IJ}\bar{C}_{KL}} = \frac{1}{\Omega_a}\frac{1}{2}\sum_{s}^{r*}\sum_{l}^{r*}(\frac{\partial^2\varphi_p}{\partial r^2}\frac{\partial r}{\partial\bar{C}_{IJ}}\frac{\partial r}{\partial\bar{C}_{KL}} + \frac{\partial\varphi_p}{\partial r}\frac{\partial^2 r}{\partial\bar{C}_{IJ}\bar{C}_{KL}})\,. \tag{5.7}$$

The use of the reduced metrics in the definition of the energy density is not essential, but allows one to maintain the correct symmetry no matter how large is the applied deformation. Indeed, while the use of (2.20) ensures that $GL(2,\mathbb{Z})$ is preserved indefinitely, the conventional Cauchy-Born based methods would actually need to use increasing values of the cut off radius in order to maintain the periodicity of the energy landscape when deformation are large. In Figure 5.1 we give a schematic representation of this effect. Indeed, while the reduction ensures that the atoms over which the energy is sampled are contained inside the cut-off radius, this does not happen when one uses non-reduced metrics, as the sampled region becomes increasingly distorted.

5.1.1 Energy Landscape

In the following we will refer to the strain energy density defined above as *Homogeneous Lennard Jones* (HLJ). In Figure 5.2 we illustrate the isochoric part of the obtained energy

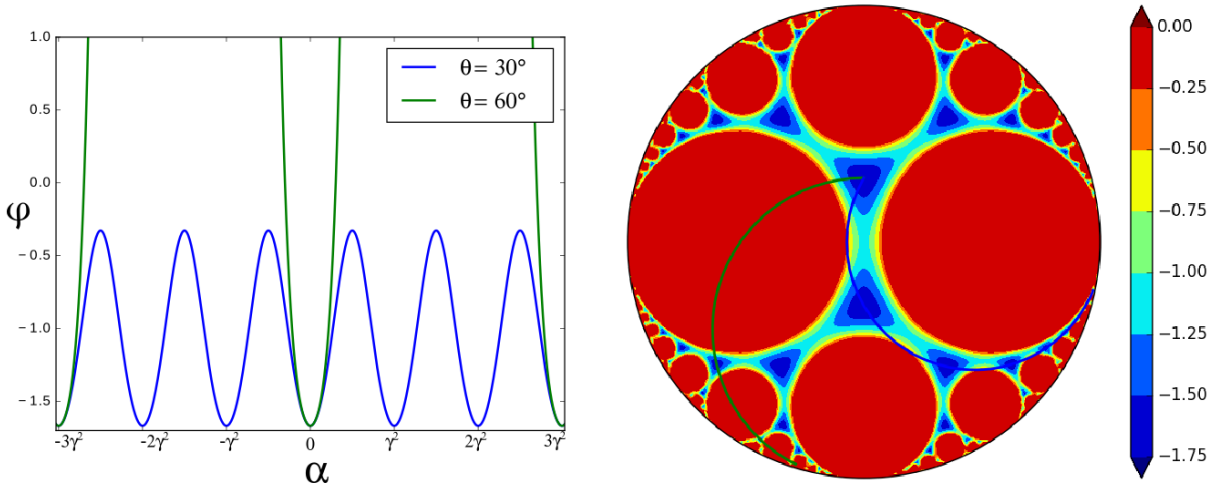

Figure 5.2: **Energy landscape for the HLJ energy:** (isochoric part) obtained from the considered Lennard-Jones potential is shown on the Poincaré disk with evidence on the shearing paths $\theta = 30°$ and $\theta = 60°$. Cut-off $= 0$ has been used for an improved visualization of low-energy barriers and wells. Notice how, qualitatively, the landscape resembles the one obtained for the polynomial energy.

landscape on the Poincaré disk. Note that the qualitative shape of the energy does not differ significantly from the one obtained from the polynomial energy in the case of the triangular crystal (Figure 2.7, on bottom). This is somewhat expected, as the global periodic behavior is dictated by the $GL(2,\mathbb{Z})$ directly.

The implementation of HLJ and its use in numerical simulations highlighted the importance of the volumetric part of the energy. As we have already mentioned, it is automatically accounted for in the case of HLJ, if we use procedure (5.5), where Lagrange reduction is invoked only for volume-preserving deformations. We recall that, in the polynomial potential, the volumetric term was added explicitly using a phenomenological function of $\det \mathbf{C}$. This arbitrariness was justified by the fact that volume-related effects are generally thought to have limited influence in plasticity, since the slip associated with dislocation flow is volume preserving. Our study instead, highlights some interesting effects arising exactly from the specifics of the volumetric response.

To be more precise, we consider the patterns obtained from the homogeneous nucleation analysis in the case of shearing path $\theta = 60°$, see in Figure (5.3). Observing the distribution of metric tensors in the configurational space, one can notice that the pattern obtained for HLJ is much sparser than the pattern in the polynomial model. Histograms of the metric components C_{12} (see Figure 5.4) confirm that the well $\mathbf{T}_1^{60°}$ (with $C_{12} = -0.577$) is the most engaged in both cases. However, HLJ show the secondary activation of other wells and the appearance of other defects, that looks like voids or nanocracks. Those always

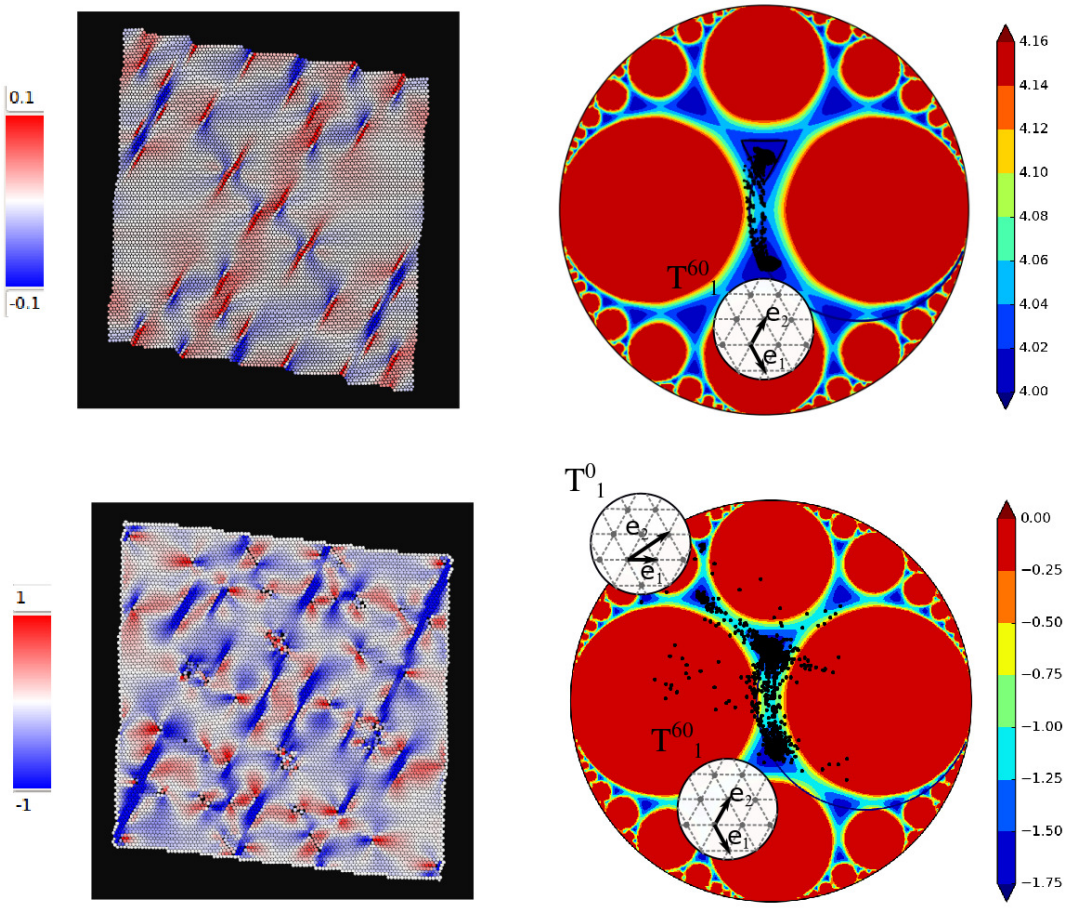

Figure 5.3: **Comparison of Post-Instability Patterns in Polynomial and HLJ:** Post-instability patterns (on a $N = 10^4$ domain) for the $\theta = 60°$ simple shear are shown in terms of Cauchy stress component σ_{xy}. Polynomial energy on top and HLJ on bottom. While the overall behaviour of the crystal is the same, the case of HLJ is richer, more wells are engaged and different types of defects appear.

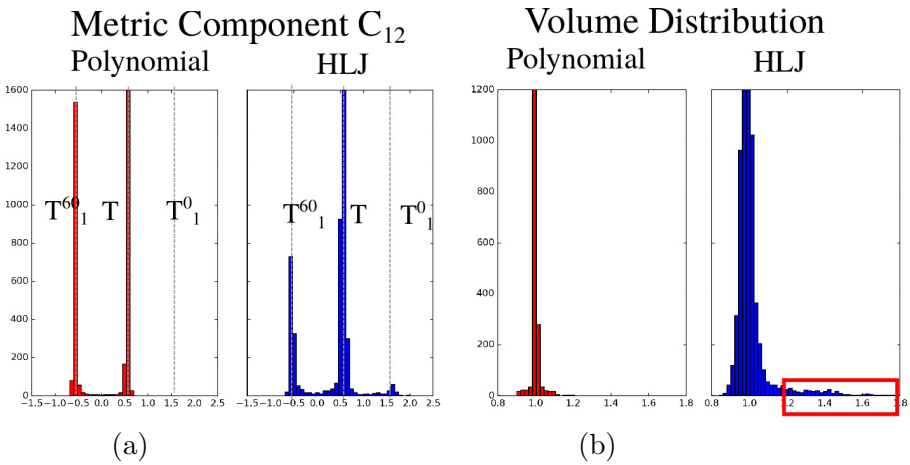

Figure 5.4: **Histograms of Metric Component C_{12} and of Elements Volume:** (a) Distribution of metric component C_{12} show that $\mathbf{T}_1^{60^\circ}$, of metric $C_{12} = -0.5774$, is the most active well (other than reference well $\mathbf{T}$, with metric component $C_{12} = 0.5774$) for both polynomial and HLJ energies. (b) Distribution of elements volume, the great majority of elements preserve their volume (unitary), but HLJ shows the presence of few elements whose volume is very high. Histogram y-axis has been cut to better visualize the distribution.

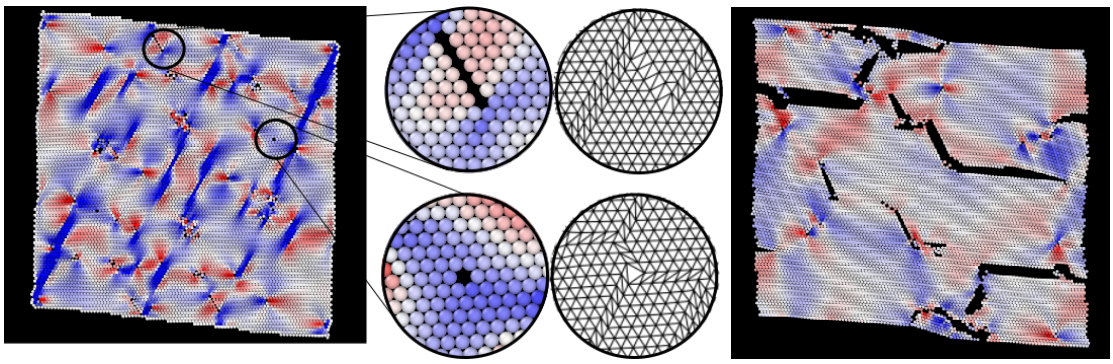

Figure 5.5: **Volumetric Defects:** (a) HLJ energy is characterized by the appearence of defects such as voids and nano-cracks, associated, in our modeling framework, with element dilatation. (b) The instability of a sample, to which dilatation is imposed, manifests itself with the formation of more pronounced nano-cracks.

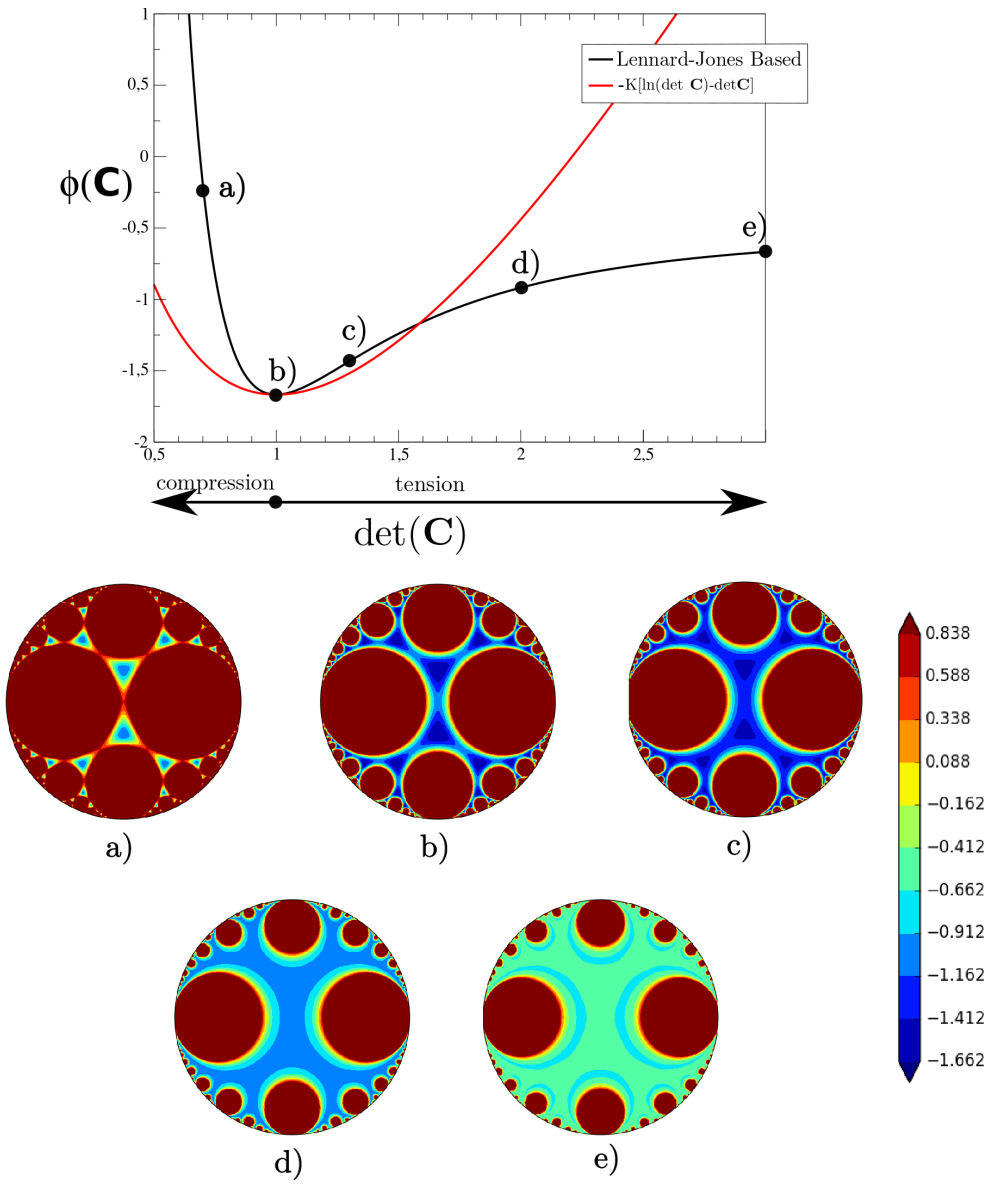

Figure 5.6: **Volumetric Response** On top: response to uniaxial tension and compression of the Polynomial and HLJ energies is compared. The pair-potential based strain energy density is characterized by a flattening in correspondence of tension. On bottom, we show the evolution of the HLJ energy landscape in correspondence of different values of det $\mathbf{C}$. While in compression one observes an overall increase of the energy density which causes steepening of the barriers, the tension response is characterized by a progressive flattening of the overall landscape.

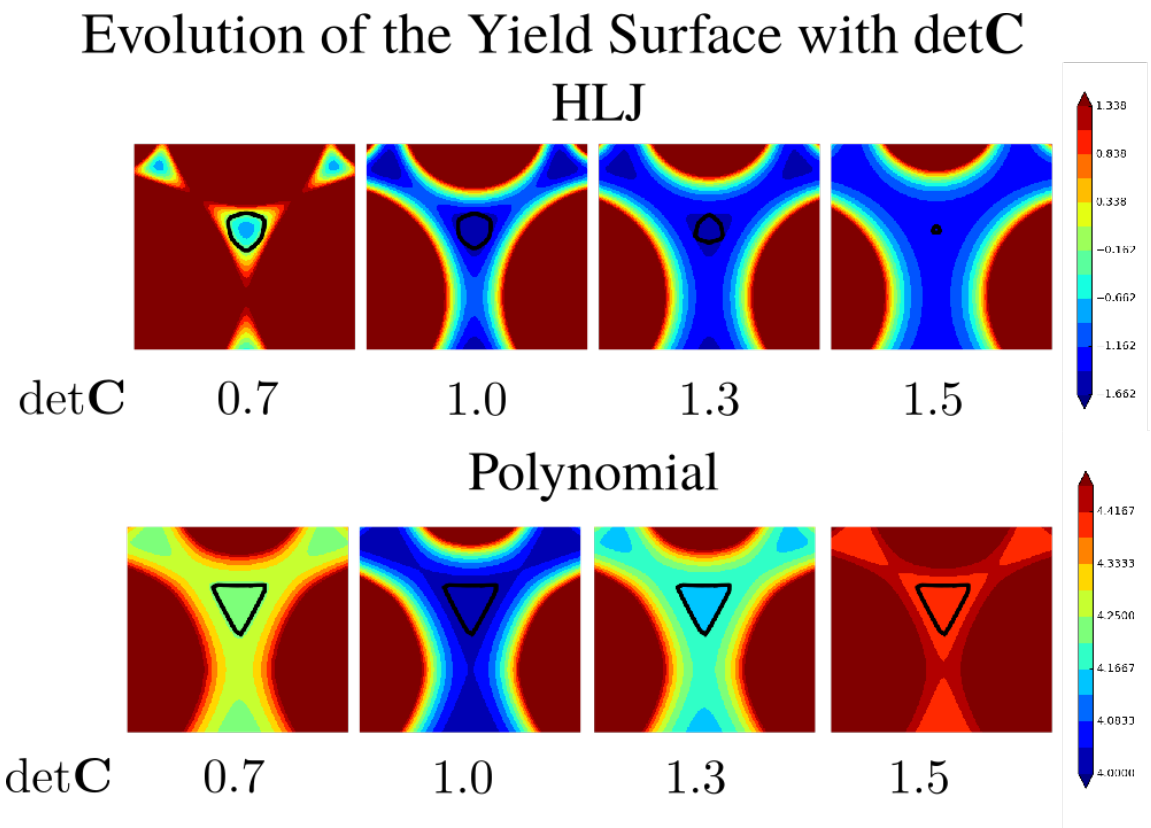

Figure 5.7: **Dependence on** $\det \mathbf{C}$ **of the Yield Surface:** Evolution of the stability region, that we called *yield-surface*, is shown for the Polynomial and the HLJ energy. The peculiar response to tension in the HLJ energy causes the progressive shrinking of its stability region, up to a complete disappearance.

appear in HLJ, while they are not observed when we use the polynomial energy. In Figure 5.5 we illustrate these defects in detail. The void-like defects may be interpreted also as vacancies. By looking at the element triangulation, we observe that these defects originate from the dilatation of some of the elements. This is confirmed by histograms of volume element distribution, showed in Figure 5.4. Indeed, while the polynomial energy show a more or less symmetric distribution of volume values for shrunken and dilated elements, the case of HLJ is characterized by an asymmetry towards very high volumes.

This asymmetry can be easily explained when we observe the different response that the two energies show for uniaxial tension and compression along the vertical axis $\mathbf{Y}$, see Figure 5.6. The phenomenological term $-K(\ln(\det \mathbf{C}) - \det \mathbf{C})$ increases indefinitely for both compression ($\det \mathbf{C} < 1$) and tension ($\det \mathbf{C} > 1$). Instead, HLJ shows a sharp increase in compression, but it reaches a plateau in tension for a certain value of $\det \mathbf{C} > 1$. This Lennard-Jones like behavior is also observed in correspondence of others biaxial and uniaxial deformations and is a general feature coming directly from the chosen pair-interaction potential.

To better illustrate this point, in Figure 5.6 we show also the evolution of the energy landscape as we change the value of $\det \mathbf{C}$. We observe an overall steepening of the valleys and the increase of the energy barriers in correspondence of compression. For tension, the landscape gradually flattens, up to the point of the disappearance of both the barriers and the wells. This means that beyond a certain value of $\det \mathbf{C} > 1$ elements may expand with almost no energetic cost. As a result, the system will undergo an instability with the formation of what can be interpreted as a crack. We show an example of this in Figure 5.5.

This difference in behavior can also be seen in the structure of the stability region. Indeed, while in the case of the polynomial energy the yield surface does not change significantly with changing $\det \mathbf{C}$, in the case of HLJ it progressively shrinks under increasing $\det \mathbf{C}$, up to a point where it reduces to a point. We highlight that cracks are never observed if we use the term $-K(\ln(\det \mathbf{C}) - \det \mathbf{C})$ for the description of our volumetric response, and their appearance is indeed related to the flattening of HLJ potential at large values of $\det \mathbf{C}$. This type of behavior is not a feature of the chosen Lennard-Jones interaction, but is common to all pair-potentials (the interaction goes to zero for distances $r_{ij} > r_c$).

5.1.2 Homogeneous Nucleation

In this subsection we discuss the results obtained from the homogeneous nucleation tests for the HLJ energy. The objective is to show that the interesting features highlighted by the use of the polynomial energy are general and are encountered in HLJ based model as well. In particular, we would like to check the robustness of the coupling between differ-

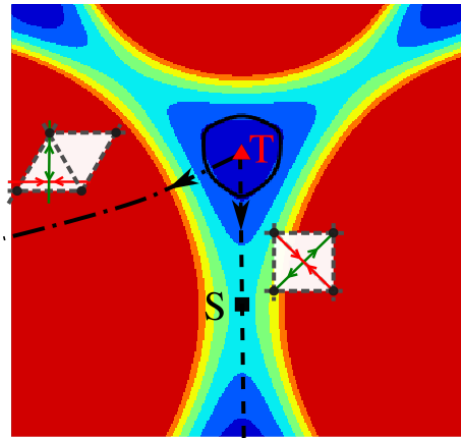

Figure 5.8: **HLJ Yield Surface:** By using criterion (4.10), the yield surface is constructed. As in the Polynomial energy, maximum and minimum values of α_c are found along the fat rhombic and the skinny rhombic shear paths, respectively.

ent slip systems, due to the presence of the square saddle point **S**, and the ubiquity of the "banded modes" preceding instability. For the moment, we limit our analysis to the loading paths evolving along the hyperbolic surface $\det \mathbf{C} = 1$. In the next Section we will consider also deformations with nonzero volumetric component.

The same paths considered previously in the case of the polynomial energy are analyzed here, in particular, the two pure shears describing the skinny rhombic (2.31) and the fat rhombic (2.38) configurations, and the two simple shears $\theta = 60°$ and $\theta = 30°$. As before, these paths are chosen to guarantee a comprehensive sampling of the landscape, with both highly symmetric and generic directions taken into account.

Using criterion (4.10) we identified the yield surface for the HLJ energy, see Figure 5.8. As in the polynomial energy case, the maximum and the minimum value of the critical load α_c are found along the fat rhombic and the skinny rhombic pure shear paths, with values $\alpha_c = 0.164$ and $\alpha_c = 0.130$, respectively. Note, however, that the shape of this yield surface is rounder than in the case of the polynomial energy (Figure 4.16). Moreover, the instability is encountered at lower values of α, which makes the elastic region enclosed by the yield surface smaller.

As we have done in the previous Chapter, we look at directions $\mathbf{n}$ and polarization vectors $\mathbf{m}$ along the selected paths. We recall that, once a non-trivial vector $\mathbf{n}$ delivering equality in (4.10) has been found, the associated vector $\mathbf{m}$ is obtained solving the eigenproblem (4.6). We show the graphs presenting $\det q_{ik}$ profiles as a function of the angle ξ, which characterize the orientation of $\mathbf{n}$. While in the case of the polynomial energy we

always observed that $\mathbf{n}^{\perp} \parallel \mathbf{m}$, a fact that is characteristic of incompressible materials, this does not happen in general for HLJ.

Using the HLJ energy, we observe along the fat rhombic path the simultaneous appearance of two instability directions, respectively $\xi_1 = 87.93°$ and $\xi_2 = -19.49°$ (see Figure 5.9). The corresponding polarization vectors, inclined with respect to the horizontal direction with angles $\chi = -20.69°$ and $\chi = 89.17°$, are not perpendicular to wave directions. Moreover, neither $\mathbf{n}_i^{\perp}$ and $\mathbf{m}_i$ are oriented along crystallographic planes.

Along all the other considered paths we obtain only one unstable wave direction. A peculiarity of the skinny rhombic path is that $\mathbf{n}^{\perp}$ is almost perpendicular to the horizontal axis and is practically parallel to the corresponding polarization vector $\mathbf{m}$, as we illustrate in detail in Figure 5.9.

Results for the two simple shears $\theta = 60°$ and $\theta = 30°$ are illustrated in Figure 5.10. Along these directions, $\mathbf{m}$ and $\mathbf{n}^{\perp}$ are not parallel and none of them is aligned with crystallographic planes.

Despite the presence of a certain misalignment between $\mathbf{n}^{\perp}$ and $\mathbf{m}$ in the majority of cases, the angles between them are always much smaller than 90°. Therefore, as in the case of the polynomial energy, we expect a shear-like instability appearing as nucleation of dislocation dipoles oriented along $\mathbf{n}^{\perp}$.

Simulation Results

As for the previous Chapter, we repeated simulations for different boundary conditions and different system sizes. Here we show the results obtained for $N = 10^4$. Quasi-static loading is applied with load increments of $\Delta\alpha = 10^{-3}$ which are subsequently refined to $N = 10^{-4}$ when value of $\det q_{ik}$ approaches 0. The loading at which the first instability is observed numerically, α_c^*, is in very good agreement with the analytical value α_c as we show in Figure 5.11. In contrast to the polynomial case, we do not encounter here a systematic delay of the numerical instability, and the difference between α_c and α_c^* are of the order of 10^{-3}.

The characteristic modulation preceding the dislocation nucleation instability is still observed. In Figure 5.11 we show the periodic modulation obtained for the two simple shear directions. The bands are aligned along the directions $\mathbf{n}^{\perp}$ as it is predicted by the stability analysis. Dislocation nucleation develops through the same mechanism as in the case of the polynomial energy, with dislocation dipoles developing as a result of the spreading of the modulation bands (see Figure 4.21). We find again that the instability manifests

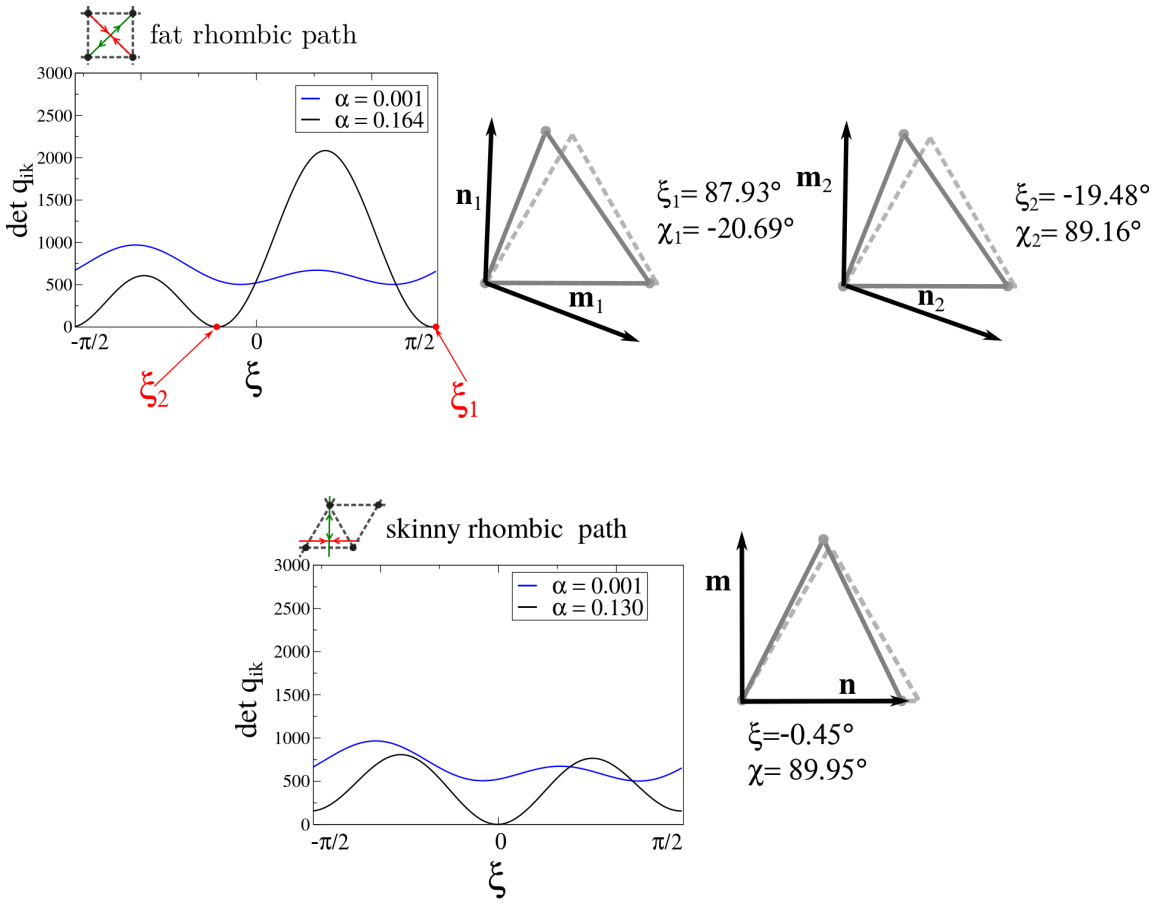

Figure 5.9: **HLJ** $\det q_{ik}$ **Profiles along the Fat Rhombic and the Skinny Rhombic Paths:** Evidence on load α_c for which equality in (4.10) is satisfied. the fat rhombic pure shear (on top) shows the simultaneous appearance of two instability directions, while just one appears in case of skinny rhombic path (on bottom). On the side of each graph we illustrate the orientation of the wave directions $\mathbf{n}$ and the polarization vectors $\mathbf{m}$, with respect of the deformed lattice cell at $\alpha = \alpha_c$. In the fat rhombic path, differently from the polynomial energy, wave polarization $\mathbf{m}$ is not aligned with $\mathbf{n}^{\perp}$, (while it is still the case in the skinny rhombic path).

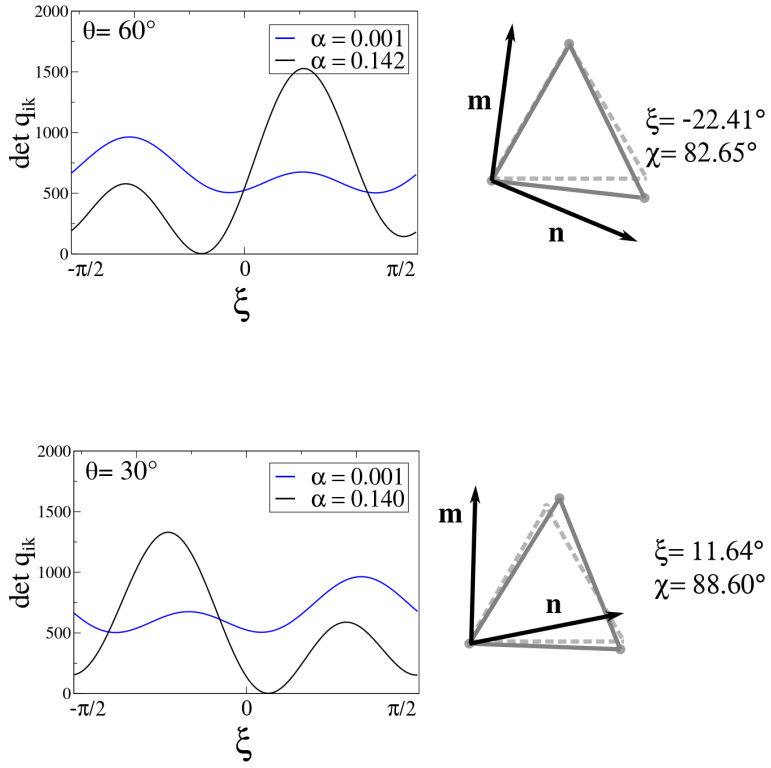

Figure 5.10: **HLJ** $\det q_{ik}$ **Profiles along** $\theta = 60°$ **and** $\theta = 30°$ **Simple Shear Paths:** Profiles for $\theta = 60°$ and $\theta = 30°$ loading paths are shown with evidence on load α_c for which equality in (4.10) is satisfied. Both these simple shears are characterized by the presence of one unstable mode only, not aligned with the crystallographic directions. Differently from the polynomial energy, the wave polarization $\mathbf{m}$ is not aligned with $\mathbf{n}^{\perp}$.

itself in the configuration space through the spreading of the element points along an elongated interval pointing towards point **S**. The configurational points then spread along the valley in the energy landscape and eventually reach the neighboring wells. The fact that the modulation formation is influenced by the presence of the saddle **S**, highlights the importance of this point in characterizing the ultimate defect pattern.

Most importantly, the double slip activation associated with the fat rhombic path is encountered also in HLJ, and both wells $\mathbf{T}_1^{60^\circ}$ and $\mathbf{T}_{-1}^{0^\circ} \equiv \mathbf{T}_1^{120^\circ}$ end up being be engaged in the post instability pattern. This mechanism is independent of the used boundary conditions, and in Figure 5.12 we report similar results for fixed and periodic boundaries. Activation of the two slip systems is clearly observable in Figure 5.14 where a detail of the triangulation (for periodic boundary) is illustrated.

Along the other pure shear path we observe the same behavior as in the case of the polynomial energy. The instability develops tangentially to the yield surface and, after the appearance of a vertical modulation, we obtain a stable configuration in which elements are arranged periodically in differently oriented regions. The relative misorientation is less pronounced than in the case of the polynomial energy, but still clearly present, see Figure 5.13. Under further loading, the system evolves towards collective nucleation of dislocations along the slip systems $\mathbf{T}_1^{60^\circ}$ and $\mathbf{T}_{-1}^{0^\circ}$, which are symmetrically oriented with respect to the vertical direction, that is parallel to $\mathbf{n}^\perp$. A detail of the triangulation, showing clearly the presence of these two slip systems, is shown in Figure 5.14.

To summarize, we have shown as the main phenomena exhibited by the polynomial model are robust as long as the energy density respects the $GL(2,\mathbb{Z})$ symmetry. The observed differences, such as the misalignment between $\mathbf{n}^\perp$ and $\mathbf{m}$, are likely to be related to the volumetric part. This volumetric component is also what causes the appearance of a broader variety of defects, such as voids and nano-cracks.

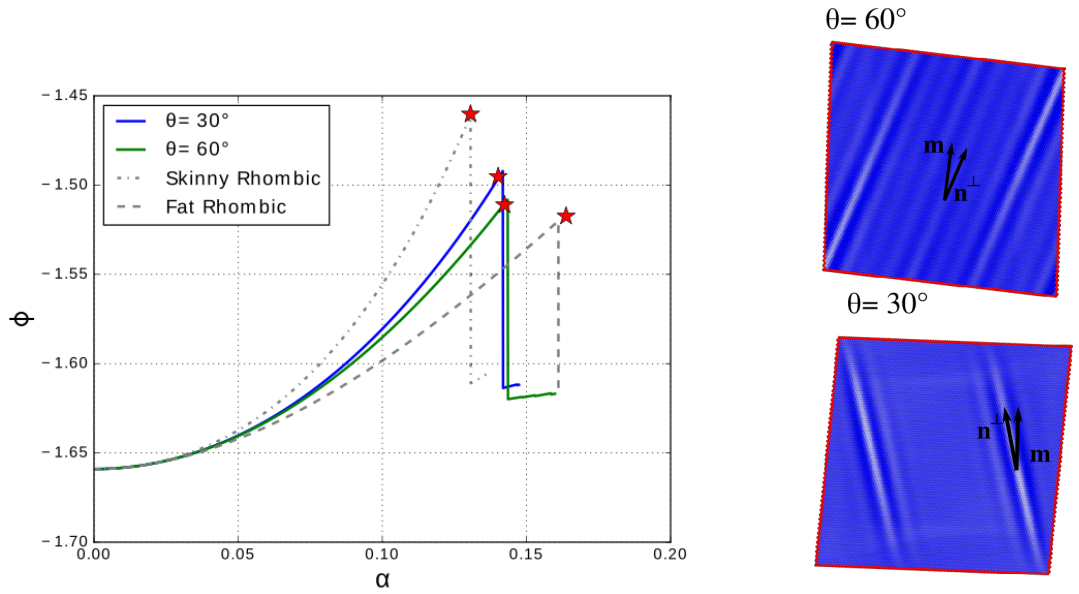

Figure 5.11: **First Instability in HLJ:** On top, profiles of the energy density from $\alpha = 0$ up to first instability α_c^*, together the considered path, are shown for simulations of $N = 10^4$ nodes and fixed boundary conditions. In all cases, there is a good agreement with the analytical prediction α_c (highlighted with a red star symbol). On bottom, the equilibrium configuration just preceding instability is shown. Even in this case, it is possible to observe the appearance of a modulation oriented along $\mathbf{n}^\perp$.

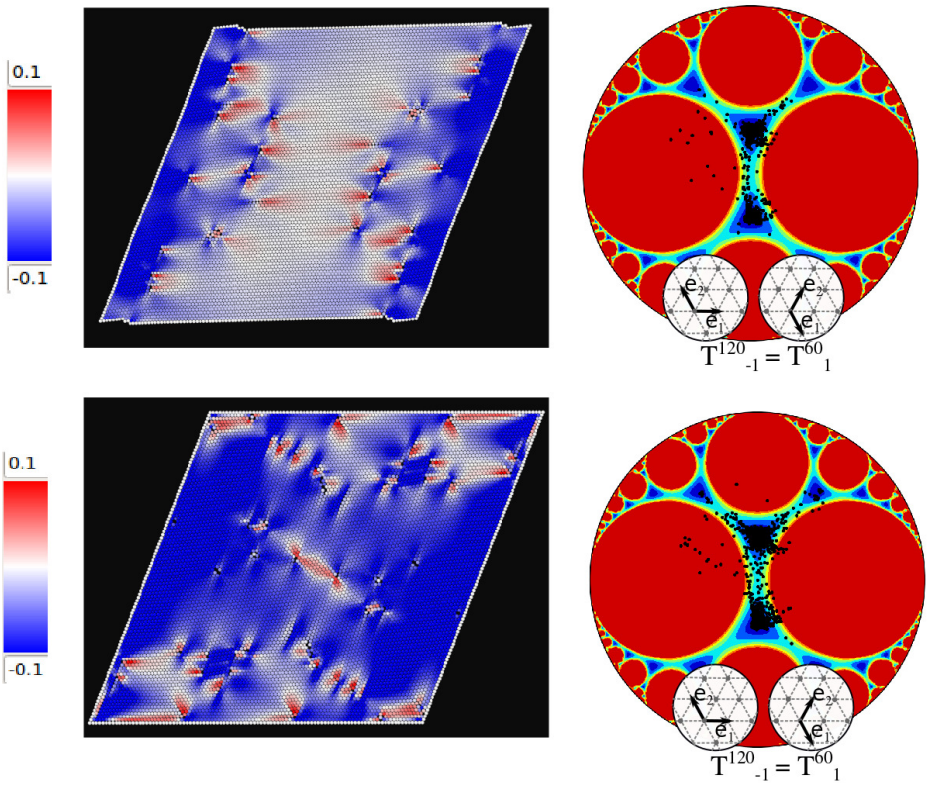

Figure 5.12: **Post-Instability Pattern along the Fat Rhombic Pure Shear:** A $N = 10^4$ domain is considered. on the top and bottom, results from simulations with fixed and periodic boundary conditions are shown respectively. (a)Cauchy stress σ_{xy} field is showed in the full domain. (b) Elements distribution in the configuration space. The simultaneous presence of the three wells $\mathbf{T}$, $\mathbf{T}_1^{60^\circ}$, and $\mathbf{T}_{-1}^{0^\circ}$ is evident when one considers the corresponding triangulation, of which we show a detail in Figure 5.14.

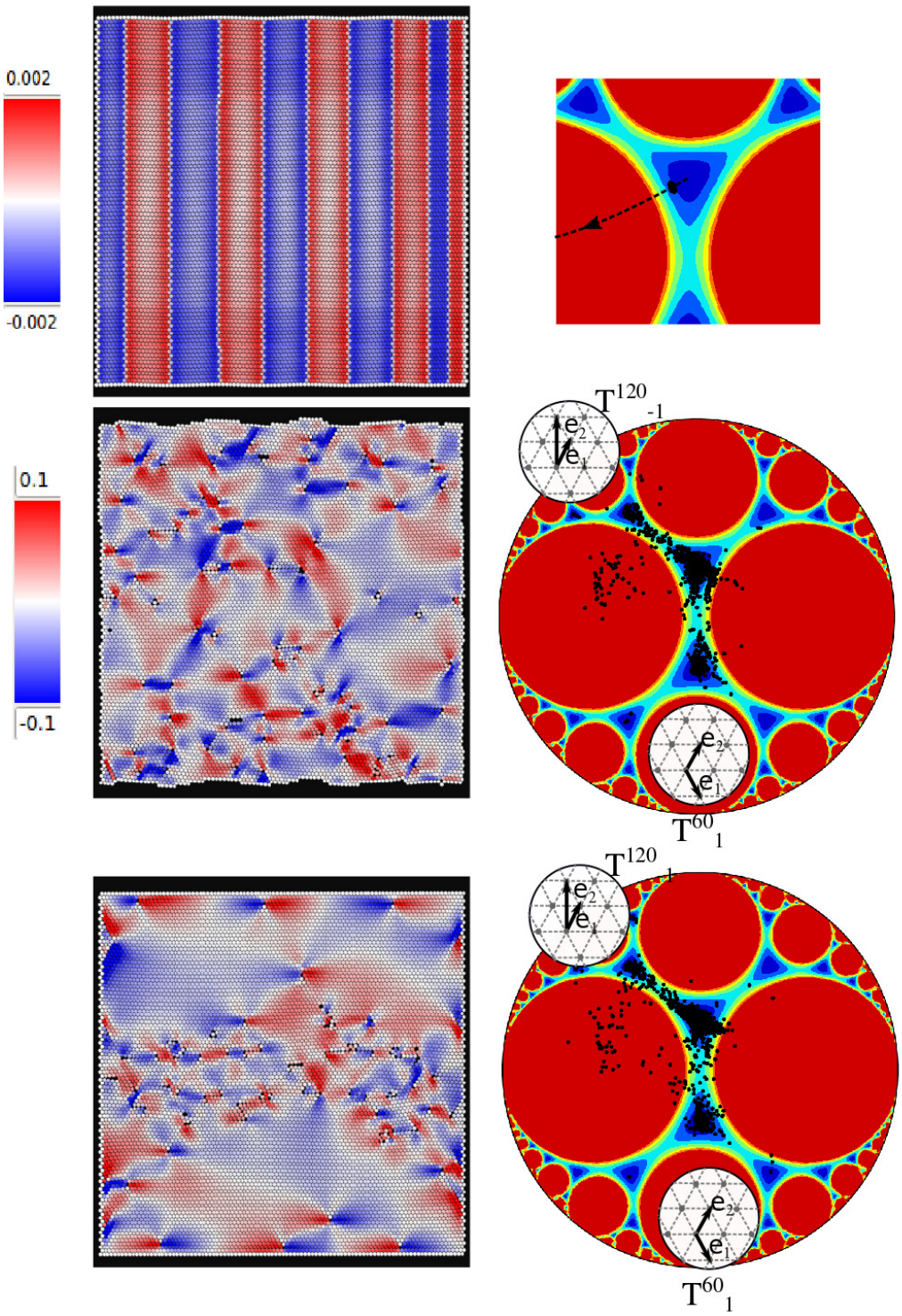

Figure 5.13: **Post-Instability Pattern along the Skinny Rhombic Pure Shear:** A $N = 10^4$ domain is considered. on the top and bottom, results from simulations performed with fixed and periodic boundary conditions are shown, respectively. (a) Cauchy stress σ_{xy} field is shown in the full domain. (b) Elements distribution in the configurational space. The simultaneous presence of the three wells $\mathbf{T}$, $\mathbf{T}_1^{60^\circ}$, and $\mathbf{T}_{-1}^{120^\circ}$ is evident when one considers the corresponding triangulation (Figure 5.14). When periodic boundaries are used, dislocation nucleation is preceded by a stable modulation, illustrated on the top of the figure.

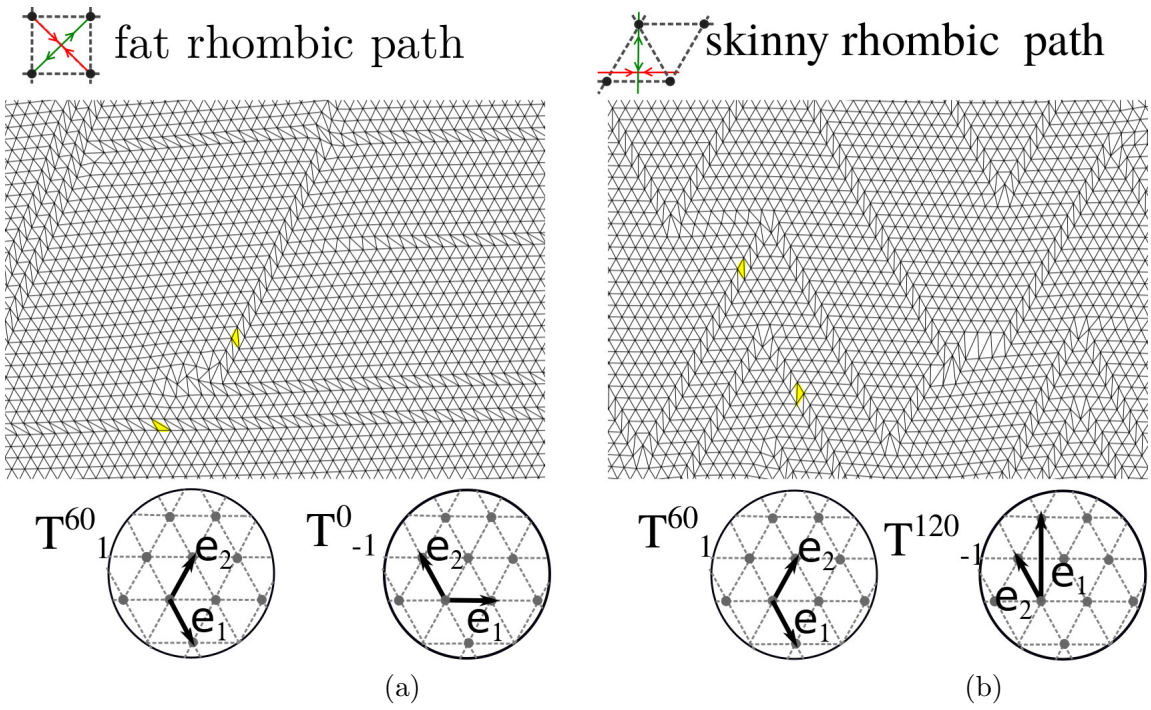

Figure 5.14: **Details of the Post-Instability Patterns along the two Rhombic Pure Shears:** Details of the triangulation corresponding to post instability patterns along the fat rhombic (a), and the skinny rhombic (b) pure shears show clearly the activation of two different wells simulaneously. These are $\mathbf{T}_1^{60^\circ}$, and $\mathbf{T}_{-1}^{0^\circ}$ in the case of the fat rhombic path, and $\mathbf{T}_1^{60^\circ}$ and $\mathbf{T}_{-1}^{120^\circ}$ in the case of the skinny rhombic path.

5.2 Comparison with Molecular Statics

In the previous Section we compared two different $GL(2,\mathbb{Z})$-invariant theories: one constructed starting from a phenomenological polynomial potential and another one obtained from an interatomic potential directly. They were shown to share common properties and exhibit analogous behavior during dislocation nucleation (first instability), with some differences related to the volumetric response.

In this Section we compare the predictions of the HLJ model with the fully atomistic simulations, performed using MS (both approaches use interatomic potential (5.1)). The purpose of such comparison is to characterize more quantitatively the differences between these two approaches and to highlight the atomistic features that the coarse-grained HLJ is capable, or not capable, to capture. Indeed, due to its inherent locality, HLJ is expected to lose at least some features of the fully atomistic description. On the other hand, since it does not require the resolution of all particle to particle interactions, is more effective computationally.

Cauchy-Born based energy densities are known to describe dislocation cores [TPO96], which can nucleate and stabilize due to the fact $GL(2,\mathbb{Z})$ symmetry is accounted for. However, the deformations developing at distances shorter than the cut-off radius cannot be properly described, and therefore these cores are coarser than the ones observed in the fully non-local atomistic simulations. Some authors consider these local representation of dislocations to be too coarse and prefer to adopt other methods [TSBK99, MR08]. Here we develop a systematic comparison between simulations using a $GL(2,\mathbb{Z})$ invariant energy and the MS approach with the objective to quantify the limits of the local representation of dislocation.

In the following Sections we neglect the fact that each element in our mesh actually represents a (small) cluster of atoms deforming homogeneously. To make the comparison more direct, we compare the HLJ model with MS simulations with a number of atoms comparable with the number N of discretization nodes used in the mesoscopic model. Therefore, one may see HLJ as atomistic scale simulations in which the actual inhomogeneity of each particle environment is neglected. Even in this atomistic perspective, HLJ remain advantageous because one does not need to look for all neighboring particles and the nodal forces are computed directly from the deformation gradient $\mathbf{F}$. Moreover, the method offers a straightforward coarse-graining procedure through simple reduction the actual number of nodes.

We begin the comparison by presenting the structure of a single dislocation core. Then we perform homogeneous nucleation simulations to ensure that predictions based on condition (4.10) remain valid also in a fully atomistic setting. Simulations are performed

for different values of det $\mathbf{C}$ and obtained patterns are compared. We conclude the chapter showing some example of nano-indentation tests. All the presented MS simulations were performed using the open-source molecular dynamics code LAMMPS (Large-scale Atomic/Molecular Massively Parallel Simulator) [Pli95b].

5.2.1 Dislocation Core

The representation of the dislocation core is an essential test allowing one to asses the possibility of using HLJ for modeling plasticity. Considering this, we put in direct comparison dislocation cores structures as they appear in MS and HLJ. Volterra displacement field (3.44) is enforced on the MS and HLJ domains, and then allowed to relax. In both cases, an edge dislocation structure emerges in the middle of the domain. Both such dislocations are characterized by similar distribution of the energy density, which we illustrate by comparing the energy profiles along the horizontal axis passing through the core (Figure 5.15). However, the associated stress fields are different in scale, as we illustrate in Figure 5.16 [2].

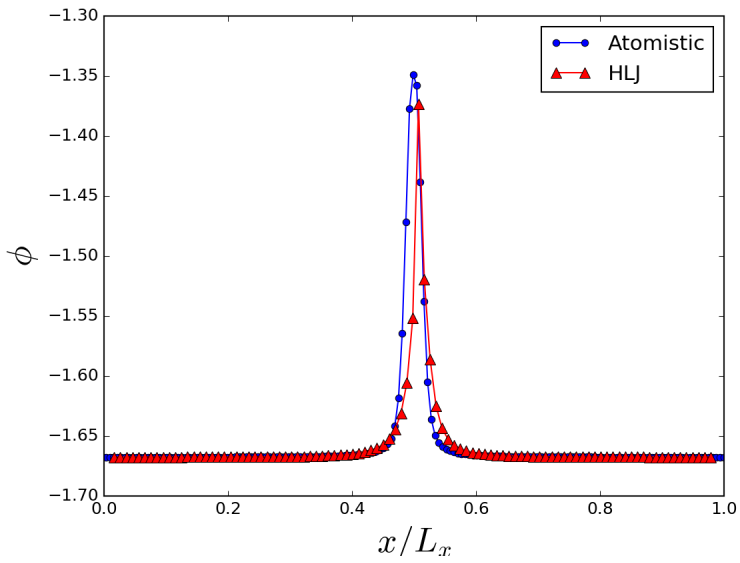

Figure 5.15: **Dislocation Energy Density:** Comparison between the energy density associated to an edge dislocation core in HLJ and MS.

[2] We recall that in MS stresses are not obtained directly, as they are macroscopic measures, but are evaluated post-processing atomistic forces in neighboring atoms (see for instance [TPM09])

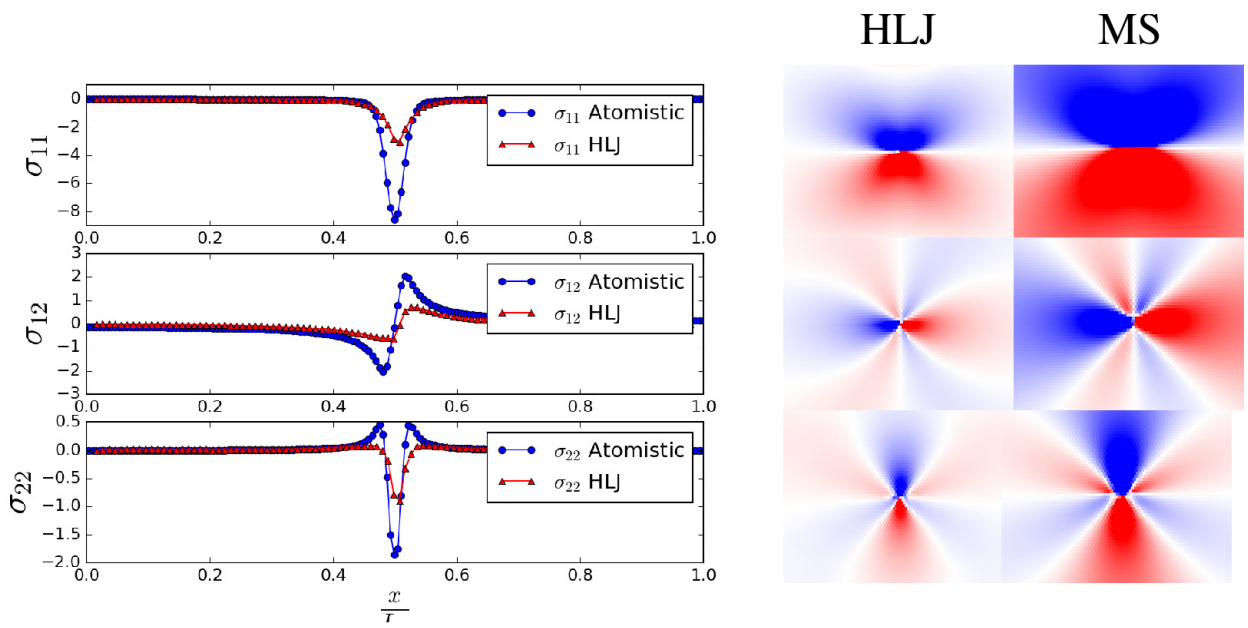

(a) (b)

Figure 5.16: **Dislocation Stress Field:** Comparison between dislocation stress fields for a single dislocation in HLJ and MS.

Both representations of dislocations start from the same initial configuration, however the atomistic cores exhibit higher stress fields than the cores obtained using HLJ. At the same time, the qualitative shapes of the stress fields are similar (as it was also the case for the polynomial energy). This confirms that HLJ can be seen as a coarse representation of MS where some details of the core structure are lost.

One way to improve the continuum description would be to include gradient terms in the development of ϕ, as it is done in other continuum theories attempting the fine description of the core regions [LMA06]. For the moment, we remain with our local representation even if the cores are somewhat misrepresented in terms of the associated stresses. We believe that this is not a crucial flaw in view of the fact that the main application of the method is the description of a large number of interacting dislocations (rather than a detailed description of a single defect).

5.2.2 Homogeneous Nucleation

In this Section we compare the results obtained from the MS homogeneous nucleation tests with what observed for the model using the HLJ energy. Moreover, in addition to the

reference case $\det \mathbf{C} = 1$, we study three different situations when the imposed deformation has either $\det \mathbf{C} = 0.7$ (compressed) or $\det \mathbf{C} = 1.3$ (extended). In this way, we include volumetric effects in the comparison. Instead of simple shear (2.28) we apply a slightly different deformation field:

$$\mathbf{F} = \kappa \mathbf{I} + \alpha \mathbf{a} \otimes \mathbf{n}\,, \tag{5.8}$$

where $\kappa = \sqrt[4]{\det \mathbf{C}}$.

Consider three distinct surfaces $\det \mathbf{C} = \textit{constant}$. In Figure 5.17 we show their Poincaré disk representation, we also show the energy landscape along some simple shears trajectories intersecting the fundamental domain, thus highlighting the periodic behavior of the energy and the surface-dependent heights of the energy barriers. We remark that the homogeneous energy landscape is identical for MS and HLJ models. We note again that compression causes a steepening of the barriers while extension makes the overall energy landscape flatter.

MS simulations were performed on square domains with about 10^4 atoms and they are compared with HLJ simulations describing similar number of nodes. Both fixed and periodic boundary conditions were used, to ensure independence of the observed patterns from the loading mode. First of all, we verified the agreement of the observed critical load α_c^* with the analytical value α_c obtained from the acoustic tensor analysis. In the previous Sections we reported (see Figure 5.8) the yield surface obtained analytically using the condition (4.10) and illustrated its progressive shrinking as the value of $\det \mathbf{C}$ is increased. In Figure 5.18 we presented, along with the analytic yield surface, the points for which first instability is observed in MS simulations (grey stars). These points correspond to shearing deformations with angles between $\theta = 30^\circ \div 60^\circ$, spanning the fundamental domain (see also Figure 5.17). Even if instability takes place slightly later than what predicted analytically, there is an overall agreement with the analytical results for the yield surface, in particular, its shrinking is observed as predicted for $\det \mathbf{C} > 1$. Boundary conditions do not affect these results significantly, and analogous pictures are observed in the case of fixed or periodic boundary conditions.

Homogeneous nucleation is an unusual test for MS, and $\alpha{*_c}$ is known to be very sensitive to both quenched disorder and the tolerance of the computational algorithm. For this reason, we specifically studied the dependence of α_c^* on the noise and observed that there is indeed convergence of the instability threshold when noise is sufficiently small. A similar study, comparing homogeneous nucleation in MS with acoustic tensor predictions, has been performed along specific deformation paths by Steinmann and coauthors in [SES06]. They also observed an overall agreement between the first instability and the analytical prediction based on the acoustic tensor criterion, and showed a progressive convergence of α_c^* towards α_c for increasing system sizes.

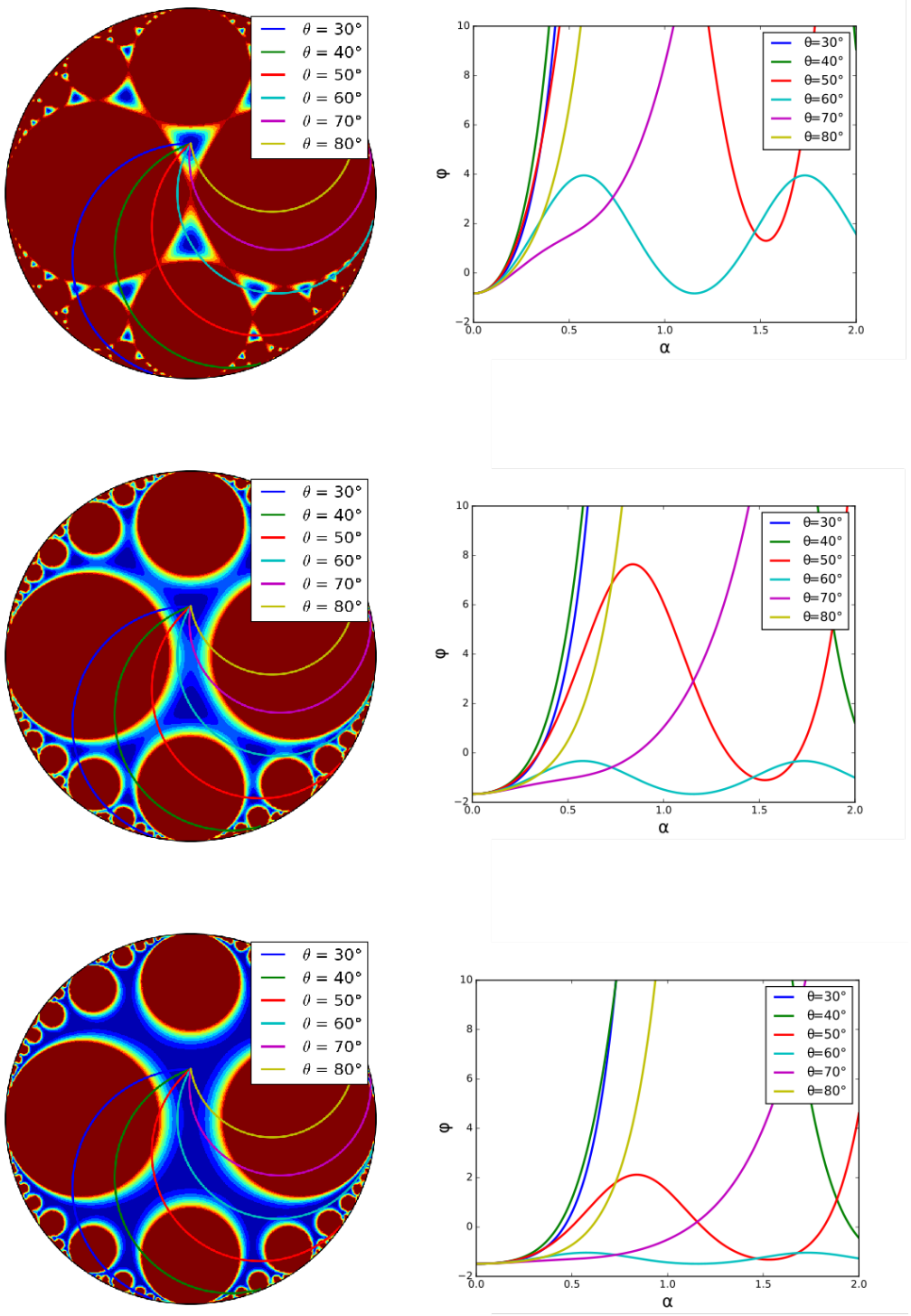

Figure 5.17: **Energy Landscape for Different Values of** $\det \mathbf{C}$ From top to bottom, we show the HLJ energy landscape in corresponedence of different values of $\det \mathbf{C}$, respectively, we use $\det \mathbf{C} = 0.7$, 1.0 and 1.3.

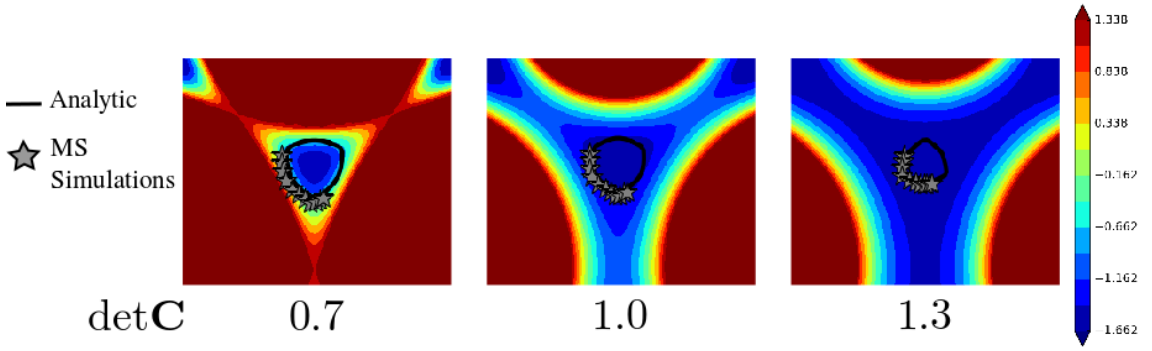

Figure 5.18: **Analytic Yield Surface and MS Calculations:** The black line show the yield surface evaluated analytically, based on acoustic tensor criterion (4.10). Grey stars show (C_{11}, C_{12}, C_{22}) points at which first instability was observed in MS simulations, along different shearing deformations. The showed results are obtained from simulations performed on a domain containing $\approx 10^4$ atoms deformed with fixed boundaries.

We now turn to the study of post-instability patterns and the corresponding element distributions in the configuration space. Components of the metric tensor are not defined directly in the MS simulations. In order to compute them, we need to post-process the data. More precisely, we labeled the atoms in their reference, homogeneous state and drew a grid in a way that every atom has six neighbors, constructing six triangular "elements" for each atom. Then, we looked at the images of these pseudo-elements in the post-instability state and computed the corresponding $\mathbf{C}$ tensors. In other words, we treated the atoms as they were keeping the same neighbors after the instability. In this way, one can plot points in the configuration space, as we have done for the $GL(2,\mathbb{Z})$-invariant model.

Among all the shearing paths, we illustrate the results obtained for the $\theta = 60°$ and $\theta = 30°$ simple shears. These are reported, in terms of energy density, in Figures 5.19 and 5.20. A feature that immediately captures one's attention is the formation of fractures in the $\det \mathbf{C} = 1.3$ case, which is observed for both shearing paths. These fractures have basically the same orientation in MS and HLJ models. More precisely, they appear along the direction of what would have been the activated slip system in the $\det \mathbf{C} = 1$ case (that is, the one associated to wells $\mathbf{T}_1^{60°}$ and $\mathbf{T}_{-1}^{120°}$ respectively). In Figure 5.22 we show the details of the triangulation. Observe that these cracks emerge from the dilatation of a row of elements. The remaining crystal regions shrink restoring their original size.

For the other two values of $\det \mathbf{C}$, only edge dislocations are observed. More than one slip system is activated, but most dislocations glide along the slip system $\mathbf{T}_1^{60°}$ for the $\theta = 60°$ shear and along the slip system $\mathbf{T}_{-1}^{120°}$ for $\theta = 30°$. These dislocations are

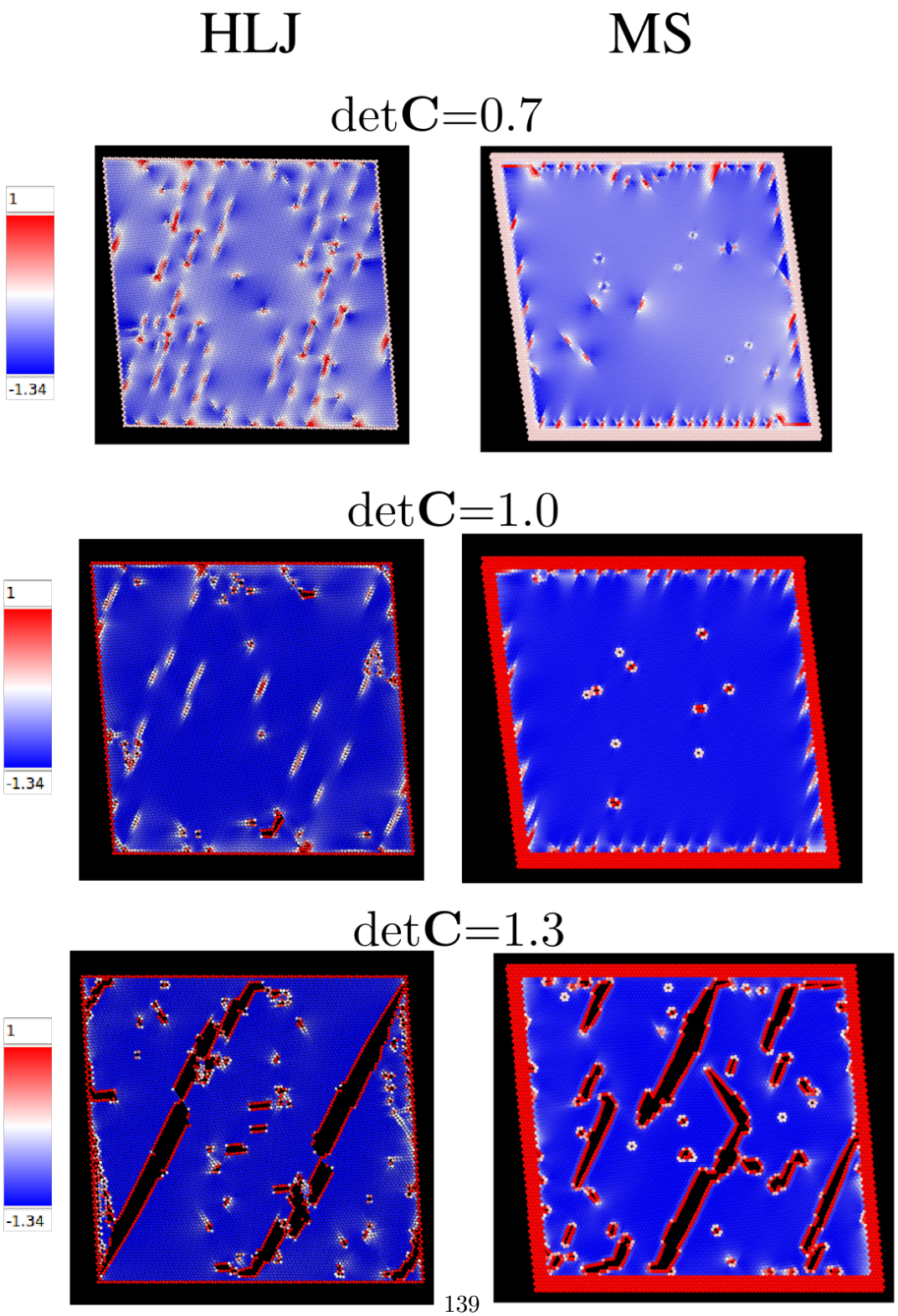

Figure 5.19: $\theta = 60°$ **Post-Instability Patterns at Different Values of** $\det \mathbf{C}$**:** From top to bottom, post instability patterns corresponding to $\det \mathbf{C} = 0.7$, $\det \mathbf{C} = 1.0$ and $\det \mathbf{C} = 1.3$ shearing deformations are shown for HLJ and MS, respectively. Edge dislocations are observed in the first two cases, together with voids and other volumetric defects. The patterns obtained for $\det \mathbf{C} = 1.3$ show the localization of the deformation along cracks.

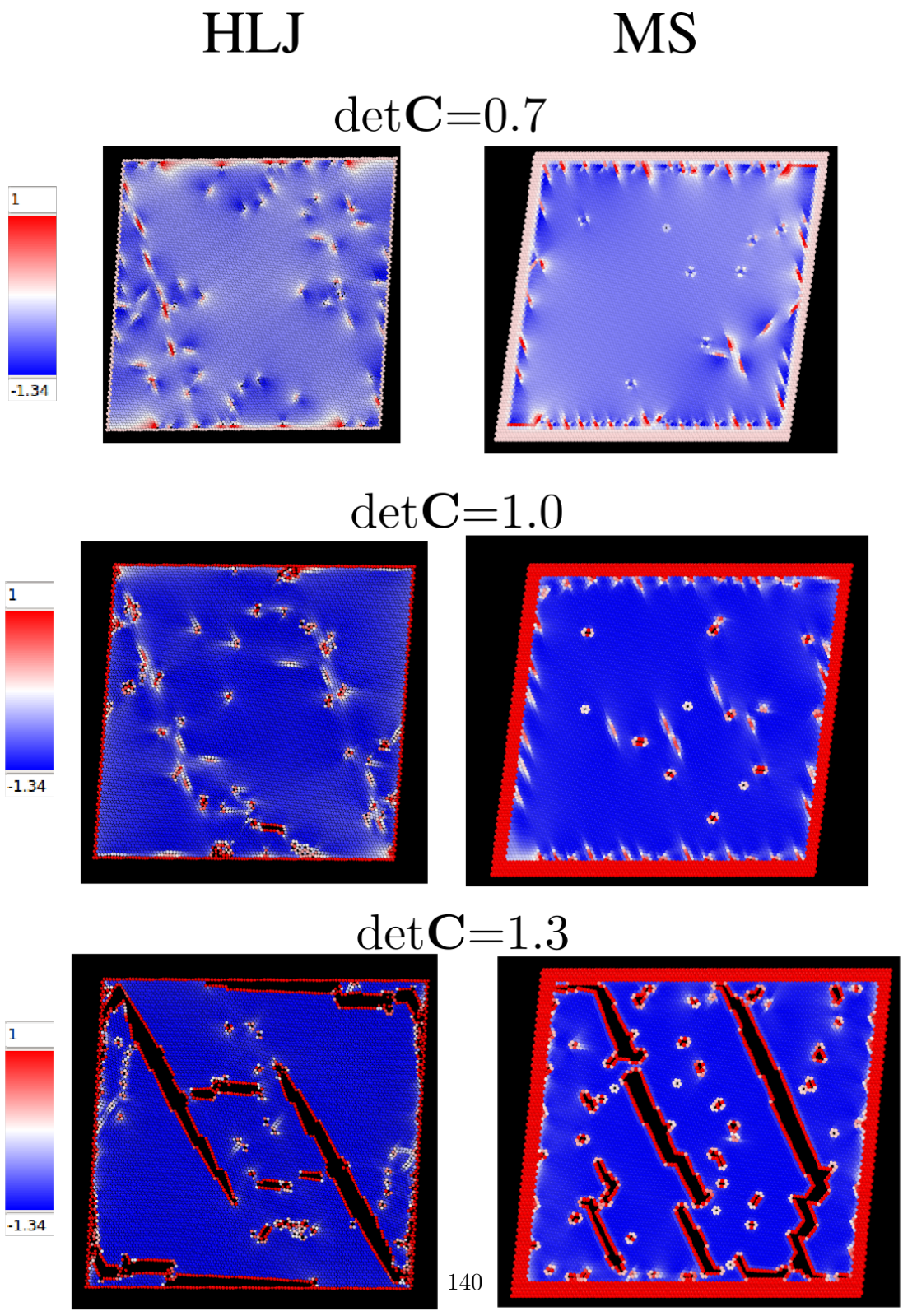

Figure 5.20: $\theta = 30°$ **Post-Instability Patterns at Different Values of** $\det \mathbf{C}$**:** From top to bottom, post instability patterns corresponding to $\det \mathbf{C} = 0.7$, $\det \mathbf{C} = 1.0$ and $\det \mathbf{C} = 1.3$ shearing deformations are shown for HLJ and MS, respectively. Edge dislocations are observed in the first two cases, together with voids and other volumetric defects. The patterns obtained for $\det \mathbf{C} = 1.3$ show the localization of the deformation along cracks.

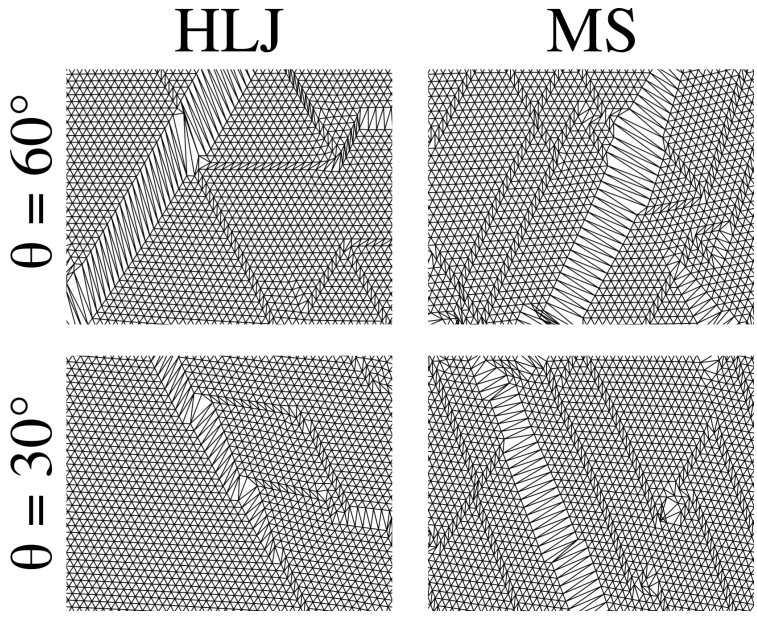

Figure 5.21: **Detail of the** $\det \mathbf{C} = 1.3$ **Post-Instability Patterns:** Fractures appear in the HLJ model in the form of highly extended elements. The same interpretation can be used in MS simulations plotting atoms and their links with the initial neighbours.

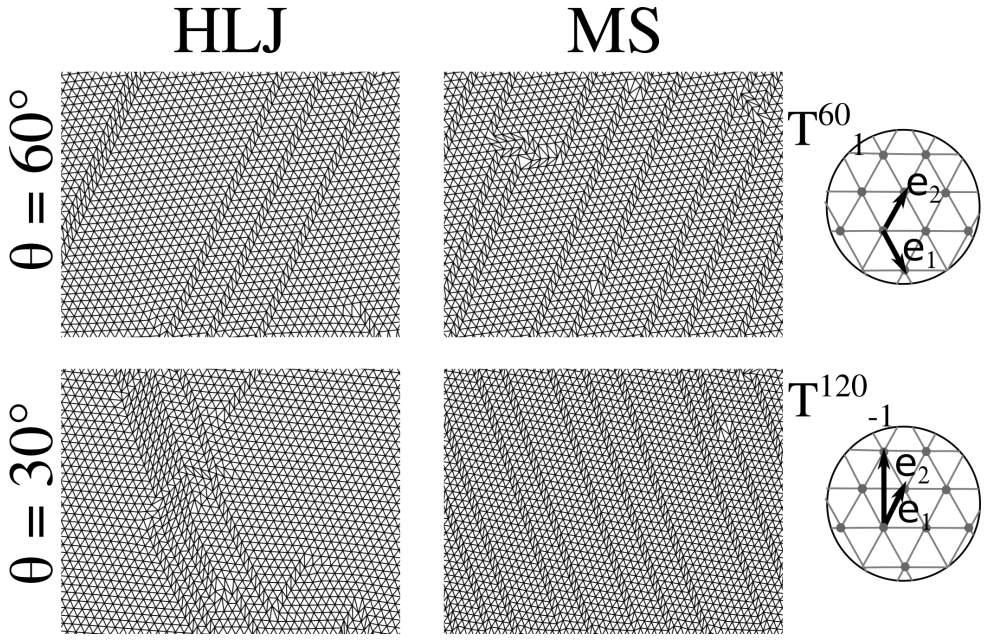

Figure 5.22: **Detail of the** $\det \mathbf{C} = 1.0$ **Post-Instability Patterns:** Activation of the same slip system is observed in HLJ and MS simulations.

more sparsely distributed for the HLJ model while in the case of MS they mostly migrate towards the boundary. Both type of simulations are characterized by the appearance of voids and nano-cracks, independently of the considered value of $\det \mathbf{C}$. Interestingly, these defects appear as expanded elements in our fixed-neighbors, post-processing triangulations. The overall picture is similar to the one illustrated in Figure 5.5 for the HLJ model.

In order to make more quantitative the considerations presented above, we now consider in more detail the case $\det \mathbf{C} = 1$. The corresponding element distribution in the configuration space and the histogram of the metric components are shown in Figures 5.23 and 5.24. Clearly, both models show the engagement of the same energy valleys (slip systems). Histograms (whose y-axis has been cut) show the major dominance of the wells $\mathbf{T}_1^{60^\circ}$ and $\mathbf{T}_{-1}^{120^\circ}$ (for the loading path with $\theta = 60^\circ$ and $\theta = 30^\circ$, respectively). The overall distribution of metric components is comparable in MS and HLJ models. In the MS simulations more elements occupy these slip-related wells, producing more dislocations than in the HLJ model. In Figure 5.22 we illustrate a detail of the triangulation, which clearly shows the activated slip planes.

An analogous discussion can be presented for the case $\det \mathbf{C} = 0.7$. The corresponding element distribution in the configuration space is shown in Figure 5.25. Also in this case there is a qualitative agreement between HLJ and MS models, which both show the activation of the same energy valleys.

To summarize, our study of the homogeneous dislocation nucleation under uniform loading, confirmed that the HLJ model is able to represent most of the features observed in atomistic simulations. The local criterion based on the analysis of the acoustic tensor gives a reliable prediction of the yielding threshold. The post-instability mechanisms described by $GL(2,\mathbb{Z})$ symmetric potentials are also encountered in MS simulations. This re-enforces the idea that $GL(2,\mathbb{Z})$-invariant energies, with their periodic arrangement of wells, can effectively describe the evolution of dislocations configurations in the presence of several slip systems, even if the dislocation cores and the short range interactions are not represented exactly. Moreover, the use of CBR in the construction of the energy density allows one to account for other interesting effects such as the formation of cracks and voids. The difference between the two approaches (mesoscopic theory and MS) shows in the global arrangement of dislocations, which in MS simulations migrate more easily towards the boundaries.

The above observations should be viewed as only preliminary since homogeneous nucleation is a highly idealized test of the theory. We recall that the main objective of our approach is to study the evolution of the dislocation patterns under continuous loading. In the next Section we extend the comparison of the HLJ model with MS simulations to the case when nucleation is induced by a strongly inhomogeneous strain field.

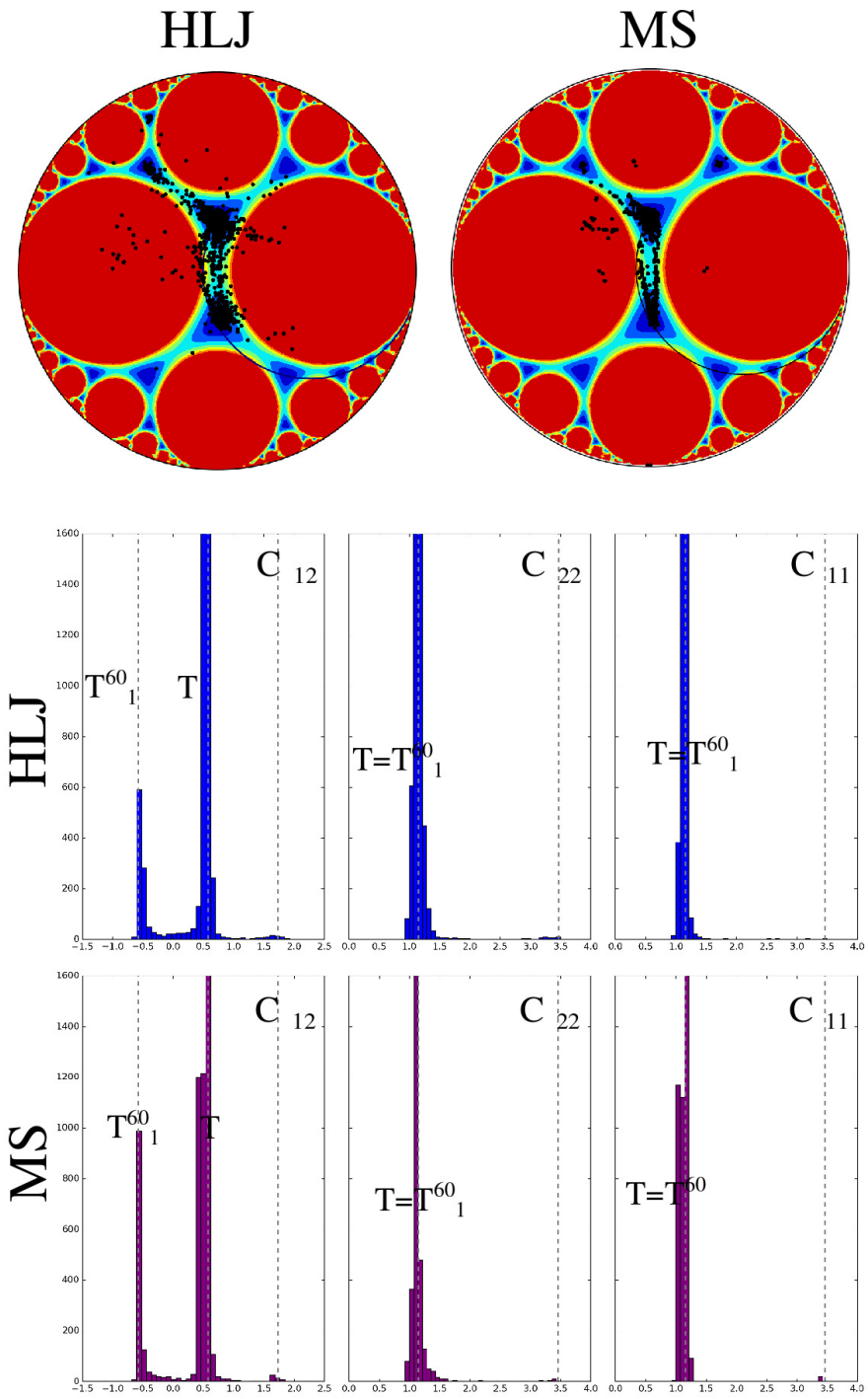

Figure 5.23: $\theta = 60°$ **Element Distribution in the Configuration Space and Histograms of Metric Components:** Distribution of elements in the configuration space is similar in HLJ and MS simulations, and shows the clustering of a large number of elements along the low-energy valley connecting wells **T** and $\mathbf{T}_1^{60^\circ}$. Analogies in the distributions can be deduced also looking at the histograms of metric components.

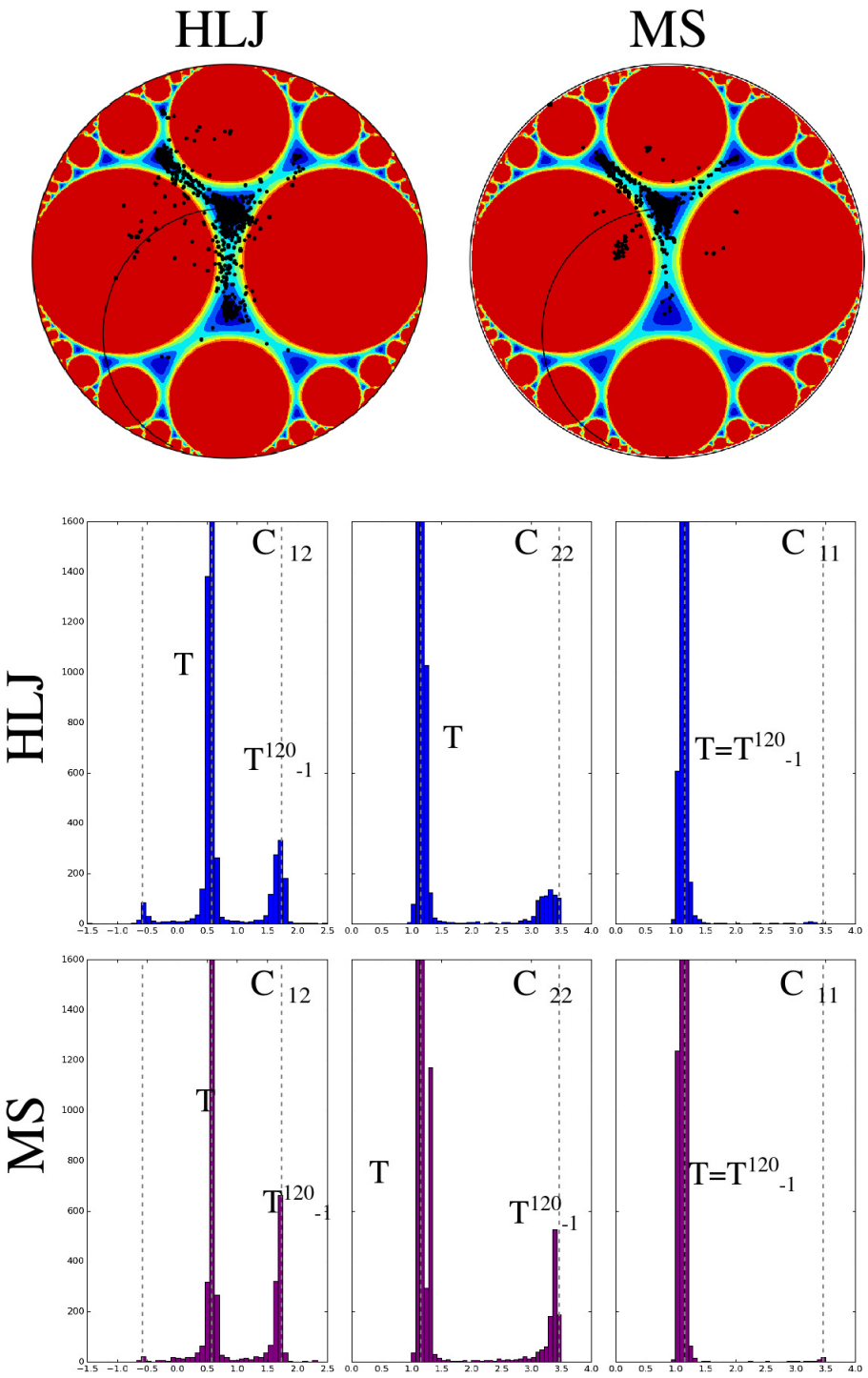

Figure 5.24: $\theta = 30°$ **Element Distribution in the Configuration Space and Histograms of Metric Components:** Distribution of elements in the configuration space is similar in HLJ and MS simulations. Elements are sparser with respect of the shearing path $\theta = 60°$, but a large number of elements along the low-energy valley connecting wells $\mathbf{T}$ and $\mathbf{T}_{-1}^{120°}$ is observable, together with a minor engagement of several other wells. Analogies in the distributions can be deduced also looking at the histograms of metric components.

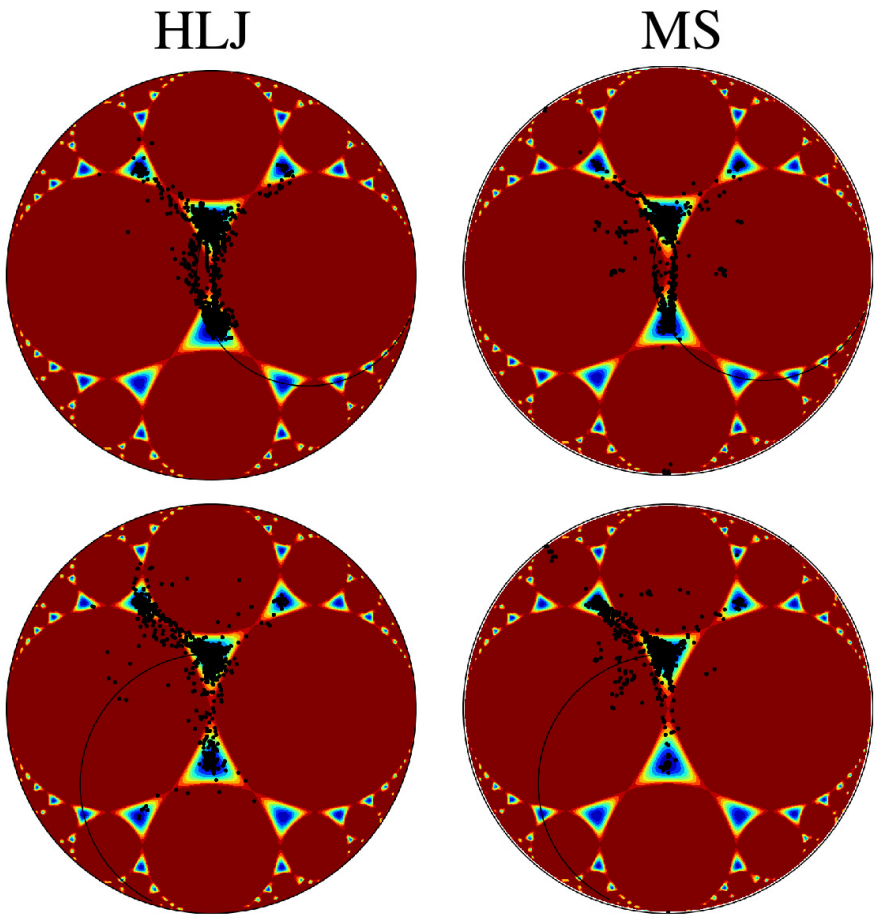

Figure 5.25: $\det \mathbf{C} = 7$ **Element Distribution in the Configuration Space :** elements arrange similarly in HLJ and MS simulations, showing the major activation of the same energy valley.

5.2.3 Nanoindentation

In the current literature, most of the studies of the homogeneous nucleation focus on nano-indentation tests. This is a test in which a nanometric piston is pressed down on the material, under displacement or force control. Nano-indentation tests performed on perfect crystals show an elastic response up to a point in which a discontinuous behavior, characterized by discrete jumps, emerges [VVLZ$^+$03]. This transition coincides with the appearance of plastic deformation in the material, which manifests itself through the homogeneous nucleation of dislocation dipoles in the regions where the strongly inhomogeneous strain field achieves its peak value.

Many papers have been dedicated to the study of homogeneous nucleation under nanoindentation with the objective of understanding the mechanisms of incipient plasticity in perfect crystals. In particular, many studies were focused on the definition of a suitable criterion of yield predicting the critical indentation penetration depth and the location of the nucleating defects. Early on, Van Vliet et al. [VVLZ$^+$03] proposed the acoustic tensor criterion as a suitable tool for predicting nucleation under nano-indentation and performed continuous simulations using a variant of the Cauchy-Born, pair-potential based energy density[ZLVV$^+$04, ZZ08]. Later, Miller and Rodney, however, criticized the predictions based on the study of the acoustic tensor[MR08]. Indeed, due to its inherent locality, such criterion can not take into account non-local effects, which play an important role in the indentation induced dislocation nucleation process. In [GM16] Garg and Maloney partially mitigate this strong opinion showing that the acoustic tensor criterion always predicts correctly the nucleation site observed in MS simulations. Moreover they observed an agreement between the associated direction and polarization vectors and the nucleating dipole. However, nucleation appeared only after the acoustic tensor has become negative over a certain region.

Our study contributed to this debate as a local and a non-local approaches are compared directly. While for the case of a homogeneous loading, as the one discussed in the previous subsection, a good agreement with acoustic tensor based predictions could be expected, this is no more the case for the case of nano-indentation, where the imposed strain field $\mathbf{F}$ is highly inhomogeneous.

In our numerical experiments we used HLJ and MS domains with the same parameters. More specifically, we considered domains for which the vertical scale L_y is half the horizontal scale L_x, we analyzed different scales for the indenter radius: $R = 25, 50, 100$. Simulations were then performed for different values of $L_x = 50, 100, 200$. Emerging dislocations and activated slip planes are also known to depend on the orientation of the crystal

with respect of the indenter [GM16]. Here we considered two orientations: with the horizontal plane of the crystal aligned with the horizontal boundary of the domain (orientation O_1) and with the crystal is rotated at 90° (orientation O_2). The indenter was modeled as spherical and it is assumed to be frictionless and infinitely rigid. The simulations were performed quasi-statically, by imitating slow pressing of the indenter in the displacement control. We compared the critical indentation depths d_c and the post instability patterns generated in our mesoscopic model with the ones obtained in the MS simulatios.

The results obtained for $L_x = 100$, and $R = 25$, 50 are reported in Figure 5.26 where we considered the orientation O_1 and in Figure 5.27 where we analyzed the orientation O_2. Looking at the energy-penetration graphs, one can observe an overall agreement in terms of the critical indenter depth, even if the latter is systematically underestimated in the HLJ model. Results obtained in all simulations are summarized in the graphs shown in Figure 5.28. Here one can see that the critical depth scales similarly in HLJ and MS simulations, with the exception of smaller scale simulations where the representation given by the HLJ model is too coarse.

Post-instability patterns generated in the two types of simulations appear to be basically similar, however, important differences are also present. The overall agreement concerns the nucleation sites and the activated slip planes, and there is also an agreement with what was reported in other more detailed studies (see, for instance [MR08, GM16]).

For the orientation O_1 the instability is observed, as expected, to initiate from a single region, aligned with the center of the indenter and located at a certain depth away from the surface. While in [GM16] a single dislocation dipole was found, we mostly saw the activation of two dislocation dipoles simultaneously, and observed just one only at small values of R (see the case $L_x = 100$, $R = 25$ in Figure 5.26). The main difference between the MS and HLJ pictures is in fact that in HLJ simulations the double dipole activation causes the formation of a high energy defect in the nucleation site (as is clearly visible in the $R = 50$ pattern illustrated in Figure 5.26). We will come back to this point shortly.

The orientation O_2 shows nucleation at higher penetration depths with respect of O_1, with nucleation of dislocations starting from two different points disposed symmetrically with respect of the indenter. For small values of R, dislocations nucleate from the immediate proximity of the surface and migrate towards the lower boundary along the vertical direction. At larger values of R, the two symmetric nucleation sites are located at higher depths and dislocations appear along the slip planes oriented of $\theta \pm 30°$ with respect of the horizontal axis, as it was also observed observed in [GM16]. Comparing to MS, the HLJ model also shows the formation of a larger disordered region in the proximity of the indenter, which is characterized by high energy localization.

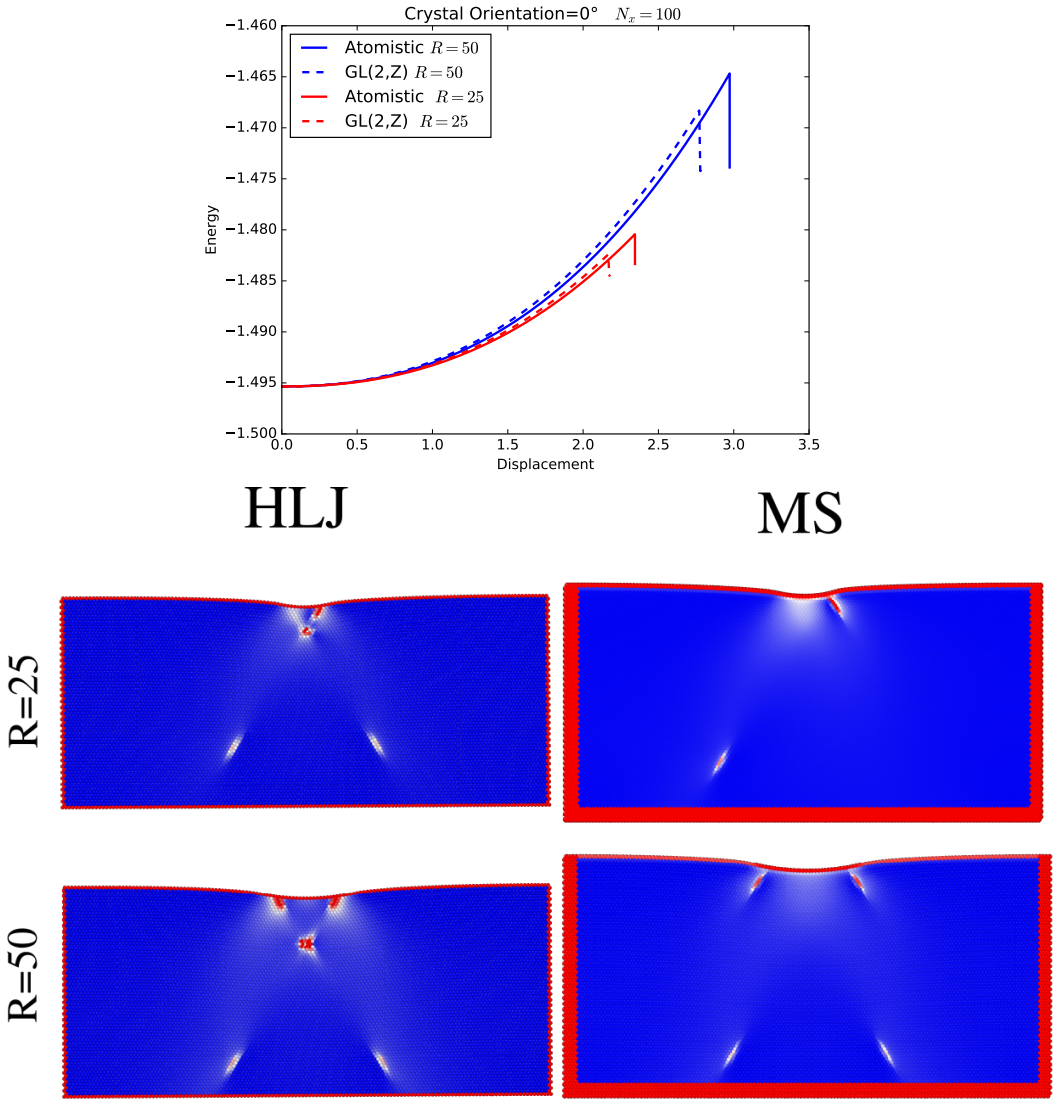

Figure 5.26: $GL(2,\mathbb{Z})$ **and Atomistic simulations for two different values of indenter radius** R. Crystal orientation is 0°.

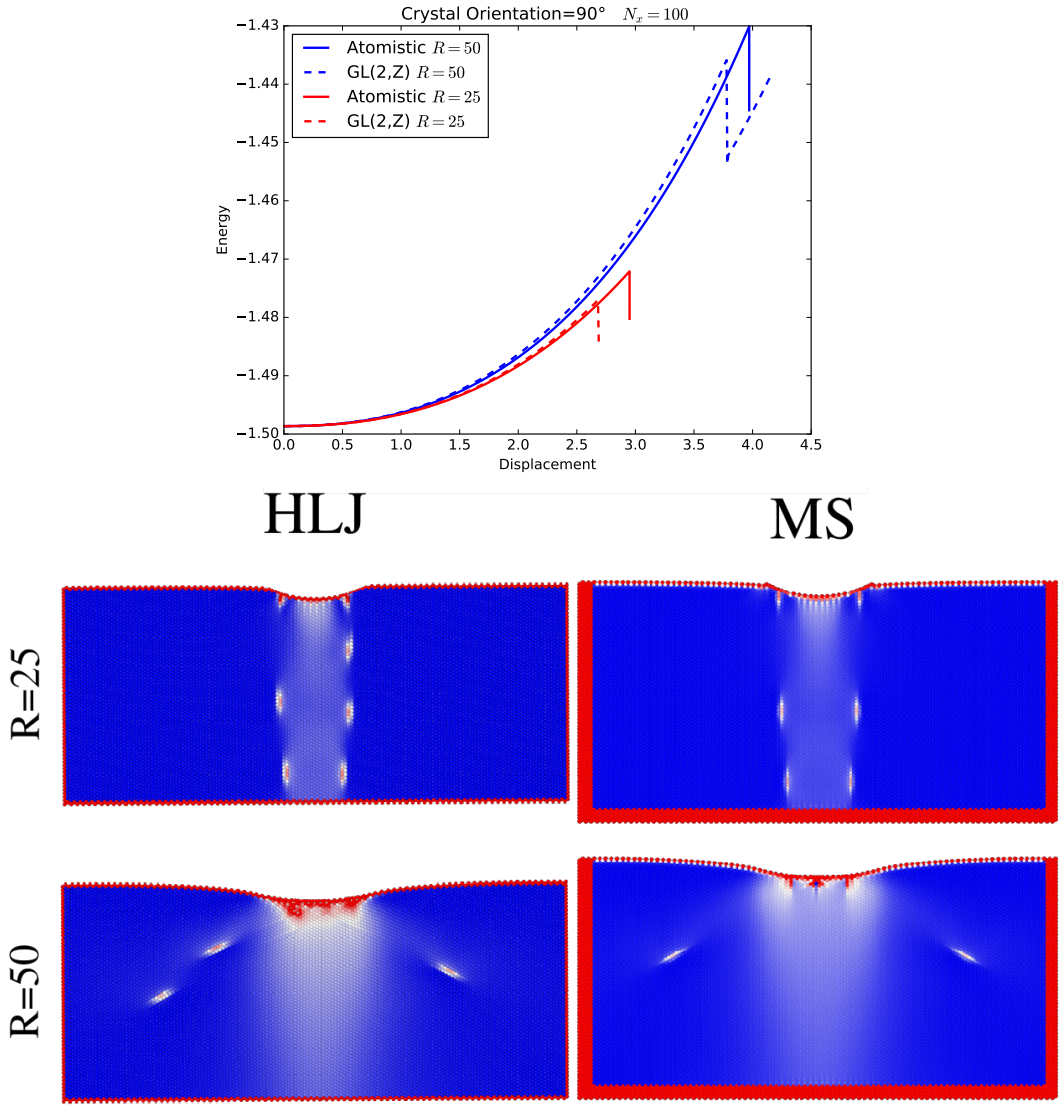

Figure 5.27: $GL(2,\mathbb{Z})$ **and Atomistic simulations for two different values of indenter radius** R. Crystal orientation is 90°.

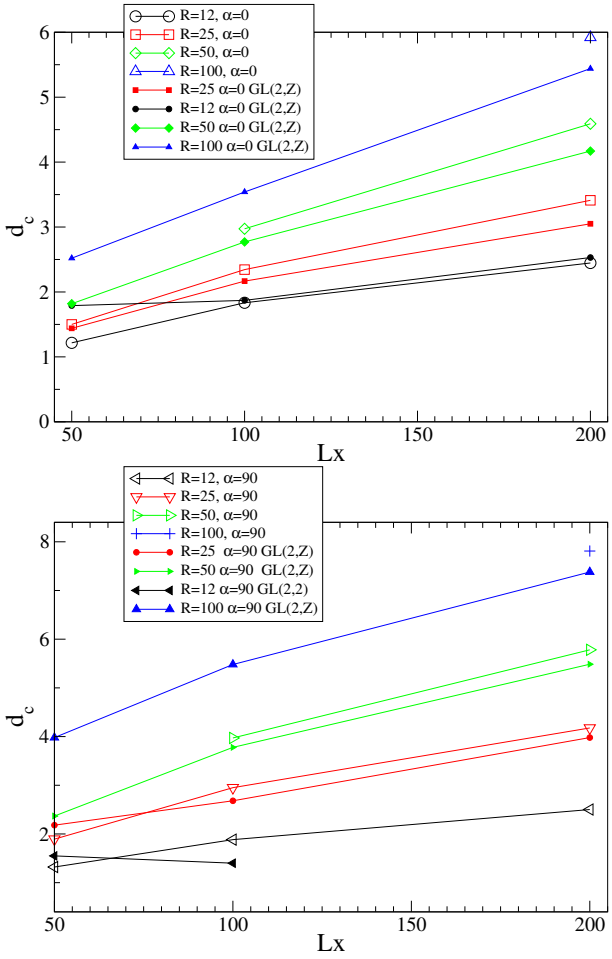

Figure 5.28: **Critical indenter depht d_c:** on top, orientation O_1, on bottom orientation O_2. Critical indenter depht d_c in MS simulations and in the mesoscopic model for different system sizes and values of the indenter radius R.

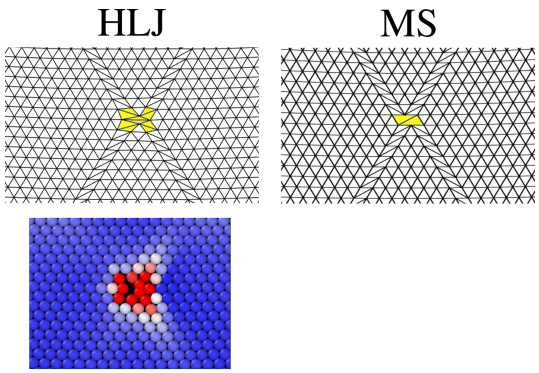

Figure 5.29: **A detail of the Post-Nucleation Pattern:** In the right we show a detail of the HLJ post-instability pattern from a O_1 nanoindentation test, while on the left we illustrate a detail from an analogous MS simulation. Clearly, the compatibility requirement implicit in the $GL(2,\mathbb{Z})$-invariant model results in an excessive constraintment.

Considering all this, the limits of the local HLJ approach vs fully atomistic MS simulations are not related to its capability to predict correctly the critical depth d_c and the location of the incipient dislocation dipole, but rather to represent in detail the nucleated defects. Indeed, in contrast to what we see in MS, the HLJ model predicts the formation of a high energy cluster of deformed elements in the most inhomogeneously deformed regions. This is particularly clear for the orientation O_1, where the double dipole formation leaves behind a region of distorted elements. To better illustrate this effect, we report a detail of the corresponding triangulation in Figure 5.29. While in the HLJ model, the elements are constrained to preserve their topology this constraint does not exist in MS where particles move freely and change neighbors during the deformation. As a consequence, the high energy residual defect region is not resolved in the same manner and most probably spurious strains appear as a result of the continuity constraint. This case can be viewed as an example showing that not all dislocations entanglements can be resolved adequately using our mesoscopic description.

5.2.4 Concluding Remarks

In this Chapter we illustrated how to obtain a $GL(2,\mathbb{Z})$-invariant energy directly from the knowledge of pair-interactions using the CBR. Differently from the already existing approaches which extract the energy density using analogous procedures, our method allows one to preserve the $GL(2,\mathbb{Z})$ invariance for large deformations by defining the reference energy on the fundamental domain, and then imposing the condition (2.20).

We have shown that the isochoric component of the energy obtained using the CBR is analogous to the polynomial construction discussed in the others Chapters of the Thesis. The interesting effects that were observed in the previous Chapter regarding the dislocation

patterning during the homogeneous nucleation have been also encountered in the pair-potential based model. In particular, we also observed the appearance of a modulation preceding the formation of the dislocation dipoles (oriented as predicted analytically), and the double slip activation along the two pure shears limiting the fundamental domain. The use of the pair-potential based energy emphasized the importance of the volumetric component of the energy density, which has been shown to be responsible for the appearance of voids and nano-cracks. The correct account for the volumetric effects also allows one to describe the appearance of fractures under tensile loads. Comparison with the atomistic simulations showed that in our mesoscopic model some truly discrete effects are inevitably lost. The dislocation cores are represented coarsely and some spurious entanglements of defects arise from the compatibility constraint necessarily enforced on the mesoscopic elements. On the positive side, the global features of the emerging patterns, including the activated slip systems, appear to be well captured.

Chapter 6

Conclusions and Perspectives

In this Thesis, we showed that the use of a hyperelastic, geometrically non-linear model can by itself be sufficient to describe plastic flow and dilsocation motion, given that the symmetry is correctly accounted for. This means that one has to account for the presence of lattice invariant transformations, originated from the global symmetry described by the group $GL(n, \mathbb{Z})$. The resulting energy landscape has an infinite number of wells, arranged periodically in a way that is fully compatible with a finite strain formulation. In this framework, plasticity emerges when, as a result of elastic instability, some regions of the originally homogeneous system leave the reference well and variously distribute in strain space, occupying different wells and thus producing complex patterning. Plastic mechanisms are not assigned a priori, but arise directly from the $GL(n, \mathbb{Z})$ invariance requirement. They assume the form of low energy valleys, connecting the periodically distributed energy wells.

In [BAB$^+$19], we have stressed that this formulation can be seen as a Landau theory for crystal plasticity. In this Landau framework, the (infinite) symmetry-related wells represent the shear-invariant, equivalent crystal configurations and the non-linear strain assumes the function of the order parameter. The plastically deformed solid can then be seen as a mixture of these infinite equivalent phases, with dislocations appearing at their boundary.

Periodicity of energy landscape is strictly connected to the Cauchy-Born hypothesis, as individuals atoms are not subjected to a perfectly periodic energetic environment. Moreover, this assumption is needed to place the energy density in a continuum hyperelastic framework. The resulting approach is inherently local and some features of the atomistic level description are inevitably lost. The internal length scale implied by this model characterizes an imaginary mesoscopic cluster of atoms always deforming homogeneously. One way to interpret this hypothesis is to assume that the model is atomistic, but that the inhomogeneity of the deformation is intentionally neglected in the local interactions. Both interpretations result in the fact that the microstructure appears coarse grained, in

particular dislocation cores are represented in a somewhat "blurred" way.

Considering this, the model is similar in its spirit to QC, where the smallest elements are assumed to coincide with atomic cells, but, at the same time, the possibility to neglect micro-inhomogeneities in the continuum region allows one to reduce the number of degrees of freedom and therefore to cut the computational cost. Comparing to QC, the proposed approach renounces the full resolution of non-local features, thus avoiding the necessity of defining patching regions, whose description is non-trivial. It is also different from the local version of the QC method, by the fact that $GL(n,\mathbb{Z})$ invariance is imposed globally, while in the local QC it is obtained numerically using the CBR, and consequently potentially violated at large deformations.

The PFM method, briefly discussed in the Introduction, also appears on the first sight similar to the approach presented in this Thesis. It also uses periodic functions and introduces dislocations using the symmetry of lattice invariant strains. However, these analogies are only apparent. While in the PFM the slip systems are imposed a priori with reference to pre-designed mechanisms, in our model they emerge as a consequence of $GL(n,\mathbb{Z})$ symmetry alone. Moreover, in the PFM, the periodic energy landscape linked to the slip is formulated in terms of linearized strains, which makes the global representation of symmetries questionable. Another feature of the PFM is that some mathematical tricks are needed to ensure that the plastic strain parameters take integer values and that the dislocation cores are regularized properly, while none of this is needed in our $GL(n,\mathbb{Z})$-invariant mesoscopic approach.

The DDD method needs even more phenomenological rules as dislocations are mimicked by discrete segments with cores reduced to lines. Consequently, all core effects need to be modeled phenomenologically, including dislocation annihilation and locking. The non-linear hyperelastic nature of the problem is not taken into account directly, as the forces acting on dislocation line-segments are computed on the basis of linear elasticity.

The advantage of our proposed method is that the description of dislocational flow is obtained in a fully coherent framework with minimal assumptions. Using our approach, we were able to describe the dependence of the dislocation patterning on the orientation of the load and on crystal symmetry. During homogeneous loading, dislocations nucleate collectively. The critical load was shown to be in agreement of with the analytical predictions based on the ellipticity loss criterion, which also effectively predicts the geometrical nature of the emerging unstable modes. Patterns different from developed dislocations were observed in the case of square symmetry for particular loading conditions, leading away from the energy valleys. On the other hand, in the triangular symmetry case the instability always leads to the activation of one or multiple slip systems, preceded by a diffuse modulation, and in the particular cases, by a banded structure. In both symme-

tries, it was shown that some high symmetry lattice configurations, located at the corner of the fundamental domain, play a crucial role in fomenting complexity, being related to a simultaneous activation of the two energy valleys converging there.

The use of two different potentials confirms that the observed effects are sufficiently general and are induced exclusively by the global crystal symmetry. The use of the non-linear finite strain theory was shown to be essential to properly describe the associated periodic energy landscape. Linear descriptions are not able to tell apart wells and valleys that are different if we account for the finite strains effects. Instead, the proposed model allows one to analyze the evolution of the system in an infinite energy landscape where all slips, including the large ones, are described correctly. A more complete description should take into account rotations, which are unimportant for the computation of the energy, but would be useful to distinguish the configurations which differ only by a rigid rotation (this is particularly interesting in the case of the triangular symmetry).

The use of a pair potential-based energy density reveals some important effects related to the volumetric component of the energy. In particular, the corrected account of the system's response under tension, allows one to capture fracture, which is implicitly included into the range of phenomena covered by this model.

Our preliminary comparison with the fully atomistic simulations suggests that, even if dislocation cores are described in a coarse form, the main features of the dislocation patterning are captured correctly. In view of this, our method is suitable for studying the evolution of systems containing a large number of interacting dislocations, even if the detailed description of isolated defects, for which MD already performs well, may be challenging. Therefore, the objective of the method should be the study of dislocation patterning under monotone and cyclic loading, and the analysis of the statistics of the associated plastic avalanches.

The most obvious limitation of the model presented in this Thesis is its 2D character, which prevents modeling of the realistic crystal structures. In this Thesis, the use of a 2D formulation was mostly due to the desire to study the simplest situation first. The transparent 2D setting made it possible to represent the associated three-dimensional configurational space in a straightforward manner, while in a fully 3D formulation the configurational space would have to be five dimensional (as the symmetric matrix $\mathbf{C}$ is a third order tensor). Now, that the most basic features of the $GL(n,\mathbb{Z})$ invariance have been highlighted, it would be interesting to see how the same effects look in a fully 3D setting. This would require lots of further implementation work and some additional effort in the visualization of the associated configurational space. However, there are no particular theoretical limits for the development of a 3D extension of the model. Higher dimensional procedures equivalent to Lagrange reduction exists, in particular, the Seeber reduction

scheme for 3D and the Minkowski reduction scheme one for a general, n-dimensional case (see, for instance, Chapter 4 of [Eng12]). The construction of a polynomial energy, ensuring the required smoothness on the associated 5D fundamental domain, however, is far from being an easy task. On the other hand, the Cauchy-Born procedure presented in Chapter 5 is immediately extendable to 3D. The resulting energy will possess the required continuity provided that the utilized pair potential is continuous.

To conclude, we consider the presented approach as a powerful tool in the description of small scale plasticity, where the representation of both long and short range elastic interactions is achieved with minimal phenomenological assumptions. The fact that the problem is formulated in the framework of finite hyperelaticity means that such macroscopic quantities as stresses and strains are directly accounted for without sacrificing the lattice symmetry. Moreover, the type of the boundary and of the loading conditions that can be studied in this way is very broad.

As we have already shown, under the applied load, the system evolves showing discontinuous jumps associated with dislocation rearrangements, showing complex statistics of plastic avalanches. The associated configurational space, where available slip systems appear as low energy valleys, also offers an interesting and unusual perspective on the intermittency and the defect patterning.

Below we list our main conclusions:

1. We presented a new meso-scopic model of crystal plasticity which take a form of geometrically and physically nonlinear elasticity theory with nonconvex energy. The regularization comes from the discretization of the continuum theory with the element size serving as a regularization length scale.

2. The new model emphasizes the role of the global GL(2,Z) symmetry accounting faithfully for lattice invariant deformations which correspond to the infinity of equivalent energy wells. Then, plastic slip can be associated with the switching between the neighboring energy wells. This description allows one to represent plastic flow in a fundamentally new way: as a dynamics of points in the configurational space of metric tensors.

3. We studied two examples of nonlinear elastic potentials respecting GL(2, Z) symmetry: one phenomenological, based on the piece wise smooth polynomial interpolation, and another one semi-empirical, based on a particular choice of the interatomic potential.

4. The main advantage of the new approach is the automatic (parameter free) description of the short range dislocation interactions, individual nucleation and annihilation events and formation of various complex dislocational patterns.

5. The activation of the "plastic mechanisms", described in our theory by the extended valleys (rather ravines) in the energy landscape, is directed by the energy minimization only which accounts automatically for the coupling between different slip planes. Such coupling is largely controlled by the saddle points corresponding to the unstable high symmetry phases.

6. Despite its quasi-continuum nature, the proposed model accounts kinematically faithfully for the lattice trapping effects and incorporates a nonzero Peierls stress.

7. We showed that the model is capable of describing collective dislocation nucleation events which, in case of homogeneous nucleation, leads to the formation of complex dislocation patterns. Heterogeneous nucleation was studied through the simulation of the nano-indentation tests and results were shown to be in qualitative and quantitative agreement with molecular statics experiments.

8. Our study revealed for the first time the possibility of the development of the long-wave pre-nucleation elastic modulation preceding the ultimate emergence of plasticity.

9. The proposed model allowed us to study the effect of the crystallographic symmetry and of the orientation of the sample in the loading device on the complexity of the emerging dislocation pattern. The strong dependence of the obtained patterns on these factors places doubts on the claims of the universality in crystal plasticity.

10. The proof of principle study conducted in this Thesis suggests the effectiveness of the proposed model in dealing (in a parameter free way) with large number of dislocations. It opens the way towards the study of the complexity associated with plastic flows in crystals associated with the emergence of scale free spatial and temporal correlations.

Bibliography

[ACT+07] Athanasios Arsenlis, Wei Cai, Meijie Tang, Moono Rhee, Tomas Oppelstrup, Gregg Hommes, Tom G Pierce, and Vasily V Bulatov. Enabling strain hardening simulations with dislocation dynamics. *Modelling and Simulation in Materials Science and Engineering*, 15(6):553, 2007.

[AFA+18] Anna Ask, Samuel Forest, Benoit Appolaire, Kais Ammar, and Oguz Umut Salman. A cosserat crystal plasticity and phase field theory for grain boundary migration. *Journal of the Mechanics and Physics of Solids*, 115:167 – 194, 2018.

[AN85] Robert J Asaro and A Needleman. Overview no. 42 texture development and strain hardening in rate dependent polycrystals. *Acta metallurgica*, 33(6):923–953, 1985.

[And06] James W Anderson. *Hyperbolic geometry*. Springer Science & Business Media, 2006.

[AR77] Robert J Asaro and JR Rice. Strain localization in ductile single crystals. *Journal of the Mechanics and Physics of Solids*, 25(5):309–338, 1977.

[Asa83] Robert J Asaro. Crystal plasticity. *Journal of applied mechanics*, 50(4b):921–934, 1983.

[BAB+19] R Baggio, E Arbib, P Biscari, S Conti, L Truskinovsky, G Zanzotto, and OU Salman. Landau-type theory of planar crystal plasticity. *Physical Review Letters*, 123(20):205501, 2019.

[BAK+98] Vasily Bulatov, Farid F Abraham, Ladislas Kubin, Benoit Devincre, and Sidney Yip. Connecting atomistic and mesoscale simulations of crystal plasticity. *Nature*, 391(6668):669, 1998.

[Bar18] Carolina Baruffi. *Overdamped langevin dynamics simulations of grain boundary motion*. PhD thesis, Paris 6, 2018.

[BC06] Vasily Bulatov and Wei Cai. *Computer simulations of dislocations*, volume 3. Oxford University Press on Demand, 2006.

[BCF+04] Vasily Bulatov, Wei Cai, Jeff Fier, Masato Hiratani, Gregg Hommes, Tim Pierce, Meijie Tang, Moono Rhee, Kim Yates, and Tom Arsenlis. Scalable line dynamics in paradis. In *SC'04: Proceedings of the 2004 ACM/IEEE Conference on Supercomputing*, pages 19–19. IEEE, 2004.

[BCZZ04] Kaushik Bhattacharya, Sergio Conti, Giovanni Zanzotto, and Johannes Zimmer. Crystal symmetry and the reversibility of martensitic transformations. *Nature*, 428(6978):55–59, 2004.

[Bha98] Kaushik Bhattacharya. Theory of martensitic microstructure and the shape-memory effect. *Available from author: bhatta@ co. caltech. edu*, 1998.

[Bha03] Kaushik Bhattacharya. *Microstructure of Martensite: Why it Forms and how it Gives Rise to the Shape-memory Effect*. OUP Oxford, November 2003.

[Big12] Davide Bigoni. *Nonlinear solid mechanics: bifurcation theory and material instability*. Cambridge University Press, 2012.

[BJ89] John M Ball and Richard D James. Fine phase mixtures as minimizers of energy. In *Analysis and Continuum Mechanics*, pages 647–686. Springer, 1989.

[Bor15] Max Born. *Dynamik der kristallgitter*. Number 4. BG Teubner, 1915.

[Cau28] Augustin Louis Baron Cauchy. *Exercises de mathématiques*, volume 3. Bure frères, 1828.

[Caz13] Oana Cazacu. *Multiscale Modeling of Heterogenous Materials: From Microstructure to Macro-scale Properties*. John Wiley & Sons, 2013.

[CB03] A Carpio and LL Bonilla. Edge dislocations in crystal structures considered as traveling waves in discrete models. *Physical review letters*, 90(13):135502, 2003.

[CB05] A Carpio and L L Bonilla. Discrete models of dislocations and their motion in cubic crystals. *Phys. Rev. B Condens. Matter*, 71(13):134105, April 2005.

[CCPS10] Yong S Chen, Woosong Choi, Stefanos Papanikolaou, and James P Sethna. Bending crystals: emergence of fractal dislocation structures. *Physical review letters*, 105(10):105501, 2010.

[Che02] Long-Qing Chen. Phase-field models for microstructure evolution. *Annual review of materials research*, 32(1):113–140, 2002.

[CK88] Michel Chipot and David Kinderlehrer. Equilibrium configurations of crystals. *Archive for Rational Mechanics and Analysis*, 103(3):237–277, 1988.

[CM03] Willian A Curtin and Ronald E Miller. Atomistic/continuum coupling in computational materials science. *Modelling and simulation in materials science and engineering*, 11(3):R33, 2003.

[CN64] Bernard D Coleman and Walter Noll. Material symmetry and thermostatic inequalities in finite elastic deformations. *Archive for Rational Mechanics and Analysis*, 15(2):87–111, 1964.

[CO93] Alberto M Cuitino and Michael Ortiz. Computational modelling of single crystals. *Modelling and Simulation in Materials Science and Engineering*, 1(3):225, 1993.

[Cot02] AH Cottrell. Commentary. a brief view of work hardening. In *Dislocations in solids*, volume 11, pages vii–xvii. Elsevier, 2002.

[CY96] J Cai and YY Ye. Simple analytical embedded-atom-potential model including a long-range force for fcc metals and their alloys. *Physical Review B*, 54(12):8398, 1996.

[CZ04] Sergio Conti and Giovanni Zanzotto. A variational model for reconstructive phase transformations in crystals, and their relation to dislocations and plasticity. *Archive for rational mechanics and analysis*, 173(1):69–88, 2004.

[DB83] Murray S Daw and M Io Baskes. Semiempirical, quantum mechanical calculation of hydrogen embrittlement in metals. *Physical review letters*, 50(17):1285, 1983.

[DB84] Murray S Daw and Michael I Baskes. Embedded-atom method: Derivation and application to impurities, surfaces, and other defects in metals. *Physical Review B*, 29(12):6443, 1984.

[DDO+14] Julie Drouet, Laurent Dupuy, Fabien Onimus, Frédéric Mompiou, Simon Perusin, and Antoine Ambard. Dislocation dynamics simulations of interactions between gliding dislocations and radiation induced prismatic loops in zirconium. *Journal of Nuclear Materials*, 449(1-3):252–262, 2014.

[DELT07] Matthew Dobson, Ryan S Elliott, Mitchell Luskin, and Ellad B Tadmor. A multilattice quasicontinuum for phase transforming materials: Cascading cauchy born kinematics. *Journal of Computer-Aided Materials Design*, 14(1):219–237, 2007.

[DG15] Benoit Devincre and Riccardo Gatti. Physically justified models for crystal plasticity developed with dislocation dynamics simulations. 2015.

[DK97] B Devincre and LP Kubin. Mesoscopic simulations of dislocations and plasticity. *Materials Science and Engineering: A*, 234:8–14, 1997.

[dlFZG+02] O Rodríguez de la Fuente, JA Zimmerman, MA Gonzalez, J De la Figuera, JC Hamilton, Woei Wu Pai, and JM Rojo. Dislocation emission around nanoindentations on a (001) fcc metal surface studied by scanning tunneling microscopy and atomistic simulations. *Physical review letters*, 88(3):036101, 2002.

[DMM+11] Benoit Devincre, Ronan Madec, G Monnet, S Queyreau, R Gatti, and L Kubin. Modeling crystal plasticity with dislocation dynamics simulations: The 'micromegas' code. *Mechanics of Nano-objects*, pages 81–100, 2011.

[DMS12] Michel Destrade, Jerry G Murphy, and Giuseppe Saccomandi. Simple shear is not so simple. *International Journal of Non-Linear Mechanics*, 47(2):210–214, 2012.

[DPB+92] B Devincre, V Pontikis, Y Brechet, G Canova, M Condat, and L Kubin. Three-dimensional simulations of plastic flow in crystals. In *Microscopic simulations of complex hydrodynamic phenomena*, pages 413–423. Springer, 1992.

[DRGT88] VP Dmitriev, SB Rochal, Yu M Gufan, and P Toledano. Definition of a transcendental order parameter for reconstructive phase transitions. *Physical review letters*, 60(19):1958, 1988.

[DV16] C Denoual and A Vattré. A phase field approach with a reaction pathways-based potential to model reconstructive martensitic transformations with a large number of variants. *Journal of the Mechanics and Physics of Solids*, 90:91–107, 2016.

[EA94] Furio Ercolessi and James B Adams. Interatomic potentials from first-principles calculations: the force-matching method. *EPL (Europhysics Letters)*, 26(8):583, 1994.

[Eng12] Peter Engel. *Geometric crystallography: an axiomatic introduction to crystallography*. Springer Science & Business Media, 2012.

[Eri53] JL Ericksen. On the propagation of waves in isotropic incompressible perfectly elastic materials. *Journal of Rational Mechanics and Analysis*, 2:329–337, 1953.

[Eri73] JL Ericksen. Loading devices and stability of equilibrium. In *Nonlinear Elasticity*, pages 161–173. Elsevier, 1973.

[Eri77] Jerald L Ericksen. Special topics in elastostatics. In *Advances in applied mechanics*, volume 17, pages 189–244. Elsevier, 1977.

[Eri79] JL Ericksen. On the symmetry of deformable crystals. *Archive for Rational Mechanics and Analysis*, 72(1):1–13, 1979.

[Eri80] JL Ericksen. Some phase transitions in crystals. *Archive for Rational Mechanics and Analysis*, 73(2):99–124, 1980.

[Eri87] Jerry L Ericksen. Twinning of crystals (i). In *Metastability and incompletely posed problems*, pages 77–93. Springer, 1987.

[Eri91] JL Ericksen. Weak martensitic transformations in bravais lattices. In *Mechanics and Thermodynamics of Continua*, pages 145–158. Springer, 1991.

[Eri97] JL Ericksen. Equilibrium theory for x-ray observations of crystals. *Archive for Rational Mechanics and Analysis*, 139(2):181–200, 1997.

[Eri05] JL Ericksen. The cauchy and born hypotheses for crystals. *Mechanics and mathematics of crystals: selected papers of JL Ericksen. Singapore: World Scientific Publishing Co*, pages 117–33, 2005.

[Eri08] Jerald L Ericksen. On the cauchy—born rule. *Mathematics and mechanics of solids*, 13(3-4):199–220, 2008.

[Esh57] John Douglas Eshelby. The determination of the elastic field of an ellipsoidal inclusion, and related problems. *Proceedings of the Royal Society of London. Series A. Mathematical and Physical Sciences*, 241(1226):376–396, 1957.

[FC99] MC Fivel and GR Canova. Developing rigorous boundary conditions to simulations of discrete dislocation dynamics. *Modelling and Simulation in Materials Science and Engineering*, 7(5):753, 1999.

[FGC96] MC Fivel, TJ Gosling, and GR Canova. Implementing image stresses in a 3d dislocation simulation. *Modelling and Simulation in Materials Science and Engineering*, 4(6):581, 1996.

[FK39] J Frenkel and T Kontorova. On the theory of plastic deformation and twinning. *Izv. Akad. Nauk, Ser. Fiz.*, 1:137–149, 1939.

[FLBGS10] A Finel, Y Le Bouar, A Gaubert, and U Salman. Phase field methods: Microstructures, mechanical properties and complexity. *C. R. Phys.*, 2010.

[FLH12] Haidong Fan, Zhenhuan Li, and Minsheng Huang. Toward a further understanding of intermittent plastic responses in the compressed single/bicrystalline micropillars. *Scripta materialia*, 66(10):813–816, 2012.

[Fon87] Irene Fonseca. Variational methods for elastic crystals. *Archive for Rational Mechanics and Analysis*, 97(3):189–220, 1987.

[For98] S Forest. Modeling slip, kink and shear banding in classical and generalized single crystal plasticity. *Acta Materialia*, 46(9):3265–3281, 1998.

[Gin04] Vitaly L Ginzburg. Nobel lecture: On superconductivity and superfluidity (what i have and have not managed to do) as well as on the "physical minimum" at the beginning of the xxi century. *Reviews of Modern Physics*, 76(3):981, 2004.

[GM16] Akanksha Garg and Craig E. Maloney. Universal scaling laws for homogeneous dislocation nucleation during nano-indentation. *Journal of the Mechanics and Physics of Solids*, 95:742 – 754, 2016.

[GO08] M Yu Gutkin and IA Ovid'ko. Homogeneous nucleation of dislocation loops in nanocrystalline metals and ceramics. *Acta Materialia*, 56(7):1642–1649, 2008.

[GVVS01] Andrew Gouldstone, Krystyn J Van Vliet, and Subra Suresh. Nanoindentation: Simulation of defect nucleation in a crystal. *Nature*, 411(6838):656, 2001.

[Had03] Jacques Hadamard. *Leçons sur la propagation des ondes et les équations de l'hydrodynamique*. A. Hermann, 1903.

[HB01] Derek Hull and David J Bacon. *Introduction to dislocations*. Butterworth-Heinemann, 2001.

[HC01] SY Hu and LQ Chen. Solute segregation and coherent nucleation and growth near a dislocation—a phase-field model integrating defect and phase microstructures. *Acta materialia*, 49(3):463–472, 2001.

[HDA88] SV Harren, HE Deve, and RJ Asaro. Shear band formation in plane strain compression. *Acta Metallurgica*, 36(9):2435–2480, 1988.

[HGK89] B Horovitz, RJ Gooding, and JA Krumhansl. Order parameters for reconstructive phase transitions. *Physical review letters*, 62(7):843, 1989.

[Hil58] R1 Hill. A general theory of uniqueness and stability in elastic-plastic solids. *Journal of the Mechanics and Physics of Solids*, 6(3):236–249, 1958.

[Hil62] Rodney Hill. Acceleration waves in solids. *Journal of the Mechanics and Physics of Solids*, 10(1):1–16, 1962.

[Hil66] Rodney Hill. Generalized constitutive relations for incremental deformation of metal crystals by multislip. *Journal of the Mechanics and Physics of Solids*, 14(2):95–102, 1966.

[HJY+15] Tao Hu, Lin Jiang, Hanry Yang, Kaka Ma, Troy D Topping, Joshua Yee, Meijuan Li, Amiya K Mukherjee, Julie M Schoenung, and Enrique J Lavernia. Stabilized plasticity in ultrahigh strength, submicron al crystals. *Acta Materialia*, 94:46–58, 2015.

[HK64] Pierre Hohenberg and Walter Kohn. Inhomogeneous electron gas. *Physical review*, 136(3B):B864, 1964.

[HL06] John Price Hirth and Jens Lothe. *Theory of dislocations*. McGraw-Hill, 2006.

[HR72] R Hill and JR Rice. Constitutive analysis of elastic-plastic crystals at arbitrary strain. *Journal of the Mechanics and Physics of Solids*, 20(6):401–413, 1972.

[HSLK11] Abigail Hunter, Faisal Saied, Chinh Le, and Marisol Koslowski. Large-scale 3d phase field dislocation dynamics simulations on high-performance architectures. *The International Journal of High Performance Computing Applications*, 25(2):223–235, 2011.

[Hug12] Thomas JR Hughes. *The finite element method: linear static and dynamic finite element analysis*. Courier Corporation, 2012.

[Hut76] John Woodside Hutchinson. Bounds and self-consistent estimates for creep of polycrystalline materials. *Proceedings of the Royal Society of London. A. Mathematical and Physical Sciences*, 348(1652):101–127, 1976.

[ILVSVP+16] A Irastorza-Landa, H Van Swygenhoven, S Van Petegem, N Grilli, A Bollhalder, S Brandstetter, and D Grolimund. Following dislocation patterning during fatigue. *Acta Materialia*, 112:184–193, 2016.

[ILZ+14] Péter Dusán Ispánovity, Lasse Laurson, Michael Zaiser, István Groma, Stefano Zapperi, and Mikko J Alava. Avalanches in 2d dislocation systems: Plastic yielding is not depinning. *Physical review letters*, 112(23):235501, 2014.

[JL16] Mahdi Javanbakht and Valery I Levitas. Phase field approach to dislocation evolution at large strains: Computational aspects. *International Journal of Solids and Structures*, 82:95–110, 2016.

[KC92] LP Kubin and G Canova. The modelling of dislocation patterns. *Scripta metallurgica et materialia*, 27(8):957–962, 1992.

[Kha13] Armen G Khachaturyan. *Theory of structural transformations in solids*. Courier Corporation, 2013.

[Kin87a] David Kinderlehrer. Remarks about equilibrium configurations of crystals. 1987.

[Kin87b] David Kinderlehrer. Twinning of crystals (ii). In *Metastability and incompletely posed problems*, pages 185–211. Springer, 1987.

[Kin09] Davis E King. Dlib-ml: A machine learning toolkit. *Journal of Machine Learning Research*, 10(Jul):1755–1758, 2009.

[KKKL93] AS Kovalev, AD Kondratyuk, AM Kosevich, and AI Landau. Theoretical description of the crowdion in an anisotropic crystal based on the frenkel-kontorova model including and elastic three-dimensional medium. *physica status solidi (b)*, 177(1):117–127, 1993.

[KMG+10] D Kiener, C Motz, W Grosinger, D Weygand, and R Pippan. Cyclic response of copper single crystal micro-beams. *Scripta Materialia*, 63(5):500–503, 2010.

[KS65] Walter Kohn and Lu Jeu Sham. Self-consistent equations including exchange and correlation effects. *Physical review*, 140(4A):A1133, 1965.

[LCL+10] YH Lai, HM Chen, CJ Lee, JC Huang, and JSC Jang. Strain burst speeds in metallic glass micropillars. *Intermetallics*, 18(10):1893–1897, 2010.

[LEA04] Xiang-Yang Liu, Furio Ercolessi, and James B Adams. Aluminium interatomic potential from density functional theory calculations with improved stacking fault energy. *Modelling and Simulation in Materials Science and Engineering*, 12(4):665, 2004.

[LL13] Lev Davidovich Landau and Evgenii Mikhailovich Lifshitz. *Course of theoretical physics*. Elsevier, 2013.

[LMA06] Markus Lazar, Gérard A Maugin, and Elias C Aifantis. Dislocations in second strain gradient elasticity. *International Journal of Solids and Structures*, 43(6):1787–1817, 2006.

[LN89] Dong C Liu and Jorge Nocedal. On the limited memory bfgs method for large scale optimization. *Mathematical programming*, 45(1-3):503–528, 1989.

[LS86] PS Lomdahl and DJ Srolovitz. Dislocation generation in the two-dimensional frenkel-kontorova model at high stresses. *Physical review letters*, 57(21):2702, 1986.

[Man72] Jean Mandel. Plasticité classique et viscoplasticité: course held... udine, september-october 1971, 1972.

[MAS93] PE McHugh, RJ Asaro, and CF Shih. Computational modeling of metal matrix composite materials—i. isothermal deformation patterns in ideal microstructures. *Acta metallurgica et materialia*, 41(5):1461–1476, 1993.

[McD19] David L McDowell. Multiscale modeling of interfaces, dislocations, and dislocation field plasticity. In *Mesoscale Models*, pages 195–297. Springer, 2019.

[McH04] Peter E McHugh. Introduction to crystal plasticity theory. In *Mechanics of Microstructured Materials*, pages 125–171. Springer, 2004.

[MCM11] Paolo Moretti, Benedetta Cerruti, and M-Carmen Miguel. Yielding and irreversible deformation below the microscale: Surface effects and non-mean-field plastic avalanches. *PloS one*, 6(6):e20418, 2011.

[MH94] Jerrold E Marsden and Thomas JR Hughes. *Mathematical foundations of elasticity*. Courier Corporation, 1994.

[MMP+01] Yu Mishin, MJ Mehl, DA Papaconstantopoulos, AF Voter, and JD Kress. Structural stability and lattice defects in copper: Ab initio, tight-binding, and embedded-atom calculations. *Physical Review B*, 63(22):224106, 2001.

[MO07] Akihiko Minami and Akira Onuki. Nonlinear elasticity theory of dislocation formation and composition change in binary alloys in three dimensions. *Acta materialia*, 55(7):2375–2384, 2007.

[MR08] Ronald E Miller and David Rodney. On the nonlocal nature of dislocation nucleation during nanoindentation. *Journal of the Mechanics and Physics of Solids*, 56(4):1203–1223, 2008.

[MT02] Ronald E Miller and Ellad B Tadmor. The quasicontinuum method: Overview, applications and current directions. *Journal of Computer-Aided Materials Design*, 9(3):203–239, 2002.

[Nab47] FRN Nabarro. Dislocations in a simple cubic lattice. *Proceedings of the Physical Society*, 59(2):256, 1947.

[Nab51] FRN Nabarro. Cxxii. the synthesis of elastic dislocation fields. *The London, Edinburgh, and Dublin Philosophical Magazine and Journal of Science*, 42(334):1224–1231, 1951.

[NN09] KS Ng and AHW Ngan. Deformation of micron-sized aluminium bi-crystal pillars. *Philosophical Magazine*, 89(33):3013–3026, 2009.

[NS15] Tomoaki Niiyama and Tomotsugu Shimokawa. Atomistic mechanisms of intermittent plasticity in metals: Dislocation avalanches and defect cluster pinning. *Physical Review E*, 91(2):022401, 2015.

[Ogd97] Raymond W Ogden. *Non-linear elastic deformations*. Courier Corporation, 1997.

[Onu03] Akira Onuki. Nonlinear strain theory of plastic flow in solids. *Journal of Physics: Condensed Matter*, 15(11):S891, 2003.

[OP98] Michael Ortiz and Rob Phillips. Nanomechanics of defects in solids. In *Advances in Applied Mechanics*, volume 36, pages 1–79. Elsevier, 1998.

[Oro34] E Orowan. Plasticity of crystals. *Z. Phys*, 89(9-10):605–659, 1934.

[PAN83] Daniel Peirce, Robert J Asaro, and A Needleman. Material rate dependence and localized deformation in crystalline solids. *Acta metallurgica*, 31(12):1951–1976, 1983.

[Par76] Gareth P Parry. On the elasticity of monatomic crystals. In *Mathematical Proceedings of the Cambridge Philosophical Society*, volume 80, pages 189–211. Cambridge University Press, 1976.

[Par80] Robert G Parr. Density functional theory of atoms and molecules. In *Horizons of Quantum Chemistry*, pages 5–15. Springer, 1980.

[Pau93] Wolfgang B Paul. Molecular dynamics simulation, elementary methods. by jm haile, wiley, chichester 1992, 489 pp., hardcover,£ 47.50, isbn 0-471-81966-2. *Advanced Materials*, 5(3):223–224, 1993.

[PCB07] I Plans, A Carpio, and LL Bonilla. Homogeneous nucleation of dislocations as bifurcations in a periodized discrete elasticity model. *EPL (Europhysics Letters)*, 81(3):36001, 2007.

[Pit84] M Pitteri. Reconciliation of local and global symmetries of crystals. *Journal of Elasticity*, 14(2):175–190, 1984.

[PKM13] Jitesh H Panchal, Surya R Kalidindi, and David L McDowell. Key computational modeling issues in integrated computational materials engineering. *Computer-Aided Design*, 45(1):4–25, 2013.

[Pli95a] Steve Plimpton. Fast parallel algorithms for short-range molecular dynamics. *Journal of Computational Physics*, 117(1):1 – 19, 1995.

[Pli95b] Steve Plimpton. Fast parallel algorithms for short-range molecular dynamics. *Journal of computational physics*, 117(1):1–19, 1995.

[Pol34] M Polanyi. Lattice distortion which originates plastic flow. *Zeit Phys*, 89:660–662, 1934.

[PRTZ09] Francisco J Perez-Reche, Lev Truskinovsky, and Giovanni Zanzotto. Martensitic transformations: from continuum mechanics to spin models and automata. *Continuum Mechanics and Thermodynamics*, 21(1):17–26, 2009.

[PWW+19] Yan Pan, Haijun Wu, Xiaofei Wang, Qiaoyan Sun, Lin Xiao, Xiangdong Ding, Jun Sun, and Ekhard KH Salje. Rotatable precipitates change the scale-free to scale dependent statistics in compressed ti nano-pillars. *Scientific reports*, 9(1):3778, 2019.

[PZ02] Mario Pitteri and Giovanni Zanzotto. *Continuum models for phase transitions and twinning in crystals*. Chapman and Hall/CRC, 2002.

[REH+10] Franz Roters, Philip Eisenlohr, Luc Hantcherli, Denny Dharmawan Tjahjanto, Thomas R Bieler, and Dierk Raabe. Overview of constitutive laws, kinematics, homogenization and multiscale methods in crystal plasticity finite-element modeling: Theory, experiments, applications. *Acta Materialia*, 58(4):1152–1211, 2010.

[Ric71] James R Rice. Inelastic constitutive relations for solids: an internal-variable theory and its application to metal plasticity. *Journal of the Mechanics and Physics of Solids*, 19(6):433–455, 1971.

[Ric76] James R Rice. The localization of plastic deformation. 1976.

[RLBF03] D Rodney, Y Le Bouar, and A Finel. Phase field methods and dislocations. *Acta materialia*, 51(1):17–30, 2003.

[RLBF17] Antoine Ruffini, Yann Le Bouar, and Alphonse Finel. Three-dimensional phase-field model of dislocations for a heterogeneous face-centered cubic crystal. *Journal of the Mechanics and Physics of Solids*, 105:95–115, 2017.

[RNS07] E Rabkin, H-S Nam, and DJ Srolovitz. Atomistic simulation of the deformation of gold nanopillars. *Acta materialia*, 55(6):2085–2099, 2007.

[RSB+01] Moono Rhee, James S Stolken, Vasily V Bulatov, Tomas Diaz de la Rubia, Hussein M Zbib, and John P Hirth. Dislocation stress fields for dynamic codes using anisotropic elasticity: methodology and analysis. *Materials Science and Engineering: A*, 309:288–293, 2001.

[Sal09] Oguz Umut Salman. *Modeling of spatio-temporal dynamics and patterning mechanisms of martensites by phase-field and Lagrangian methods*. PhD thesis, Paris 6, 2009.

[SES06] P Steinmann, A Elizondo, and R Sunyk. Studies of validity of the cauchy–born rule by direct comparison of continuum and atomistic modelling. *Modelling and Simulation in Materials Science and Engineering*, 15(1):S271, 2006.

[SET14] Viacheslav Sorkin, Ryan S Elliott, and Ellad B Tadmor. A local quasicontinuum method for 3d multilattice crystalline materials: Application to shape-memory alloys. *Modelling and Simulation in Materials Science and Engineering*, 22(5):055001, 2014.

[SFDS12] Oguz Umut Salman, Alphonse Finel, Rémi Delville, and Dominique Schryvers. The role of phase compatibility in martensite. *J. Appl. Phys.*, 111(10):103517, May 2012.

[SMC02] LE Shilkrot, RE Miller, and WA Curtin. Coupled atomistic and discrete dislocation plasticity. *Physical review letters*, 89(2):025501, 2002.

[SMC04] LE Shilkrot, Ronald E Miller, and William A Curtin. Multiscale plasticity modeling: coupled atomistics and discrete dislocation mechanics. *Journal of the Mechanics and Physics of Solids*, 52(4):755–787, 2004.

[SMF19] Oguz Umut Salman, Benson Muite, and Alphonse Finel. Origin of stabilization of macrotwin boundaries in martensites. *Eur. Phys. J. B*, 92(1):20, January 2019.

[SMT+99] VB Shenoy, Ronald Miller, EB Tadmor, David Rodney, Rob Phillips, and Michael Ortiz. An adaptive finite element approach to atomic-scale mechanics—the quasicontinuum method. *Journal of the Mechanics and Physics of Solids*, 47(3):611–642, 1999.

[SR97] GF Smith and RS Rivlin. The strain-energy function for anisotropic elastic materials. In *Collected Papers of RS Rivlin*, pages 541–559. Springer, 1997.

[SSL01] Mahdi Sanati, A Saxena, and T Lookman. Domain wall modeling of bcc to hcp reconstructive phase transformation in early transition metals. *Physical Review B*, 64(9):092101, 2001.

[ST11] Oğuz Umut Salman and Lev Truskinovsky. Minimal integer automaton behind crystal plasticity. *Physical review letters*, 106(17):175503, 2011.

[ST12] Oguz Umut Salman and Lev Truskinovsky. On the critical nature of plastic flow: One and two dimensional models. *International Journal of Engineering Science*, 59:219–254, 2012.

[Str00] Bjarne Stroustrup. *The C++ programming language*. Pearson Education India, 2000.

[SW85] Frank H Stillinger and Thomas A Weber. Computer simulation of local order in condensed phases of silicon. *Physical review B*, 31(8):5262, 1985.

[Tay34] Geoffrey Ingram Taylor. The mechanism of plastic deformation of crystals. part i.—theoretical. *Proceedings of the Royal Society of London. Series A, Containing Papers of a Mathematical and Physical Character*, 145(855):362–387, 1934.

[Teo13] Cristian Teodosiu. *Elastic models of crystal defects*. Springer Science & Business Media, 2013.

[TM11] Ellad B Tadmor and Ronald E Miller. *Modeling materials: continuum, atomistic and multiscale techniques*. Cambridge University Press, 2011.

[TN04] Clifford Truesdell and Walter Noll. The non-linear field theories of mechanics. In *The non-linear field theories of mechanics*, pages 1–579. Springer, 2004.

[TOP96] Ellad B Tadmor, Michael Ortiz, and Rob Phillips. Quasicontinuum analysis of defects in solids. *Philosophical magazine A*, 73(6):1529–1563, 1996.

[TPM09] Aidan P Thompson, Steven J Plimpton, and William Mattson. General formulation of pressure and stress tensor for arbitrary many-body interaction potentials under periodic boundary conditions. *The Journal of chemical physics*, 131(15):154107, 2009.

[TPO96] Ellad B Tadmor, Rob Phillips, and Michael Ortiz. Mixed atomistic and continuum models of deformation in solids. *langmuir*, 12(19):4529–4534, 1996.

[TSBK99] EB Tadmor, GS Smith, N Bernstein, and E Kaxiras. Mixed finite element and atomistic formulation for complex crystals. *Physical Review B*, 59(1):235, 1999.

[TVMN19] Christian Thiel, Jendrik Voss, Robert J Martin, and Patrizio Neff. Shear, pure and simple. *International Journal of Non-Linear Mechanics*, 112:57–72, 2019.

[Vol07] Vito Volterra. Sur l'équilibre des corps élastiques multiplement connexes. In *Annales scientifiques de l'École normale supérieure*, volume 24, pages 401–517, 1907.

[VVLZ+03] Krystyn J Van Vliet, Ju Li, Ting Zhu, Sidney Yip, and Subra Suresh. Quantifying the early stages of plasticity through nanoscale experiments and simulations. *Physical Review B*, 67(10):104105, 2003.

[WG05] D Weygand and P Gumbsch. Study of dislocation reactions and rearrangements under different loading conditions. *Materials Science and Engineering: A*, 400:158–161, 2005.

[Wil54] Alan Herries Wilson. The theory of metals. 1954.

[WJCK01] Yu U Wang, YM Jin, AM Cuitino, and AG Khachaturyan. Nanoscale phase field microelasticity theory of dislocations: model and 3d simulations. *Acta Materialia*, 49(10):1847–1857, 2001.

[WSS87] Michael Widom, Katherine J. Strandburg, and Robert H. Swendsen. Quasicrystal equilibrium state. *Phys. Rev. Lett.*, 58:706–709, Feb 1987.

[Zan96] Giovanni Zanzotto. The cauchy–born hypothesis, nonlinear elasticity and mechanical twinning in crystals. *Acta Crystallographica Section A*, 52(6):839–849, 1996.

[ZLVV+04] Ting Zhu, Ju Li, Krystyn J Van Vliet, Shigenobu Ogata, Sidney Yip, and Subra Suresh. Predictive modeling of nanoindentation-induced homogeneous dislocation nucleation in copper. *Journal of the Mechanics and Physics of Solids*, 52(3):691–724, 2004.

[ZRHdlR00] HM Zbib, M Rhee, JP Hirth, and T Diaz de la Rubia. A 3d dislocation simulation model for plastic deformation and instabilities in single crystals. *Journal of the Mechanical Behavior of Materials*, 11(1-3):251–256, 2000.

[ZRSOB17] Luis A Zepeda-Ruiz, Alexander Stukowski, Tomas Oppelstrup, and Vasily V Bulatov. Probing the limits of metal plasticity with molecular dynamics simulations. *Nature*, 550(7677):492, 2017.

[ZSZ+17] Peng Zhang, Oguz Umut Salman, Jin-Yu Zhang, Gang Liu, Jérôme Weiss, Lev Truskinovsky, and Jun Sun. Taming intermittent plasticity at small scales. *Acta Materialia*, 128:351–364, 2017.

[ZT00a] O.C. Zienkiewicz and R.L. Taylor. *The Finite Element Method: The basis*. Fluid Dynamics. Butterworth-Heinemann, 2000.

[ZT00b] Olgierd Cecil Zienkiewicz and Robert Leroy Taylor. *The finite element method: solid mechanics*, volume 2. Butterworth-heinemann, 2000.

[ZZ08] Yuan Zhong and Ting Zhu. Simulating nanoindentation and predicting dislocation nucleation using interatomic potential finite element method. *Computer Methods in Applied Mechanics and Engineering*, 197(41-42):3174–3181, 2008.

[ZZNH18] Songlin Zheng, Dongchang Zheng, Yong Ni, and Linghui He. Improved phase field model of dislocation intersections. *npj Computational Materials*, 4(1):20, 2018.